# ATOMISTIC SIMULATIONS OF DISLOCATION NUCLEATION IN SINGLE CRYSTALS AND GRAIN BOUNDARIES

A Dissertation
Presented to
The Academic Faculty

by

Mark A. Tschopp Jr.

In Partial Fulfillment
of the Requirements for the Degree
Doctor of Philosophy in
Materials Science and Engineering

Materials Science and Engineering
Georgia Institute of Technology
August 2007

# ATOMISTIC SIMULATIONS OF DISLOCATION NUCLEATION IN SINGLE CRYSTALS AND GRAIN BOUNDARIES

Approved by:

Professor David L. McDowell, Advisor
Materials Science and Engineering
*Georgia Institute of Technology*

Professor Arun Gokhale
Materials Science and Engineering
*Georgia Institute of Technology*

Professor Thomas Sanders
Materials Science and Engineering
*Georgia Institute of Technology*

Professor Naresh Thadhani
Materials Science and Engineering
*Georgia Institute of Technology*

Professor Min Zhou
Mechanical Engineering
*Georgia Institute of Technology*

Date Approved: June 29, 2007

*To my wife Meredith and my son Samuel*

# TABLE OF CONTENTS

# LIST OF TABLES

# LIST OF FIGURES

# LIST OF SYMBOLS OR ABBREVIATIONS

**ATGB** Asymmetric tilt grain boundary.

**BCC** Body-centered cubic.

**CINEB** Climbing image nudged elastic band.

**CTB** Coherent twin boundary.

**CSL** Coincident site lattice.

**CN** Coordination number.

**DOF** Degrees of freedom.

**DSC** Displacement shift complete.

**EBSD** Electron backscatter diffraction.

**EAM** Embedded-atom method.

**FCC** Face-centered cubic.

**FIB** Focused ion beam.

**GSF** Generalized stacking fault.

**GB** Grain boundary.

**GBE** Grain boundary engineering.

**HCP** Hexagonal close-packed.

**HRTEM** High resolution transmission electon microscopy.

**ISF** Intrinsic stacking fault.

**LPF** Lineal path function.

**MRSS** Maximum resolved shear stress.

**MEMS** Micro electromechanical systems.

**MEAM** Modified embedded-atom method.

**2NN MEAM** Second nearest neighbor modified embedded-atom method.

**MD** Molecular dynamics.

**MS** Molecular statics.

| | |
|---|---|
| **nc** | Nanocrystalline. |
| **NEMS** | Nano electromechanical systems. |
| **NPT** | Ensemble with constant atoms, pressure and temperature, *i.e.*, an isothermal-isobaric ensemble. |
| **NVT** | Ensemble with constant atoms, volume and temperature. |
| **QS** | Quasistatic. |
| **RBT** | Rigid body translation. |
| **SEM** | Scanning electron microscope. |
| **SC** | Single crystal. |
| **SFE** | Stacking fault energy. |
| **SU** | Structural unit. |
| **SUM** | Structural unit model. |
| **SITB** | Symmetric incoherent twin boundary. |
| **STGB** | Symmetric tilt grain boundary. |
| **TEM** | Transmission electron microscopy. |
| **TPCF** | Two-point correlation function. |
| **VMD** | Visual molecular dynamics code. |
| **WARP** | Parallel molecular dynamics and molecular statics code. |
| **2D** | Two-dimensional. |
| **3D** | Three-dimensional. |
| $a_0$ | Lattice constant. |
| $A_{GB}$ | Grain boundary area. |
| $b$ | Burgers vector. |
| $\mathbf{c}_\mathrm{i}$ | Tilt direction vector in crystal $i$. |
| $C_{ij}$ | Elastic moduli. |
| $d$ | Grain size. |
| $d_{GB}$ | Distance between grain boundaries in the periodic computational cell. |

| | |
|---|---|
| $d_{ijk}$ | Distance between grid point and nearest atom core, used for free volume calculations. |
| $d_i$ | Interplanar spacing for crystal $i$. |
| $D_c$ | Nanoporosity damage parameter [1], which gives an approximation of the grain boundary free volume. |
| $D_c^*$ | Nanoporosity damage parameter, normalized for comparison of grain boundary free volume content. |
| $E$ | Elastic modulus, in general. |
| $E_{[hkl]}$ | Elastic modulus for direction [$hkl$]. |
| $F\left(\overline{\rho}^i\right)$ | Energy to embed atom $i$ into the background electron density for EAM potentials. |
| $f_1$ | Volume fraction occupied by free volume. |
| $f_1^*$ | Volume fraction occupied by free volume normalized by grain boundary area. |
| $\mathbf{F}^{\mathrm{i}}$ | Interatomic force vector on atom $i$ due to its surroundings. |
| $\mathbf{F}_{\mathrm{ij}}$ | Deformation gradient. |
| $\mathbf{F}_\alpha^{\mathrm{ij}}$ | Force vector between atom $i$ and atom $j$ in the direction $\alpha$. |
| $F_n$ | Force normal to the interface. |
| $\mathbf{h}$ | Basis vectors describing the boundaries of the simulation cell box. |
| $\mathbf{I}$ | Identity tensor. |
| $k_B$ | Boltzmann's constant. |
| $K^bc$ | Elastic stiffness for a bicrystal configuration. |
| $L$ | Length, with subscripts denoting facet lengths, etc. |
| $\ell_{ij}$ | Direction cosines relating a coordinate axis fixed to the slip plane to a fixed specimen coordinate system. |
| $L_{11}(\mathbf{r_k})$ | Lineal path function for free volume in the direction $\mathbf{r_k}$. |
| $L_{11}^*(\mathbf{r_k})$ | Lineal path function for free volume in the direction $\mathbf{r_k}$, normalized for grain boundaries. |
| $\mathbf{M}$ | Misorientation matrix. |
| $m^i$ | Mass of the $i^{th}$ atom. |

| | |
|---|---|
| $N$ | Total number of atoms in the simulation cell. |
| $N^*$ | Number of nearest neighbor atoms for atom $i$. |
| $N_s$ | Number of slipped nearest neighbor atoms for atom $i$. |
| $N_s$ | Number of slipped nearest neighbor atoms for atom $i$. |
| $\mathbf{n}_\mathrm{i}$ | Grain boundary normal vector in crystal $i$. |
| $n_x$ | Number of grid points in the x, y ($n_y$), and z ($n_z$) directions; used for free volume calculations. |
| $N_{ijk}$ | An indicator matrix that defines whether each grid point is associated with free volume or not. |
| $NF$ | Normal factor, which resolves the applied stress into a stress normal to the slip plane. |
| $NF_0$ | Normal factor defined in the initial configuration, prior to deformation. |
| $\mathbf{P}_\mathrm{ext}$ | External pressure of the surroundings for an NPT ensemble. |
| $P^i$ | Centrosymmetry parameter for atom $i$. |
| $P_{11}(\mathbf{r}_\mathrm{k})$ | Two-point correlation function for free volume in the direction $\mathbf{r_k}$. |
| $P^*_{11}(\mathbf{r}_\mathrm{k})$ | Two-point correlation function for free volume in the direction $\mathbf{r_k}$, normalized for grain boundaries. |
| $\mathbf{p}^\mathrm{i}$ | Momentum vector of the $i^{th}$ atom. |
| $\mathbf{p}_\mathrm{i}$ | Grain boundary period vector in crystal $i$. |
| $PF$ | Coslip factor, which resolves the applied stress into a shear stress normal to the slip direction on the slip plane. |
| $Q$ | Activation energy. |
| $Q^*$ | Activation energy in the absence of applied stress. |
| $r_cut$ | Cutoff radius used for coordination number analysis. |
| $\mathbf{r}_\mathrm{N}$ | Position vectors for N atoms within the system. |
| $\mathbf{r}^\mathrm{i}$ | Position vector of the $i^{th}$ atom. |
| $\mathbf{r}^\mathrm{ij}$ | Distance vector between atoms $i$ and $j$. |
| $\mathbf{R}_0$ | Center of mass of the system. |
| $R^2$ | Correlation coefficient. |

| | |
|---|---|
| $s^i$ | Slip vector for atom $i$. |
| $S_{ij}$ | Elastic compliances. |
| $SF$ | Schmid factor, which resolves the applied stress into a shear stress in the slip direction on the slip plane. |
| $SF_0$ | Schmid factor defined in the initial configuration, prior to deformation. |
| $SF^{\max}_{(hkl)}$ | Maximum Schmid factor on the ($hkl$) slip plane. |
| $T$ | Temperature, in general. |
| $T\,(t)$ | Instantaneous temperature. |
| $\mathrm{T_m}$ | Melting temperature. |
| $\mathrm{T_{ext}}$ | External temperature of the surroundings for NVT/NPT ensembles. |
| $U\,(\mathbf{r}_\mathrm{N})$ | Potential energy as a function of the atomic position vectors. |
| $V$ | Volume of the computational cell. |
| $\mathbf{v}^\mathrm{i}$ | Velocity vector of the $i^{th}$ atom. |
| $w$ | Dissociation width. |
| $W^{bc}$ | Work required for dislocation nucleation from a bicrystal configuration. |
| $\mathbf{x}^\mathrm{ij}$ | Distance vector between atoms $i$ and $j$ in the current configuration. |
| $\mathbf{X}^\mathrm{ij}$ | Distance vector between atoms $i$ and $j$ in the reference configuration. |
| $\alpha$ | Minimum boundary plane inclination angle separating two symmetric tilt grain boundaries of the same CSL system, *e.g.*, $\alpha = 45^\circ$ for the $\langle 100 \rangle$ system and $\alpha = 90^\circ$ for the $\langle 110 \rangle$ system. |
| $\gamma$ | Isobaric damping constant – a dampening term that augments the evolution of the isobaric friction coefficient, $\eta$. |
| $\gamma^i$ | Potential energy of atom $i$. |
| $\gamma^i_{bulk}$ | Bulk potential energy for atom $i$. |
| $\gamma_{GB}$ | Grain boundary energy. |
| $\gamma_{ISF}$ | Intrinsic stacking fault energy per unit volume. |
| $\gamma_\Phi$ | Asymmetric grain boundary energy as a function of the inclination angle, $\Phi$. |
| $\gamma_{Surface}$ | Surface energy. |
| $\gamma_{SF}$ | Stable stacking fault energy. |

| | |
|---|---|
| $\gamma_{USF}$ | Unstable stacking fault energy. |
| $\delta_n$ | Displacement normal to the interface. |
| $\epsilon$ | Strain. |
| $\epsilon^{bc}_{\max}$ | Strain corresponding to the maximum attainable stress for a bicrystal configuration. |
| $\zeta$ | Thermodynamic friction coefficient. |
| $\eta$ | Isobaric friction coefficient. |
| $\theta$ | Grain boundary misorientation angle. |
| $\mu_s$ | Coefficient for the nucleation stress model that modifies the relative weight of the resolved Schmid shear stress in the slip direction on the slip plane. |
| $\mu_n$ | Coefficient for the nucleation stress model that modifies the relative weight of the resolved non-Schmid stress normal to the slip plane. |
| $\mu_p$ | Coefficient for the nucleation stress model that modifies the relative weight of the resolved non-Schmid shear stress perpendicular to the slip direction on the slip plane. |
| $\nu_0$ | Jump frequency. |
| $\nu_T$ | Thermostating rate for NVT/NPT ensembles. |
| $\nu_P$ | Barostating rate for an NPT ensemble. |
| $\xi$ | Parameter describing the mean boundary plane, as defined by Sutton and Vitek [2]. |
| $\bar{\rho}^i$ | Averaged background electron density at atom $i$ due to the neighboring atoms. |
| $\Sigma$ | Reciprocal density of coincident sites at the boundary. |
| $\sigma$ | Stress, in general. |
| $\sigma$ (t) | Instantaneous stress tensor as a function of time. |
| $\sigma_0$ | Friction stress required to move individual dislocations. |
| $\sigma_{NF}$ | Resolved stress normal to the {111} slip plane. |
| $\sigma_Y$ | Yield stress. |
| $\sigma^{bc}_{\max}$ | Maximum attained stress for a bicrystal configuration, which corresponds to the dislocation nucleation stress. |

| | |
|---|---|
| $\sigma_{\max}^{sc}$ | Maximum attained stress for a single crystal configuration, which corresponds to the dislocation nucleation stress. |
| $\tau$ | Shear modulus. |
| $\tau_{ideal}$ | Ideal shear strength. |
| $\tau_{PF}$ | Resolved shear stress in the coslip direction on the {111} slip plane. |
| $\tau_{SF}$ | Resolved shear stress in the slip direction on the {111} slip plane. |
| $\tau(w)$ | Interaction energy between two 'boundaries' for a dissociated grain boundary. |
| $\Phi$ | Inclination angle of the grain boundary plane from a specified grain boundary. |
| $\phi\left(r^{\mathrm{ij}}\right)$ | Pair interaction energy for atoms $i$ and $j$, separated by the scalar distance $r_{\mathrm{ij}}$. |
| $\Omega$ | Activation volume. |

# SUMMARY

The interest in nanocrystalline materials has been partially motivated by improvements in mechanical properties over coarser grained polycrystalline materials through the classical Hall-Petch relationship. The mechanisms through which nanocrystalline materials plastically deform are primarily due to the increased fraction of grain boundaries at these scales and are not as well understood as those at larger grain sizes. Atomistic simulations have provided much insight into the inelastic deformation behavior of nanocrystalline materials, as in-situ experiments at this scale are often very difficult. In line with these simulations, this research will concentrate on the nucleation of dislocations from the grain boundaries in face-centered cubic aluminum and copper through atomistic simulations.

One area of interest is how the grain boundary degrees of freedom impact the interface structure and dislocation nucleation. The recent ability to experimentally characterize both grain boundary misorientation and grain boundary plane inclination has shown that asymmetric tilt grain boundaries (ATGBs) have the highest frequency in polycrystals. Moreover, research in grain boundary engineering has concentrated on grain boundaries with a high density of coincident sites in the boundary plane, *i.e.*, low $\Sigma$ values.

Consequently, this dissertation primarily focuses on low order $\Sigma$ asymmetric tilt grain boundaries. First, the structure and energy of these faceted, dissociated grain boundary structures is investigated. Atomistic simulations show that $\Sigma 3$ ATGBs can be decomposed into the structural units of the $\Sigma 3$ symmetric tilt grain boundaries (STGBs), *i.e.*, the coherent and incoherent twin boundaries. Moreover, the energy for all $\Sigma 3$ ATGBs can be predicted with only the energies of the $\Sigma 3$ STGBs and the inclination angle. Understanding the structure of $\Sigma 3$ ATGBs provides insight into dislocation nucleation from these boundaries. Further work into the structure and energy of other low order $\Sigma$ ATGBs and the

spatial distribution of free volume within the grain boundaries also provides insight into dislocation nucleation mechanisms.

Molecular dynamics simulations are used to apply uniaxial tension perpendicular to these boundaries. The resulting dislocation nucleation mechanisms in Σ3 ATGBs are highly dependent on the faceted structure of these boundaries. Grain boundary dislocation sources can act as perfect sources/sinks for dislocations or may violate this premise by increasing the dislocation content of the boundary during nucleation. Furthermore, simulations under uniaxial tension and uniaxial compression have shown that dislocation mechanisms – *e.g.*, nucleation of the second partial dislocation in Cu – are highly dependent on the loading directionality.

Models that use the resolved stress components on the slip system of dislocation nucleation to predict the atomic stress required for dislocation nucleation from single crystals and grain boundaries are investigated as well. The first step in predicting the nucleation stress for grain boundaries is to isolate the effect of lattice orientation, *i.e.*, single crystal deformation simulations. It is found that the resolved stress normal to the slip plane on which the dislocation nucleates plays a commanding role in the dislocation nucleation stresses and mechanisms. The influence of thermal activation on grain boundary dislocation nucleation can be accounted for with activation volumes and activation energies calculated from atomistic simulations.

The synthesis of all aspects of this dissertation provides a better fundamental understanding of how the grain boundary character influences dislocation nucleation in nanocrystalline materials.

# CHAPTER I

# INTRODUCTION

## *1.1 Motivation*

Grain boundaries, interfaces separating grains of dissimilar orientation, play a vital role in the bulk properties of polycrystalline materials. Recently, the need for a better of understanding of the role of grain boundaries in polycrystals has increased because of the ability to generate nanocrystalline materials [3–6], whereby the grain size is on the order of nanometers and the fraction of atoms in the grain boundaries is dramatically increased. Nanocrystalline materials represent an interesting research area because while their properties relate to the underlying material length scale (grain size), these nanometer-sized microstructures can be produced in bulk materials. Much of the recent scientific interest in nanocrystalline materials has regarded their mechanical properties and the atomic-level plastic deformation in the grain boundaries [7–29]. In line with these studies, this dissertation will concentrate mainly on plasticity in face-centered cubic (FCC) nanocrystalline materials, with a specific focus on dislocation nucleation phenomena occurring at grain boundaries in copper and aluminum.

The interest in nanocrystalline (nc) materials has been motivated by potential improvements in mechanical properties over coarser grained polycrystalline materials [30] through the classical Hall-Petch relationship [31, 32], which is defined as,

$$\sigma_Y = \sigma_0 + \frac{k}{\sqrt{d}} \tag{1.1}$$

In this equation, $\sigma_Y$ is the yield stress, $\sigma_0$ is the friction stress required to move individual dislocations, $k$ is the constant, and $d$ is the grain size. The increase in yield strength

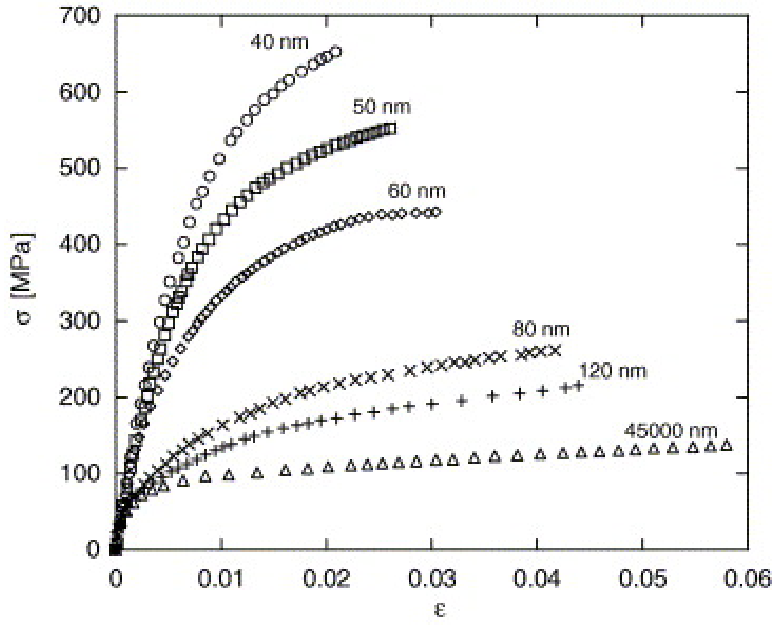


**Figure 1.1:** True stress-true strain curves for nanocrystalline aluminum at a strain rate of 0.0001 $s^{-1}$, with different grain size due to milling for different time duration, as in Khan *et al*. [35].

with decreasing grain size is directly attributed to the grain boundaries, which serve as obstacles to dislocation motion. Therefore, as the grain size is decreased to the nanoscale, the strength of the polycrystalline materials should increase. Early studies of the strength of nanocrystalline materials [33, 34] had difficulty separating the strengthening effect of the nanocrystalline grain size from the weakening effect of small pores due to processing. However, later studies have shown much higher yield strengths and significantly better ductilities for nanocrystalline materials [35–39]. For example, Figure 1.1 shows the true stress-true strain curves for nanocrystalline aluminum formed by ball milling, whereby different grain sizes (from 40 nm to 45, 000 nm) were obtained by varying the time durations of milling. A large increase in the yield strength of the nanocrystalline aluminum was observed with a decreasing grain size.

Numerous mechanical experiments on nanocrystalline materials have shown that there is a physical limit to the strength increase predicted by the Hall-Petch relation with decreasing grain size [34, 40], *i.e.*, the "inverse" Hall-Petch behavior. Experiments have revealed

the breakdown of applicability of the classical Hall-Petch relation at grain sizes typically somewhere between 10-20 nm, whereby the nc material has a lower yield strength with decreasing grain size in this regime. A multitude of theories have been proposed to explain the softening effect with further decreases in the grain size. As explained by Li [41], one school of thought considers the material as a composite of a grain boundary (GB) phase and a grain interior phase, whereby the softening is due to a soft GB phase [42], an increase in the GB thickness with decreasing grain size [43], or an amorphous GB phase of constant thickness with a pressure dependent yield stress [44]. Other theories consider a change in the mechanism within the grain boundary for smaller grain sizes: *e.g.*, a Coble creep mechanism [34] or a grain boundary sliding mechanism based on atomistic simulations [18, 45]. Li [41] has shown that impurity segregation and grain boundary porosity can also explain the grain size dependence of yield stress in nanocrystalline materials. Numerous models have been developed based on these theories to capture the material length scale effect (grain size) associated with the Hall-Petch and inverse Hall-Petch behavior (*e.g.*, [46, 47]).

In terms of atomistic simulations, these length scale effects are manifested by underlying physical mechanisms associated with inelastic deformation. For ordinary grain size polycrystals (micron scale), dislocations are nucleated and emitted by Frank-Read sources within grains, which are most likely associated with prior defect content or impurities. However, as the grain size decreases, the grain boundary volume fraction increases, resulting in heterogeneous nucleation and emission of dislocations from the grain boundaries. Below a certain critical grain size, on the order of 10 nm, dislocation nucleation becomes limited and grain boundary-mediated processes (*e.g.*, grain boundary sliding and grain rotation) become dominant deformation mechanisms. These deformation mechanisms are confirmed by in situ transmission electron microscopy (TEM) experiments, which show grain boundaries emitting partial dislocations that form stacking faults and deformation twins in nc Al and Cu [48, 49], as well as grain boundary sliding and rotation processes during deformation in nc Ni [20] as shown in Fig. 1.2. While the deformation mechanisms

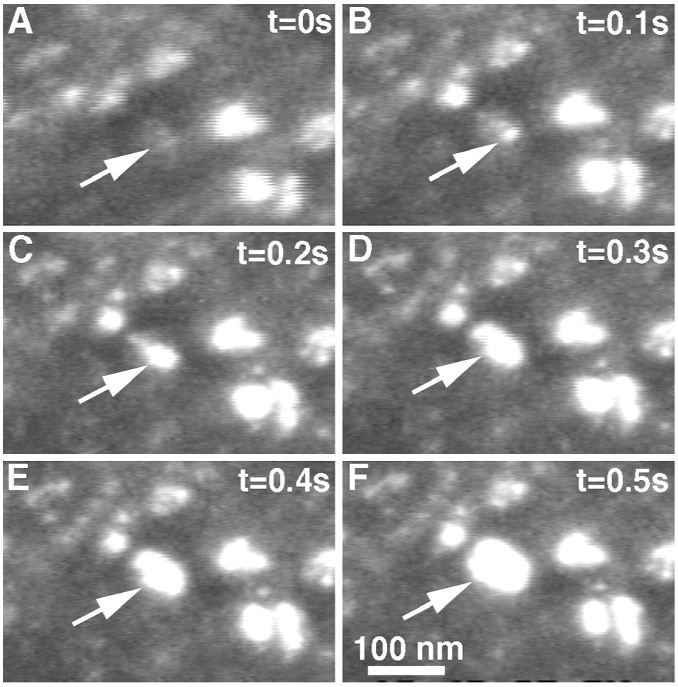


**Figure 1.2:** In situ dark-field TEM images of grain rotation in nanocrystalline nickel. Images are from Shan and coworkers [20].

at larger scales have been well studied for decades, a comprehensive understanding of the deformation mechanisms for nc materials is still being developed. However, the atomic level details of how dislocation nucleation occurs at the grain boundary is still not well-understood.

While some insight into the deformation mechanisms of nc materials was obtained from in situ high resolution TEM (HRTEM) experiments [20, 48, 49], these experiments are often very difficult to perform. In many cases, atomic simulations of plasticity phenomena actually preceded the experimental observation of the same phenomena. For example, Yamakov and coworkers predicted deformation twinning in aluminum with molecular dynamics simulations [25, 50] prior to the experimental TEM evidence of deformation twinning in nanocrystalline aluminum by Chen and colleagues [10]. However, a clear understanding of the deformation mechanisms at the nanoscale are vital to the design and reliability of engineered nanodevices (*e.g.*, MEMS and NEMS). Unfortunately, experiments at the nanoscale can be very time consuming and costly, often ambiguous, and require expensive

equipment and sensors. In situ TEM capabilities to monitor deformation mechanisms are very specialized, complicated and often ambiguous due to lack of constraint of the thin foils examined. This explains the limited amount of experiments dealing with deformation mechanisms in the literature. Accordingly, the difficulty with conducting critical experiments at the nanoscale motivates the use of atomistic simulations to better understand deformation mechanisms at the nanoscale.

Molecular dynamics (MD) simulations can serve as an effective tool for analyzing dislocation nucleation mechanisms and GB sliding processes in nc FCC materials [25, 51–58]. MD has been utilized to investigate the critical grain size for transition between dislocation emission-mediated and GB-mediated deformation modes, which also corresponds to the peak strength in FCC materials [19] and the breakdown of the classical Hall-Petch relation [31, 32]. Below this critical grain size, MD simulations have shown that GB sliding becomes the dominant deformation mechanism [59], giving rise to grain rotation. Furthermore, Van Swygenhoven and colleagues [54] have shown that GB sliding is triggered by atomic shuffling and stress-assisted free volume migration from triple junctions; the emission of dislocations from GBs was limited. In addition, three-dimensional nanocrystals that undergo grain rotation have also displayed the inverse Hall-Petch response, *i.e.*, the peak stress decreases with decreasing grain size [18, 59]. Above this critical grain size, MD simulations have shown that partial dislocation nucleation from GBs was accompanied by atomic shuffling in the GB [52, 60]. Schiøtz [61] predicted the formation of dislocation pileups at the GB in nc Cu samples with grain sizes above 15-20 nm. MD simulations have shown that nanocrystalline Ni does not emit a trailing partial dislocation even for grain sizes as large as 30 nm, but trailing partial dislocations were observed in nc Al [62] and nc Cu for grain sizes above 15-20 nm. Van Swygenhoven and coworkers [53] have also shown that dislocation propagation through a thermally activated pinning/depinning mechanism operates in fcc nanocrystalline materials. The deformation mechanisms observed in these MD simulations qualitatively agree with limited experimental results.

## *1.2 Problem statement*

Dislocation nucleation in molecular dynamics simulations of three-dimensional (3D) nanocrystalline materials is very complex, though. The combined tilt and twist character of grain boundaries and the inclination of the boundary plane with respect to the tensile axis complicates the analysis of the role of specific GB structures in nc simulations. Additionally, different boundaries may nucleate and emit dislocations at different stresses in nc simulations; it becomes very difficult to separate out the individual effects of GB structural units on dislocation nucleation. An alternative method is to use bicrystal simulations to study the dislocation nucleation mechanism for specific GBs [63, 64]. For example, Spearot and colleagues [64] have shown that the spacing between dissociated structural units for symmetric tilt grain boundaries (STGBs) impacts dislocation nucleation in Cu and Al. However, while many bicrystal simulations have focused on STGBs, experimental characterization shows that most boundaries in polycrystalline materials are actually asymmetric tilt grain boundaries (ATGBs) [65]. In view of the interest in boundaries with a high density of coincident sites (*i.e.*, $1/\Sigma$) for grain boundary engineering (GBE) purposes [66, 67], low order coincident site lattice (CSL) asymmetric tilt grain boundaries from the $\Sigma3$, $\Sigma5$, $\Sigma9$, $\Sigma11$, $\Sigma13$ systems were chosen for this research. Copper and aluminum were chosen as two FCC metals with significantly different stacking fault energies. Asymmetric tilt grain boundaries present an interesting case for studying dislocation nucleation behavior because of the faceted structure and dissimilar adjoining crystal orientations.

While molecular dynamics simulations are frequently used to study the deformation mechanisms at the nanoscale, relatively few studies have ventured from relatively simple symmetric tilt grain boundaries to study the structure-property relationships of more complex grain boundaries, such as asymmetric tilt grain boundaries. Due to the limited work in the area of asymmetric tilt grain boundaries, there are a multitude of research questions that will be addressed in this dissertation.

1. How does the grain boundary structure for a specific CSL system change as a function of the grain boundary plane orientation? What is the most effective methodology for obtaining the minimum energy structures of asymmetric tilt grain boundaries? Do asymmetric tilt grain boundaries have a well-defined boundary structure? Do they facet at an atomic level? How does the structure of asymmetric tilt grain boundaries relate to symmetric tilt grain boundaries? What is the role of low index planes in the structure of asymmetric tilt grain boundaries? Are there differences between the structure of different CSL systems and how they organize? Are there differences in structure between a low and high stacking fault energy FCC metal?

2. How does the grain boundary energy for a specific CSL system change as a function of the grain boundary plane orientation? What is the best form for describing the energy of asymmetric tilt grain boundaries? Does this help describe experimental observations of high frequencies of asymmetric tilt grain boundaries? How does this change as a function of the tilt axis, the $\Sigma$-value of the boundary systems, or the stacking fault energy of the material? Does the asymmetric tilt grain boundary energy provide insight into the structure of these boundaries, or vice versa? How?

3. How do grain boundary degrees of freedom affect mechanisms of dislocation nucleation in asymmetric tilt grain boundaries? How do they affect the relative ease of nucleation and emission? What is the relationship between grain boundary structure/energy and dislocation nucleation in asymmetric tilt grain boundaries? What is the role of faceting or dissociated partial dislocations on dislocation nucleation? Is dislocation nucleation in asymmetric tilt boundaries similar to that observed in symmetric tilt grain boundaries? How is it different? What is the role of dissimilar lattice orientations and resolved stress components on dislocation nucleation in asymmetric tilt grain boundaries?

4. What insight of dislocation nucleation in atomistic simulations can be incorporated

into higher order models? For instance, can the stress required for dislocation nucleation be predicted? If so, what parameters are important for such a model?

The answers to these research questions will provide a fundamental understanding of the relationship between asymmetric tilt grain boundary structures, energies, and inelastic properties, specifically dislocation nucleation. However, there are still unanswered research questions that relate to dislocation nucleation in symmetric tilt grain boundaries and single crystals as well.

5. What is the relationship between grain boundary structure and free volume? How does the spatial distribution of free volume affect properties? What is the best methodology for characterizing free volume in atomistic simulations? How does the free volume or its spatial distribution affect dislocation nucleation from boundaries?

6. What are the differences in dislocation nucleation between uniaxial tension and uniaxial compression applied perpendicular to the boundary? How does the stress required for dislocation nucleation change with loading directionality? How does the mechanism change? Does the boundary structure and free volume play an important role in tension and compression?

7. How does the uniaxial loading orientation of a single crystal affect homogeneous dislocation nucleation? How does uniaxial tensile and compressive loading influence single crystal dislocation nucleation mechanisms? How do resolved stress components impact homogeneous dislocation nucleation? Can simulations of homogeneous dislocation nucleation in single crystals provide insight for heterogeneous dislocation nucleation from grain boundaries? How are these mechanisms related? How are these different?

The synthesis of findings from all of these studies will allow for a more complete understanding of homogeneous and heterogeneous dislocation nucleation at the atomic level.

## *1.3 Research objective*

The research objective of this dissertation is to use atomistic simulations to examine the structure and dislocation nucleation/emission behavior of symmetric and asymmetric tilt grain boundaries in FCC copper and aluminum. This research objective is met through designing and performing systematic studies that answer the aforementioned research questions and any subsequent questions that arise.

Research questions 1 and 2 are motivated by the lack of understanding of asymmetric tilt grain boundary structure and energy. Consequently, the minimum energy equilibrium structure is obtained for each symmetric and asymmetric grain boundary to investigate the relationship between structure/energy and grain boundary degrees of freedom. This requires the development and implementation of a robust methodology that incorporates a nonlinear conjugate gradient algorithm [68] into the parallel molecular statics and dynamics code, WARP [69], that is used for these simulations. Additionally, the crystallographic orientations for a number of boundary structures with different grain boundary plane orientations and equivalent misorientation angles is needed for the bicrystal computational cell. The analysis of the results used post-processing computational codes to analyze the atomic coordinates at and nearby the boundary to identify the structural building blocks of different grain boundaries. The energy of these equilibrium structures represents the thermodynamically favorable configuration and can answer a number of the questions posed in question 2.

There is a distinct lack of understanding of the underlying physics of deformation (dislocation nucleation, emission, absorption, transmission) in asymmetric tilt grain boundaries as well. Consequently, uniaxial tensile deformation is applied perpendicular to the minimum energy boundary structure in the bicrystal computational cell to ascertain the dislocation nucleation/emission mechanisms and to address research question 3. For dislocation nucleation, the motion of the simulation cell bounds are prescribed to avoid any adverse effects on the instantaneous dislocation nucleation event. The analysis of the mechanical

behavior and the mechanisms as a function of the grain boundary degrees of freedom is combined with knowledge of the boundary structure and energy to provide a clear picture of dislocation emission from boundaries of complex structure. As a follow-up to deformation studies with uniaxial tension, several grain boundary configurations were deformed under an applied uniaxial compressive stress to examine asymmetries in dislocation nucleation behavior (question 6). To the authors knowledge, this is the first study to analyze tension-compression asymmetries in dislocation nucleation from boundaries.

Once the atomic scale dislocation nucleation mechanisms in asymmetric tilt grain boundaries are better understood, this insight must be incorporated into models that operate at higher length scales. In this work, the stress required for dislocation nucleation is correlated with parameters used in constitutive models to examine the potential validity of using atomistic results to inform continuum models at higher length scales. The model formulated helps address research question 4. In particular, parameters that resolve the uniaxial load into Schmid and non-Schmid stress components were considered along with an approximate measure of the grain boundary free volume. A model correlating the atomistic stress required for grain boundary dislocation nucleation with the resolved stress and free volume parameters has shown good agreement for many symmetric tilt grain boundaries. However, this model was unable to capture the influence of the E structural unit in some symmetric tilt grain boundaries, presumably due to its high free volume. A stereologically-based methodology was pursued to investigate the spatial correlation of free volume within these boundaries. This systematic study on grain boundary free volume addresses question 5.

The dependence of homogeneous dislocation nucleation on the single crystal loading orientation in uniaxial tension and compression is investigated to properly address question 7. In this manner, the role of lattice orientation on dislocation nucleation is isolated; this helps describe the role that the adjoining crystal lattices play on the heterogeneous nucleation of dislocations from grain boundaries.

## *1.4 Significance of this research*

Understanding fundamental material behavior at the nanoscale can lend insight into experiments as well as higher order simulations for modeling. Additional impetus for using atomistic simulations to investigate inelastic deformation processes is to inform higher scale models, such as continuum or dislocation dynamics models. For example, Warner *et al.* [70] implemented a continuum model for nc Cu informed by quasicontinuum deformation simulations for grain boundaries with different structural units [71, 72]. Additionally, Potirniche *et al.* [73] used molecular dynamics to investigate nanoscale void growth and coalescence in single crystal Ni for potential application to macroscopic constitutive relations. Similarly, dislocation dynamics simulations have been used to model the three-dimensional character of dislocation mechanisms for coupling with continuum finite element models [74]. As discussed in later chapters, the results of the current dissertation have potential applicability for informing cohesive zone finite element models, dislocation nucleation phenomena in dislocation dynamics models, or continuum constitutive relations [64]. The insight from atomistic simulations may have implications on the formulation of higher scale models and their assumptions.

Dislocation nucleation from grain boundaries at the nanoscale can also be used for grain boundary engineering purposes [75], whereby the character of the grain boundary structure can be designed to control the grain boundary dislocation processes and the bulk mechanical properties. Improved understanding of dislocation nucleation and emission behavior in nanocrystalline materials may lead to opportunities for grain boundary engineering at the nanoscale in the regime where grain boundaries act as the source of dislocations and plastic deformation. For instance, if the active nanoscale mechanisms can be accurately modeled, then materials can be engineered to take advantage of our fundamental knowledge of how materials deform. For example, Lu *et al.* [13] have recently shown that varying the processing parameters for electrodeposition in nanocrystalline copper introduces different growth

twin spacings (*i.e.*, Σ3 coherent twin boundaries), which results in significantly higher tensile strengths than coarse-grained Cu while retaining the high electrical conductivity of copper. In this respect, the nanoscale growth twins act as barriers to dislocation motion, but their low electrical resistivity compared to other high angle boundaries suppress the detrimental effects due to a higher grain boundary area in nanocrystalline materials. Increasing the distribution of Σ3 coherent twin boundaries in coarser grained polycrystals is a widely used technique for grain boundary engineering low stacking fault energy materials [66, 67].

The objective of grain boundary engineering is to increase the number of boundaries with favorable properties while decreasing the number of boundaries with detrimental properties. Grain boundaries with favorable properties are labeled "special" boundaries, while all other boundaries are termed "random" boundaries. While "special" boundaries have been associated with low order CSL boundaries, *i.e.*, a low Σ value, this is mainly due to the distinctly different properties of the Σ3 coherent twin. However, there is a wide range of possible Σ3 structures and associated properties, as will be discussed in later chapters. More recent viewpoints on "special" boundaries have re-examined the low Σ value criteria and suggested that "special" boundaries should refer specifically to the associated properties and not the Σ value. In line with these studies, the change in the grain boundary plane orientation shows how properties change for a boundary with a fixed Σ value (*i.e.*, fixed misorientation angle). Therefore, the atomic simulations in this work provide a more refined definition of "special" with regard to how grain boundary structure affects dislocation nucleation.

## *1.5 Dissertation structure*

This dissertation is organized as follows. Background information about grain boundaries and the simulation methodology used throughout this dissertation is presented in Chapter 2. The research results for this dissertation are broken down into three categories:

grain boundary structure simulations, grain boundary dislocation nucleation simulations, and continuum models for dislocation nucleation in single crystals and grain boundaries. The format of each chapter is based on submitted and published journal papers [64, 76–82], whereby an "introduction-methodology-results-summary" format is used. In this respect, each chapter is self-contained, although some knowledge of concepts in other chapters may be required. The simulation methodology for some chapters has been moved to Chapter 2 and discussed there, to reduce redundancy.

The structure, energy, and free volume of grain boundaries are investigated in chapters 3-5. Specifically, Chapter 3 examines the structure and energy of $\Sigma 3$ asymmetric tilt grain boundaries in copper and aluminum as a function of the grain boundary plane orientation. Chapter 4 examines the structure and energy of several low order CSL asymmetric tilt grain boundaries ($\Sigma 5$, $\Sigma 9$, $\Sigma 11$, $\Sigma 13$) in copper and aluminum as a function of the grain boundary plane orientation. Chapter 5 examines the structure and free volume in symmetric tilt grain boundaries with the E structural unit, because of the large associated free volume with this structural unit.

The dislocation nucleation mechanisms for symmetric and asymmetric tilt grain boundaries are investigated in chapters 6-8. Chapter 6 examines dislocation nucleation from $\Sigma 3$ asymmetric tilt grain boundaries in copper and aluminum as a function of the grain boundary plane orientation. Chapter 7 examines dislocation nucleation from symmetric tilt grain boundaries with the E structural unit in both uniaxial tension and uniaxial compression. Chapter 8 summarizes some general insight regarding dislocation sources provided from atomistic simulations of dislocation nucleation from grain boundaries in this work.

A model that correlates atomistic stresses required for dislocation nucleation with continuum parameters is presented in Chapters 9-11. Chapter 9 examines the relationship between single crystal homogeneous dislocation nucleation and grain boundary heterogeneous dislocation nucleation to formulate a model to predict the dislocation nucleation stresses. Chapter 10 expands the model for homogeneous dislocation nucleation in single

crystals by incorporating loading orientations from all over the [100]-[110]-[111] stereographic triangle. Chapter 11 thoroughly examines the influence of resolved stress components on homogeneous dislocation nucleation for single crystals under both uniaxial tension and compression. In addition to a more refined model that incorporates the evolution of the resolved stress components, Chapter 11 also examines tension-compression asymmetries in dislocation nucleation mechanical responses and mechanisms.

Chapter 12 summarizes the significant overall contribution of this dissertation as a whole. A summary of each chapter is discussed along with several important conclusions for each chapter. Last, future research directions that build upon this work are discussed.

# CHAPTER II

# BACKGROUND AND SIMULATION METHODOLOGY

## *2.1 Atomistic simulation methodology*

This research uses atomistic simulations to investigate the structure and properties of grain boundaries. Two main types of atomistic simulations are used in this work: molecular statics (MS) and molecular dynamics (MD). Molecular statics simulations employ numerical optimization techniques to minimize the potential energy of the system at 0 K. On the other hand, molecular dynamics simulations augments the atomic coordinates with atomic velocities to incorporate the effects of temperature into the system. Then, in an iterative manner, Newton's second law of motion is numerically integrated to solve for the evolution of atomic positions and velocities as a function of time. A brief overview of molecular statics, molecular dynamics, the potentials used, and other atomistic necessities are provided in this section along with the post-processing visualization techniques. For further information, Allen and Tildesley [83] and Haile [84] provide a more comprehensive review of atomistic simulations.

In these simulations, each atom is represented as a point mass in space while an interatomic potential provides a description of the potential energy as a function of interatomic spacing. The interatomic force on an atom $i$ is given as $\mathbf{F}^{\mathrm{i}}$ and is related to the interatomic potential $U$ through the relation,

$$\mathbf{F}^{\mathrm{i}} = -\frac{\partial U\left(\mathbf{r}_{\mathrm{N}}\right)}{\partial \mathbf{r}^{\mathrm{i}}} \tag{2.1}$$

Here, $U\left(\mathbf{r}_{\mathrm{N}}\right)$ denotes that the potential energy is a function of the position vectors of N atoms within the system ($\mathbf{r}_{\mathrm{N}}$). The negative derivative of $U$ with respect to the position vector of the $i^{th}$ atom ($\mathbf{r}^{\mathrm{i}}$) gives the force vector on atom $i$. In this equation and subsequent

equations in this chapter, the superscripts denote the atomic labels. Note that the choice of interatomic potential gives the functional form of $U(\mathbf{r}_N)$.

### 2.1.1 Molecular statics

Molecular statics (MS) considers athermal interactions (0 K) whereby the atomic positions are calculated via the minimization of the potential energy of the system. One numerical method is the Monte Carlo method [85] or the Metropolis sampling method [86]; these methods use a random rearrangement of atoms with an acceptance criterion to search for the minimum energy configuration. Another method is the conjugate gradient method [87, 88]; this method determines specific positional rearrangements of atoms, conjugate to the previous rearrangements, that follows the direction of steepest descent on the potential energy curve. The nonlinear conjugate gradient method is used to iteratively solve for the minimum energy configuration for the atomic positions within a predefined convergence limit.

In this research, it is vital that the initial grain boundary structures are accurately described prior to the deformation process. Thus, the initial grain boundary structures were obtained using a nonlinear conjugate gradient algorithm which incorporates the secant method to determine the appropriate step length and the Polak-Ribière formulation for the search direction [68]. For more details of the conjugate gradient method, the reader is referred to an article by Shewchuk [68]. The implementation of the nonlinear conjugate gradient algorithm into the molecular statics framework has been reviewed by Spearot [89].

Unfortunately, there is no algorithm that guarantees determination of the global minimum energy configuration. Thus, this work uses a large number of initial starting positions to increase the probability that the global minimum energy configuration is attained, as in previous bicrystal energy minimization calculations (*cf.* [90–92]). This is accomplished systematically by removing atomic layers at the interface or by manually translating the lattice regions normal and parallel to the interface plane and allowing the energy minimization

procedure to rearrange the interface atoms as necessary (resolving the microscopic degrees of freedom of the grain boundary). For example, to access the minimum energy GB structures for many asymmetric tilt grain boundaries discussed in subsequent chapters, energy minimization calculations utilize over 2700 initial configurations with different in-plane rigid body translations and atom deletion criterion [78]. Tschopp and McDowell found that some asymmetric tilt grain boundaries have accessibilities [90] as low as 0.1%. The methodology used to obtain these structures in discussed in more detail in Section 2.2.2.

### 2.1.2 Molecular dynamics

In molecular dynamics (MD), the motion of atoms is described by the interatomic potential (energy function), which is a function of the positions of the atoms in a system. The evolution of atom positions and velocities for each time step in the simulation is calculated using Newton's second law of motion. The equations of motion for all atoms are coupled to the equations of motion of all other atoms in the system through the conservative forces. By discretizing time into specific time steps, the coupled equations are solved based on the atomic positions and velocities at the previous time step. In this research, the velocity Verlet algorithm [93] is employed with a time step of 1 femtosecond. Once all the forces on the atoms have been computed using Eq. 2.1, then the Verlet algorithm can be employed by using Newton's second law of motion, *i.e.*,

$$\dot{\mathbf{p}}^{\mathrm{i}} = \mathbf{F}^{\mathrm{i}} = m^{i}\dot{\mathbf{v}}^{\mathrm{i}} \tag{2.2}$$

where

$$\dot{\mathbf{r}}^{\mathrm{i}} = \frac{d\mathbf{r}^{\mathrm{i}}}{dt} = \frac{\mathbf{p}^{\mathrm{i}}}{m^{i}} \tag{2.3}$$

In these equations, $m^{i}$ is the mass, $\mathbf{p}^{\mathrm{i}}$ is the momentum and $\mathbf{v}^{\mathrm{i}}$ is the velocity, where the superscript $i$ denotes the $i^{th}$ atom. The first derivative with respect to time is denoted by a dot. Equations 2.2 and 2.3 are the equations of motion for a perfectly isolated system.

However, most systems are not in perfect isolation and will interact with their surroundings. In this case, the equations of motion need to be augmented with additional differential equations to correctly describe the interaction between the system and its surroundings. Hoover [94] has shown that the formulation for the equations of motion for a constant volume, constant temperature (NVT) ensemble is given as

$$\begin{aligned} \dot{\mathbf{r}}^{\mathrm{i}} &= \frac{\mathbf{p}^{\mathrm{i}}}{m} \\ \dot{\mathbf{p}}^{\mathrm{i}} &= \mathbf{F}^{\mathrm{i}} - \zeta \mathbf{p}^{\mathrm{i}} \\ \dot{\zeta} &= \nu_T^2 \left( \frac{T(t)}{T_{ext}} - 1 \right) \end{aligned} \tag{2.4}$$

Here, $\zeta$ is a thermodynamic friction coefficient that evolves with the deviation of the instantaneous temperature, $T\,(t)$, from the external temperature of the surroundings, $\mathrm{T_{ext}}$. The thermostating rate, $\nu_T$, specifies the rate of the evolution of $\dot{\zeta}$.

The equations of motion can be similarly represented for the case of a system with constant pressure and temperature, *i.e.*, a isothermal-isobaric (NPT) ensemble. Melchionna *et al.* [95] have shown that the correct NPT distribution function is obtained using a modification to Nose and Hoover's [94, 96] original equations for the isothermal-isobaric case:

$$\begin{aligned} \dot{\mathbf{r}}^{\mathrm{i}} &= \frac{\mathbf{p}^{\mathrm{i}}}{m} + \eta \left( \mathbf{r}^{\mathrm{i}} - \mathbf{R}_0 \right) \\ \dot{\mathbf{p}}^{\mathrm{i}} &= \mathbf{F}^{\mathrm{i}} - (\eta + \zeta \mathbf{I})\, \mathbf{p}^{\mathrm{i}} \\ \dot{\zeta} &= \nu_T^2 \left( \frac{T(t)}{T_{ext}} - 1 \right) \\ \dot{\eta} &= \frac{\nu_P^2}{N k_B T_{ext}} V \left( \sigma\,(\mathbf{t}) - \mathbf{P}_{\mathrm{ext}} \mathbf{I} \right) \\ \dot{\mathbf{h}} &= \eta \mathbf{h} \end{aligned} \tag{2.5}$$

In Eq. 2.5, $\eta$ is the isobaric friction coefficient that acts to balance the deviation between the instantaneous stress tensor ($\sigma\,(\mathrm{t})$) and the specified external pressure ($\mathbf{P}_{\mathrm{ext}}$), $\mathbf{R}_0$ is the center of mass of the system, $\nu_P$ is the barostating rate, $N$ is the number of atoms, $k_B$ is Boltzmann's constant, $V$ is the system volume, and $\mathbf{h}$ is a tensor that contains the basis vectors for the box. In Eq. 2.5, $\dot{\zeta}$ and $\dot{\eta}$ act to control the system deviation from the temperature and pressure of the external reservoir, respectively. Furthermore, the integration of Eq. 2.5

is efficient, stable over a large number of timesteps, and minimal in memory requirements since no scaling is required.

The disadvantage of using Eq. 2.5 for dislocation nucleation simulations in an NPT ensemble is that the external pressure must be specified. The equations of motion move the simulation cell boundaries in an NPT ensemble based on the difference between the desired and current system pressures; since the cell boundaries are driven by the difference in pressures, the strain rate in the system is not constant. Yamakov *et al.* [56] have shown that by setting the desired system pressure in a given direction above a critical pressure, dislocation nucleation and emission occurs at the grain boundaries. However, if the desired system pressure is set below this critical pressure, the only deformation is due to grain boundary mediated processes, such as grain boundary sliding and diffusion.

Spearot *et al.* [97] have modified the Melchionna *et al.* [95] equations of motion such that the rate of change of the cell boundaries is prescribed and, hence, the applied strain rate is constant. As described by Spearot *et al.* [89, 97], the modified equations for the isothermal-isobaric case with a specified strain rate are given by

$$\begin{aligned}
\dot{\mathbf{r}}^{\mathrm{i}} &= \tfrac{\mathbf{p}^{\mathrm{i}}}{m} + \eta\left(\mathbf{r}^{\mathrm{i}} - \mathbf{R}_0\right) \\
\dot{\mathbf{p}}^{\mathrm{i}} &= \mathbf{F}^{\mathrm{i}} - (\eta + \zeta\mathbf{I})\,\mathbf{p}^{\mathrm{i}} \\
\dot{\zeta} &= \nu_T^2\left(\tfrac{T(t)}{T_{ext}} - 1\right) \\
\dot{\eta} &= \tfrac{\nu_P^2}{Nk_BT_{ext}} V\left(\sigma(t) - \mathbf{P}_{\mathrm{ext}}\mathbf{I}\right) - \gamma\eta \\
\dot{\mathbf{h}} &= \eta\mathbf{h}
\end{aligned} \tag{2.6}$$

Here, the evolution of the isobaric friction coefficient is augmented by the term $\gamma\eta$, an additional damping term necessary for smooth motion of the system boundaries. These NPT equations of motions are combined with a mixed set of boundary conditions, whereby the motion of one simulation cell boundary is specified with the other two boundaries following the equations of motion. This is accomplished by prescribing the rate of change of $\dot{\mathbf{h}}$ in the uniaxial loading direction and allowing the other two boundaries to move with

Eq. 2.6.

### 2.1.3 Virial stress

Stress calculations in atomistic simulations have been formulated in several ways. The virial stress is one example, *i.e.*,

$$\sigma = \frac{1}{V}\left[\frac{1}{2}\sum_{\mathrm{i}}\sum_{\mathrm{i}\neq\mathrm{j}}\frac{U'}{\mathbf{r}^{\mathrm{ij}}}\mathbf{r}_{\alpha}^{\mathrm{ij}}\mathbf{r}_{\beta}^{\mathrm{ij}} - \sum_{\mathrm{i}}\mathbf{m}^{\mathrm{i}}\mathbf{v}^{\mathrm{i}}\mathbf{v}^{\mathrm{i}}\right] \tag{2.7}$$

where $U'$ is the derivative of the potential energy with respect to position and $\mathbf{r}^{\mathrm{ij}}$ is the distance vector between atoms $i$ and $j$, *i.e.*, $\mathbf{r}^{\mathrm{ij}} = \mathbf{r}^{\mathrm{i}} - \mathbf{r}^{\mathrm{j}}$. The subscripts $\alpha$ and $\beta$ denote components in the $\alpha$ and $\beta$ directions, respectively.

For MD deformation simulations, this work will use the continuum stress measure of Zhou and McDowell [98] and Zhou [99] for a quantitative deformation response variable. The virial stress [83, 100–102] has been commonly used, but Zhou and McDowell [98] and Zhou [99] have shown that the virial stress is not equivalent to the continuum measure of Cauchy stress. Specifically, the microkinetic contribution to the virial stress formulation violates the classical conservation of momentum. Since this research aims at linking atomistic results to higher scale continuum models, the choice of stress measure must be equivalent to the continuum stress. While other authors have proposed different continuum stress measures for atomistics (*e.g.*, the Hardy stress in Zimmerman *et al.* [103]), the Zhou and McDowell formulation of the atomic stress is perhaps most appropriate for the current deformation simulations.

Consequently, the system stress was calculated using the virial definition without the kinetic portion [99], *i.e.*,

$$\sigma_{\alpha\beta} = \frac{1}{V}\sum_{i}^{N}\sum_{j(\neq i)}^{N^*}\mathbf{F}_{\alpha}^{\mathrm{ij}}\mathbf{r}_{\beta}^{\mathrm{ij}} \tag{2.8}$$

where $\mathbf{F}_{\alpha}^{\mathrm{ij}}$ is the force vector between atoms $i$ and $j$ in the direction $\alpha$, $\mathbf{r}_{\beta}$ is the distance vector in direction $\beta$, $N^*$ is the number of neighbor atoms for atom $i$, $N$ is the total number

of atoms in the simulation cell, and $V$ is the simulation cell volume. The volume averaged stress tensor $\sigma_{\alpha\beta}$ is the same as the global stress used in the MD simulations of Horstemeyer *et al*. [104, 105] to investigate length scale effects on yield. This stress measure is used throughout this work.

The stress measure in Eq. 2.8 is used to obtain critical stress components that relate to the dislocation nucleation event. Specifically, the **stress required for dislocation nucleation** is defined as the maximum uniaxial tensile stress in the bicrystal simulations. Visualization of selected grain boundary configurations with the centrosymmetry parameter [106] and the slip vector [107] have shown that dislocations are nucleated at a strain very close to that corresponding to the maximum tensile stress in both asymmetric tilt grain boundaries and single crystals. In some cases, dislocations appeared to nucleate slightly before reaching the maximum tensile stress (< 1.0% below the maximum tensile stress). However, in light of the difficulty of visually ascertaining exactly when the dislocation nucleates (*i.e.*, how many spatially clustered, disordered atoms on the slip plane constitute the nucleation of a dislocation?), the maximum tensile stress will provide an accurate indication of the stress required for dislocation nucleation throughout this work.

### 2.1.4 Embedded atom method potential

This research uses the embedded atom method (EAM) interatomic potential developed by Daw and Baskes [108, 109], which is applicable to FCC lattices with metallic bonds. Daw and Baskes based the EAM on the quasiatom [110] and effective medium [111] theories, in which an impurity is embedded in a host of atoms. The EAM views the energy of the system as the sum of the energy to embed an atom into a local electron density of all other atoms in the system and the energy of the pair interactions in the system. The total energy for the EAM potential is described as

$$U = \sum_i \left( F\left(\bar{\rho}^i\right) + \frac{1}{2} \sum_{j(\neq i)} \phi\left(r^{ij}\right) \right) \tag{2.9}$$

In these equations, $\overline{\rho}^i$ is the averaged background electron density at atom $i$ due to the remaining atoms in the system, $F\left(\overline{\rho}^i\right)$ is the energy to embed atom $i$ into the background electron density, and $\phi\left(r^{ij}\right)$ is the pair interaction for atoms $i$ and $j$, separated by the scalar distance $r^{ij}$. The background electron density is a superposition of the electron density contributed by all other atoms in the system, *i.e.*,

$$\overline{\rho}^i = \sum_{j(\neq i)} \rho\left(r^{ij}\right) \tag{2.10}$$

where the atoms $j$ in the summation are within a specified cutoff distance from atom $i$. The function $\rho\left(r^{ij}\right)$ characterizes the decay of electron density as a function of distance $r^{ij}$ from atom $j$.

An important assumption in the derivation of EAM is that the electron background density is spherically distributed. This restricts the use of EAM potentials to materials in which angular bonding is deemed unimportant, *e.g.*, certain FCC metals. In FCC metals, by empirically fitting to several key parameters (*e.g.*, equilibrium lattice constant, elastic moduli, *etc.*), Foiles *et al.* [112] show that the EAM potential accurately reproduces several properties of both pure metals and binary alloys, such as the vacancy migration energy, the vacancy formation volume, divacancy binding energy, divacancy migration energy, self-interstitial formation energy, self-interstitial formation volume, self-interstitial migration energy, surface energy, and impurity segregation energy. In addition, for MD simulations of deformation, reproducing the intrinsic and unstable stacking fault energies are essential for simulations of nucleation and motion of partial dislocations in FCC crystals.

The EAM assumption of non-directional bonding is inaccurate for body-centered cubic (BCC) and hexagonal close-packed (HCP) material systems; even certain FCC metals, such as Al, exhibit more directional bonding than others such as Cu [113]. For these materials, Baskes *et al.* [114–117] developed the modified embedded-atom method (MEAM), which uses the same formalism as EAM to account for the directionality of bonding to reproduce physical properties in various crystal structures including silicon, germanium, and

diamond cubic as well as HCP, BCC, and FCC crystal structures. However, when applied to MD simulations, the original MEAM has several shortcomings: the (111) surface energy is lower than the (100) surface energy in most BCC metals, contrary to experimental results [118,119], and a structure more stable than the original structure is created during MD simulations of some metallic crystal structures (*e.g.*, HCP metals in Mae *et al.* [120]). Lee and Baskes [121] show that by modifying the original MEAM formalism to partially include the interactions of the second nearest neighbors, the second nearest neighbor MEAM (2NN MEAM) agrees better with the experimental data for surface energies and with the structure in MD simulations. The 2NN MEAM has been applied to both BCC transition metals [122] and FCC metals [123] to alleviate both of the aforementioned problems with the original MEAM formulations. However, the 2NN MEAM still does not predict stacking fault energies for Al better than EAM potentials; in view of the focus on dislocations in this research, the EAM potential is therefore used for both the Cu and Al interatomic potentials.

Embedded atom method potentials for Cu [124] and Al [125] were used for this research. These potentials were experimentally fit to give the correct physical properties for Cu and Al, including the equilibrium lattice parameter, the cohesive energy, three elastic constants, and the vacancy formation energy, to name a few. The calculated stacking fault energies for these potentials are consistent with experimental data and *ab initio* calculations; for Al, the stable stacking fault energy (SFE) was even included as a highly weighted fitting parameter. The stable SFE is critical for atomistic simulations of fracture and deformation because it determines the width of dislocation dissociation in the lattice; this not only affects full and partial dislocation emission, but also the GB structure of materials. These particular EAM potentials also approximate the unstable SFE adequately; this is important for capturing dislocation nucleation events [126]. The choice of EAM potentials determines the accuracy of deformation results, especially in Al where EAM potentials

have chronically underestimated the stable stacking fault energy [127]. The stable and unstable stacking fault energy calculated by the EAM potentials of Mishin *et al.* are closer to density functional theory calculations [128] than other EAM potentials (*e.g.*, Foiles *et al.* [112], Voter and Chen [129], Ercolessi and Adams [130], Liu *et al.* [131]).

Recent simulations have argued the importance of both the stable and unstable stacking fault energy for simulating dislocation processes with embedded atom method potentials. For example, Van Swygenhoven and colleagues [23, 132] argued the importance of both the intrinsic and unstable stacking fault energies, $\gamma_{SF}$ and $\gamma_{USF}$ to model grain boundary structure and dislocation nucleation. Moreover, Van Swygenhoven *et al.* proposed that the transition between partial and full dislocation emission can be correctly understood in terms of the generalized planar fault energy curve, which considers both the intrinsic and the unstable stacking fault energies. They find that the ratio of intrinsic to unstable stacking fault energies is a critical parameter for determining whether a trailing partial dislocation is emitted from the GB in nanocrystalline materials; as this ratio approaches unity, the energy barrier for creating a trailing partial dislocation is very low. Mishin *et al.* reported excellent agreement between the intrinsic stacking fault energy computed with their Cu and Al potentials as compared with experimental and *ab initio* calculations. Moreover, an analysis by Boyer *et al.* [133] and Zimmerman *et al.* [127] of stress-displacement, atomic relaxation, and the $\gamma$-surface for $\{111\}\langle 112\rangle$ shear indicated that the Mishin *et al.* Cu and Al potentials capture the essential characteristics of deformation, including the unstable stacking fault energy, in line with *ab initio* electronic structure calculations. Thus, the EAM potentials utilized in this research are considered sufficient to model the structure of symmetric and asymmetric tilt grain boundaries as well as the nucleation of dislocations from these boundaries.

### 2.1.5 Visualization of atoms

In atomistic simulations, post-processing of the atomic information requires various techniques and computational tools to effectively visualize dislocation activity during the deformation process. Several approaches have been used to visualize dislocation activity. Dislocations are typically visualized with either centrosymmetry [106], common neighbor analysis [134, 135], slip vector [107], energy [136] or coordination number [137]. Figure 2.1 shows some examples of how these different visualization tools are used to visualize dislocations. This research mainly employed the visualization methods in Fig. 2.1(a) and 2.1(b), *i.e.*, the centrosymmetry parameter and slip vector, respectively.

The centrosymmetry parameter [106] characterizes the position of an atom with respect to its nearest neighbors. The centrosymmetry parameter exploits that a centrosymmetric FCC material will remain centrosymmetric upon elastic deformation, *i.e.*, each atom has pairs of equal and opposite bonds to its nearest neighbors. In an local elastic environment, the centrosymmetry for an atom is zero. However, the centrosymmetry parameter is non-zero for atoms at free surfaces, dislocations, stacking faults, grain boundaries and other lattice defects. The centrosymmetry parameter for each atom is defined as

$$P^i = \sum_{j=1,6} \left| \mathbf{r}^j + \mathbf{r}^{j+6} \right|^2, \tag{2.11}$$

where $\mathbf{r}^j$ and $\mathbf{r}^{j+6}$ are the bond length vectors of two neighboring atoms on opposite sides of the atom in question. The summation of 1 to 6 incorporates the 12 nearest neighbors (or 6 bond pairs) for an atom in an FCC material. The centrosymmetry parameter ($P^i$) increases from zero as the centrosymmetry for atom $i$ decreases.

The slip vector [107] quantifies the Burgers vectors of dislocations created during deformation by computing the displacement of atoms from their initial positions relative to their nearest neighbors. The slip vector ($s^i$) for atom $i$ is defined as

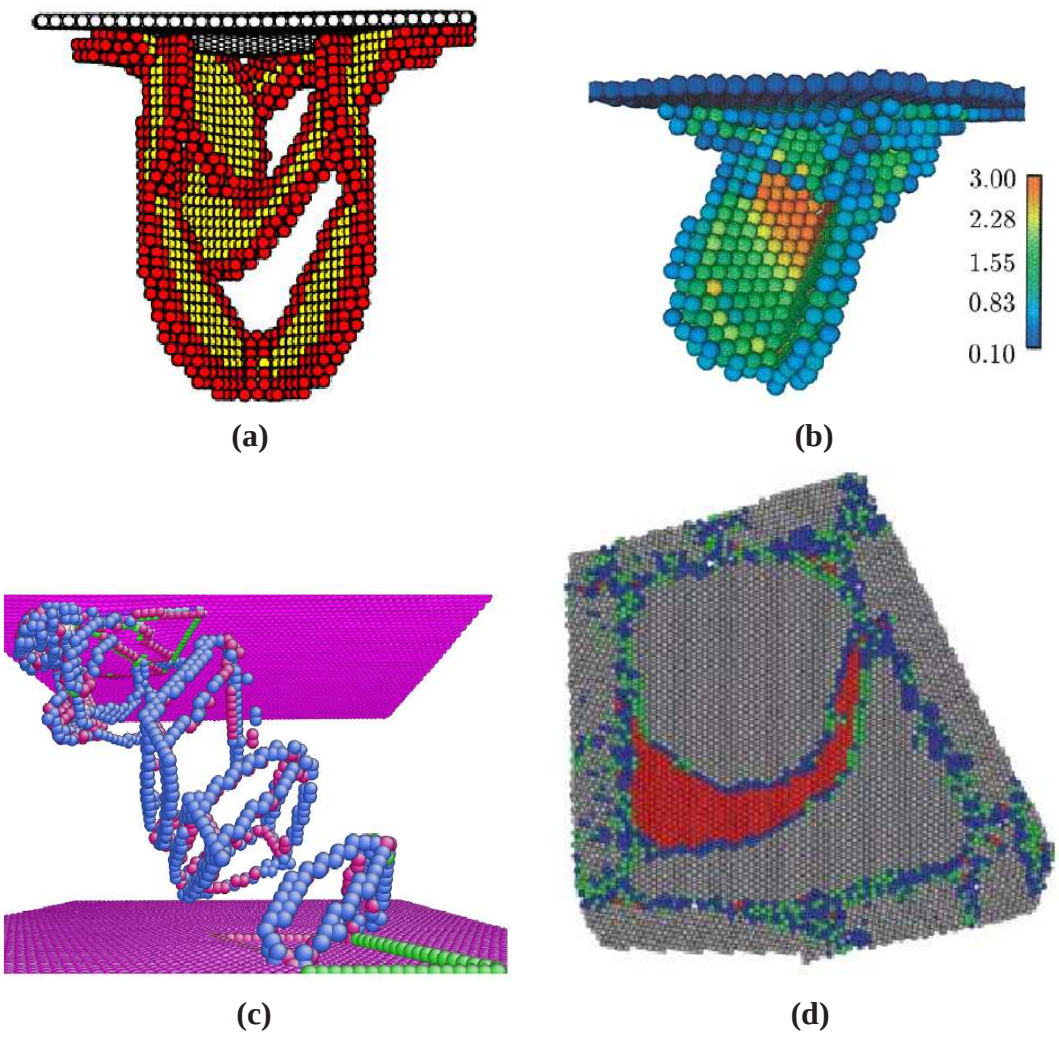


**Figure 2.1:** Methods for visualizing dislocations in atomistic simulations: (a) Centrosymmetry parameter [106], (b) slip vector parameter [107], (c) coordination number [137], and common neighbor analysis [134, 135] (from Ref. [138]).

$$s^i = -\frac{1}{N_s}\sum_{j\neq i}^{N^*}\left(\mathbf{x}^{ij} - \mathbf{X}^{ij}\right), \tag{2.12}$$

where $N^*$ is the number of nearest neighbors for atom $i$, $N_s$ is the number of slipped neighbors for atom $i$, and $\mathbf{x}^{ij}$ and $\mathbf{X}^{ij}$ are the distance vectors between atoms $i$ and $j$ in the current and reference configurations, respectively. The slip vector is applicable to any material system since it does not require the atomic configuration to be centrosymmetric, as with the centrosymmetry parameter [106].

In addition to viewing dislocation activity, deformation processes at the atomic scale may require visualizing the free volume associated with grain boundary and/or triple junction regions. Farkas *et al.* [11] defined the free volume by overlaying a grid onto a nanocrystalline Ni sample. For every point on the grid, the nearest atomic distance was calculated and if the nearest atom distance is greater than a defined critical distance, the grid point was considered free volume. With this free volume method, Farkas *et al.* observed the evolution of free volume ahead of a crack tip in a nanocrystalline Ni grain structure. A similar method for visualizing free volume has been developed by Tschopp *et al.* [82] for characterizing the volume fraction and spatial distribution functions for free volume within the grain boundary. This method was applied to ⟨110⟩ symmetric tilt grain boundaries with the E structural unit and is discussed with the simulation results in Chapter 5.

## *2.2 Simulation specific methodology*

Here, the simulation methodology employed for generation of the computational cell and the minimum energy structure is discussed along with various techniques that are used within multiple chapters, such as the identification of grain boundary structural units.

### 2.2.1 Computational cell and boundary conditions

A computational cell with Born-von Karman three-dimensional (3D) periodic boundary conditions consisting of two grains was used in the atomistic simulations in this work. Figure 2.2 show an example of the computational cell used to obtain the equilibrium 0 K GB structure and excess energy, and to nucleate dislocations in the uniaxial deformation simulations. For symmetric and asymmetric tilt grain boundaries, the tilt axis, $\mathbf{c}_i$, is the same for both crystals; in Fig. 2.2 the tilt axis is arbitrarily shown as $\left[1\bar{1}0\right]$. This computational cell has been previously used to model grain boundary structure [90] and to study dislocation nucleation in selected $\langle 100 \rangle$ and $\langle 110 \rangle$ symmetric tilt GBs [97, 139]. There are two crystallographically identical GBs in each simulation cell: one periodic GB at the upper and lower bounds of the simulation cell ($GB_1$) and one GB in the middle of the cell ($GB_2$). The 3D periodic boundary conditions ensure that there are no fixed regions of atoms within the computational cell, *i.e.*, free surfaces. For generation of the minimum energy structure, this allows the crystal lattices to translate during energy minimization if such a translation is energetically favorable. For the deformation of this computational cell, this removes the effects involved with free surfaces, which may have detrimental effects on the nucleation of dislocations, and also allows the use of the NPT equations of motion for deformation, as used in the deformation of 3D nanocrystalline materials (*e.g.*, [23, 45, 50, 53, 140–142]).

The geometry and dimensions of the cells are similar to that used in previous works. For example, for generation of the minimum energy structure, Rittner and Seidman [90] used a similar computational cell with a spacing between grain boundaries of 5 nm to create their minimum energy symmetric tilt grain boundary structures. The size of the computational cell must be large enough to eliminate any interaction between the two GBs while minimizing the number of atoms in the computational cell. A minimum distance between GBs ($d_{GB}$) of 5 nm in Cu was used. This distance is identical in the two crystals; *i.e.*, $d_{GB} = x\,|\mathbf{n_1}| = y\,|\mathbf{n_2}|$ where $x$ and $y$ are positive numbers, and $\mathbf{n}_i$ is the GB normal in crystal $i$. Identical distances in terms of lattice units are used for both Cu and Al; this results is

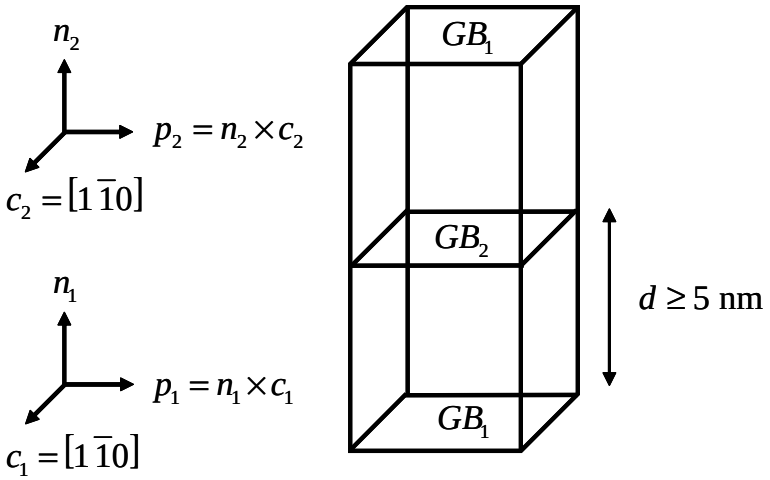


**Figure 2.2:** Schematic of the 3D periodic bicrystal computational cell showing crystal orientation notation. Note that the tilt axis for both crystals is $\left[1\bar{1}0\right]$ and the spacing between periodic GBs is greater than 5 nm.

slightly larger distances in Al ($a_0$= 4.032 Angstroms) than in Cu ($a_0$= 3.615 Angstroms). Simulations show that the error in GB energy associated with the distance $d_{GB} \geq 5$ relative to a distance $d_{GB} \geq 60$ is approximately 0.5% for the $\Sigma 3\,(111)_1 / \left(11\bar{5}\right)_2$ $\Phi$ = 70.53° ATGB in Cu, where $\Phi$ is the inclination angle from the coherent twin boundary. The minimum period in the X and Z directions (*i.e.*, the GB plane) was chosen to reduce the size of the boundary region and the number of atoms in the simulations. Simulations confirm that this assumption does not affect either the GB excess energy calculations or the GB structure. With these conditions, the simulation cells in Chapter 3 contain between 288 atoms for the $\Sigma 3\,(112)$ $\Phi$ = 90° incoherent twin boundary and 21,084 atoms for the $\Sigma 3\,(111)_1 / \left(11\bar{5}\right)_2$ $\Phi$ = 70.53° ATGB.

For deformation of the grain boundaries, the dimensions in all directions are increased to counteract the image constraints caused by the periodic boundary conditions. The simulation cell dimensions were set to a minimum length of 16 nm in the GB plane directions and a minimum distance of 16 nm between the periodic GBs (*i.e.*, a total length of 32 nm or greater in the direction normal to the GB). Appropriate dimensions were used to enforce the 3D boundary conditions. Simulations that investigated the effect of the distance

between the boundaries validated that the stress required for dislocation nucleation was essentially unaffected by further increases in the size of the simulation cell. For example, there was an error of approximately 1.0% in the peak tensile stress between a simulation cell with a 16 nm distance between boundaries (as used in this work) and a cell with a 24 nm distance between boundaries for the $\Sigma 3\,(557)_1 / \left(11\bar{3}\right)_2$ ATGB at 10 K.

Spearot *et al.* [89] justified their choice of the distance between periodic grain boundaries by computing the stress field generated by the dislocations in the interface. They found that a spacing between interfaces of $\geq$ 10 nm was sufficiently large to minimize effects on nucleation of the first dislocation. Spearot *et al.* [89] have shown that dislocation nucleation is accompanied by distortion of the structural units in the interface. Moreover, if this distortion is represented as a single dislocation placed at the dislocation point, the magnitude of the shear stress at the opposite boundary is generally less than 10% of the ideal shear strength derived from first principles calculations [143]. Since the 16 nm distance between GBs in this work exceeds that in Spearot *et al*. [97, 139], it is deemed sufficient to avoid significant effects of periodic boundaries on the 3D dislocation nucleation dynamics.

The same notation for the computational cell is used throughout this work, whereby the grain boundary period direction is specified as the X-direction, the grain boundary normal direction is specified as the Y-direction, and the tilt axis direction is specified as the Z-direction. In some cases the Miller indices are necessary to describe the directions associated with the grain boundary. Here, the grain boundary period, normal and tilt direction vectors are specified by $\mathbf{p}_i$, $\mathbf{n}_i$, and $\mathbf{c}_i$ where *i* refers to the crystal.

When generating the minimum energy grain boundary structures, the periodic simulation cell boundaries normal to the boundary (Y-direction) are permitted to move to allow for volume expansion at the GB and to relieve the internal pressure within the cell. The lateral simulation cell boundaries are fixed to maintain the correct equilibrium lattice constant in the bulk crystal lattice regions. For the uniaxial loading simulations, the applied load is always along the Y-direction, perpendicular to the boundary plane. The lateral cell

boundaries are allowed to move via the NPT equations of motion in Eq. 2.6.

### 2.2.2 Generation of minimum energy grain boundary structure

For each initial configuration, the ATGB generation step constructs identical atomic structures at the two periodic GBs: $GB_1$ and $GB_2$ in Figure 2.2. This is important because without identical atomic structures at the grain boundaries in the generation stage, energy minimization may produce different GB energies and structures at the two GBs. For example, this may result in a higher energy metastable GB at $GB_1$ and a stable GB at $GB_2$, which may be detrimental to further simulations that use this periodic atomic configuration. The methodology presented here results in identical GB structures at $GB_1$ and $GB_2$ and this methodology can be extended to more complex boundaries with both tilt and twist character. There are three vital steps in generating the grain boundary structures.

#### *2.2.2.1 Rigid body translation*

After creating atoms in the two crystal lattice regions, rigid body translations (RBTs) of one lattice with respect to the other was used to sample a number of different initial configurations, improving the chance of finding the correct equilibrium GB structures [90]. The RBT vectors consist of two components parallel to $\mathbf{p}_i$ and $\mathbf{c}_i$. The translational components are divided into a grid of points to sample the in-plane translations uniformly; these components are characterized using the displacement shift complete (DSC) lattice [144]. Applying this to GBs, the translational vectors of the DSC lattice result in the conservation of the boundary atom positions of the two lattices, *i.e.*, this results in the same atom positions. A grid spacing of 0.25 DSC lattice vectors or $a_0/8[1\bar{1}0]$ in the $\mathbf{c}_i$ direction is used for each boundary. The grid spacing in the $\mathbf{p}_i$ direction is the smaller of the two grain boundary periods multiplied by 1/4 (*i.e.*, $(1/4)\mathbf{p}_1$ if $|\mathbf{p}_1| < |\mathbf{p}_2|$). This results in exactly 16 RBT vectors for each selected grain boundary; for GBs with a large $|\mathbf{p}_i|$, additional RBT vectors in the $\mathbf{p}_i$ direction are used to increase the chance of locating the equilibrium 0 K GB structure.

#### 2.2.2.2 Criterion for atom deletion

In the atom generation and translation steps, atoms were built up to the GBs; hence, neighboring grains may contain atoms that were physically too close. Atoms too close to each other were removed by defining a critical distance between neighboring atoms for deletion. This criterion was used for removing atoms at the two periodic GBs. For this work, distances between $0.275a_0$ and $0.700a_0$ in increments of $0.005a_0$ were sampled for each RBT. In addition, the interplanar spacing often differs in each ATGB crystal lattice, so the initial configuration may be different depending on whether atoms are deleted from crystal 1 or crystal 2; therefore, both cases were included. For each grain boundary studied, this resulted in 172 different initial configurations for each RBT vector (*i.e.*, 2752 configurations total). The criterion for atom deletion increased the number of different initial configurations, while maintaining identical structures at $GB_1$ and $GB_2$ for each initial configuration sampled by removing an identical number of atoms from each periodic GB.

The criterion for atom deletion differs from methodologies used for obtaining GB energies available in the literature. Some methods translate the atom build origin in the direction normal to the GB plane. Either methodology may be used to obtain the minimum energy configuration as long as there are a sufficient number of initial configurations. Furthermore, some methods do not use periodic boundary conditions in the direction perpendicular to the boundary plane. Free surfaces are often employed and this may actually result in a simpler calculation of the minimum energy grain boundary structure. However, the 3D periodic configuration was chosen because of its applicability to MD simulations following the generation of these structures: *e.g.*, the nucleation of partial dislocations from ATGBs [77], as examined in STGBs [64, 97, 139].

#### 2.2.2.3 Molecular statics

A parallel MD code that employs domain decomposition [69] was used for molecular statics simulations. The MD code was modified by adding a nonlinear conjugate gradient

algorithm for energy minimization along with the necessary subroutines to iterate over the different initial configurations for each GB. The nonlinear conjugate gradient subroutine employed both the Polak-Ribière formula and the secant method for calculating the new search direction (*i.e.*, for atom movement) and the appropriate step size (magnitude of movement), respectively. The conjugate gradient algorithm terminated when the residual of the potential energy (*i.e.*, the force vector) fell below a predefined value that corresponds to an error in the interface energy of approximately 0.1% when compared to a much lower, computationally more expensive, value.

Molecular statics simulations rearrange atoms to identify the equilibrium 0 K GB structures and energies. Since energy minimization techniques often require numerous initial configurations to locate the minimum energy configuration, the relative ease of accessing the equilibrium structure was examined. The accessibility of the equilibrium 0 K structure is defined as percentage of initial configurations required to obtain that structure [90]. Figure 2.3 shows the accessibility for the $\Sigma 3\,(111)_1 \,/\, \left(11\bar{5}\right)_2$ $\Phi = 70.53^\circ$ ATGB as a function of the GB energy. Assigning a width of 2 mJ/m$^2$ for each bin, 15 individual GB structures were obtained. The accessibility of the equilibrium 0 K GB structure was approximately 8.76%. While many of the ATGBs have accessibilities greater than 10%, the accessibilities of some ATGBs are < 1%. The multiplicity of energies for each ATGB corresponds to different atomic configurations, as in Wang *et al.* [145], but only the lowest energy structure was used for the structural analyses.

#### *2.2.2.4 Methodology validation*

The above methodology was used to create 48 STGBs in the ⟨110⟩ tilt axis system corresponding to different misorientation angles in both Cu and Al. The calculated energy values are in excellent agreement with previously calculated EAM GB energies for Cu and Al ( [92] and [146], respectively). Additionally, the trend of the Al curve is in agreement with the experimentally measured ⟨110⟩ energy curve determined from the Herring

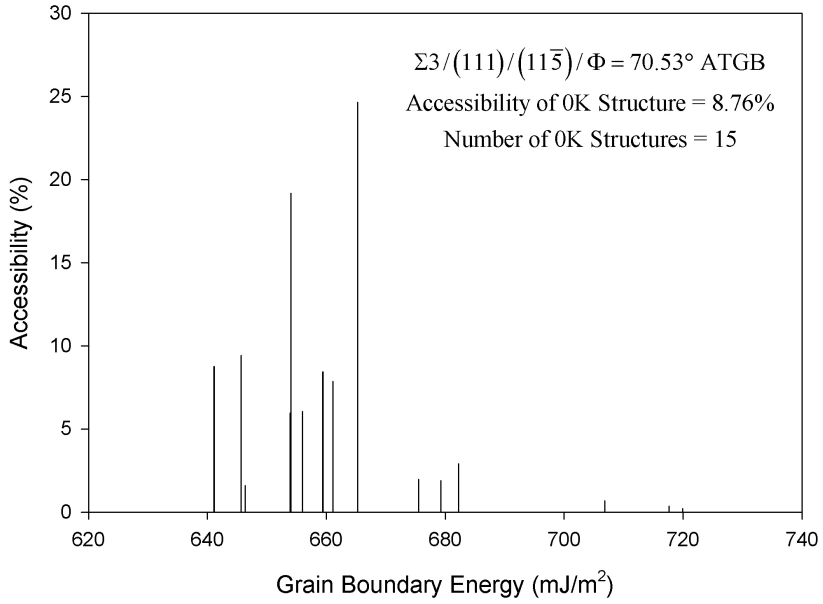


**Figure 2.3:** Graph showing the accessibility of the different stable and metastable GB configurations for the $\Sigma 3(111)_1/(11\bar{5})_2\Phi = 70.53^\circ$ ATGB. Notice that 15 different 0 K structures are generated, but the minimum energy 0 K grain boundary structure is only accessed 8.76% of the time.

relationship by Hasson and coworkers [147]. Several of the GB structures generated are compared to the simulated GB structures for low and high SFE materials [72, 91, 148] as well as experimentally observed GB structures using high resolution transmission electron microscopy [90, 149, 150]; the GB structures predicted using this methodology are in agreement with both the calculated and experimental GB structures. In addition to this validation, the symmetric and asymmetric tilt grain boundary structures and energies are compared with available HRTEM structures and experimentally measured energies, which is discussed in the subsequent chapters.

### 2.2.3 Identification of grain boundary structural units

The grain boundary structures were identified using the centrosymmetry parameter of Kelchner *et al.* [106]. Recall that the centrosymmetry parameter permits the identification of those atoms whose local environment is elastically deformed (*i.e.*, bulk crystal lattice)

from atoms whose local environment is distorted due to lattice defects or, in this case, grain boundary structural units (SUs). The centrosymmetry parameter is given by Eq. 2.11. A threshold of $P^i = 0.25$ was used as a guideline to delineate atoms belonging to GB SUs from those belonging to the bulk lattice. Once GB atoms were identified, these atoms were divided into SUs that are consistent with the structural units of the symmetric tilt grain boundaries with identical Σ value for the ATGBs or with previously calculated structural units (*e.g.*, [90, 148, 151]) for STGBs.

### 2.2.4 Grain boundary energy

The grain boundary energy ($\gamma_{GB}$) is defined as the excess energy of a bicrystal containing a grain boundary with respect to an equal number of atoms in a perfect crystal. In our work, the GB energy is calculated by the following technique:

1. The total energy is calculated by summing the potential energy of each atom ($\gamma^i$) over all atoms within the system, $\gamma_{total} = \sum_i \gamma^i$.

2. The total excess energy is calculated from the difference between the energy of the bicrystal configuration and that of the same number of atoms in a perfect bulk single crystal, *i.e.*, $\gamma_{xs} = \sum_i \gamma^i - \gamma^i_{bulk}$.

3. The interfacial excess energy is calculated by dividing by the interfacial area, *e.g.*, $2A_{GB}$ for this configuration. Therefore, the expression for obtaining the grain boundary energy is $\gamma_{GB} = \left(1/2A_{gb}\right) \sum_i (\gamma_i - \gamma_{bulk})$ where $i$ sums over all atoms within the computational cell.

### 2.2.5 Deformation of grain boundary structure

There are two essential steps that must be performed prior to the deformation simulations under a uniaxial load. First, after the minimum energy configuration is attained via molecular statics calculations as discussed in Section 2.2.2, this structure is generated in the larger computational cell necessary for the deformation simulations. The same parameters

are used to access the minimum energy structure; the periodic grain boundaries generated in the larger simulation cell will have the same grain boundary structure and energy as the smaller simulation cell used for generating the minimum energy structure[1]. Second, molecular dynamics simulations are used to equilibrate the computational cell to a specified pressure of 0 bar and the temperature of interest, 10 K or 300 K. The Melchionna *et al.* [95] equations of motion given in Eq. 2.5 are used to control the simulation cell boundaries.

Once the configuration has achieved the specified pressure and temperature, then uniaxial deformation can begin. For many simulations, the bicrystal configuration is deformed in uniaxial tension applied normal to the boundary plane (Y-direction) at a constant strain rate of $10^9$ $s^{-1}$. The movement of the simulation cell boundary corresponding to the Y-direction is prescribed, while the motions of the lateral cell boundaries (X and Z) are governed by the modified Melchionna *et al.* [95] equations of motion (Eq. 2.6), as in Spearot *et al.* [89]. For all simulations in this work, the lateral boundaries are specified as stress-free. The $10^9$ $s^{-1}$ strain rate was chosen for its computational efficiency vs. lower strain rates and to avoid the detrimental effects (*e.g.*, inducing shock waves within the computational cell) that are introduced at higher strain rates. Moreover, atomistic simulations of grain boundary dislocation nucleation in uniaxial tension and compression under quasistatic loading conditions (as applied in Ref. [152]) have shown similar stress-strain responses and dislocation nucleation mechanisms to the dynamic strain rate used here. These results are discussed for ⟨110⟩ symmetric tilt grain boundaries with the E structural unit in Chapter 7. Therefore, this strain rate is deemed sufficient for investigating dislocation nucleation from grain boundaries.

[1]Recall that the smaller simulation cell bounds were used because several thousand trial configurations are often necessary to locate the one minimum energy structure

## *2.3 Grain boundaries*

### 2.3.1 Grain boundary degrees of freedom

The geometry for grain boundaries starts with identifying the grain boundary in terms of degrees of freedom. The GB can be identified by eight degrees of freedom total: five degrees of freedom (DOF) referring to macroscopic parameters and three degrees of freedom relating to microscopic parameters [65, 153]. The five macroscopic degrees of freedom are divided into two grain boundary normal directions (4 DOF) and an angle (1 DOF). Note that to specify a direction in three-dimensional space, only two degrees of freedom are required. The three microscopic degrees of freedom correspond to the relative translation between the two lattices at an atomic level. When defining a GB, the five macroscopic degrees of freedom are used to identify the misorientation between the two crystallographic lattices as well as the grain boundary plane. The following subsections will discuss the common methods used to define GBs. Note that the three microscopic degrees of freedom are typically not specified.

The grain boundary are primarily defined in two ways [153]:

1. **Interface Plane Scheme**. This scheme specifies the GB normals in the two adjoining crystal lattices (*i.e.*, $\mathbf{n}_1$ and $\mathbf{n}_2$) along with the rotation angle ($\theta$).

2. **Angle/Axis Scheme**. This scheme specifies the misorientation across the GB with an axis of misorientation ($UVW$) along with an angle ($\theta$); this gives the GB misorientation but not the GB plane. One of the grain boundary normals (*i.e.*, $\mathbf{n}_1$ or $\mathbf{n}_2$) is needed to completely specify both the misorientation and the grain boundary plane.

An alternative notation to the angle/axis notation is to use the misorientation matrix ($\mathbf{M}$) to describe the rotation required to transform one crystal lattice to an adjacent crystal lattice. However, the misorientation matrix also fails to give the grain boundary plane so one of the GB normals ($\mathbf{n}_1$ or $\mathbf{n}_2$) is required to fully describe a grain boundary with a misorientation matrix. In this work, a combination of the angle interface plane scheme

and the angle/axis scheme is used. For the most part, the angle/axis scheme is used for symmetric tilt grain boundaries and the interface plane scheme is used for asymmetric tilt grain boundaries.

### 2.3.2 Symmetric versus Asymmetric Tilt Grain Boundaries

Grain boundaries are also typically classified as tilt or twist grain boundaries. In the angle/axis notation, tilt grain boundaries are formed by a rotation about a tilt axis that lies within the grain boundary plane. On the other hand, twist boundaries are formed by a rotation about a tilt axis that lies perpendicular to the boundary plane.

Tilt grain boundaries are separated further into symmetric and asymmetric tilt grain boundaries based on the orientation of the grain boundary plane. For symmetric tilt grain boundaries (STGBs), the grain boundary plane is oriented such that the adjoining lattices are mirror images of each other, *i.e.*, STGBs are symmetric about the boundary plane. Due to the symmetry for this class of boundaries, STGBs are often specified by a tilt axis, a misorientation angle about that tilt axis, and one grain boundary normal or the plane that this normal describes. For example, the $\Sigma 3$ incoherent twin boundary can be obtained by a $70.53^\circ$ rotation about the $\langle 110 \rangle$ tilt axis with a $\langle 111 \rangle$ GB normal direction defining the (111) plane in one of the adjoining lattices. In this work, this boundary is referred to as a $\Sigma 3\,(111)\,\theta = 109.47^\circ$ STGB. For asymmetric tilt grain boundaries (ATGBs), the grain boundary plane is oriented such that the adjoining lattices are asymmetric with respect to the grain boundary plane. Asymmetric tilt grain boundaries are often specified by a tilt axis, two grain boundary normals or the planes that these normal vectors describe, and the degree of rotation from a STGB of the same misorientation (the inclination angle). Since twist boundaries are formed by a rotation perpendicular to the boundary plane, there is no sub-classification as symmetric or asymmetric, *i.e.*, all twist boundaries are symmetric.

The terminology often used for characterizing the structure of coincident site lattice (CSL) grain boundaries is the sigma ($\Sigma$) designation. A CSL boundary arises if the two

lattices surrounding the grain boundary are viewed as penetrating through the boundary into the other lattice, with points that are coincident to both lattices forming “coincident lattice points”. The period of the coincident lattice points is defined through the symbol, $\Sigma$. For example, if one in three atoms are coincident, this is a $\Sigma 3$ CSL boundary; this can be obtained by a $109.47^\circ$ rotation about the $\langle 110 \rangle$ axis in an FCC material. In addition, many of the low energy CSL boundaries have special properties related to them such as creep, diffusivity, ductility, energy, fatigue, precipitation characteristics, *etc*.

# CHAPTER III

# STRUCTURES AND ENERGIES OF Σ3 ATGBS

Chapter 3 is the first of two chapters that focus on the structure and energy of several asymmetric tilt grain boundary systems. In this chapter, atomistic simulations are used to investigate the energy and structure of symmetric and asymmetric Σ3 ⟨110⟩ tilt grain boundaries. A nonlinear conjugate gradient algorithm was employed along with an embedded atom method potential for Cu and Al to generate the equilibrium 0 K grain boundary structures. A total of 25 ⟨110⟩ grain boundary structures were explored to identify the various equilibrium and metastable structures. Simulation results show that the Σ3 asymmetric tilt grain boundaries in the ⟨110⟩ system are composed of only structural units of the two Σ3 symmetric tilt grain boundaries. The energies for the Σ3 grain boundaries are similar to previous experimental and calculated grain boundary energies. A structural unit and faceting model for Σ3 asymmetric tilt grain boundaries fits all of the calculated asymmetric grain boundary structures. The significance of these results is that the structural unit and facet description of all Σ3 asymmetric tilt grain boundaries may be predicted from the structural units of the Σ3 coherent twin and incoherent twin boundaries for both Cu and Al.

## *3.1 Introduction*

Grain boundaries (GBs) are important microstructural features of polycrystalline materials that impact the bulk properties [154]. Watanabe first introduced the concept of grain boundary design [75] to describe the ability to effectively control the grain boundary character of materials to enhance their beneficial effects and reduce their detrimental effects within the bulk polycrystalline material. Some of the first experiments focused on improving the intergranular fracture process in polycrystals through increasing the fraction of low order coincidence site lattice (CSL) boundaries [155]. The application of this concept has

dramatically expanded to improve other functional and mechanical bulk properties, such as intergranular stress-corrosion resistance [156] as well as creep strength and superplasticity in materials [157]. The term 'grain boundary engineering' (GBE) implies the ability to manipulate the grain boundary character distribution by processing methods to attain certain bulk polycrystalline properties. Much of the focus of GBE has been on increasing the distribution of Σ3 GBs in low stacking fault energy (SFE) materials [66, 67]; the most commonly cited Σ3 GB is the coherent twin boundary. While some early GBE research primarily characterized the GBs in polycrystalline materials according to their CSL representation, some current research considers the role of the grain boundary plane as well. The grain boundary properties depend not only upon the misorientation between grains (which defines the CSL content), but also upon the orientation of the grain boundary plane. As an example that relates to this chapter, for all Σ3 tilt GBs with a ⟨110⟩ misorientation axis, the GB plane determines whether the Σ3 boundary is a coherent twin boundary (CTB) or a symmetric incoherent twin boundary (SITB). In addition to these two symmetric tilt grain boundaries (STGBs), all grain boundary planes between the CTB and SITB are asymmetric tilt grain boundaries (ATGBs). The orientation of the grain boundary plane for these Σ3 GBs can have strong effects on properties such as the GB energy [158, 159], GB diffusion [160], or intergranular corrosion resistance [161]. In light of the role of grain boundary plane orientation, Randle proposed the concept of 'grain boundary plane engineering' to maximize the proportions of desirable grain boundary planes [162, 163].

Consequently, many experiments investigate the role of the boundary plane in the Σ3 system to find the distribution of Σ3 boundaries in polycrystals and to characterize the effect of the CTB on properties. Experiments using an EBSD analysis include the GB plane as part of the description of the GB character distribution to show the role of GB plane in defining which Σ3 boundaries are present in the polycrystal. In high stacking fault energy pure Al, the CTB was observed 25 times more frequently than expected in a random distribution [164]. In the same study, the SITB was not observed. In a low

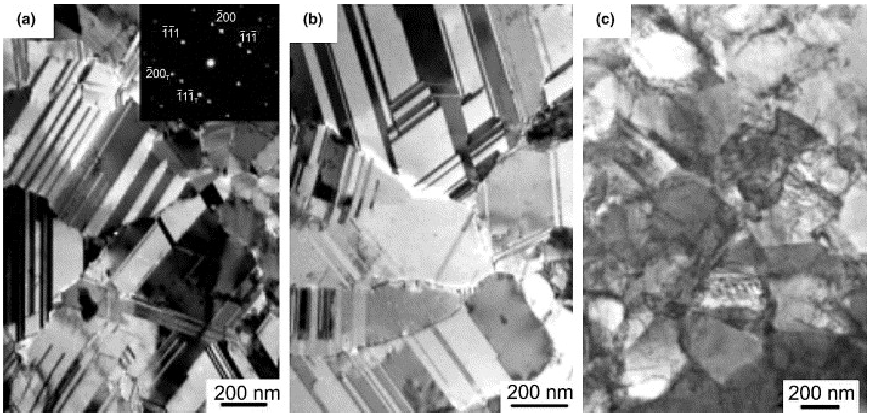


**Figure 3.1:** TEM images of the as-processed microstructure of (a) Cu with a higher twin density, (b) Cu with a lower twin density, and (c) control ultrafine-crystalline Cu essentially without twins. Images are from Lu and coworkers [174].

stacking fault energy grain boundary engineered $\alpha$-brass, the CTB was observed over 2200 times more frequently than the random expectation [165]. The latter experiment shows that low stacking fault energy materials can be engineered to produce a higher fraction of coherent twin boundaries in the polycrystal. Different processing methods have shown the ability to alter the grain boundary character distribution including thermomechanical processing [166–168] or application of external magnetic fields [169–171]. The ability to engineer low stacking fault energy polycrystals to increase the CTB fraction is utilized to enhance the deformation behavior of polycrystalline materials. For example, the introduction of coherent twin boundaries with nanoscale spacing (*i.e.*, nanoscale twins) into the grains of polycrystal materials (*e.g.*, Fig. 3.1) has been associated with increased strength, ductility, and hardness [172–177]. Additional experimental work has investigated the effects of both growth (or recrystallization, or annealing) twins and deformation twins on the mechanical properties and inelastic behavior of materials. For example, TEM images at different stages of deformation in fine-grained Ag have shown that annealing twin boundaries (i) emit dislocations, (ii) act as a barrier to slip sometimes and (iii) transmit dislocations other times [178]. A better understanding of how the grain boundary plane influences the structure of $\Sigma 3$ ATGBs may help to explain experimentally observed phenomena.

Atomistic simulations are also useful for providing insight into the effects of CTBs on

inelastic deformation behavior. Molecular dynamics (MD) simulations with grown-in twin boundaries have shown that the deformation mechanism of nanocrystalline (nc) materials may change in some FCC metals to a twin boundary migration mechanism by emitting partial dislocations [55, 62]. Additional simulations have investigated the effect of vicinal twin boundaries on the dislocation activity in nc Al [179]. Vicinal twin boundaries are GBs that deviate slightly from the misorientation of the CTB. These simulations show that the step structures within the vicinal twin boundaries act as dislocation sources. Furthermore, Frøseth *et al.* [180] used MD simulations to show that an increased fraction of Σ3 GB clusters in a nanocrystalline sample results in a lower potential for accommodating strain in 5 nm diameter grains. Other MD simulations have shown the mechanism for transmission of screw dislocations through a CTB [181]. With the large amount of experimental work on the presence of Σ3 GBs and their effect on deformation behavior, atomistic simulations that focus on Σ3 GBs can promote understanding of the role of the grain boundary plane in deformation.

Atomistic simulations can also be leveraged to examine the effect of the grain boundary plane on the energy, structure, and other GB properties. Wolf conducted several comprehensive atomistic simulations of structure and energy as a function of misorientation angle for symmetric tilt and twist GBs [92, 182–184]. However, very few atomistic simulations have explored the role of the grain boundary plane orientation on the structure and energy of ATGBs. The atomistic simulations that do explore the grain boundary plane can be categorized into several areas. First, some of the initial atomistic simulations that explored the energy and/or structure of ATGBs [185] may have been limited by the accuracy of potentials (*i.e.*, Lennard Jones) or the methodology, which may skew either the calculated energies or GB structures. Many of these studies have not been repeated despite the advances in embedded atom method (EAM) potentials and methodology that can increase the understanding of the energies and structures of these ATGBs. A second category of atomistic simulations of ATGBs has focused on the structure of specific grain boundary

planes (*e.g.*, the 9R phase) to help explain the observed GB structure from HRTEM images (*cf.* [186–189]) or calculate certain GB properties (*e.g.*, the shear deformation response of a few specific ATGBs [72]). Yet another category of ATGB atomistic simulations are those that investigated the effect of the grain boundary plane orientation on the GB properties or mechanisms. For example, Zhang and Srolovitz studied both the GB mobility and self-diffusivity properties as well as the atomic migration mechanisms for Σ5 GBs in Ni [177, 190]. While this highlights some of the different types of ATGB atomistic simulations available in the literature, the fact remains that few simulations examine the structure of ATGBs in terms of atomistic faceting and the geometry of structural units as a function of the orientation of the grain boundary plane.

The objective of this chapter is to study the influence of the grain boundary plane orientation on the structure and energy for 25 Σ3 GBs using embedded atom method potentials for Cu and Al that accurately reflect both stable and unstable stacking fault energies. This chapter is organized as follows. The first section outlines the simulation methodology used to obtain the equilibrium 0 K grain boundary structures. The second section presents the energy results for this study and compares the Cu results with the atomistically calculated and experimentally measured GB energies of Wolf and coworkers [158]. The third section shows some selected symmetric tilt and asymmetric tilt Σ3 GB structures in terms of structural units from the CTB and SITB. The fourth section compares the faceting behavior and structural units to other studies available in the literature. Additionally, this section illustrates the fit to an energetic model for Σ3 ATGBs and presents a structural unit and faceting model for Σ3 asymmetric tilt grain boundaries.

## *3.2 Simulation methodology*

### 3.2.1 Asymmetric tilt grain boundary geometry

Table 3.1 lists all 25 Σ3 grain boundaries studied in this research, including 2 symmetric tilt grain boundaries (STGBs) and 23 asymmetric tilt grain boundaries (ATGBs). Note that

in the CSL notation, the designation Σ3 denotes that if the two crystal lattices are allowed to overlap, one in every three points is coincident; this occurs for a specific misorientation angle $\theta = 70.53^\circ$ about the $[1\bar{1}0]$ tilt axis. This is the misorientation angle ($\theta$) for all grain boundaries in Table 3.1; accordingly, they can be classified as Σ3 GBs. This CSL notation only considers the grain boundary misorientation angle $\theta$ between the two lattices and does not consider the grain boundary plane; additional consideration of the GB plane completely defines the GB. For this purpose, the term inclination angle Φ is used to define the relative rotation of the grain boundary plane about the tilt axis. Recall that the two STGBs in the Σ3 system are the coherent twin boundary (CTB) and the symmetric incoherent twin boundary (SITB); the CTB and SITB are defined as $\Phi = 0^\circ$ and $\Phi = 90^\circ$, respectively. All other Σ3 boundaries with intermediate inclination angles are ATGBs. The inclination angle and grain boundary normals for the two adjoining lattices are given in Table 3.1; ATGBs require both normals to be specified to account for both the misorientation and inclination angles.

Figure 3.2 shows a schematic depicting the change in inclination angle from the $\Sigma3\,(111)\,\Phi = 0^\circ$ CTB to the $\Sigma3\,(110)_1 / (114)_2\,\Phi = 35.26^\circ$ ATGB to the $\Sigma3\,(112)\,\Phi = 90^\circ$ SITB; the subscripts for the ATGB denotes the grain boundary normal directions for the upper and lower lattices (see Figure 3.2(c)). In this schematic, the grain boundary plane is represented by the long dotted horizontal line, the grain boundary normals are the short vertical dotted lines, and the lattice is shown as a rectangle for the $\left(1\bar{1}0\right)$ plane of the FCC unit cell. Consequently, Figure 3.2(a) represents the perfect single crystal since the crystal lattices in regions 1 and 2 are identical. Figure 3.2(b) shows the $\Sigma3\,(111)\,\Phi = 0^\circ$ CTB which is obtained by rotating the lattices in (a) by $+54.74^\circ$ and $-54.74^\circ$ (*i.e.*, misorientation angle $\theta = 109.47^\circ$ based on a [001] reference crystallographic direction). Figure 3.2(c) shows the $\Sigma3\,(110)_1 / (114)_2\,\Phi = 35.26^\circ$ ATGB which is obtained by rotating both crystal lattices in (b) by $35.26^\circ$ in the clockwise direction. Last, the $\Sigma3\,(112)\,\Phi = 90^\circ$ SITB in Figure 3.2(d) is obtained by rotating both lattices in (b) by $90^\circ$ in the clockwise direction. Notice that the misorientation angle of Figure 3.2(d) (*i.e.*, $\theta = 70.53$) is defined with respect

to the [001] reference direction; the misorientation between the two lattices has not changed in Figures 3.2(b)-(d). Note that all clockwise rotations to both lattices between 0° and 90° - Figures 3.2(b) and 3.2(d), respectively - result in Σ3 ATGBs. Note that in this schematic, the orientations of the lattices are rotated while the grain boundary plane is fixed. An alternative representation of inclination angle is to view the lattices as fixed and the grain boundary plane as rotating (*cf.* Figure 1 in [191]).

The remaining computational methodology is discussed in Chapter 2. A computational cell with Born-von Karman 3D periodic boundary conditions consisting of two grains was used to obtain the equilibrium 0 K GB structure and excess energy. The embedded atom method (EAM) potentials for Cu [124] and Al [125] were used for this study. The grain boundary generation methodology is presented in Section 2.2.

## *3.3 Results: Atomistic calculations of ATGB energy*

The GB energies for the 25 Cu and Al boundary configurations are listed in Table 3.1. The Cu GB energies from this study are shown in Figure 3.3(a) along with the calculated GB energies for 12 Cu bicrystal configurations by Wolf and coworkers [158]. Additionally, the experimental results from 9 Σ3 GBs obtained by thermal grooving experiments are included [158]. The y-axis is the GB energy, $\gamma_{GB}$, divided by the ⟨110⟩ surface energy, $\gamma_{Surface}$ (*i.e.*, 1476 mJ/m$^2$ for the EAM potential in this study). Potential reasons for the discrepancy between calculated and experimental values may be due to the temperature difference (*i.e.*, the experimental values were obtained at a temperature of 1313 K). An increase in temperature for the simulated GB structures may result in changes to the GB and surface energies; this, in turn, may result in a lower ratio of $\gamma_{GB}/\gamma_{Surface}$. While the magnitude of the calculated energies deviates slightly from experimental energies, the trend between the experimental and calculated values is in good agreement.

There is also good agreement between the two Cu GB energy curves considering the different Cu potentials, simulation cell setup, and methodologies that are used for each

**Table 3.1:** The inclination angles and GB normals for the 25 GBs investigated in this study. The periods in the X and Y directions are given in terms of lattice units since the magnitudes of the GB normals and GB periods are not equal for the two crystals of each ATGB. The calculated GB energies for Cu and Al are also given.

| Inclination Angle | $(hkl)_1/(hkl)_2$ | $X_{period}$ | $Y_{period}$ | Cu Energy | Al Energy |
|---|---|---|---|---|---|
| 0.00° | $\left(11\bar{1}\right)_1 / (111)_2$ | 2.45 | 13.86 | 22.2 | 75.2 |
| 6.21° | $\left(14, 14, \bar{1}1\right)_1 / (445)_2$ | 32.03 | 22.65 | 108.4 | 116.8 |
| 10.02° | $\left(33\bar{2}\right)_1 / (7, 7, 10)_2$ | 9.95 | 14.07 | 161.6 | 141.5 |
| 13.26° | $\left(77\bar{4}\right)_1 / (558)_2$ | 7.55 | 21.35 | 205.5 | 161.6 |
| 15.79° | $\left(22\bar{1}\right)_1 / (447)_2$ | 12.73 | 18.00 | 238.3 | 176.8 |
| 19.47° | $\left(55\bar{2}\right)_1 / (112)_2$ | 5.20 | 14.70 | 281.5 | 197.7 |
| 22.00° | $\left(33\bar{1}\right)_1 / (5, 5, 11)_2$ | 18.49 | 26.15 | 306.6 | 211.8 |
| 25.24° | $\left(44\bar{1}\right)_1 / (225)_2$ | 8.12 | 17.23 | 337.0 | 225.5 |
| 29.50° | $\left(77\bar{1}\right)_1 / (113)_2$ | 14.07 | 19.90 | 375.6 | 243.6 |
| 35.26° | $(110)_1 / (114)_2$ | 3.00 | 16.97 | 426.9 | 267.1 |
| 40.32° | $(881)_1 / (2, 2, 11)_2$ | 16.06 | 22.72 | 471.0 | 285.3 |
| 43.31° | $(551)_1 / (117)_2$ | 10.10 | 14.28 | 493.7 | 296.2 |
| 46.69° | $(772)_1 / (1, 1, 10)_2$ | 7.14 | 20.20 | 521.7 | 305.8 |
| 48.53° | $(331)_1 / (1, 1, 13)_2$ | 18.49 | 26.15 | 533.8 | 312.5 |
| 54.74° | $(221)_1 / (001)_2$ | 4.24 | 15.00 | 577.2 | 329.0 |
| 60.50° | $(332)_1 / \left(1, 1, \bar{1}4\right)_2$ | 9.95 | 14.07 | 610.6 | 343.5 |
| 62.06° | $(775)_1 / \left(1, 1, \bar{1}1\right)_2$ | 15.68 | 22.18 | 616.1 | 346.8 |
| 64.76° | $(554)_1 / \left(1, 1, \bar{8}\right)_2$ | 5.74 | 16.25 | 629.2 | 352.2 |
| 67.01° | $(887)_1 / \left(2, 2, \bar{1}3\right)_2$ | 18.81 | 26.61 | 633.8 | 357.0 |
| 70.53° | $(111)_1 / \left(11\bar{5}\right)_2$ | 7.35 | 15.59 | 638.6 | 361.1 |
| 74.21° | $(778)_1 / \left(11\bar{4}\right)_2$ | 9.00 | 25.46 | 626.4 | 363.0 |
| 76.74° | $(445)_1 / \left(22\bar{7}\right)_2$ | 10.68 | 15.10 | 609.3 | 364.7 |
| 79.98° | $(557)_1 / \left(11\bar{3}\right)_2$ | 14.07 | 19.90 | 586.6 | 364.0 |
| 81.95° | $(223)_1 / \left(4, 4, \bar{1}1\right)_2$ | 17.49 | 24.74 | 583.2 | 363.0 |
| 90.00° | $(112)_1 / \left(11\bar{2}\right)_2$ | 1.73 | 14.70 | 591.9 | 354.4 |

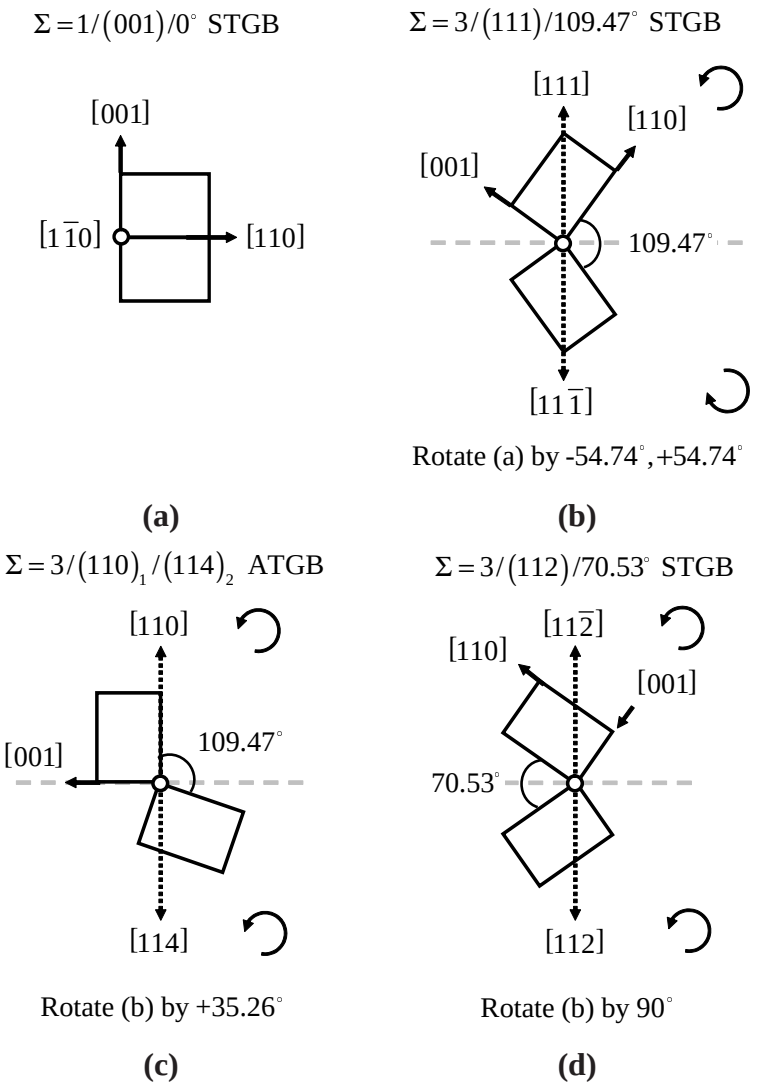


**Figure 3.2:** Schematic showing the effect of misorientation and inclination angle for four ⟨110⟩ tilt grain boundaries: (a) $\Sigma1(001)\theta = 0°$ STGB, (b) $\Sigma3(111)\theta = 109.47°$ coherent twin boundary, (c) $\Sigma3(110)_1/(114)_2\Phi = 35.26°$ ATGB, (d) $\Sigma3(112)\theta = 70.53°$ incoherent twin boundary. In this study, the inclination angles for (b-d) are 0°, 35.26°, and 90°, respectively.

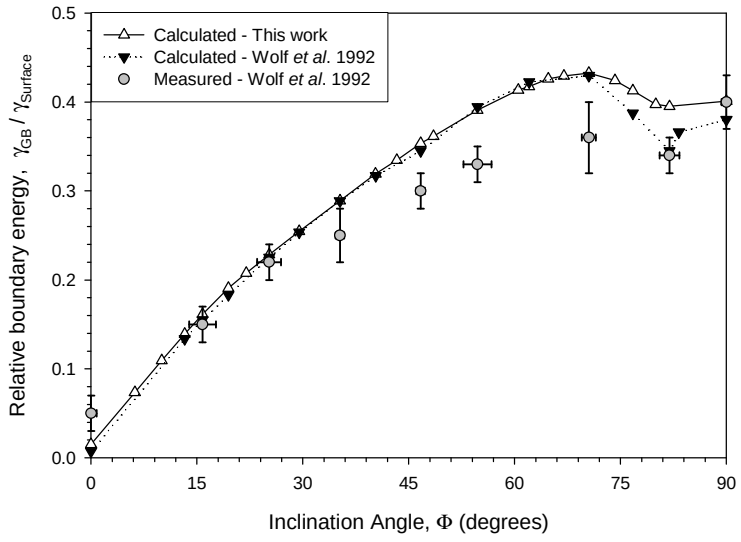


**(a)**

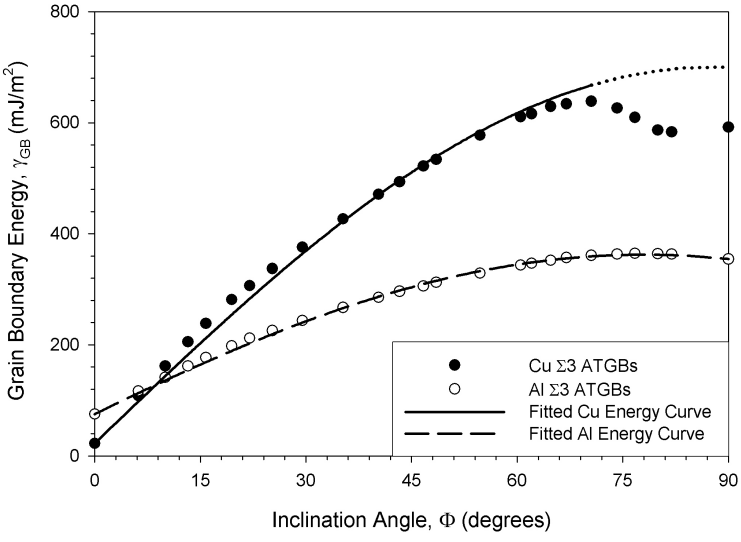


**(b)**

**Figure 3.3:** (a) Grain boundary energy divided by the surface energy $\gamma_{GB}/\gamma_{Surface}$ as a function of inclination angle for Cu. The values calculated in this work are compared with both calculated values and experimental measurements [158]. (b) Grain boundary energy as a function of inclination angle for Cu and Al. The fits for these values are described in Section 3.5.2.

of the studies. The Wolf *et al.* [158] study used the EAM potential for Cu developed by Foiles, Baskes, and Daw [112]. Their simulation cell consisted of one GB bounded by two free surfaces at a distance 4-7 nm away from the GB. The configurations were relaxed using a conjugate gradient method. Interestingly, the grain boundary energy normalized by the surface energy shows almost no difference with respect to potential in this region. However, the difference between ATGB energies and the normalized energy (Figure 3.3(a)) is particularly pronounced for inclination angles $\Phi > 70.53°$. In this GB region there is a different phase at the GB in Cu; the rhombohedral 9R phase is formed from an intrinsic stacking fault on every third plane in an FCC structure. The presence of the 9R phase may explain the larger difference in GB energies in this region; the higher stable and unstable stacking fault energies of the Mishin *et al.* EAM potential [97] may show a more prominent effect in dissociated GB regions (*i.e.*, the ATGBs with the 9R phase). In addition to its presence in the Cu $\Sigma 3$ system, the R-phase is also important in martensitic transformations in shape memory alloys (*e.g.*, intermediate austenitic to martensitic phase transitions in Ni-Ti alloys [192, 193]).

The calculated and experimentally determined cusp inclinations are also in agreement. First, the two relative minimum GB energies for Cu are at the CTB ($\Phi = 0°$) and at an inclination angle approximately 8° from the SITB ($\Phi = 90°$). While Wolf and coworkers show a deep cusp at the $\Sigma 3(223)_1/(4,4,\bar{1}1)_2\Phi = 81.95°$ ATGB relative to the surrounding ATGBs, the present study shows a more gradual decrease in GB energies from the $\Sigma 3(111)_1/(11\bar{5})_2\Phi = 70.53°$ ATGB to the relative minimum GB energy of the $\Sigma 3(223)_1/(4,4,\bar{1}1)_2\Phi = 81.95°$ ATGB. This difference may be due to either the free surfaces in their simulation cell or proximity of the two periodic GBs in ours. To investigate this difference, the distance between $GB_1$ and $GB_2$ is increased to 100 nm for the minimum energy configurations with inclination angles $\Phi > 70.53°$; the energies and structures given for these configurations use the 100 nm minimum distance between $GB_1$ and $GB_2$. However, despite this difference in energies, both studies predict that the minimum energy GB

in this region is $\Phi = 81.95^\circ$ ATGB. Moreover, the thermal grooving experimental results also show that the $\Sigma3(223)_1/(4,4,\bar{1}1)_2\Phi = 81.95^\circ$ ATGB is the preferred facet in Cu. The agreement between these two studies with respect to GB energy values, the energy curves, and the relative minimum energy configurations validates that the methodology used for obtaining the GB structure results is appropriate.

Figure 3.3(b) plots both the Cu and Al GB energies from this study as a function of the inclination angle. The $\Sigma3$ ATGB energy curve for Al differs from Cu with respect to both the shape of the curve as well as the two minimum energy configurations. The Al energy curve slowly increases to a maximum value at the $\Sigma3(445)_1/(22\bar{7})_2\Phi = 76.74^\circ$ ATGB and exhibits only two GB energy minima, one at the CTB and one at the SITB. The difference in the shape of the energy curve for Al results from the high SFE of Al which suppresses GB dislocation dissociation and formation of the 9R phase.

Two geometric criteria that have been used to compare GB structures to determine various properties, including low interfacial energy. The two most commonly used geometric criteria for GBs are the planar coincident site density $\Gamma$ [194] and the average interplanar spacing, $\langle d \rangle = 1/2\,(d_1 + d_2)$, where $d_i$ is the interplanar spacing for crystal $i$. Both of these geometric criteria calculate that the CTB is the most singular GB in this study. Minkwitz *et al.* [160] used these two geometric criteria to explain the inclination dependence of diffusion in Cu; they found that the $\Gamma$ criterion correlated best with their experimental data. However, in this case, the calculated energy curves for Cu and Al in Figure 3.3(b) exhibit different minima and maxima with respect to inclination angle. The maximum GB energy in Cu occurs at $\Phi = 70.53^\circ$, while Al exhibits a maximum energy at $\Phi = 76.74^\circ$. Additionally, Cu exhibits a minima energy cusp at $\Phi = 81.95^\circ$, while Al exhibits a minima energy cusp at the SITB, $\Phi = 90^\circ$. In agreement with the review of Sutton and Baluffi [195], albeit this work investigated the energy of $\Sigma3$ ATGBs, it is found that no single geometric criterion is able to describe the $\Sigma3$ ATGB energy because a geometric criterion cannot account for the physics of the interface structure.

## *3.4 Results: Atomistic calculations of ATGB structures*

### 3.4.1 Identification of grain boundary structures

The grain boundary structures for all the Σ3 ATGBs were identified using the methodology described in Section 2.2.3. The presence of the 9R phase for Cu necessitates that the GB structures for Cu should be separated into two distinct groups, those with inclination angles $\Phi = 70.53°$ and those with $\Phi \geq 70.53°$. These structures are presented in the next two subsections for Cu and then the GB structures generated with the Al potential are compared to the Cu GB structures.

### 3.4.2 Inclination angles $\Phi < 70.53°$

Figure 3.4(a)-(f) shows the equilibrium 0 K GB structures in Cu for six boundaries with inclination angles $0° \leq \Phi < 70.53°$. The structures are viewed along the $[1\bar{1}0]$ tilt axis and the atoms on two consecutive $(2\bar{2}0)$ planes are shown as black and white. The GB normal and period vectors for the lower and upper crystal are shown in the corner boxes on the left-hand for each GB. The two arrows in the upper right corner correspond to the ideal location of the CTB and SITB facets based on the GB inclination angle (also shown). There are two facets for each Σ3 ATGB: one facet corresponds to the SUs of the CTB and one facet corresponds to SUs associated with the SITB. Consequently, the only SUs present are the SUs that are observed in the Σ3 STGBs: the C and D SUs (see Figure 3.4(a) and 3.5(f)). The C SU is composed of four atoms arranged in a diamond shape, while the D SU is a line connecting two atoms. The D SU is closely related to a Shockley partial dislocation and is frequently found terminating an intrinsic stacking fault (*e.g.*, in the Σ3(112) SITB).

After the SUs for the Σ3 ATGBs are identified, they can then be associated with either the CTB or the SITB facets. The CTB facet contains only D SUs that correspond to the $\Sigma3(111)\theta = 109.47°$ STGB. The number of D SUs on the CTB facet decreases as the inclination angle increases; the $\Sigma3(77\bar{4})_1/(558)_2\Phi = 13.26°$ ATGB contains 12 D SUs on every CTB facet while the $\Sigma3\,(110)_1\,/\,(114)_2\,\Phi = 35.26°$ ATGB only contains 4 D

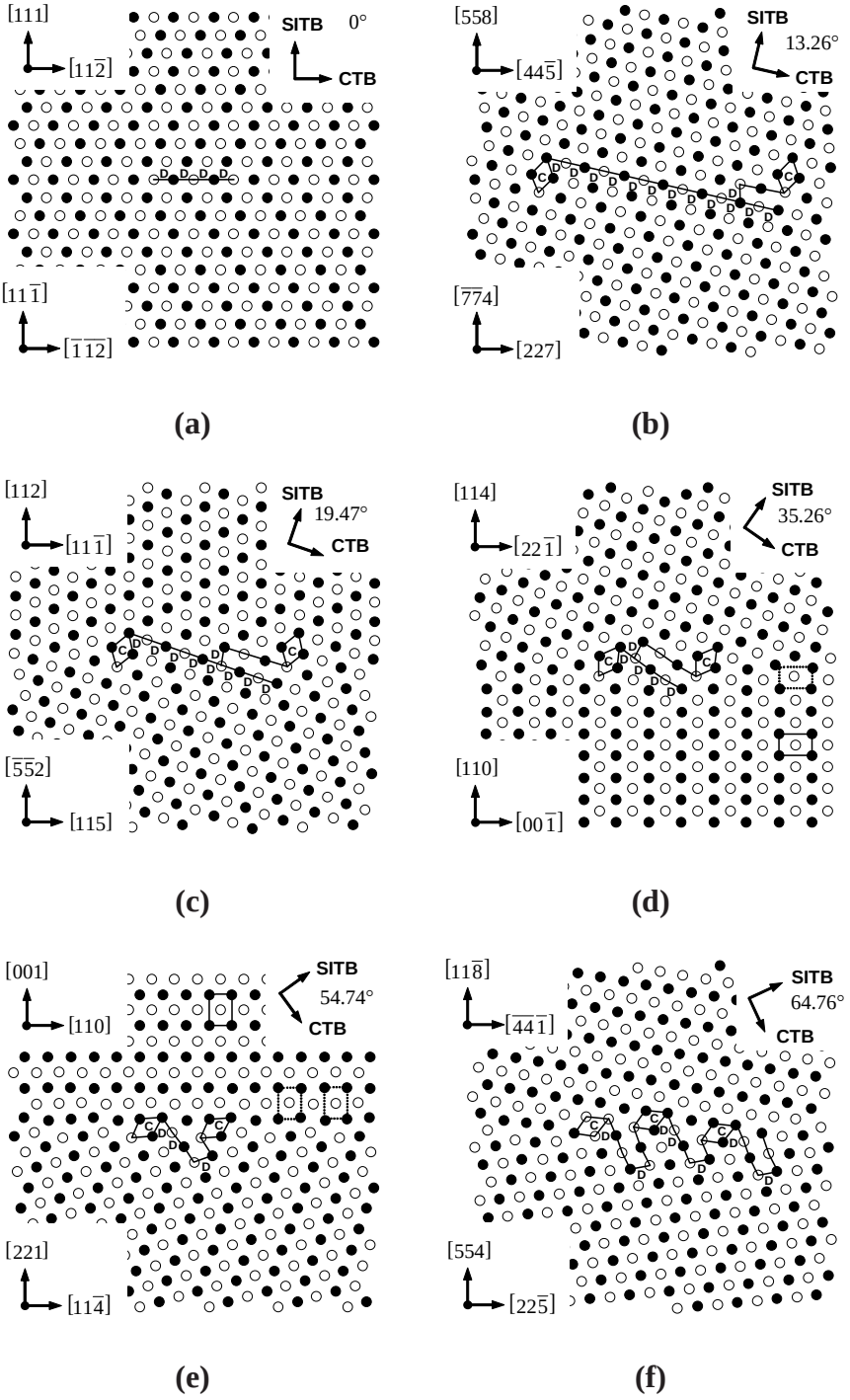


**Figure 3.4:** Six Σ3 grain boundary structures in Cu for various inclination angles $\Phi < 70.53°$. The structures are viewed along the $\left[1\bar{1}0\right]$ tilt axis; atoms on consecutive $\left(2\bar{2}0\right)$ planes are shown as black and white. The grain boundary normal and period vectors for the lower and upper crystal are shown in the corner boxes on the left-hand side for each grain boundary. The inclination angle is shown in the upper right corner. Note that (a) is the CTB, while all other GBs are Σ3 ATGBs.

SUs on every CTB facet. The SITB facet contains the C and D SUs corresponding to the $\Sigma 3\,(112)\,\theta = 70.53°$ STGB. All |*DC*| units for ATGBs with $\Phi < 70.53°$ are separated by at least one D SU on the CTB facet; *i.e.*, a |*DCDC*| structure could occur on the SITB facet, but this would be a metastable atomistic configuration. Also, notice that the D SU associated with the SITB dissociates in a direction parallel to the CTB facet. For Figures 3.4(b)-(d), the D SU only dissociates in one direction. However, for inclinations angles $\Phi \geq 54.74°$ (Figures 3.4(e)-(f)) the D SU dissociates in the opposite direction. This transition of the dissociated D SU from one side of the C SU to the other side depends on the relative proximity of the facets. For Σ3 ATGBs, the spacing between both the CTB and SITB facets determines the local strain state, which then influences the directionality of dissociation of the D SU. In Figure 3.4(d), directly before this transition, the dissociated D SU approaches the C SU on the adjacent SITB facet. The local strain state surrounding this C SU acts as a barrier and appears to pin the dissociated D SU, which causes the dissociation to proceed in the opposite direction. It is also interesting to note that all D SUs associated with the SITB dissociate, while none of the D SUs associated with the low energy CTB facet dissociate. Last, in Figures 3.4(d) and (e), the unit cell is outlined both away from the boundary and at the boundary to show the distortion in the unit cell at the GB. Note that these two boundaries have a low index GB normal (*i.e.*, [001] and [110]), but do not have a GB structure (or GB energy) that deviates significantly from GBs with similar inclination angles.

Table 3.2 summarizes the GB structure for the six GBs depicted in Figure 3.4. In Table 3.2, the GB structure is characterized with a notation format that identifies the SUs, the GB period, the relative displacement of SUs in the tilt axis direction, and the facet that the SU belongs to. The bars around the structure denotes one GB period perpendicular to the tilt axis, while the dot preceding an individual SU signifies a relative displacement of $a_0/4\left[1\bar{1}0\right]$ along the tilt axis from other similar SUs. The slash is used to represent a transition from one facet to another; all GB structures start on the CTB facet. This notation

**Table 3.2:** GB structural unit description of the six GBs in Fig. 3.4.

| $\Phi$ | $(hkl)_1/(hkl)_2$ | GB SU Description | # $\|DC\|$ SUs | # D SUs |
|---|---|---|---|---|
| 0.00° | $\left(11\bar{1}\right)_1$ / $(111)_2$ | $\|D.D\|$ | 0 | 2 |
| 13.26° | $\left(77\bar{4}\right)_1$ / $(558)_2$ | $\|6(D.D)/DC\|$ | 1 | 12 |
| 19.47° | $\left(55\bar{2}\right)_1$ / $(112)_2$ | $\|4(D.D)/DC\|$ | 1 | 8 |
| 35.26° | $(110)_1$ / $(114)_2$ | $\|2(D.D)/DC\|$ | 1 | 4 |
| 54.74° | $(221)_1$ / $(001)_2$ | $\|D.D/DC\|$ | 1 | 2 |
| 64.76° | $(554)_1$ / $\left(11\bar{8}\right)_2$ | $\|D.D/DC/D/.D.C/.D/DC\|$ | 3 | 4 |

helps to distinguish D SUs on the CTB facet from D SUs on the SITB facet. Additionally, the notation 6(D.D) denotes that there are 12 D SUs on this CTB facet that alternate with respect to their relative translation in the tilt axis direction. As noted above, the ratio of the D SUs on the CTB facets to the $|DC|$ units on the SITB facets decreases as the inclination angle increases.

### 3.4.3 Inclination angles $\Phi \geq 70.53°$

Figure 3.5(a)-(f) shows the equilibrium 0 K GB structures in Cu for six boundaries with inclination angles $\Phi \geq 70.53°$. This particular set of GBs has attracted a significant amount of interest due to the 9R phase transformation occurring between two boundaries in several low SFE materials: *e.g.*, Cu [158, 159], Ag [186, 188], and Au [196]. This section investigates the effect of inclination angle on the GB structure by comparing numerous GB structures within the 9R region. First, the maximum in GB energy occurs at the $\Sigma3(112)\theta = 70.53°$ ATGB, which is a transitional GB structure for the 9R phase in the $\Sigma3$ system in Cu. For this structure, the number of $|DC|$ units on the SITB is equal to the number of D units on the CTB; all ATGBs with inclination angles greater (less) than 70.53° have a larger (smaller) ratio of SITB SUs than CTB SUs. All D SUs for ATGBs with $\Phi \geq 70.53°$ are separated by at least one $|DC|$ unit on the SITB facet; *i.e.*, only a metastable 0 K configuration will contain two D units on the same CTB facet. For each of these structures, the D SU on the SITB facet dissociates to the same side of the adjacent C SU continuing the trend shown in Figure 3.4(e)-(f). The intrinsic stacking fault caused

**Table 3.3:** GB structural unit description of the six GBs in Fig. 3.5.

| $\Phi$ | $(hkl)_1/(hkl)_2$ | GB SU Description | # $\|DC\|$ SUs | # D SUs |
|---|---|---|---|---|
| 70.53° | $(111)_1$ / $\left(11\bar{5}\right)_2$ | $\|D/.D.C/.D/DC\|$ | 2 | 2 |
| 74.21° | $(778)_1$ / $\left(11\bar{4}\right)_2$ | $\|D/.D.C/.D/DC/D/.D.C.D.C/.D/DC\|$ | 5 | 4 |
| 76.74° | $(445)_1$ / $\left(22\bar{7}\right)_2$ | $\|D/.D.C/.D/DCDC\|$ | 3 | 2 |
| 79.98° | $(557)_1$ / $\left(11\bar{3}\right)_2$ | $\|D/.D.C.D.C/.D/DCDC\|$ | 4 | 2 |
| 81.95° | $(223)_1$ / $\left(4,4,\bar{11}\right)_2$ | $\|D/.D.C.D.C.D.C/.D/DCDC\|$ | 5 | 2 |
| 90.00° | $(112)_1$ / $\left(11\bar{2}\right)_2$ | $\|DC\|$ | 1 | 0 |

by the dissociation of the D SU on every third plane creates the 9R phase. Table 3.3 summarizes the GB structure for the six GBs depicted in Figure 3.5. The ratio of the D SUs on the CTB facets to the $|DC|$ units on the SITB facets decreases as the inclination angle increases.

All ATGBs with the 9R phase are separated by two boundaries. The misorientation change across these GBs occur along the two sub-boundaries that contain the 9R phase (viewed from upper to lower crystal of Figures 3.5(b)-(e)). The first boundary that alters the misorientation is the boundary of C SUs which rotates the upper lattice to coincide with the 9R phase lattice. The dissociation of the D SUs from the SITB facet allows the C SUs to rearrange to minimize strain at this upper boundary; this allows only a partial rotation of the lattice to occur. The opposite boundary of the 9R phase is a small angle dislocation boundary composed of the dissociated D SUs; this sub-boundary rotates the lattice additionally to coincide with the given misorientation between the upper and lower crystals.

Figure 3.6 compares the calculated $\Sigma 3$ $\Phi = 81.95°$ asymmetric tilt grain boundary structure containing the 9R phase in Cu with an experimental HRTEM image of the 9R phase in Ag [188]. Although different materials, both Cu and Ag have low stacking fault energies and an FCC crystal structure, which enables the 9R phase to form. Figure 3.6(a) shows the structural unit description of the ATGB used to generate a simulated image in Fig. 3.6(b), which is compared with the experimentally observed HRTEM image in Fig. 3.6(c). The 2D projected view of the {111} planes, in white, shows the agreement between the simulated

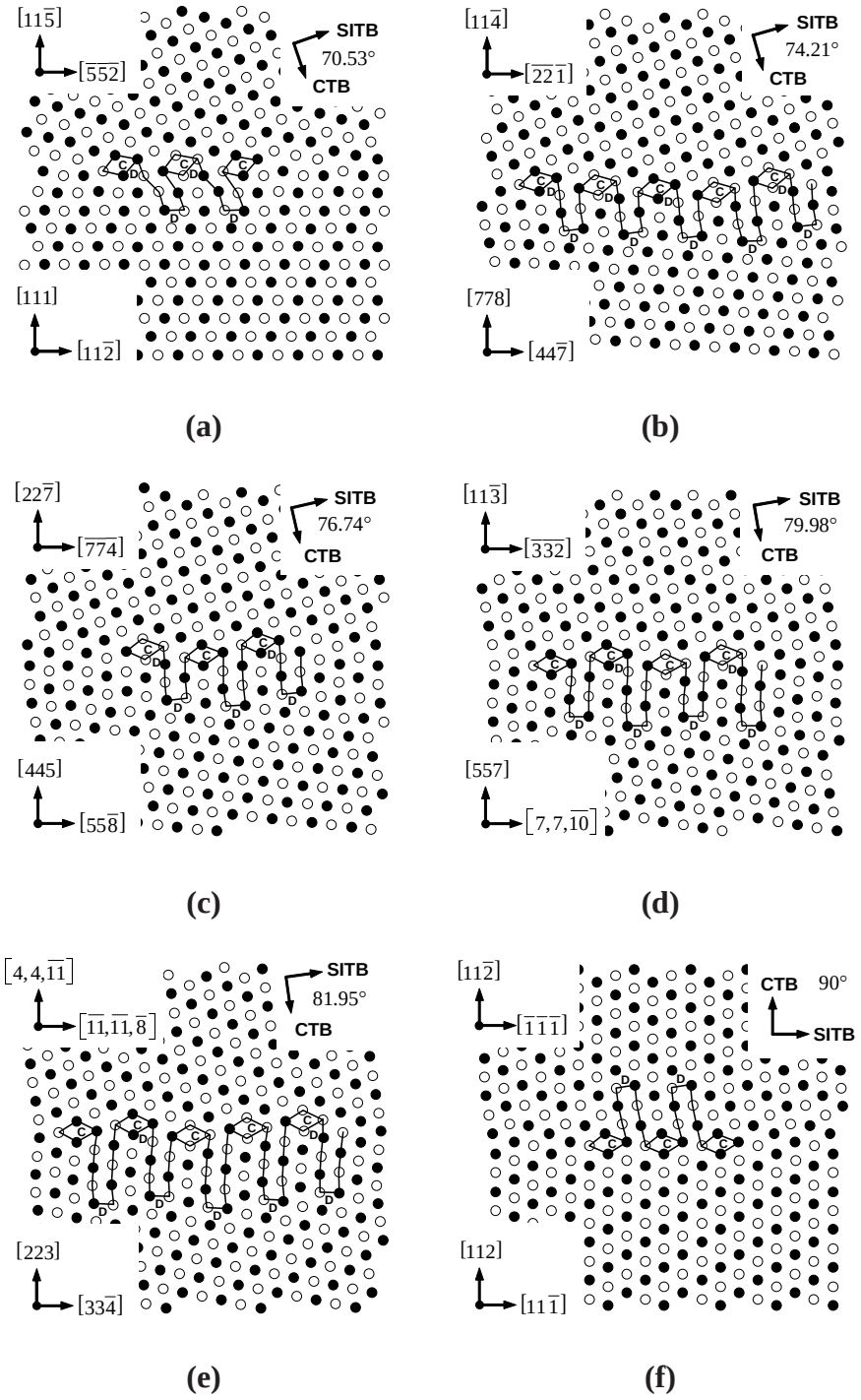


**Figure 3.5:** Six Σ3 grain boundary structures in Cu for various inclination angles 70.53° ≥ Φ ≥ 90°. The same format as Figure 3.4 is used for illustrating the grain boundary structures.

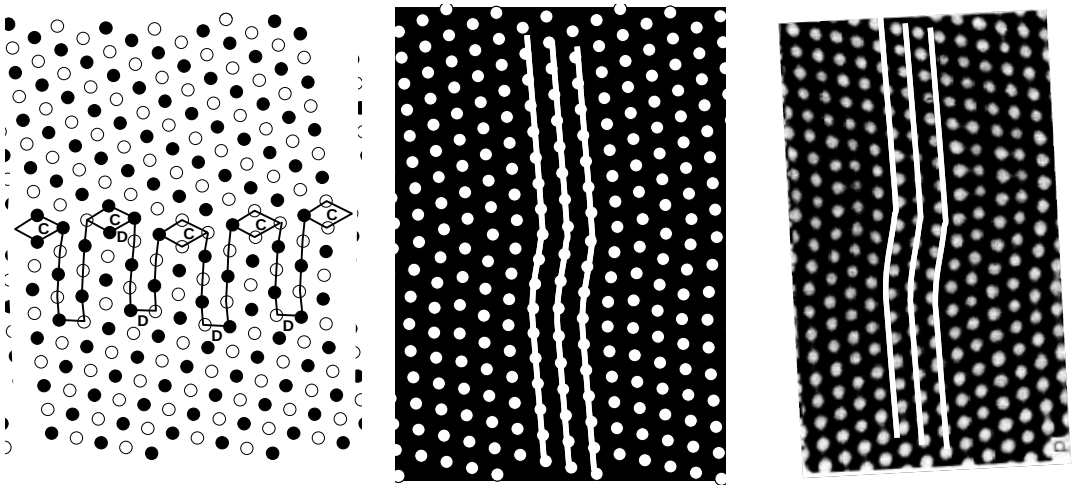


**Figure 3.6:** Comparison of calculated $\Sigma 3$ $\Phi = 81.95°$ asymmetric tilt grain boundary structure with the 9R phase in Cu with experimental HRTEM image of the 9R phase in Ag [188]. (a) Interface structure with structural units outlined, (b) simulated image using atom positions from (a), and (c) HRTEM image of Ernst and coworkers [188]. The white lines correspond to the {111} planes in the adjoining crystals and at the interface.

and experimental images. In fact, these images also have similar widths of the 9R phase, despite the finding by Campbell and coworkers [197] that the width of the 9R phase often increases with time in the HRTEM.

The rotation of the structural units on the different facets were calculated to further characterize the change in the GB structure within the 9R phase ATGBs. The average angles of rotation were calculated for the D SUs in the CTB facet and the C SUs in the SITB facet based on the schematic in Figure 3.7(a). Figure 3.7(b) plots the rotation of the CTB and SITB facets based on inclination angle against the calculated rotation angles of the D SUs in the CTB facets and the C SUs in the SITB facets. The calculated angles of rotation for the structural units should ideally coincide with the inclination angles; for $\Phi < 70.53°$, this is the case. However, for $\Phi > 70.53°$, the calculated angles of rotation for the SUs in the CTB and SITB facets deviates from those based only on the inclination angle. For example, the C SUs are inclined at 72.7° compared to the ideal inclination of 81.95° for the $\Sigma 3(223)_1/(4,4,\bar{1}1)_2\Phi = 81.95°$ ATGB. In the same ATGB, the D SUs for

the CTB facet are inclined at 90°, *i.e.*, greater than the inclination angle. This observed phenomenon stems from the interaction between the individual facets and the surrounding crystal lattices to minimize the total GB energy.

The width of the 9R phase is caused by the degree of dissociation of the D SU on the SITB facet and this width changes as a function of the inclination angle for ATGBs with $\Phi > 70.53°$. As shown in Figure 3.5, the dissociation width increases with $\Phi > 70.53°$ until the $\Sigma 3(223)_1/(4,4,\bar{1}1)_2\Phi = 81.95°$ ATGB and then decreases at some point to the width calculated in the SITB. All these GBs, including the SITB, contain the correct 9R phase stacking sequence caused by the intrinsic stacking faults on every third plane. However, this 9R phase may not be present in some boundaries, because there is an energetic penalty to dissociate the D SU further and expand the 9R phase. In Figure 3.5(a), notice the distortion of the intrinsic stacking fault associated with the dissociated D SUs, which may restrict the expansion of the 9R phase. However, as the lattices and structural units are rotated with increasing inclination, the width of the dissociation and the 9R phase increase.

So, what are the differences that contribute to the dissociation width in these ATGBs? All ATGBs have the |*DC*| structural units associated with the SITB and all D SUs dissociate to some degree. The main differences are the orientation of the surrounding lattices, the rotation of the C SUs, and the frequency of the D SU on the CTB facets. All three of these differences contribute to the dissociation width. Interestingly, based on the calculations in Figure 3.7(b), the $\Sigma 3(223)_1/(4,4,\bar{1}1)_2\Phi = 81.95°$ ATGB contains a D SU on the CTB facet with a Burgers vector that is closest to lying within the plane of the boundary. The strain field from this dislocation may provide additional impetus to expand the 9R phase by further dissociating the boundary of D SUs. In addition, Marquis *et al.* [198] show that the finite size of the SITB (bounded by CTBs) affects the high-resolution electron microscopy structure observed in Au. Relating this to the present study, the spacing between the D SUs on the CTB facets may also present certain length effects relating to both the SITB facet structure and the dissociated D SUs along the SITB facets.

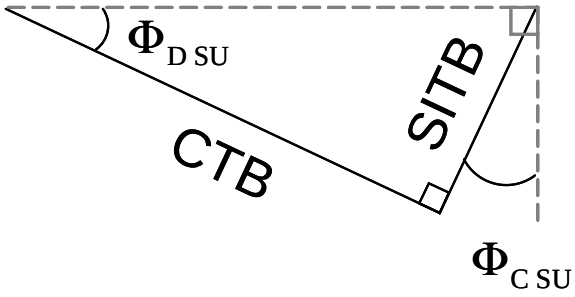


**(a)**

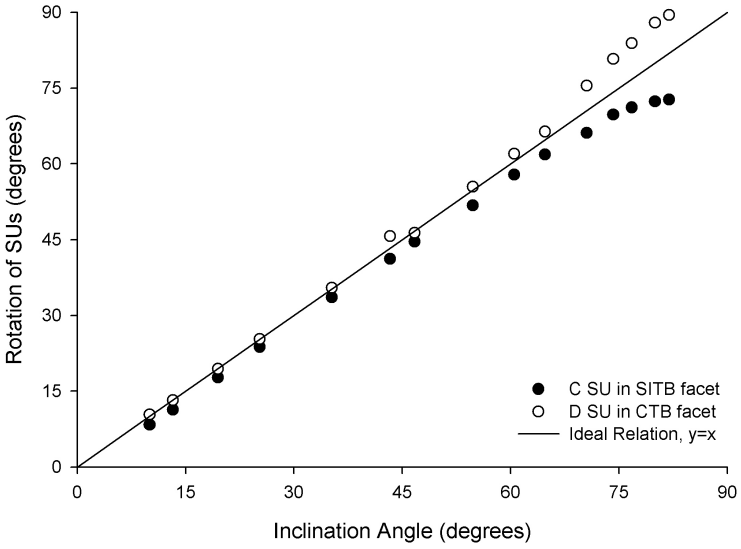


**(b)**

**Figure 3.7:** (a) Schematic depicting the rotation angles calculated for the D SU on the CTB facet and the C SU on the SITB facet. (b) Rotation angles of these two structural units as a function of the grain boundary inclination angle. Notice that the structural units rotate away from the ideal facet orientation for ATGBs displaying the 9R phase (*i.e.*, for $70.53° \geq \Phi \geq 90°$).

Last, the EAM potential must provide an accurate description of the fcc→9R phase transition. Mishin *et al.* [124] have shown that their EAM potential calculates an energetic path from the FCC phase to the 9R phase that is in agreement with *ab initio* calculations. Additionally, the low calculated barrier of ≈ 20 meV, or ≈ 0.020 eV, correlates well with the experimental observation of the 9R phase at Σ3 grain boundaries [158, 188].

### 3.4.4 Comparison of Cu and Al grain boundary structures

The Σ3 ATGB structures for Cu and Al are compared to study the differences the GB structures between a low (Cu) and high (Al) SFE material. The GB structures differ in several ways. First, the D SU on the SITB facet does not dissociate as far in Al as in the Cu Σ3 ATGBs. However, the D SU on the SITB facet dissociates in the same directions as the Σ3 ATGBs in Cu. The second difference between Cu and Al is for GB structures with inclination angles, $\Phi \geq 70.53°$. The 9R phase is not observed in Al. However, the rotation of the C units from the ideal geometric description of the SITB facet plane is still observed. Otherwise, the GB structures are very similar between the two materials. The main similarity is that the GB structures given in Tables 3.2 and 3.3 are also applicable for Al; *i.e.*, the $\Sigma3(111)_1/(11\bar{5})_2\Phi = 70.53°$ ATGB has a $|D/.D.C/.D/DC|$ structure in both Al and Cu. This implies that the SU description of Σ3 ATGBs may be similar between both low and high SFE materials, even though certain SUs may dissociate more in some materials than others.

## *3.5 Discussion*

### 3.5.1 Faceting behavior

Many experimental studies have investigated the faceting and de-faceting of ATGBs as a function of temperature, impurity content, or material system [123, 199–204]. Hsieh and Baluffi [204] have shown the first direct experimental observation of a reversible roughening/de-faceting phase transition whereby faceted Σ3 and Σ11 ATGBs were observed to transition to a curved GB structure upon heating above a transition temperature.

Straumal *et al.* [201] have shown that as the temperature is increased for a cylindrical Cu $\Sigma 3$ bicrystal, the number of facets decreases from six different facet structures at $0.35T_m$ to two different structures at $0.95T_m$, where $T_m$ is the melting temperature. The two structures observed at high temperatures are the CTB and the $\Sigma 3(223)_1/(4,4,\bar{1}1)_2\Phi = 81.95^\circ$ ATGB. Additionally, thermal grooving measurements from atomic force microscopy were used to determine the equilibrium crystal shape as a function of temperature; the Wulff construction [205], or $\gamma$-plot, evolves as a function of temperature [203]. Using data from Table 3.1, Figure 3.8 shows the $\gamma$-plot for Cu and Al, where the CTB and SITB are on the vertical and horizontal axes, respectively. The $\gamma$-plot for Cu predicts that the 0 K equilibrium crystal shape is bounded by the CTB and the $\Sigma 3(223)_1/(4,4,\bar{1}1)_2\Phi = 81.95^\circ$ ATGB, which agrees with the structures observed experimentally at $0.95T_m$, but not at $0.35T_m$. The $\gamma$-plot predicts the faceting at a scale comparable with experimental SEM images, *i.e.*, macro-faceting. However, the faceting discussed in the current study is at the atomistic level, where the facets are on the order of a nanometer, *i.e.*, micro-faceting. In fact, many of the facets in this study may only be observed as facets with atomic scale resolution and prior knowledge of the SUs of STGBs (*e.g.*, Figures 3.4(d-f) and 3.5(a-e)). Aside from the aforementioned faceting experiments, the faceting referred to in this work is micro-faceting, not macro-faceting.

The ATGB structures observed in these simulations raise several questions with respect to the atomistic studies of faceting. First, the facets that are observed have as few SUs as possible for the given inclination angle; *i.e.*, it is not energetically favorable for these facets to increase in size. One explanation may be that the periodic boundary conditions on the faces perpendicular to the grain boundary plane are assigned to the minimum possible period; this may potentially constrain the length of the boundary facets [2]. However, increasing the size of the simulation cell in these directions does not result in a different structure or energy, which counters this assertion. The other explanation is that the faceting behavior observed is the energetically favorable grain boundary structure at 0 K. Brokman

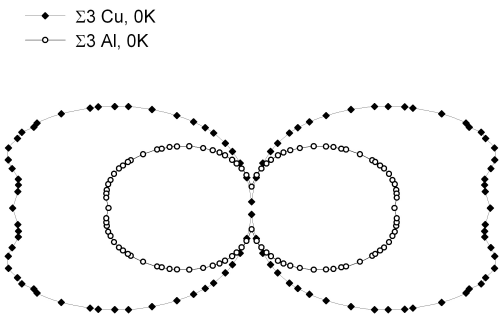


**Figure 3.8:** Wulff construction or $\gamma$-plot for the $\Sigma 3$ ATGB energies in Cu and Al as a function of inclination angle using data from Table 3.1. The CTB and SITB are located on the vertical and horizontal axes, respectively.

*et al.* [206] separated the energy of a faceted GB as the sum of two energy contributions: the "self-energy" of the individual facets and the "interaction energy" between the different facets. While the self-energy is independent of the scale of the faceting, the interaction energy is dependent on the number of intersections of different facets. Based on the GB structures generated in this work, the interaction energy is negative; *i.e.*, it is energetically favorable to have a large number of intersections of the CTB and SITB facets. This results in atomistically small facet lengths that are stable against growth. Another way of viewing the energy of facets is in terms of continuum defects such as dislocations. The facet self-energy is the GB dislocation energy and the interaction energy is the energy produced by the interaction of the GB dislocation stress fields from different facets. In the case of these simulations, the energy associated with the interaction between GB dislocations on different facets is reduced by the introduction of more facets. Since molecular statics was employed, the equilibrium GB structures generated are at 0 K (athermal); MD simulations of equilibration at 300 K for 10,000 fs for several ATGBs with larger GB dimensions (*i.e.*, greater than 16 nm in the GB plane directions) show that the GB structure

retains its atomistically faceted structure. However, it is possible that experimentally observed macro-faceting may be affected by even higher temperatures, low concentrations of impurity atoms, dislocation content in the grain interior, vacancies, or internal stresses.

### 3.5.2 Energetic model for Σ3 ATGBs

Assuming that the self-energies of the individual facets corresponding to the CTB and the SITB contribute additively (*i.e.*, no interaction energy), the equation for the GB energy can be derived for Σ3 ATGBs. First, the ideal relation between the inclination angle Φ and the lengths of the CTB and SITB facets ($L_{CTB}$ and $L_{SITB}$, respectively) is $\tan\Phi = L_{SITB}/L_{CTB}$. Note that this relation holds only if the two faceted segments are perpendicular. From this relation, the Σ3 ATGB energy for an arbitrary inclination angle, $\gamma_\Phi$, is given by,

$$\gamma_\Phi = \gamma_{CTB}\cos(\Phi) + \gamma_{SITB}\sin(\Phi) \tag{3.1}$$

where $\gamma_{CTB}$ and $\gamma_{SITB}$ correspond to the CTB and SITB energies. This equation is plotted against the calculated GB energies from this study in Figure 3.3(b). The Al curve fits the calculated ATGB energies with constants that correspond to the calculated CTB and SITB energies, *i.e.*, $\gamma_{CTB} = 75.2$ mJ/m$^2$ and $\gamma_{SITB} = 354.4$ mJ/m$^2$. The Cu curve fits the calculated GB energies with constants that correspond to the calculated CTB energy, *i.e.*, $\gamma_{CTB} = 22.2$ mJ/m$^2$, and the hypothetical, unrelaxed SITB energy, *i.e.*, $\gamma_{SITB} = 700$ mJ/m$^2$. The hypothetical, unrelaxed SITB energy for Cu is a fitting parameter that corresponds to the SITB energy without the dissociation of dislocation SUs (as used in [189]). This fitting parameter was calculated using a nonlinear regression for ATGBs with inclination angles $\Phi < 70.53°$. For Cu, the low SFE causes a difference between the unrelaxed and relaxed energies in some GBs due to the dissociation of GB dislocations. The curve predicted using equation 3.1 fits both the calculated Al ATGB energies for Al and the calculated Cu ATGB energies with an inclination angles $\Phi < 70.53°$ very well. However, notice the deviation of GB energies from the predicted curve in Cu for inclination angles $\Phi > 70.53°$.

The good agreement with the facet self-energies shows that the energy contribution due to interaction energy is negligible in comparison. So, while the interaction energy is important for the faceting behavior of the ATGB structure, it is not a significant component in terms of predicting the ATGB energy.

To entirely fit the calculated GB energy values in Cu, the aforementioned equation requires additional terms to describe the interaction energy between the two dissociated boundaries in the 9R phase GB region, *i.e.*, for ATGBs with $\Phi \geq 70.53^\circ$. The additional terms reduce the energy of the GB by dissociating and creating the 9R phase. The extended dissociation of the D SUs in the 9R phase is energetically favorable if the following inequality is true [91]: $\gamma_{1/2} > [\gamma_{1/3} + \gamma_{2/3} + \gamma_{ISF} w + \tau(w)]$. In this equation, $\gamma_{1/2}$ is the GB energy between crystal lattices 1 and 2 prior to dissociation; $\gamma_{1/3}$ and $\gamma_{3/2}$ are the energies of the two new boundaries formed after the D SUs dissociate to form the 9R phase (lattice 3). The energy per unit volume of the intrinsic stacking faults $\gamma_{ISF}$ is multiplied by the dissociation width $w$ to give the energy per unit interfacial area. The term $\tau(w)$ corresponds to the interaction energy between the two boundaries. The dissociative width is finite at equilibrium because the energy terms $\gamma_{ISF} w$ and $\tau(w)$ act against each other with respect to $w$. Rittner and Seidman originally used this equation to describe the energy of dissociated structural units in $\langle 110 \rangle$ GBs with tilt angles between $50.48^\circ$ and $109.47^\circ$ as well as generalizing to the 9R phase. This same form is used for discussion purposes only. Notice that several terms in this equation change with respect to the inclination angle for the 9R phase. Both $\gamma_{1/3}$ and $\gamma_{3/2}$ change with inclination angle since the length of the SITB facet per unit length of ATGB increases slightly for $\Phi \geq 70.53^\circ$. As is observed in Figure 3.5, the width of the intrinsic stacking fault created by the dissociated D SU evolves as a function of the inclination angle; this is caused by the change in the interaction energy between the two boundaries due to differing orientations of the structural units as a function of inclination. Interestingly, $\gamma_{1/2}$ may be viewed as corresponding to the dotted portion of the Cu fitted curve in Figure 3.3(b); the actual calculated energies result from a lower

energy due to dissociation, *i.e.*, $\gamma_{1/3} + \gamma_{2/3} + \gamma_{ISF} w + \tau(w)$. Last, the stacking fault energy of the material is directly related to $\gamma_{ISF}$. For Al, the higher stacking fault energy results in a smaller dissociation width relative to that of Cu. Hence, no 9R phase transition is observed in Al. While this equation helps explain the source of the energy terms required for the 9R phase, the energy of these boundaries may best be described through a dislocation description [90, 91] or continuum description of these dissociated grain boundaries.

### 3.5.3 Structural unit and microfacet description of Σ3 ATGBs

The structural unit model [148] is used to predict the variation in atomistic structures for STGBs within certain misorientation ranges. This model is similar to the work of Bishop and Chalmers [207], which characterized the STGB description in terms of ledges from the adjoining lattices that coincide at the GB. In the structural unit model, certain grain boundaries with only one type of repeating SU are termed favored grain boundaries. Grain boundaries with misorientations that lie between two favored GBs can be composed of SUs from the two favored GBs. While the structural unit model has successfully predicted the GB structures in high SFE materials, Rittner and Seidman have shown that this model only explains some of the structures found in the ⟨110⟩ STGBs [91]. Conversely, for ATGBs of the same CSL system, the variation in GB structures as a function of inclination is explained through microfaceting associated with the mean boundary plane, defined by the parameter $\xi$ [2]. However, as noted by Sutton and Vitek [208], while it is possible for a particular coincidence system to facet into the corresponding STGBs, it is not necessarily energetically favourable. This concept of atomistic faceting of asymmetric tilt grain boundaries has also been previously proposed by Brokman *et al.* [206]. Still, whether an ATGB will facet into two STGBs depends on the anisotropy on the interfacial energies of the two STGBs; for the case of Σ3 ATGBs, the anisotropy of the energies allows this faceting to occur at all inclination angles. The model presented here reflects new insight based on the atomistic description of Σ3 ATGBs.

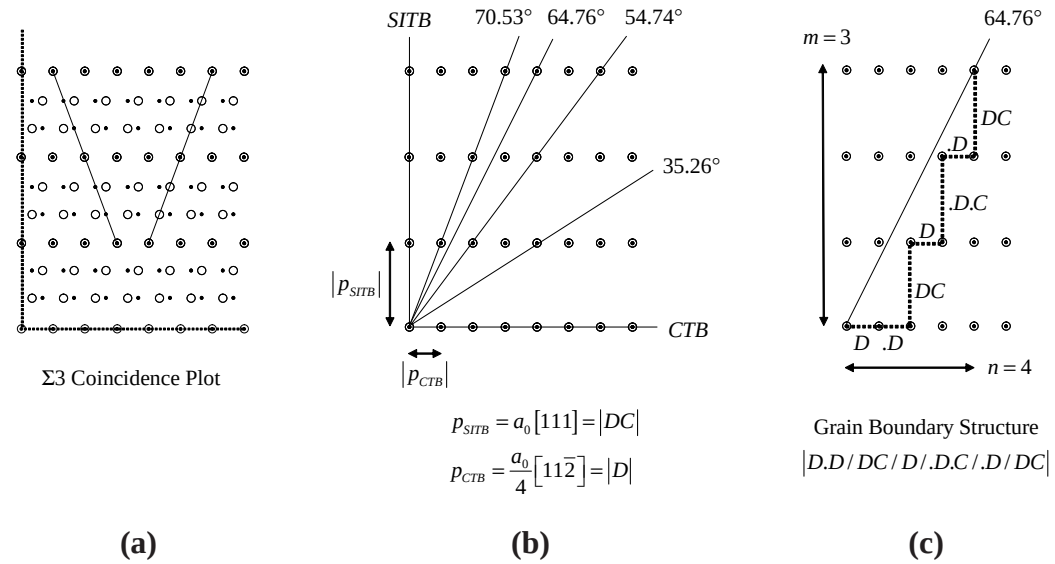


**Figure 3.9:** Structural unit and microfacet model for Σ3 ATGBs. (a) Coincident plot for the Σ3 system rotated around the $[1\bar{1}0]$ tilt axis. (b) Schematic of the coincident points from (a) along with several GB planes of varying inclination angles. The GB periods of the CTB and SITB correlate to specific atomic SUs. (c) The SU description of the $\Sigma 3\,(554)_1 / \left(11\bar{8}\right)_2$ $\Phi = 64.76°$ ATGB is predicted based solely on the coincident points from (a) and the SUs from the two Σ3 STGBs. Compare to Table 3.2 and Fig. 3.4(f).

In a method motivated by the structural unit model, the atomistic SUs *and* their corresponding facets can be predicted for Σ3 ATGBs. The Σ3 ATGB structures for Cu and Al can be determined using the coincidence plot [209] along with the atomistic GB structures of the STGBs. In this respect, the following method used for predicting the Σ3 ATGB structure is very similar to the decomposition lattice method (*cf.* [148]) or strip method of quasicrystallography (*cf.* [154, 210]); the strip method is used to determine the structural unit sequence for rational boundaries. Figure 3.9 shows how the coincidence plot along with the SUs for the STGBs is used to predict the GB structural unit description in Σ3 ATGBs in Cu and Al. First, shown in Figure 3.9(a), the coincidence plot is created by defining a misorientation angle (*i.e.*, $\theta = 70.53°$ in this case) and allowing the two crystal lattices to overlap. The coincidence plot visually illustrates the CSL concept for symmetric and asymmetric tilt grain boundaries.

The GB plane is then realized by connecting any two coincident points, as shown in

Figure 3.9(b). Several GB planes are shown: the CTB, the SITB, and some intermediate ATGBs with different inclination angles. The GB periods for the CTB and SITB can be defined from either crystal lattice; in this case, the periods for the CTB and SITB are $p_{CTB} = a_0/4\left[11\bar{2}\right]$ and $p_{SITB} = a_0\,[111]$, respectively. The relationship between the inclination angle and the GB periods is defined geometrically as

$$\Phi = \tan^{-1}\left(\frac{m}{n}\frac{|p_{SITB}|}{|p_{CTB}|}\right) \tag{3.2}$$

where $m$ and $n$ are integers defining the number of CTB and SITB period vectors required to link any two coincident points. An alternate expression is that the ATGB period vector decomposes into the period vectors of the two facets, *i.e.*, $p_{ATGB} = mp_{SITB} + np_{CTB}$. At this point, atomistic simulations were then used to calculate the SUs that correspond to the GB periods of the STGBs. For the CTB, the structure can either be defined as a repeating $|D|$ SU with a period $p_{CTB} = a_0/4\left[11\bar{2}\right]$ or as a repeating $|D.D|$ SU with a period $p_{CTB} = a_0/4\left[11\bar{2}\right]$. The latter SU description was chosen because it contains additional information about the translation of SUs with respect to each other; recall that the dot preceding a SU denotes a relative translation in the direction of the tilt axis by $a_0/4\left[1\bar{1}0\right]$. This SU description requires $n$ to be an even integer. Figure 3.9(c) shows how the coincident lattice sites from (a), the GB plane from (b), and the STGB SUs were combined to predict the ATGB SU description of the $\Sigma3(554)_1/(11\bar{8})_2\Phi = 64.76°$ ATGB. Until this point, this model determines the number of SUs on each facet, but there are still some rules that govern the number and translation of SUs on each facet. Some of the rules for the $\Sigma3$ ATGB structures are:

1. For $\Phi \leq 70.53°$, all $|DC|$ SUs on the SITB facet should be separated by at least one $|D|$ SU on the CTB facet. Additionally, for $\Phi \geq 70.53°$, all $|D|$ SUs on the CTB facet should be separated by at least one $|DC|$ SU on the SITB facet. As observed in (c), this rule minimizes the number of SUs on each facet and maximizes the number of facets.

2. For all SITB facet SUs following a |*D*| SU on the CTB, there is a translation involved, *i.e.*, they are |.*D*.*C*| SUs. Additionally, for all SITB facet SUs following a |.*D*| SU on the CTB, there is no translation involved, *i.e.*, they are |*DC*| SUs. This SU translation is assigned purely by the convention used in this research to distinguish between SUs with relative translations of $a_0/4\left[1\bar{1}0\right]$; the |.*D*.*C*| and |*DC*| may be switched in the previous statements and still be correct.

The Σ3 ATGB structural unit and microfacet model was used with the $\Sigma3(554)_1/(11\bar{8})_2$ $\Phi = 64.76^\circ$ GB to predict the same SU description as the calculated grain structure shown in Figure 3.4(f) and listed in Table 3.2. Moreover, this model accurately predicts the GB SU description of all 23 Σ3 ATGBs in this study, even with the reorientation of SUs and the 9R phase formed for ATGBs with $\Phi \geq 70.53^\circ$ in Cu. Interestingly, especially considering the multiplicity of possible grain boundary structures [145], the lowest energy structures for all Σ3 ATGBs in Cu and Al follow this model for structural units and faceting.

While this structural unit and microfacet model fits the GB structures calculated for Σ3 ATGBs, it is not apparent whether these rules hold for other CSL systems. For instance, Duparc and colleagues [211] systematically investigated the variation in GB morphology for a high energy Σ11 (332) boundary grown by solidification in a bicrystal; in addition to the expected Σ11 (332) STGB structure, they found faceting into numerous Σ11 ATGB structures as well as the low energy favored Σ11 (113) STGB as a function of position in the bicrystal. While the observed ATGBs decompose into variations of the structural units from the Σ11 (332) STGB, the structural unit from the low energy Σ11 (113) STGB was not observed in these ATGBs. Moreover, the distortion of the SUs as a function of the GB plane inclination make it difficult to ascertain the SU description. This reinforces that not all asymmetric boundaries decompose into the structural units of their respective STGBs; this system is contrary to the Σ3 system, which ideally facets into the two Σ3 STGBs.

### 3.5.4 Continuum description of Σ3 ATGBs

The Σ3 ATGB structures can be applied to continuum models by using the aforementioned structural unit model along with a description of the Σ3 ATGB SUs in terms of continuum defects, such as partial dislocations or disclinations. For the purposes of this discussion, partial dislocations were chosen. The |*DC*| SUs on the SITB facet are well described by a dislocation model with three Shockley partial dislocations (*cf.*, [212, 213]). Based on experimental HRTEM images [212], Figure 3.10 shows schematics of the partial dislocation content of (a) the incoherent twin boundary and (b) a boundary with the 9R phase. In this model, the stacking faults that form on every third plane in the 9R phase are terminated by a pure-edge character 90° Shockley partial dislocation (A$\delta$ in Fig. 3.10) with a Burgers vector $b = a_0/6\langle 112\rangle$ such that a low angle boundary exists [158]. In Figures 3.5(a)-(e), the 90° Shockley partials correspond to the lower array of dissociated D SUs. Additionally, the C SUs on the opposite side of the 9R phase is represented by two 30° Shockley partial dislocations [214], *i.e.*, B$\delta$ and C$\delta$ in Fig. 3.10. These two Shockley partials are also known as double-core Shockley partial dislocations [215]. Therefore, the |*DC*| SUs on the SITB facet are associated with two 30° Shockley partials and one dissociated 90° Shockley partial. Kinematically, the net Burgers vector for the |*DC*| SUs is zero, so all three Shockley partial dislocations have a different $a_0/6\langle 112\rangle$ Burgers vector on the same slip plane. Also, on both sides of the SITB, this combination of Shockley partial dislocations gives the correct stacking sequence: ABCABCABC on one side and ACBACBACB on the other side, as seen in Fig. 3.10(a). Additionally, in Fig. 3.10(b), the intrinsic stacking fault created by the dissociated 90° Shockley partial dislocations gives the correct 9R stacking sequence of ABC/BCA/CAB, which is repeated every nine {111} planes.

Shockley partial dislocations are also required for the CTB facets to completely characterize Σ3 ATGBs in terms of continuum defects. The |*D*| SUs on the CTB facet are Shockley partial dislocations of the type $a_0/6\langle 112\rangle$. As is observed in Figures 3.5(a)-(e), the |*D*| SU on the CTB facet is also a component of GBs with the 9R phase. Hofmann and

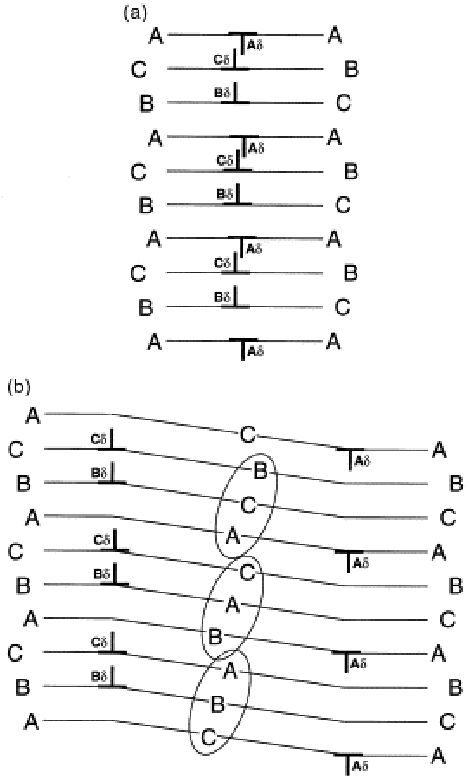


**Figure 3.10:** (a) Schematic showing the arrangement of dislocations representing the FCC incoherent twin interface. The dislocation Burgers vectors are represented in Thompson's notation. A$\delta$ is a negative 90° partial dislocation, whereas B$\delta$ and C$\delta$ are positive 30° partial dislocations. The stacking sequence of the close-packed FCC (111) planes on the two sides of the interface is indicated. (b) Schematic showing the arrangement of partial dislocations in boundaries that form the 9R phase. The schematics in this figure are from Medlin *et al.* [212].

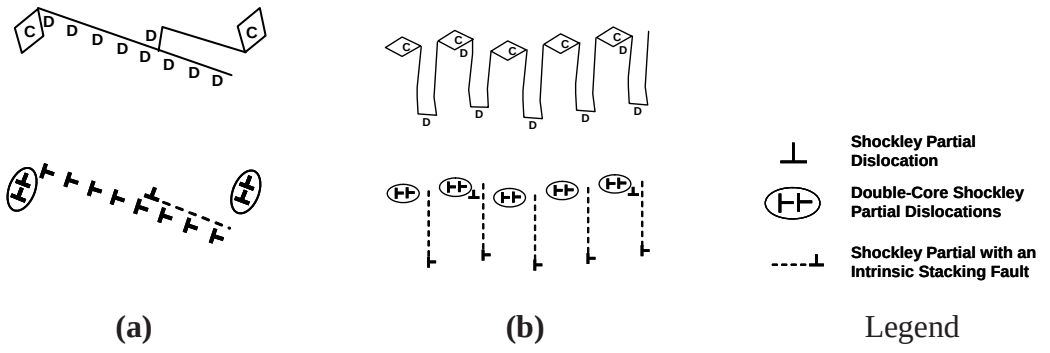


**Figure 3.11:** Partial dislocation description of (a) the $\Sigma 3\,(112)_1\,/\left(\bar{5}\bar{5}2\right)_2\,\Phi = 19.47^\circ$ ATGB and (b) the $\Sigma 3\,(223)_1\,/\left(4,4,\bar{1}\bar{1}\right)_2\,\Phi = 81.95^\circ$ ATGB. Note that the C SUs are described by double-core Shockley partial dislocations while the D SUs are described by single Shockley partial dislocations. The stacking faults on every third plane in (b) create the 9R phase.

Finnis [186] noted that their construction of ATGBs introduced DSC dislocations on the Σ3 ATGBs with a component of the Burgers vector parallel to the boundary plane. This is consistent with the $|D|$ SU on the CTB facets. While the dislocation models available in the literature are mainly applied to the SITB and GBs containing the 9R phases, these models can also be extended to all Σ3 ATGBs.

Figure 3.11 shows a schematic of the dislocation structures for two Σ3 ATGBs: (a) the $\Sigma 3(112)_1/(\bar{5}\bar{5}2)_2\Phi = 19.47^\circ$ ATGB and (b) the $\Sigma 3(223)_1/(4,4,\bar{1}\bar{1})_2\Phi = 81.95^\circ$ ATGB. In this schematic, the structural unit representation from Figures 3.4(c) and 3.5(e) is shown above the dislocation representation. Notice that the symbols used to represent the partial dislocations of the ATGB structure follow the prior discussion in this section. Additionally, atomistic calculations for the structural unit description of these boundaries are not required. Using the proposed structural unit description for Σ3 ATGBs along with the dislocation description of SUs, the dislocation structure for all Σ3 ATGBs is predicted without atomistics.

This is significant for representing GBs in certain continuum models that employ ***partial*** dislocation descriptions. For example, phase field models have been extended into dislocation dynamics by introducing phase-fields to represent dislocations similar to a phase

transition [216–219]. Additionally, Shen and Wang [220] incorporate the $\gamma$-surface into dislocation phase field models to better simulate the dissociative nature of dislocations in some low stacking fault energy FCC systems. The dislocation representation discussed here may allow for the simulation of $\Sigma 3$ ATGBs in such models. Note that continuum models may also employ disclination dipoles to represent the SUs of these boundaries, as they are kinematically compact.

## *3.6 Summary*

In this chapter, atomistic simulations were used to explore the structure and energy of ATGBs in the $\Sigma 3$ system about the $\langle 110 \rangle$ tilt axis. A nonlinear conjugate gradient algorithm was employed along with an embedded atom method potential for Cu and Al to generate the equilibrium 0 K grain boundary structures. A total of 25 $\langle 110 \rangle$ grain boundary structures were explored to identify the various equilibrium and metastable structures. Simulation results show that the $\Sigma 3$ asymmetric tilt grain boundaries in the $\langle 110 \rangle$ system are composed of only structural units of the two $\Sigma 3$ symmetric tilt grain boundaries. The energies for the $\Sigma 3$ grain boundaries are similar to previous experimental and calculated grain boundary energies. A structural unit and faceting model for $\Sigma 3$ asymmetric tilt grain boundaries fits all of the calculated asymmetric grain boundary structures. The significance of these results is that the structural unit and facet description of all $\Sigma 3$ asymmetric tilt grain boundaries may be predicted from the structural units of the $\Sigma 3$ coherent twin and incoherent twin boundaries for both Cu and Al. For citation of the work contained in this chapter, the reader is referred to Ref. [76, 78].

# CHAPTER IV

# STRUCTURES AND ENERGIES FOR LOW ORDER CSL ATGBS

This chapter focuses on the structure and energy of asymmetric tilt grain boundaries. Atomistic simulations were employed to investigate the structure and energy of asymmetric tilt grain boundaries in Cu and Al. In this chapter, the $\Sigma 5$ and $\Sigma 13$ systems with a boundary plane rotated about the $\langle 100 \rangle$ misorientation axis were examined along with the $\Sigma 9$ and $\Sigma 11$ systems rotated about the $\langle 110 \rangle$ misorientation axis. Asymmetric tilt grain boundary energies are calculated as a function of inclination angle and compared with an energy relationship based on faceting into the two symmetric tilt grain boundaries in each system. One finding is that asymmetric tilt boundaries with low index normals do not necessarily have lower energies than boundaries with similar inclination angles, contrary to previous studies. Further analysis of grain boundary structures provides insight into the asymmetric tilt grain boundary energy. The $\Sigma 5$ and $\Sigma 13$ systems in the $\langle 100 \rangle$ system agree with the aforementioned energy relationship; structures confirm that these asymmetric boundaries facet into the symmetric tilt boundaries. The $\Sigma 9$ and $\Sigma 11$ systems in the $\langle 110 \rangle$ system deviate from the idealized energy relationship. As the boundary inclination angle increases towards the $\Sigma 9$ (221) and $\Sigma 11$ (332) symmetric tilt boundaries, the minimum energy asymmetric boundary structures contain low index {111} and {110} planes bounding the interface region.

## *4.1 Introduction*

The grain boundary (GB) structure and energy are necessary for a fundamental understanding of many material properties in polycrystalline materials, such as grain growth, impurity segregation, diffusion, deformation and fracture. Atomistic simulations have provided considerable insight into the atomic structure and energy of grain boundaries [154], and

have shown very good agreement with high resolution transmission electron microscopy (HRTEM) images of GB structure (*e.g.*, [18, 158, 159, 186–188, 198, 211, 213]). The majority of atomistic simulations have focused on the structure and energy of symmetric tilt grain boundaries (STGBs) [90–92, 148, 221, 222] and twist boundaries [184, 223–230]. However, very few atomistic simulations have explored the role of the grain boundary plane orientation on the structure and energy of asymmetric tilt grain boundaries (ATGBs), even though experimental characterization has shown that most boundaries in polycrystalline materials are actually ATGBs [65].

Much of the focus on the grain boundary plane orientation, or inclination of the grain boundary plane, in ATGBs has been on the Σ3 system, mainly because the most common Σ3 GB is the coherent twin boundary. Numerous studies of Σ3 ATGBs have focused on the structure and energy of Σ3 ATGBs [18, 78, 158, 159, 186–188] as well as the influence of GB inclination on properties, such as GB diffusion [160], intergranular corrosion resistance [161], or dislocation nucleation [77]. While the Σ3 system has garnered much attention due to its high observed frequency in low stacking fault energy polycrystals [164, 231–233] and its effect on bulk material properties, very few experiments or simulations have focused on ATGBs in other low index coincident site lattice (CSL) systems: *e.g.*, Σ5, Σ9, Σ11, and Σ13. A better understanding of the structure and energy of these boundaries may provide insight into the distribution and properties of asymmetric boundaries in polycrystals. The five parameter analysis of the grain boundary character distribution of polycrystalline materials has shown that asymmetric tilt boundaries are often observed in a higher frequency than symmetric tilt boundaries (excluding the Σ3 coherent twin boundary) [234].

In this chapter, the influence of the grain boundary plane inclination on the structure and energy is studied for the Σ5, Σ9, Σ11, and Σ13 ATGB systems. Copper and aluminum were chosen as ideal FCCmaterials with moderately different stacking fault energies; these materials are well-characterized with the embedded-atom method (EAM) [109] potential. Moreover, using the results of previous calculations in the Σ3 CSL system [78], conclusions

can be drawn on the nature of the energy and structure of asymmetric tilt grain boundaries in FCC materials.

## *4.2 Simulation methodology and background*

The equilibrium 0 K structure and energy for each ATGB was calculated using a bicrystal computational cell with 3D periodic boundary conditions consisting of two grains (*cf.* [78, 90]). The minimum distance between the two periodic boundaries in each computational cell was 5 nm. Over 2700 initial configurations with different in-plane rigid body translations and an atom deletion criterion were used to access the minimum energy GB structures. A nonlinear conjugate gradient algorithm was used for energy minimization. Cu and Al embedded-atom method potentials [124, 125] were used because their stacking fault energies (stable and unstable) are consistent with available experimental data and *ab initio* calculations. This methodology yields GB energies that agree with both calculated and experimentally measured energies for Σ3 ATGBs [158, 159], as shown in Chapter 3. The GB structures associated with these energies also agree with several experimentally observed HRTEM structures for Σ3 ATGB structures with the 9R structure (*e.g.*, in Cu [159] and Ag [186, 188]). Further details of the simulation methodology that was used to obtain the 0 K minimum energy grain boundary structures can be found in Chapter 2.

### 4.2.1 Structure and energy of symmetric tilt grain boundaries

The structures and energies of symmetric tilt grain boundaries with ⟨100⟩ and ⟨110⟩ misorientation axes are important for understanding the energies of asymmetric tilt grain boundaries with the same tilt axis. Figures 4.1(a) and 4.1(b) show the grain boundary energy as a function of misorientation angle, $\theta$, for the ⟨100⟩ and ⟨110⟩ symmetric tilt grain boundaries, respectively, along with the low order CSL systems from this study. The calculated energy values for the ⟨110⟩ STGBs are in excellent agreement with previously calculated EAM GB energies for Cu and Al ( [92] and [146], respectively). Additionally, the trend of the Al curve is in agreement with the experimentally measured ⟨110⟩ energy curve determined

from the Herring relationship by Hasson and coworkers [147]. Note that the GB energy varies strongly with the misorientation angle for the ⟨110⟩ tilt axis. The two deep cusps are the $\Sigma 11(113)\theta = 50.48^\circ$ STGB and the $\Sigma 3(111)\theta = 109.47^\circ$ coherent twin boundary; there appear to be minor cusps in GB energy for the remaining Σ3, Σ9, and Σ11 STGBs. For the ⟨100⟩ tilt axis, the Σ5 and Σ13 boundaries display only minor cusps, if any, in the energy relationship. Of all STGBs, only the coherent twin boundary energy is smaller in Cu (22 $mJ/m^2$) than in Al (75 $mJ/m^2$); for all other GBs, the Cu energies are, on average, 1.7 times greater than the GB energies in Al. The energy difference for the coherent twin is mainly the result of the high stacking fault energy in Al and the low stacking fault energy in Cu, which encourages twinning.

There is a definitive relationship between grain boundary energy and the structural makeup of the boundary. Each of the STGBs has a different grain boundary structure, which can be characterized by structural units [148]. GBs with certain misorientation angles correspond to 'favored' structural units, while all other GBs consist of a combination of the structural units from the two surrounding favored boundaries [148]. Many of the favored boundaries correspond to low-order CSL systems. In this work, there are a number of favored boundaries with structural units of one type only: the $\Sigma 11\,(113)\,\theta = 50.47^\circ$ STGB (C SU) and $\Sigma 9\,(221)\,\theta = 141.06^\circ$ STGB (E SU) in ⟨110⟩ system [90], and the $\Sigma 5\,(310)\,\theta = 36.87^\circ$ STGB (C SU) and $\Sigma 5\,(210)\,\theta = 53.13^\circ$ STGB (B' SU) in the ⟨100⟩ system [145, 151]. Since there are a total of eight symmetric tilt grain boundaries for the four ATGB systems (Σ5, Σ9, Σ11, and Σ13) chosen, the other four symmetric tilt grain boundaries are not favored and contain a combination of structural units from the favored boundaries. For example, the $\Sigma 11\,(332)\,\theta = 129.53^\circ$ STGB is not a favored boundary since it can be broken down into both D and E structural units from the $\Sigma 3\,(111)\,\theta = 109.57^\circ$ coherent twin boundary and the $\Sigma 9\,(221)\,\theta = 141.06^\circ$ STGB, respectively. The Σ13 ATGB system is the only system studied that does not contain any favored STGBs, since the only favored STGBs about the ⟨100⟩ tilt axis are Σ5 boundaries.

The asymmetric tilt grain boundaries are created by a rotation of the grain boundary plane from a STGB plane about the tilt axis. The inclination angle, Φ, is subsequently used to describe the angle of rotation of the boundary plane from the STGB boundary plane. For all CSL STGBs, either (i) a rotation of the grain boundary plane about the tilt axis by 90° locates the other CSL STGB in the ⟨110⟩ system or (ii) a rotation by 45° locates the other CSL STGB in the ⟨100⟩ system. For example, an inclination of the boundary plane by 45° from the Σ5 (310) STGB is the Σ5 (210) STGB; all inclination angles in between 0° and 45° are Σ5 asymmetric tilt grain boundaries for the ⟨100⟩ system.

## *4.3 Asymmetric tilt grain boundary energy results*

As a brief review of chapter 3, recall that the change in the GB energy as a function of inclination angle for the Σ3 ATGBs in ⟨110⟩ system is shown in Figure 4.2. The energies of 25 Σ3 ATGBs in Cu and Al are plotted against a relationship that describes perfect faceting of a Σ3 ATGB into the two Σ3 STGBs. This relationship describes the Σ3 ATGB energy for an arbitrary inclination angle, $\gamma_\Phi$, *i.e.*,

$$\gamma_\Phi = \gamma_{CTB}\cos(\Phi) + \gamma_{SITB}\sin(\Phi) \tag{4.1}$$

where $\gamma_{CTB}$ and $\gamma_{SITB}$ correspond to the Σ3 (111) coherent twin boundary (CTB) and the Σ3 (112) symmetric incoherent twin boundary (SITB) energies. The Al curve fits the calculated ATGB energies by using the calculated CTB and SITB energies, *i.e.*, $\gamma_{CTB}$ = 75.2 mJ/m$^2$ and $\gamma_{SITB}$ = 354.4 mJ/m$^2$. The Cu curve fits the calculated GB energies by using the calculated CTB energy, *i.e.*, $\gamma_{CTB}$ = 22.2 mJ/m$^2$, and the hypothetical, unrelaxed SITB energy, *i.e.*, $\gamma_{SITB}$ = 700 mJ/m$^2$. The hypothetical, unrelaxed SITB energy for Cu is a fitting parameter that corresponds to the SITB energy without the dissociation of dislocation SUs [189]. Further details of the energy and structure of Σ3 ATGBs are given elsewhere [76, 78]. Two important points from Fig. 4.2 are applicable to the current study, though.

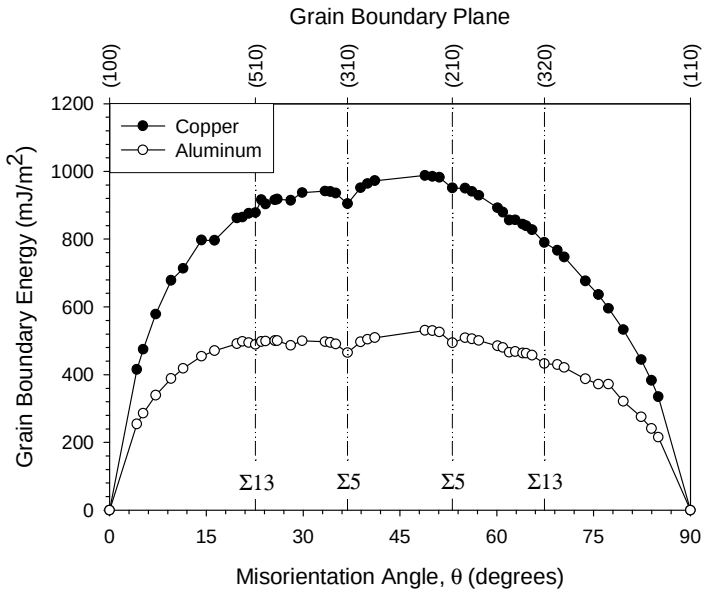


**(a)**

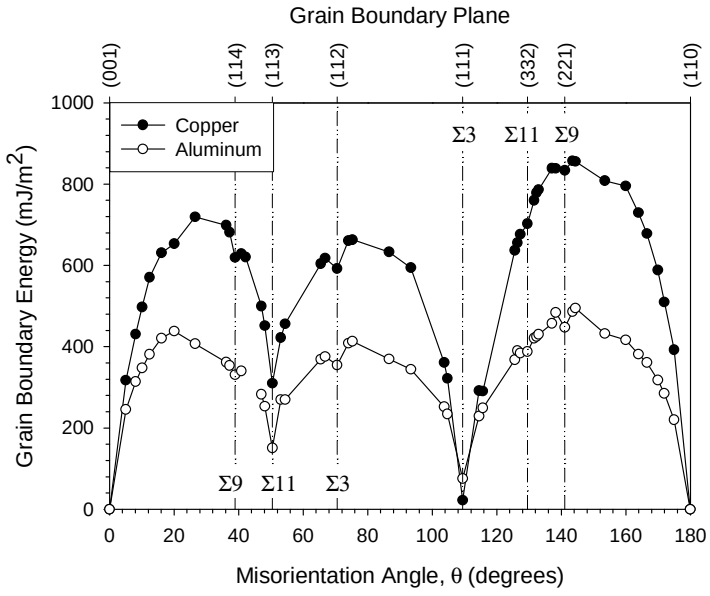


**(b)**

**Figure 4.1:** Structures and energies of symmetric tilt grain boundaries with the (a) [100] and (b) $\left[1\bar{1}0\right]$ misorientation axes.

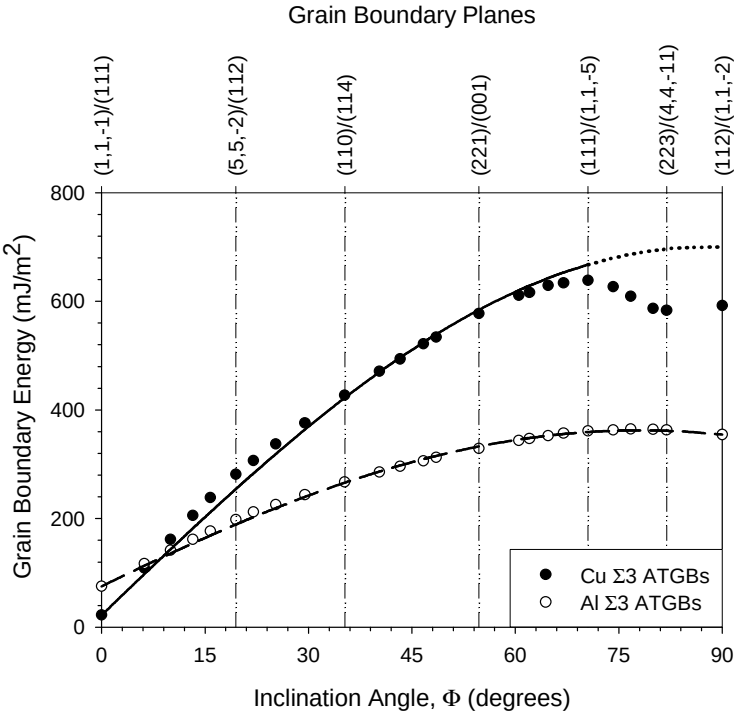


**Figure 4.2:** Grain boundary energy as a function of inclination angle for Cu and Al. The fits for these values follows Eq. 4.1. Energies are from Ref. [78].

1. A good fit to Eq. 4.1 indicates that perfect faceting of ATGBs into two STGBs is energetically favourable. The calculated Al ATGB energies and Cu ATGB energies with inclination angles $\Phi < 70.53°$ fit this relationship very well. The corresponding GB structures show facets with structural units from the two STGBs.

2. Deviation from Eq. 4.1, as in Cu Σ3 ATGBs with $\Phi > 70.53°$, indicates changes in the grain boundary structure. In this case, the ideal faceting still occurred, but it was energetically favourable for GB dislocations to dissociate further, creating the rhombohedral 9R phase.

The grain boundary energies for the ATGB configurations in this study are shown in Figs. 4.3 and 4.4 as a function of the inclination angle. The shape of the energy curves for Al are very similar to Cu for all CSL systems, which differs from the Σ3 ATGBs shown in Fig. 4.2. In each of the CSL systems in Figs. 4.3 and 4.4, an asymmetric tilt grain boundary can facet into the two symmetric tilt grain boundaries, but this decomposition is

not necessarily energetically favourable [148]. This *ideal* faceting relationship is plotted as solid (Al) and dotted (Cu) lines in Figs. 4.3 and 4.4 to compare with the calculated energies. The form of the relationship is

$$\gamma_{ATGB,\Phi} = \gamma_{STGB,1}\left[\cos\Phi - \sin\Phi\left(\frac{\cos\alpha}{\sin\alpha}\right)\right] + \gamma_{STGB,2}\left[\frac{\sin\Phi}{\sin\alpha}\right], \tag{4.2}$$

where $\gamma_{ATGB,\Phi}$ is the predicted ATGB energy, $\gamma_{STGB,1}$ and $\gamma_{STGB,2}$ are the calculated STGB energies, and $\alpha$ is the inclination angle separating two STGBs of the same CSL system ($\alpha = 45°$ for the $\langle 100 \rangle$ system and $\alpha = 90°$ for the $\langle 110 \rangle$ system). This equation reduces to a form similar to Eq. 4.1 for ATGBs in the $\langle 110 \rangle$ system. Since the ATGBs are formed by facets that correspond to the STGBs, the faceted ATGB energy is simply obtained as a weighted fraction of the relative contribution of facet lengths times the respective STGB energy.

The relationship (Eq. 4.2) between the calculated ATGB energies and the predicted energies from an ideal faceting into STGBs may allude to the corresponding GB structure. Figure 4.3 shows the calculated grain boundary energies for $\Sigma 5$ and $\Sigma 13$ boundaries misoriented about the $\langle 100 \rangle$ axis. The small deviation from Eq. 4.2 for the calculated $\Sigma 5$ and $\Sigma 13$ ATGB energies indicates faceting into the structural units of the STGBs may be energetically favourable. As might be expected, the GB structures in Section 4.4 validate that $\Sigma 5$ and $\Sigma 13$ ATGBs do facet into the structural units of their two STGB counterparts.

The $\Sigma 9$ and $\Sigma 11$ ATGBs about the $\langle 110 \rangle$ misorientation axis display a much different behavior, as shown in Fig. 4.4. The $\Sigma 11$ ATGB energies appear to follow this relationship reasonably well, with some amount of deviation, though. On the other hand, the calculated $\Sigma 9$ ATGB energies deviate greatest from Eq. 4.2, displaying an almost linear trend between the two STGB energies. This observed energetic behavior indicates that it is not energetically favourable for the $\Sigma 9$ ATGBs to facet into the corresponding $\Sigma 9$ STGB structural units. Indeed, Section 4.4 shows that faceting into the structural units of their symmetric counterparts is not energetically favourable for many $\Sigma 9$ and $\Sigma 11$ ATGBs about the $\langle 110 \rangle$

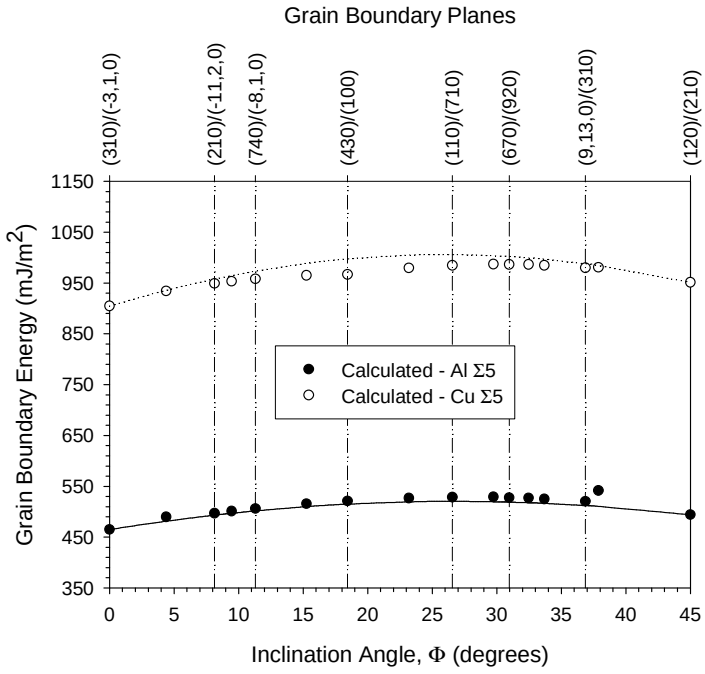


**(a)**

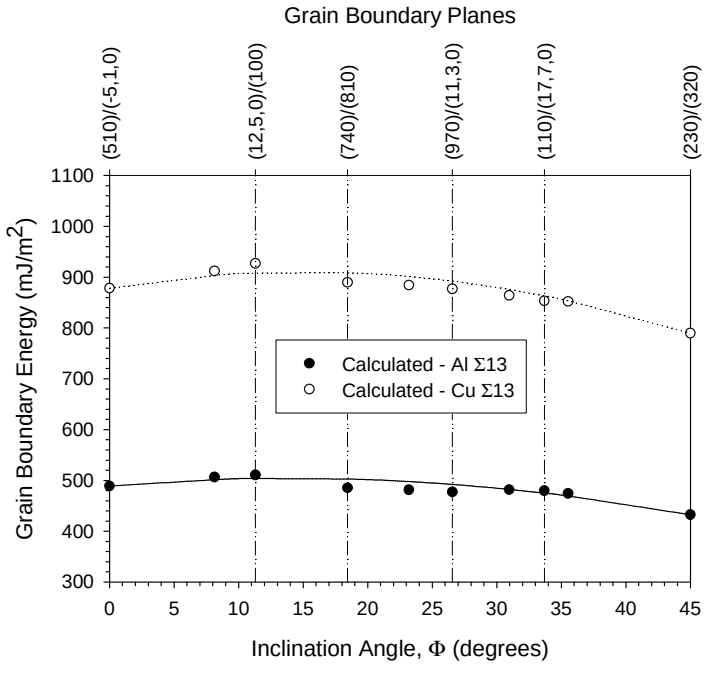


**(b)**

**Figure 4.3:** Grain boundary energy of (a) Σ5 and (b) Σ13 asymmetric tilt grain boundaries with the ⟨100⟩ tilt axis as a function of inclination angle. The trend lines represent the ideal decomposition of the asymmetric boundary into the two symmetric tilt grain boundaries for Cu (solid line) and Al (dotted) according to Eq. 4.2 with $\alpha = 45°$. The upper x-axis shows the grain boundary planes for a few select boundaries.

tilt axis.

The observations from Figs. 4.2-4.4 denote that the ATGB energy depends both on the misorientation axis of the ATGBs (⟨100⟩ or ⟨110⟩) and the CSL system (Σ3, Σ5, Σ9, Σ11, and Σ13). The differences between the misorientation axes and CSL systems may provide some insight into which ATGBs may ideally facet into the structural units of the STGBs. Equation 4.2 depends on the calculated STGB energies ($\gamma_{STGB,1}$ and $\gamma_{STGB,2}$) *and* the constant $\alpha$. Recall that the misorientation axis of the ATGB system determines the value of $\alpha$. Given equal energies of the two STGBs, as $\alpha$ decreases, the degree of anisotropy in the ATGB energies decreases and the more likely that the ATGB will ideally facet into the two STGBs, as shown in the Σ5 and Σ13 ATGBs with the ⟨100⟩ tilt axis ($\alpha = 45°$). Furthermore, based on $\alpha$ alone, it is expected that the Σ7 ATGBs about the ⟨111⟩ tilt axis ($\alpha = 30°$) would facet into the two symmetric Σ7 boundaries. However, $\alpha$ alone is unable to describe the behavior of the ATGB energies with respect to Eq. 4.2. For ATGBs with the ⟨110⟩ tilt axis, the Σ3 and Σ11 ATGBs follow the trend in Eq. 4.2 reasonably well, while the Σ9 ATGBs deviate excessively.

The anisotropy in the two STGB energies ($\Delta\gamma_{STGB} = \gamma_{STGB,1} - \gamma_{STGB,2}$) in Eq. 4.2 may also impact whether the ATGB will follow the trend in this relationship. The largest difference in GB energy for all ⟨110⟩ STGBs of the same CSL content occurs between the Σ3 (111) $\theta = 109.47°$ coherent twin and the Σ3 (112) $\theta = 70.53°$ incoherent twin boundary (*i.e.*, $\Delta\gamma_{STGB} = 570$ mJ/m$^2$ in Cu and $\Delta\gamma_{STGB} = 280$ mJ/m$^2$ in Al). The second largest energy difference is for the Σ11 GB in the ⟨110⟩ system: $\Delta\gamma_{STGB} = 390$ mJ/m$^2$ in Cu and $\Delta\gamma_{STGB} = 240$ mJ/m$^2$ in Al. In contrast to these CSL systems, the anisotropy in the Σ9 STGB energies is much lower ($\Delta\gamma_{STGB} = 214$ mJ/m$^2$ in Cu and $\Delta\gamma_{STGB} = 124$ mJ/m$^2$ in Al). The low anisotropy of the Σ9 STGB energies combined with $\alpha = 90°$ results in a high predicted ATGB energy (Eq. 4.2) due to faceting into the two Σ9 STGBs, much higher than the calculated energies of the Σ9 STGBs. In this case, the Σ9 ATGBs may reorganize via faceting into Σ3 boundaries to minimize the total inferfacial energy [185].

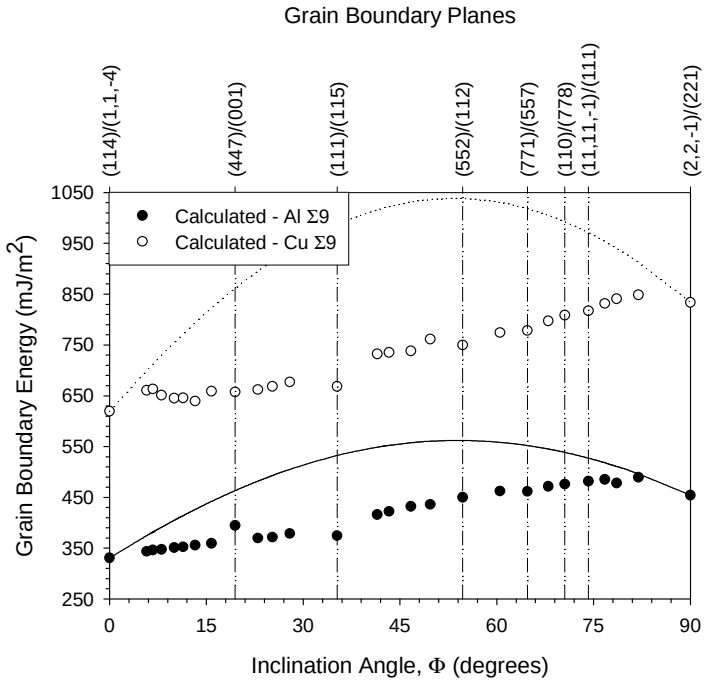


**(a)**

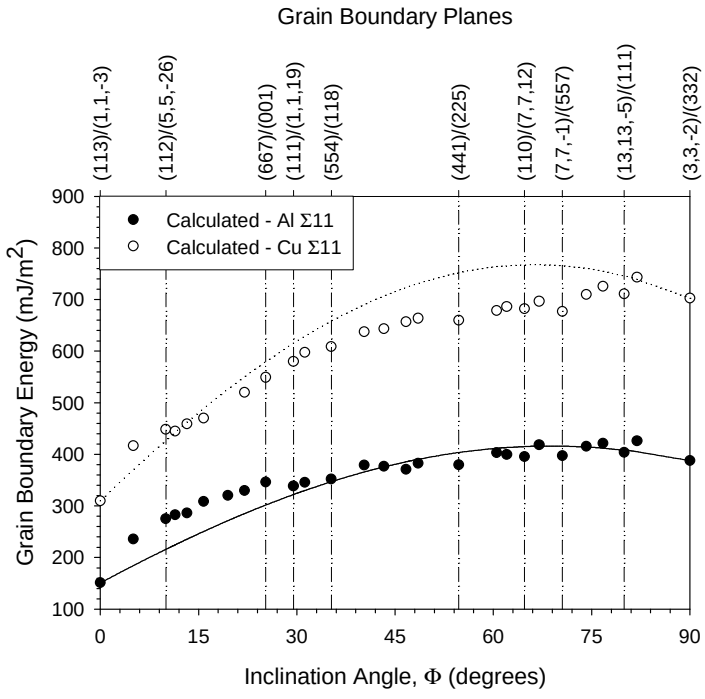


**(b)**

**Figure 4.4:** Grain boundary energy of (a) Σ9 and (b) Σ11 asymmetric tilt grain boundaries with the ⟨110⟩ tilt axis as a function of inclination angle. The trend lines represent the ideal decomposition of the asymmetric boundary into the two symmetric tilt grain boundaries for Cu (solid line) and Al (dotted) according to Eq. 4.2 with $\alpha = 90°$. The upper x-axis shows the grain boundary planes for a few select boundaries.

Merkle and Wolf [185] computed the energy of Σ9 and Σ11 ATGBs using both Lennard-Jones and EAM potentials for Au and Cu to explain the experimentally observed faceting obtained using high resolution electron microscopy. However, there are several differences between this study and the current study. First, a much larger number of grain boundaries are used in this study to ascertain the influence of inclination angle on energy and structure, as these calculations are now more computationally efficient to perform. Second, while Lennard-Jones potentials may capture the qualitative trends, the EAM potentials used in this study are more appropriate for calculating the grain boundary structure and energy. The third and major difference is in the ATGB energy results. The energies from the Merkle and Wolf study [185] shows that certain boundaries with low order indices (*e.g.*, $(001)_1 / (447)_2$ $\Phi = 19.47°$ ATGB) have much lower energies ($\Delta E = 160$ mJ/m$^2$) than nearby ATGBs with higher order indices (*e.g.*, $(112)_1 / (1,1,22)_2$ $\Phi = 15.79°$ ATGB). This is in contrast to the current study. All ATGBs with low order indices (⟨100⟩, ⟨110⟩, ⟨111⟩, ⟨112⟩) are indicated on the upper x-axis along with a few other boundaries in Figs. 4.3 and 4.4. Notice that the energies of ATGBs with similar inclination angle, but with higher indices, are very similar to ATGBs with at least one low order index normal. For example, the average energy difference in Cu between Σ9 and Σ11 ATGBs of adjoining inclination angles ($\Delta\Phi_{avg} = 3.2°$) is small ($\Delta E_{avg} = 14$ mJ/m$^2$) in comparison to the Merkle and Wolf study. No large cusps in energy are observed for boundaries with low index normals. Additionally, no ATGBs have lower grain boundary energies than both of the corresponding STGBs, as Merkle and Wolf found for some Σ9 ATGBs in both Cu and Au.

The fact that low index ATGBs do not have considerably lower energies than other high index ATGBs is not uncommon, though. For example, in the Σ3 ATGB system, there are no cusps in the energy-inclination angle relationship for the $\Sigma3\,(221)_1 / (001)_2$ $\Phi = 54.74°$, $\Sigma3\,(110)_1 / (114)_2$ $\Phi = 35.26°$, or $\Sigma3\,(111)_1 / \left(11\bar{5}\right)_2$ $\Phi = 70.53°$ ATGBs despite each boundary containing a low index GB normal. In fact, the energy cusp occurs for the higher index $\Sigma3\,(223)_1 / \left(4,4,1\bar{1}\right)_2$ $\Phi = 81.95°$ ATGB in Cu. Also, recall that these results have

also been confirmed with experimental measurements [158]. While low index GB normals have been associated with lower energy favored boundaries in STGBs, their presence in ATGBs does not provide any impetus for a low energy cusp in the energy relationship as a function of inclination angle in this study. However, the GB energy as a function of inclination angle about the tilt axis only examines one of the five GB degrees of freedom. Wolf has shown that $(111)_1$ / $(115)_2$, $(221)_1$ / $(001)_2$, and $(557)_1$ / $(113)_2$ asymmetric boundaries display cusps in energy as a function of a twist rotation from these low index ATGB structures [184]. In this example, the low index planes do not change as a function of twist, so Wolf's results also show that general asymmetric boundaries with low index GB normals can have a wide range of energy values. A possible explanation for all of these results is that there is a specific grain boundary dislocation content required for each boundary; the boundary energy is associated with the GB structure driven by local relaxations of the dislocations. For Σ3, Σ9, and Σ11 ATGBs, high index ATGBs near low index ATGBs are achieved through addition or subtraction of dislocation content necessary to accommodate the change in the inclination angle. The required change in dislocation content results in localized changes to the boundary structure, which yields GB energies not all that much different from low index ATGBs. How the energy results relate to the experimentally determined high frequency of low index boundaries will be discussed further after examination of the boundary structures.

In this work, decomposition of asymmetric boundaries into facets of the symmetric tilt boundaries was used to examine the Σ5, Σ9, Σ11, and Σ13 systems. Brokman [206] suggested this decomposition based on the premise of a lower energy of the symmetric tilt grain boundaries. However, experiments show that many systems decompose into a combination of symmetric and asymmetric facets. In fact, Goukon and coworkers [235] combined experimentally measured boundary energies of Cu Σ11 ATGBs at 1273 K with an energetic model based on facet geometry. By using eight experimentally determined boundary energies, they defined a parameter that calculated whether Σ11 ATGBs of certain inclination

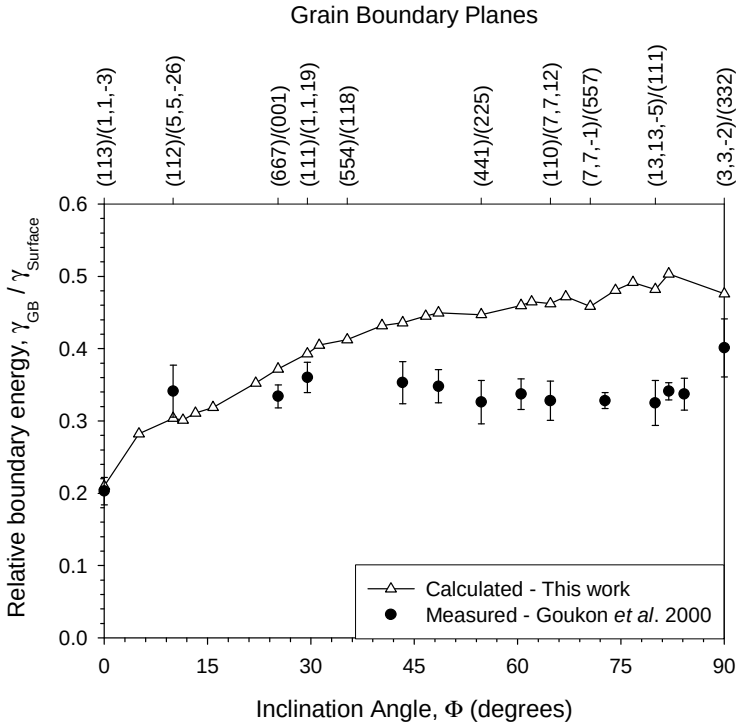


**Figure 4.5:** Comparison of the calculated and experimentally obtained relative boundary energies, $\gamma_{GB}/\gamma_{Surface}$, as a function of the inclination angle for Cu. The experimental results were obtained from the silica particle observation measurements of Goukon *et al.* [235].

angles have a tendency to facet into combinations of other Σ11 boundaries. They found that it is energetically favourable for many boundaries to facet into a combination of symmetric and asymmetric boundaries. For example, they found that the $\Sigma 11\,(001)_1 / (667)_2$ ATGB will facet into the Σ11 (113) STGB and the $\Sigma 11\,(225)_1 / (441)_2$ ATGB on the basis of the measured Σ11 energies. In the current work, however, only the validity of the decomposition of asymmetric tilt grain boundaries into symmetric tilt grain boundaries is examined.

In this same study by Goukon and colleagues [235], they calculated the Σ11 boundary energy as a function of inclination angle for Cu using the silica particle observation method. Figure 4.5 compares the measurements of Goukon *et al.* [235] at 1273 K with the calculated 0 K boundary energies normalized by the [110] surface energy (1476 mJ/m$^2$) in this

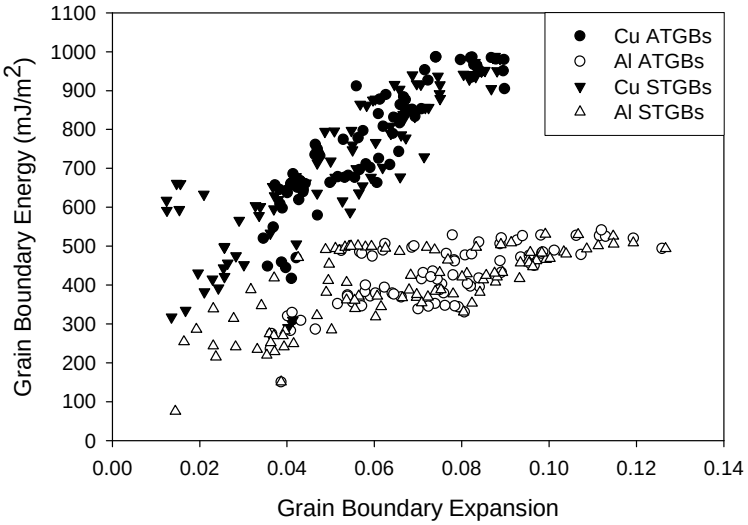


**Figure 4.6:** Grain boundary energy as a function of the grain boundary expansion for Cu and Al. The GB expansion is normalized by the lattice parameter.

work. The error bars on the experimental data represents one standard deviation. Quantitatively, the magnitudes of the calculated relative boundary energies agree fairly well with the magnitudes of the measured values, especially at low inclination angles. A similar difference in the relative boundary energy is observed for Σ3 ATGBs. The shape of the curves is slightly different though. The experimental measurements for the Σ11 ATGB energy are approximately constant as a function of inclination angle. Considering the large temperature difference, whose effect on the Σ11 grain boundary energies is not known, the general agreement is good.

Additionally, the grain boundary expansion of the calculated structures is compared to the grain boundary energy for Cu and Al, as shown in Fig. 4.6. The symmetric tilt boundary energies for the ⟨100⟩ and ⟨110⟩ tilt axis are from Fig. 4.1 while the asymmetric tilt grain boundary energies include the Σ5, Σ9, Σ11, Σ13 boundaries from this work. The grain boundary expansion [236] is in the direction normal to the GB plane since the other two directions are fixed; this quantity is normalized by the lattice parameter. The boundary expansion increases with increasing boundary energy in Cu and Al, but with significant

scatter. In general, tilt grain boundaries in Al tend to have a larger boundary expansion than Cu. Analysis of GB structures shows that dislocations dissociate more easily in low stacking fault energy Cu, which results in a lower GB expansion normal to the GB plane. These results agree qualitatively with the computer simulations of Wolf and Merkle [236].

## *4.4 Asymmetric tilt grain boundary structure*

The grain boundary structures for all the ATGBs were identified using the centrosymmetry parameter of Kelchner *et al.* [106] using the methodology described in Section 2.2.3. The structural units of the STGBs appear in all asymmetric tilt grain boundaries, but the structural ordering and faceting of SUs within the ATGBs differs for the ⟨100⟩ and ⟨110⟩ misorientation axes. Therefore, the next two subsections discuss observations regarding the structural unit and faceting description for these boundaries and how the ATGB structure is related to the interface energy.

### 4.4.1 ⟨100⟩ Asymmetric tilt grain boundaries

Figure 4.7 shows the equilibrium 0 K GB structures in Cu for six Σ5 boundaries in order of increasing inclination angle. The structures are viewed along the [100] tilt axis and the atoms on two consecutive (200) planes are shown as black and white. The GB normal and period vectors for the lower and upper crystal are shown in the corner boxes on the left-hand for each GB. The two arrows in the upper right corner correspond to the ideal location of the two Σ5 STGBs based on the GB inclination angle (also shown). There are two facets for each Σ5 ATGB: one facet corresponds to the SUs of the Σ5 (310) STGB (*C* SUs) and one facet corresponds to SUs associated with the Σ5 (210) STGB (B' SUs). Consequently, the only SUs present are those observed in the Σ5 STGBs: the $B'$ and $C$ SUs (see Figs. 4.7(a) and 4.7(f)). Also, notice that the $\Sigma 5\,(100)_1 / (430)_2$ $\Phi = 18.43^\circ$ ATGB contains an equal ratio of $C$ SUs to $B'$ SUs. Inclination angles less (greater) than $\Phi = 18.43^\circ$ contain a larger (smaller) fraction of $B'$ SUs, as shown in Figs. 4.7(b), 4.7(d), and 4.7(e). The structural units have arranged such that the majority of the non-centrosymmetric atoms bounding the

interface are on a {110} plane, as shown in Figs. 4.7(a) and 4.9(c).

There are a few possible representations of the favored C structural unit of the Σ5 (310) STGB. Figure 4.7(a) shows two outlined C structural units; one C SU with one interior atom (left) and one C SU with three interior atoms (right). For the purposes of this discussion, these structural units will be referred to as $C^1$ and $C^3$ to denote the one and three interior atom(s), respectively. The $C^3$ SU is commonly used to represent the favored structural unit of the Σ5 (310) STGB (*e.g.*, [145, 151]). However, both structural unit representations relate to the ⟨100⟩ ATGB structures. In the Cu Σ5 ATGBs, the $C^1$ structural unit is observed on the Σ5 (310) facets; the $C^3$ SU is not correlated with the non-centrosymmetric atoms of the Σ5 ATGB structures in Cu. In Al Σ5 ATGBs, the $C^3$ structural unit is observed on the Σ5 (310) facets at lower inclination angles and transitions to the $C^1$ structural unit at higher inclination angles. The slight difference in ATGB structures between Cu and Al may be due to the differences in their stacking fault energies. Note that the $C^1$ and $C^3$ structural units have identical energies in the Σ5 (310) STGB, but either structural unit may be present in the ATGBs depending on their impact on the ATGB energy. Figure 4.7 shows the $C^1$ structural unit, while Fig. 4.8 shows the $C^3$ structural unit in the ATGB structures. Fig. 4.8(a) shows that either the $C^1$ or $C^3$ structural unit can be used to represent the period for the Σ13 (510) STGB and, although not explicitly shown, the Σ13 (510) facets for the Σ13 ATGBs. This is true for both Cu and Al. Given that neither SU description is metastable in the Σ5 (310) or Σ13 (510) STGBs, both the $C^1$ and $C^3$ SUs are referred to as the C SU in the GB structure images and in the discussion that follows.

Figure 4.8 shows four grain boundary structures in the Σ13 CSL system. The grain boundary structures for the two symmetric tilt grain boundaries, Σ13 (510) and Σ13 (320), are shown in Figs. 4.8(a) and 4.8(d), respectively. The Σ13 STGBs are not favored boundaries in the ⟨100⟩ system and, consequently, are composed of a mixture of structural units from the favored boundaries: the |*DDC*| SUs for the Σ13 (510) STGB and the |*AB*′| SUs for the Σ13 (320) STGB. The Σ13 ATGBs are composed of facets with the structural units of

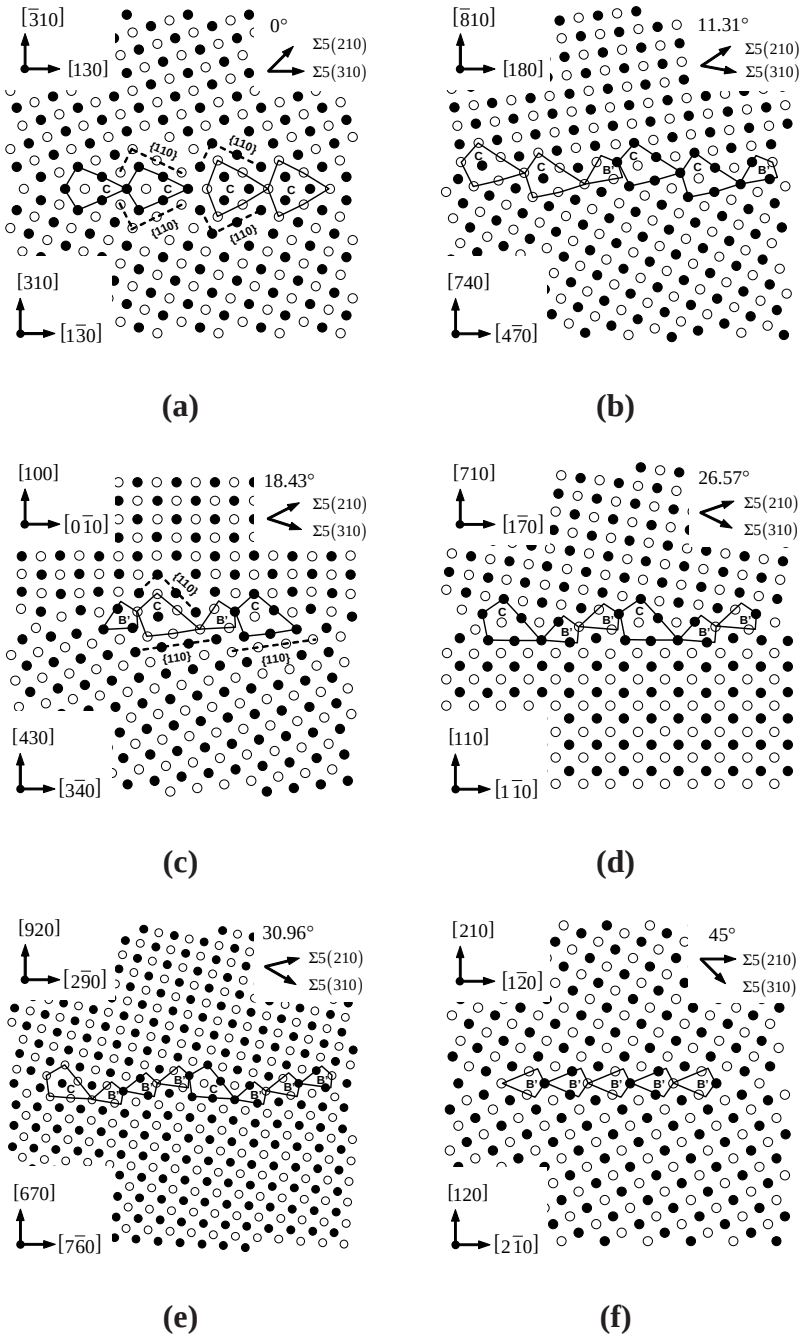


**Figure 4.7:** Six Σ5 GB structures in Cu for various inclination angles. The structures are viewed along the [100] tilt axis; atoms on consecutive {200} planes are shown as black and white. The grain boundary normal and period vectors for the lower and upper crystal are shown in the corner boxes on the left-hand side for each grain boundary. The inclination angle is shown in the upper right corner. The two Σ5 symmetric tilt grain boundaries are the (a) Σ5 (310) and (b) Σ5 (210) boundaries.

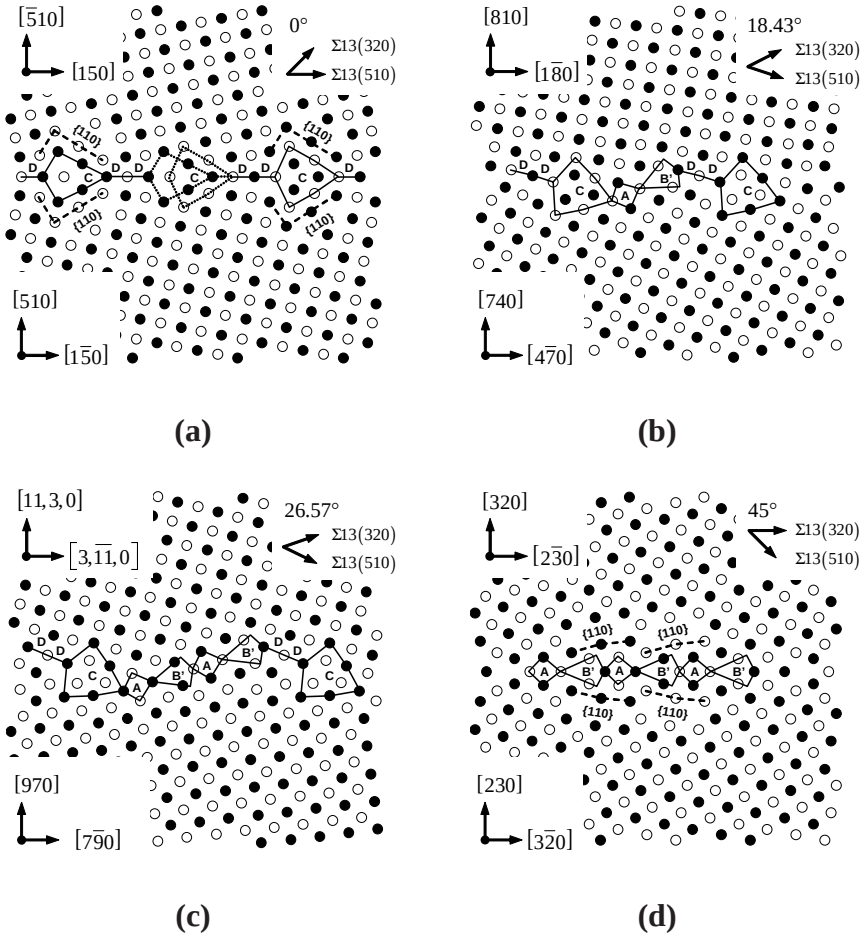


**Figure 4.8:** Four Σ13 GB structures in Cu for various inclination angles. The rest is viewed as in Fig. 4.7.

the STGBs. Each facet consists of the SUs of one period of the STGBs, as well. That is, the minimum energy GB structure does not separate either the *C* and *D* SUs or the *A* and *B′* SUs onto different facets. As in Fig. 4.7, there is a strong tendency for the ⟨110⟩ plane to bound the structural units of the Σ13 ATGBs. Figs. 4.9(a) and 4.9(d) show the {110} planes bounding the structural units of the Σ13 symmetric tilt grain boundaries.

The Σ5 boundaries show the behavior of ATGB structure with respect to the inclination angle for a favored boundary in the ⟨100⟩ tilt axis system. Likewise, the Σ13 boundaries show the change in ATGB with respect to the inclination angle for non-favored boundaries in the ⟨100⟩ system. The well-defined order of structural units and faceting of ATGBs in the

⟨100⟩ tilt system also follows the proposed model in Tschopp and McDowell [76, 78]. This model has shown that if the ATGB ideally facets in its symmetric counterparts, the ATGB grain boundary period can be decomposed into the boundary periods of the two symmetric boundaries to find the relative occurrence of the structural units of each STGB, similar to how STGBs can be decomposed into the structural units of favored boundaries [90]. For example, the period vector for the $\Sigma 13\,(11,3,0)_1 / (970)_2\,\Phi = 26.57^\circ$ ATGB is $a_0\left[7,\bar{9},0\right]$; this can be separated into one period of the $\Sigma 13\left(\bar{5}10\right)_1 / (510)_2\,\Phi = 0^\circ$ STGB and two periods of the $\Sigma 13\,(320)_1 / (230)_2\,\Phi = 45^\circ$ STGB. This reaction is given by

$$a_0\left[7\bar{9}0\right] = a_0\left[1\bar{5}0\right] + 2a_0\left[3\bar{2}0\right] \tag{4.3}$$

Note that the 1:2 ratio of $|DDC|$ SUs of the $\Sigma 13\,(510)\,\Phi = 0^\circ$ STGB to the $|AB'|$ SUs of the $\Sigma 13\,(320)\,\Phi = 45^\circ$ STGB from Eq. 4.3 is equivalent to the ratio of SUs shown in Fig. 4.8(c). The agreement of the calculated energies with Eq. 4.2 suggests that all Σ5 and Σ13 ATGBs can be decomposed in a similar manner.

### 4.4.2 ⟨110⟩ Asymmetric tilt grain boundaries

Figure 4.9 shows the GB structures in Al for four Σ11 boundaries in order of increasing inclination angle. The structures are viewed along the $\left[1\bar{1}0\right]$ tilt axis and the atoms on two consecutive $\left(2\bar{2}0\right)$ planes are shown as black and white. Figure 4.9(a) is the low energy $\Sigma 11\,(113)\,\theta = 50.48^\circ$ STGB, which is composed of C structural units. Figure 4.9(d) is the $\Sigma 11\,(332)\,\theta = 129.52^\circ$ STGB, which is a combination of D structural units from the $\Sigma 3\,(111)\,\theta = 109.5^\circ$ coherent twin boundary and E structural units from the $\Sigma 9\,(221)\,\theta = 141.1^\circ$ STGB.

Also shown are examples of calculated structures from two asymmetric tilt grain boundaries with a distinctly different ordering of structural units (Figs. 4.9(b)-4.9(c)). For instance, in Fig. 4.9(b), the $\Sigma 11\,(225)_1 / (441)_2\,\Phi = 54.74^\circ$ ATGB ideally facets into the structural units of the two symmetric tilt grain boundaries, similar to the ⟨100⟩ ATGBs and

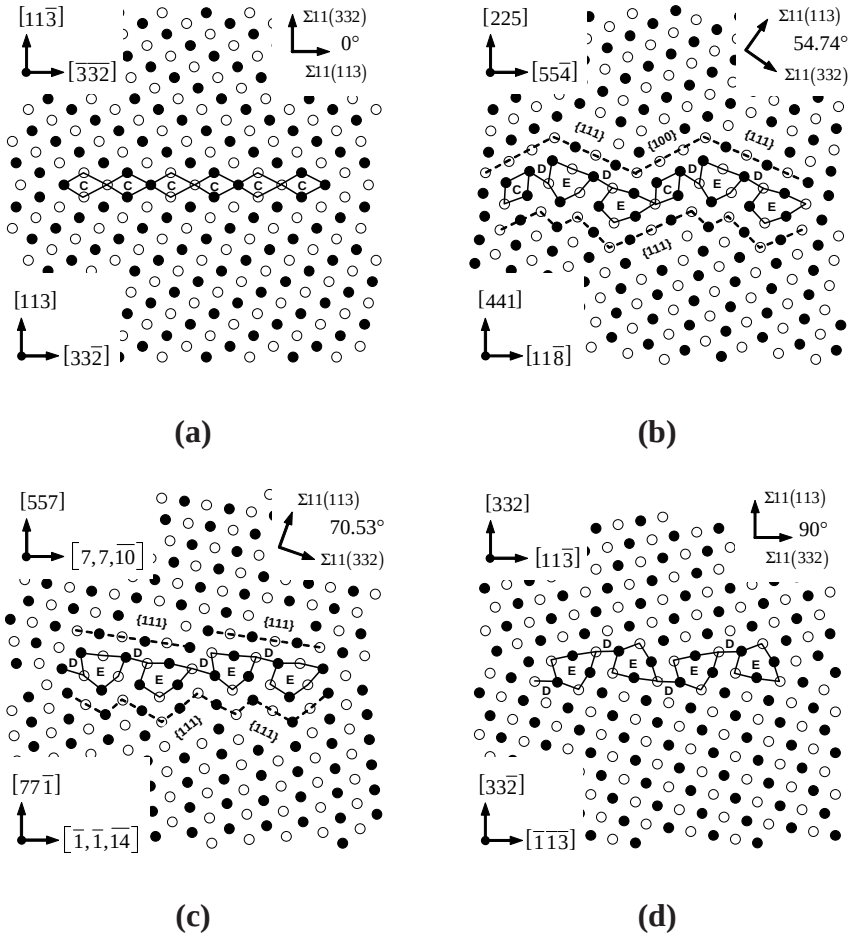


**Figure 4.9:** Four Σ11 grain boundary structures in Al for various inclination angles. The structures are viewed along the $\left[1\bar{1}0\right]$ tilt axis; atoms on consecutive {220} planes are shown as black and white. The rest is viewed as in Fig. 4.7.

the Σ3 ATGB system [76,78]. For inclination angles $\Phi \leq 54.74°$, the Σ11 ATGBs facet into the structural units of the two STGBs. Asymmetric tilt grain boundaries in the Σ11 system are similar to those in the Σ3 system in that both systems facet into their symmetric counterparts and both systems contain a relatively low energy boundary: the Σ3 coherent twin boundary and the Σ11 (113) STGB. The decomposition of the ATGB into STGB facets may be due to the low energy of the STGBs in these systems, as discussed by Muschik and coworkers for the Σ3 system [237].

At higher inclination angles $\Phi \geq 54.74°$, the Σ11 ATGBs are composed of combinations of D and E structural units, as shown in Fig. 4.9(c) for the $\Sigma 11\,(557)_1 / \left(77\bar{1}\right)_2$ $\Phi = 70.53°$ ATGB. Notice that the C structural units are no longer discernible in the boundary structure. This structure is very similar to the $\Sigma 11\,(332)\,\theta = 90°$ STGB, except that some of the E structural units are distorted and steps are present in the boundary structure. Also, the structural units have arranged such that the majority of the non-centrosymmetric atoms bounding the interface are on a {111} plane, as shown in Figs. 4.9(b) and 4.9(c). The close-packed {111} plane has the lowest surface energy in FCC metals [238], which may serve as the driving force for the observed arrangement of structural units. The {111} planes bounding the ⟨110⟩ tilt boundaries are different from the {110} planes bounding the structural units for the ⟨100⟩ ATGBs. One purely geometrical reason is that the ⟨111⟩ direction is not perpendicular to the ⟨100⟩ tilt axis, *i.e.*, the direction on which the structural units align for ⟨100⟩ tilt boundaries.

Finally, Fig. 4.10 shows six structures from the Σ9 CSL system. The two STGBs — the $\Sigma 9\,(114)\,\theta = 38.94°$ and the $\Sigma 9\,(221)\,\theta = 141.06°$ boundaries — are shown in Figs. 4.10(a) and 4.10(f). The structures of the Σ9 (114) STGB is strongly affected by the stacking fault energy of the material; hence, we only discuss the Cu GB structure for the sake of brevity. In Cu, the Σ9 (114) STGB consists of the structural units of (1) the C SU from the $\Sigma 11\,(113)\,\theta = 50.48°$ STGB and (2) the D SU from the $\Sigma 3\,(111)\,\theta = 109.47°$ coherent twin boundary. The D SUs, which can also be described as Shockley partial dislocations [91],

dissociate away from the C SU leaving behind a stacking fault. However, the stacking fault is difficult to distinguish because of the presence of two dissociated D SUs in close proximity. Conversely, the $\Sigma 9\,(221)\,\theta = 141.06^\circ$ STGB is a favored boundary that contains only the E SU (Cu and Al). This boundary has also been viewed in terms of the microfaceting along two asymmetric boundary plane orientations, $\{111\}_1$ / $\{110\}_2$, in both experimentally obtained [239] and calculated structures [90].

Several additional visuals are illustrated in Fig. 4.10(f) to aid in the interpretation of the remaining Σ9 ATGB structures. First, the dashed boxes in the perfect lattice are shown to point out the {100}, {110}, and {111} planes. Notice that the non-centrosymmetric GB atoms bordering the perfect lattice align on the {110} and {111} planes in both crystals. Second, the directions on the left in Fig. 4.10(f) show that a ⟨110⟩ direction in the bottom lattice is nearly parallel ($\Delta = 3.68^\circ$) to the ⟨111⟩ direction in the upper lattice, and vice versa.

The GB structures for several low index Σ9 ATGBs are shown in Figs. 4.10(b)-4.10(e). First, the calculated faceting into the structural units of the two Σ9 symmetric tilt grain boundaries is not observed in any of the structures for Cu or Al. A well-defined ordering of the SUs within the ATGB is often observed, but the structural units of the STGBs are not always observed. One possible reason is that Σ9 ATGBs can dissociate into facets of the Σ3 STGBs rather than facet into the higher energy Σ9 STGBs; this mechanism has been reported by several researchers [240–243]. In agreement with these studies, the $\Sigma 9\,(111)_1\,/\,(115)_2\,\Phi = 35.25^\circ$ ATGB in Fig. 4.10(b) supports a decomposition into Σ3 facets. In this structure, the C SU with the dissociated D SUs are similar to the symmetric structures in Fig. 4.10(a), but the C SUs have all rotated to face the same direction. Notice that the C and D SUs from the $\Sigma 9\,(114)$ STGB are inclined about the grain boundary period, which requires more D SUs to accommodate this rotation. At larger length scales, these three Σ3 facets would be easier to resolve. This structure may shed light on the experimentally observed triangular region of the $\Sigma 9\,(111)_1\,/\,(115)_2\,\Phi = 35.25^\circ$ ATGB with

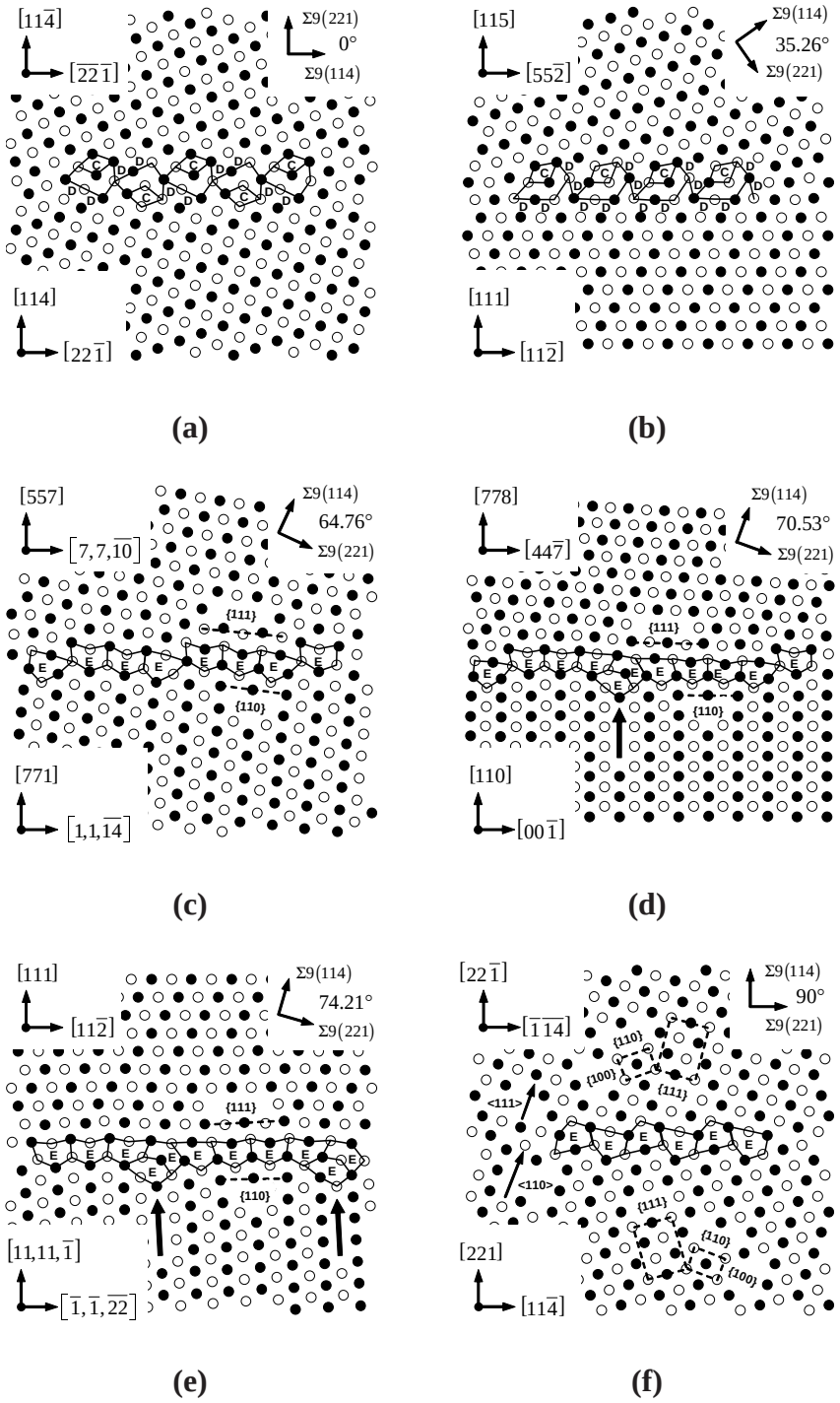


**Figure 4.10:** Six low index Σ9 grain boundary structures in Cu with various inclination angles. The rest is viewed as in Fig. 4.9. The low index planes bounding the grain boundary structure are labeled.

HRTEM [185].

Another characteristic of Σ9 ATGB structures is shown in Figs. 4.10(c)-4.10(e) for higher inclination angles. The SUs of the $\Sigma 9\,(114)\,\theta = 38.94^{\circ}$ are not present in these boundaries; instead all SUs resemble E SUs of varying degrees of distortion. One possible reason for this distortion is that the E structural unit has a relatively large free volume compared to other structural units in the ⟨110⟩ STGB system [244], which may serve as the impetus for atoms to rearrange to lower the GB energy; the E SU has been found to distort as a function of the misorientation angle in STGBs [72, 79, 90]. Additionally, notice that the atoms associated with the E SUs have rearranged to form an almost continuous line of structural units with very few steps or facets. The grain boundary planes bounding the SUs are the {111} planes on one side of the boundary and the {110} plane on the other side, which agrees with experimentally observed images [185]. Additionally, the misorientation of these boundaries is very close ($\Delta\theta = 3.68^{\circ}$) to the $\{111\}_1$ / $\{110\}_2$ ATGB, which presumably has a low energy. Therefore, small facets or GB steps may be required to make up the difference in orientation [245] (see Figs. 4.10(c)-4.10(e)).

### 4.4.3 Comparison with experimental grain boundary structures

Duparc *et al.* [246] used molecular dynamics simulations of grain boundary structures to verify experimentally observed Σ9 boundary structures. Figure 4.11 shows the calculated and HRTEM images for an observed segment of asymmetric tilt character. Interestingly, the HRTEM structure observed in Fig. 4.11(b) is very similar to the Σ9 ATGB structures at high inclination angles, *i.e.*, Figs. 4.10(c)-4.10(e). In fact, they identified the red E' structural unit as a Lomer lock dislocation configuration that terminates a row of ⟨110⟩ atoms. Again, a similar structure is observed in Figs. 4.10(d) and 4.10(e). The difference in identification of structural units is subjective. While Duparc and colleagues identify multiple A' structural units, only atoms in a distorted environment that correspond to the structural units of the Σ9 STGBs were identified here. The identification of structural units

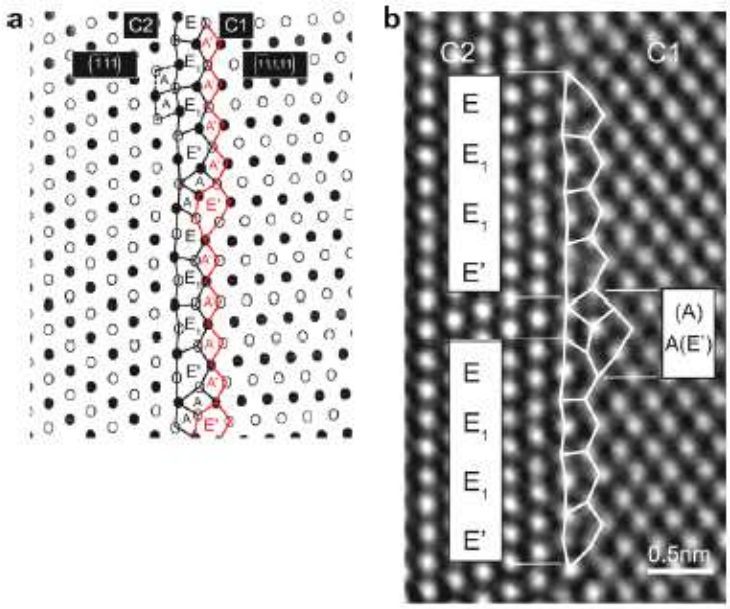


**Figure 4.11:** (a) Two-dimensional projected image of energy-minimized structure of the $\Sigma 9\ \left(\overline{1}1,1,11\right)_1/\left(\overline{111}\right)_2$ asymmetric tilt grain boundary. The black and white circles correspond to atomic positions at $\pm a/4\,\langle\overline{1}10\rangle$ along the tilt axis direction. Dashed and full lines indicate the structural units along $\left(\overline{111}\right)$ and $\left(\overline{1}1,1,11\right)$, respectively. (b) HRTEM experimental image completed with the structural units. Images are from Duparc *et al.* [246].

does not affect the underlying atomic structure, though - this is the same in both studies.

We may ask the question, can the calculated structures and energies of asymmetric tilt grain boundaries provide understanding for the experimental observations of low index planes in larger scale FCC polycrystalline materials? To this end, the notion that asymmetric tilt boundaries with low index normals have a large difference in energy compared to boundaries of similar inclination with higher index normals is not supported by this study. As shown in Figs. 4.3-4.4, our results suggest that there is not a large difference in energies (*e.g.*, $\Delta E = 4.8\ \mathrm{mJ/m^2}$) between ATGBs with a low index normal (*e.g.*, $\Sigma 9\,(001)_1\,/\,(447)_2\ \Phi = 19.47°$) and ATGBs with higher index normals (*e.g.*, $\Sigma 9\,(11,11,17)_1\,/\,(1,1,23)_2\ \Phi = 22.99°$) with respect to grain boundary inclination angle. These results agree with the calculated and experimentally measured energy relationship for $\Sigma 3$ ATGBs; in this system, the boundaries with low index normals show very similar

energies to higher index boundaries with similar inclination angles [78, 158, 159]. As discussed earlier, there is the possibility that low index asymmetric tilt grain boundaries are lower energy boundaries with respect to other GB degrees of freedom, though.

The atomistic observation of low index {111} planes bounding the interface structure in Σ9 and Σ11 ATGBs may provide insight into the experimental observations of low index planes, particularly {111} planes, at grain boundaries in larger scale FCC polycrystals. The driving force for grain boundary structural rearrangement is to minimize the total boundary energy. The low surface energy of the {111} surface compared to the {100} and {110} surfaces may explain the high frequency of {111} planes bounding the structural units in the ⟨110⟩ tilt grain boundaries. Even ATGBs with higher index planes facet in such a manner as to create low index {111} planes at the boundary. Since asymmetric tilt grain boundaries rearrange at atomic levels to increase the fraction of {111} planes bounding the interface structural units, perhaps similar microstructural rearrangement to minimize energy occurs at even higher scales through grain rotation, grain boundary migration, or grain boundary faceting. Further studies are necessary to validate this. However, the results of this paper suggest that the observed frequency of low index planes in polycrystals may be associated with the boundary structure rather than any low energy cusps in the energy-inclination angle relationship.

## *4.5 Summary*

In this chapter, atomistic simulations were used to explore the structure and energy of several low order CSL ATGB systems (Σ5, Σ9, Σ11, and Σ13) about the ⟨100⟩ and ⟨110⟩ tilt axes. The Σ5 and Σ13 systems with a boundary plane rotated about the ⟨100⟩ misorientation axis were examined along with the Σ9 and Σ11 systems rotated about the ⟨110⟩ misorientation axis. Asymmetric tilt grain boundary energies were calculated as a function of inclination angle and compared with an energy relationship based on faceting into the two

symmetric tilt grain boundaries in each system. One finding is that asymmetric tilt boundaries with low index normals do not necessarily have lower energies than boundaries with similar inclination angles, contrary to previous studies. Further analysis of grain boundary structures provides insight into the asymmetric tilt grain boundary energy. The $\Sigma 5$ and $\Sigma 13$ systems in the $\langle 100 \rangle$ system agree with the aforementioned energy relationship; structures confirm that these asymmetric boundaries facet into the symmetric tilt boundaries. The $\Sigma 9$ and $\Sigma 11$ systems in the $\langle 110 \rangle$ system deviate from the idealized energy relationship. As the boundary inclination angle increases towards the $\Sigma 9$ (221) and $\Sigma 11$ (332) symmetric tilt boundaries, the minimum energy asymmetric boundary structures contain low index $\{111\}$ and $\{110\}$ planes bounding the interface region. Based upon prior results of $\Sigma 3$ ATGBs [78] and results from $\Sigma 5/9/11/13$ ATGBs in this chapter, the observed frequency of low index planes in polycrystals does **not** appear to be associated with low energy cusps in the energy-inclination angle relationship; this conclusion is in contrast to former studies [185]. Instead, the current results indicate that the structure and faceting of asymmetric tilt grain boundaries may play a more prominent role in the observed frequency of low index planes in polycrystalline materials. For citation of the work contained in this chapter, the reader is referred to Ref. [79].

# CHAPTER V

# STRUCTURE AND FREE VOLUME OF ⟨110⟩ SYMMETRIC TILT GRAIN BOUNDARIES WITH THE E STRUCTURAL UNIT

This chapter discusses the structure and free volume of ⟨110⟩ symmetric tilt grain boundaries containing the E structural unit from the $\Sigma 9\,(221)\,\theta = 141.1^{\circ}$ grain boundary. A stereologically-based methodology is used to calculate the grain boundary free volume along with the spacing and connectivity of free volume. The minimum energy equilibrium grain boundary is generated to examine: (i) the grain boundary structure, (ii) a measure of free volume associated with the grain boundary, (iii) spatial correlation functions of the distribution of free volume, and (iv) images of grain boundary free volume distribution. Using the results from these calculations, the influence of free volume spatial distribution and grain boundary structure on dislocation dissociation and nucleation is briefly discussed for boundaries with the E structural unit subjected to tensile loading normal to the interface.

## *5.1 Introduction*

A better understanding of the grain boundary (GB) structure and free volume can provide insight into the mechanical behavior and bulk properties of nanocrystalline and larger grain polycrystalline materials. The free volume is defined as an interatomic region of low atomic density that aids the mobility of neighboring atoms, enabling GB sliding, grain rotation, and GB dislocation emission. Molecular dynamics (MD) simulations of deformation in nanocrystalline materials have shown that the initial free volume and its evolution within grain boundaries is a necessary component for GB sliding [45] and grain rotation [59] at smaller grain sizes (on the order of 10 nm and below). Partial dislocation emission from grain boundaries is important at larger grain sizes. Atomistic simulations

have shown that prior to the nucleation of partial dislocations in nanocrystalline metals, stress-assisted free volume migration is observed in the boundaries and at nearby triple junction regions [60, 141]. Local atomic shuffling enabled by the excess free volume facilitates the formation of the Burgers vector required to nucleate a partial dislocation within the boundary region [60, 141]. Bicrystal MD simulations have also been used to investigate the influence of the structure of specific grain boundaries on deformation behavior. For example, Spearot and coworkers investigated the dislocation nucleation and emission phenomenon under uniaxial tension from both aluminum [97] and copper [139] symmetric tilt grain boundaries. Tschopp and McDowell also examined how the structure of $\Sigma 3$ asymmetric tilt grain boundaries impacts dislocation nucleation [77]. These simulations show that the grain boundary acts as a dislocation source, and that the dislocation nucleation process is highly dependent on the GB structural units and their sequence within the boundary (*i.e.*, the GB dislocation content and arrangement).

This chapter investigates the structure and free volume of symmetric tilt grain boundaries with a $\langle 110 \rangle$ tilt axis in the misorientation angle range $109.5^\circ < \theta < 180^\circ$ (using a [001] crystallographic reference plane). This misorientation range corresponds to grain boundaries that contain the E structural unit [90] from the $\Sigma 9\,(221)\,\theta = 141.1^\circ$ symmetric tilt grain boundary (STGB). This work is motivated by bicrystal MD and quasicontinuum simulations that examined the tensile and shear strengths of specific grain boundaries [64, 72]. Sansoz and Molinari [72] employed quasicontinuum simulations to examine 18 symmetric and two asymmetric tilt grain boundaries with $\langle 110 \rangle$ tilt axis under shear deformation; they found that the E structural unit is associated with the onset of GB sliding by atomic shuffling. Spearot *et al.* [64] formulated an interface strength model for the nucleation stress required to emit dislocations from the GB; this model incorporates both crystallographic parameters from the surrounding lattice as well as the initial free volume of the interface. Figure 5.1 shows the stress required for dislocation nucleation and emission from STGBs with a $\langle 110 \rangle$ tilt axis. Notice the extremely low stresses to

emit dislocations from the GB for misorientation angles $\theta > 109.5°$; this corresponds to boundaries containing the E structural unit. While this interface strength model adequately captures the stress required for dislocation emission for $\langle 110 \rangle$ STGBs with $\theta < 109.5°$, the model fails to capture the large drop in strength associated with the $\theta > 109.5°$ misorientation range. They hypothesized that a higher order formulation that accounts for the distribution of free volume on the interface (*e.g.*, two-point statistics) may be required to explain this effect. Therefore, the intent of this chapter is to investigate both the structure and free volume distribution to better explain: (i) the evolution of GB structure throughout the $109.5° < \theta < 180°$ misorientation angle range, (ii) the evolution of GB free volume throughout this range using one- and two-point statistics, and (iii) the relationship between GB structure, GB free volume, and the process of dislocation dissociation and nucleation.

Consequently, this chapter is organized as follows. First, the methodology that allows for the calculation of one- and two-point statistics is presented along with the visualization of GB free volume. After molecular statics simulations are used to characterize the minimum energy GB structures within this range, the aforementioned methodology is utilized to (i) analyze the one- and two-point statistics of free volume, (ii) study the relationship between the GB structure and the free volume statistics, and (iii) visualize the evolution of GB free volume with misorientation angle for GBs with the E structural unit. Last, the effect of GB structure and free volume on GB partial dislocation dissociation, nucleation, and emission events in Cu is discussed.

## *5.2 Simulation methodology*

A simulation cell with 3D periodic boundary conditions is used to obtain the minimum energy 0K structure for each GB. The simulation cell and axis directions for this chapter are shown in Fig. 5.2. This cell consists of two grains and two periodic grain boundaries separated by a minimum distance of 12 nm. A large number of initial configurations with different in-plane rigid body translations and an atom deletion criterion are used to access

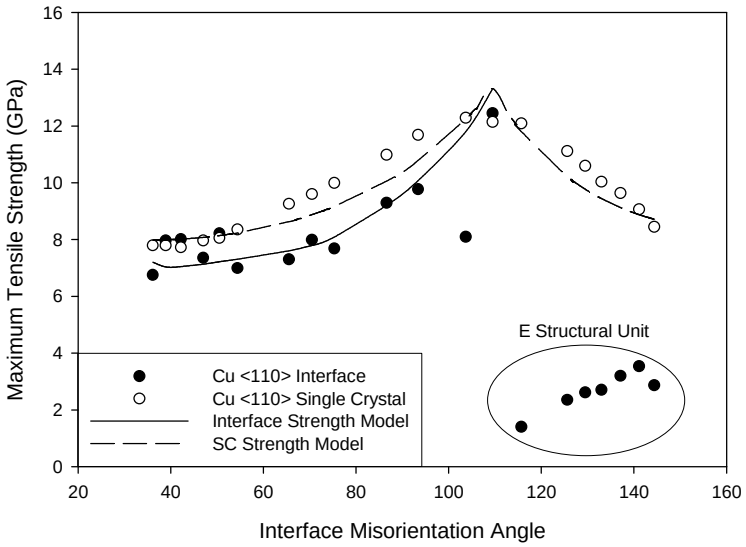


**Figure 5.1:** Maximum tensile strength versus misorientation angle for ⟨110⟩ symmetric tilt grain boundaries [64]. The stress required for dislocation nucleation in single crystal with the same orientation is also shown. Notice the large drop in stress for grain boundaries with misorientation angles greater than 109.5°.

the minimum energy GB structures. A Sandia-based parallel molecular dynamics code, Warp [69], that incorporates domain decomposition was used to calculate our GB structures. A nonlinear conjugate gradient algorithm was used for energy minimization. Further details of the methodology used to attain the grain boundary structures are given in Chapter 2 and in Tschopp and McDowell [78]. An embedded atom method (EAM) potential for Cu [124] was also employed; this reproduces stacking fault energies consistent with available experimental data and *ab initio* calculations.

Once the GB structures are generated, a post-processing code was used to characterize the initial GB free volume in terms of one-point (volume fraction) and two-point statistics (*e.g.*, two-point correlation functions and lineal path functions). To calculate two-point statistics, a grid was defined in three-dimensional space. First, a grid of points with a spacing of $0.05a_0$ or smaller, where $a_0$ is the lattice spacing, was superimposed in three dimensions ($ijk$) over the volume of interest, in this case the entire simulation box. Next, each grid point was evaluated through a criterion based on the distance, $d_{ijk}$, between the

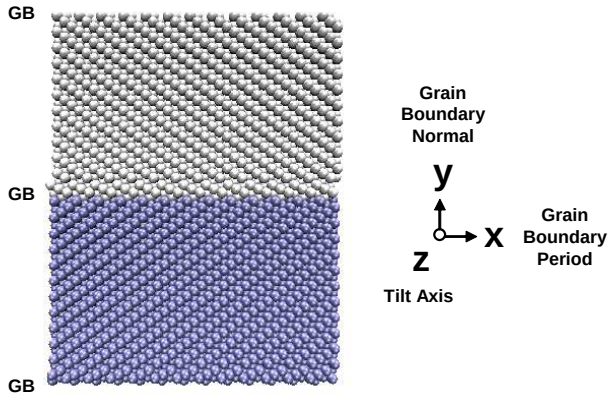


**Figure 5.2:** Schematic of the 3D periodic computational cell used for grain boundary calculations. The tilt axis is into the page.

grid point and the nearest atom core, *i.e.*,

$$N_{ijk} = \begin{cases} 1, & d_{ijk} > ca_0 \\ 0, & d_{ijk} \leq ca_0 \end{cases} \tag{5.1}$$

where $N_{ijk}$ is an indicator matrix that defines whether each grid point is associated with free volume or not, $c$ is a constant, and the subscripts $i$, $j$, and $k$ are integer values that range from 1 to the number of grid points ($n_x$, $n_y$, and $n_z$) in the X, Y and Z directions, respectively. For these simulations, $c$ was chosen such that no grid points were associated with free volume in a perfect fcc unit cell, *i.e.*, $c = 0.5$. Grid points designated as free volume were assigned the numeric value of one. Once each grid point was evaluated, several one- and two-point statistical measures were calculated.

The volume fraction $f_1$ occupied by free volume is the summation of $N_{ijk}$ over all the grid points divided by the total number of grid points, *i.e.*, $f_1 = \sum_{ijk} N_{ijk}/(n_x n_y n_z)$. However, for this bicrystal computational cell, the 3D statistics for a 3D planar structure, not a 3D microstructure, were of interest. Hence, the effect of the bulk lattice between the periodic grain boundaries was excluded. Therefore, the free volume was normalized by the GB area, *i.e.*,

$$f_1^* = \frac{1}{2A_{GB}} \left( \frac{V}{n_x n_y n_z} \right) \sum_{ijk} N_{ijk} \tag{5.2}$$

In Eq. 5.2, $2A_{GB}$ is the total GB area (from the two periodic GB planes) and $V$ is the simulation cell volume. The GB structures have different period and normal vectors, resulting in different simulation cell sizes, so it is important to use a measure that is not biased by different simulation cell sizes.

Information concerning the spatial arrangement of elements in microstructures (*e.g.*, particles, voids) is provided from two-point correlation functions (TPCFs). The traditional definition of a TPCF is the mean probability $\left\langle P_{ij}(r) \right\rangle$ that two points separated by a distance $r$ are both contained in a particular phase (*i.e.*, phase $i$ and phase $j$). In this case, the TPCF of the free volume is the quantity of interest, *i.e.*, $P_{11}(\mathbf{r}_k)$. The subscript $k$ denotes that there is directionality associated with the distance. In this chapter, the TPCFs are investigated along specific directions as outlined in Fig. 5.2: the GB period (X), the GB normal (Y), and the GB tilt axis (Z) vectors. Last, to remove the effect of the number of grid points, the TPCF was normalized by the volume fraction of free volume, $f_1$, *i.e.*,

$$P_{11}^*(\mathbf{r}_k) = \frac{P_{11}(\mathbf{r}_k)}{f_1} \tag{5.3}$$

Note that this TPCF definition forces $P_{11}^*(\mathbf{r}_k) \rightarrow 1$ as $\mathbf{r}_k \rightarrow \mathbf{0}$ since the TPCF $P_{11}(\mathbf{r}_k)$ will approach the volume fraction $f_1$ at infinitely small distances, *i.e.*, $\lim_{\mathbf{r}_k \rightarrow \mathbf{0}} P_{11}(\mathbf{r}_k) = f_1$. Other authors normalize the TPCF by $f_1^2$ so that as the distance increases the graph approaches unity (*cf.* [247]). This method is based on $\lim_{\mathbf{r}_k \rightarrow \mathbf{0}} P_{11}(\mathbf{r}_k) = f_1^2$; however, due to the perfect periodicity of the grain boundaries within this 3D periodic cell, these TPCFs do not necessarily follow this limit. Moreover, normalizing by $f_1^2$ does not eliminate the dependence on the number of grid points as does Eq. 5.3.

The lineal path function (LPF) $L_{ii}(\mathbf{r}_k)$ is the probability that a line of length $r$ located randomly in a microstructure is entirely in phase $i$. This parameter gives more insight into the connectivity and clustering tendencies of free volume. Lineal path functions for free

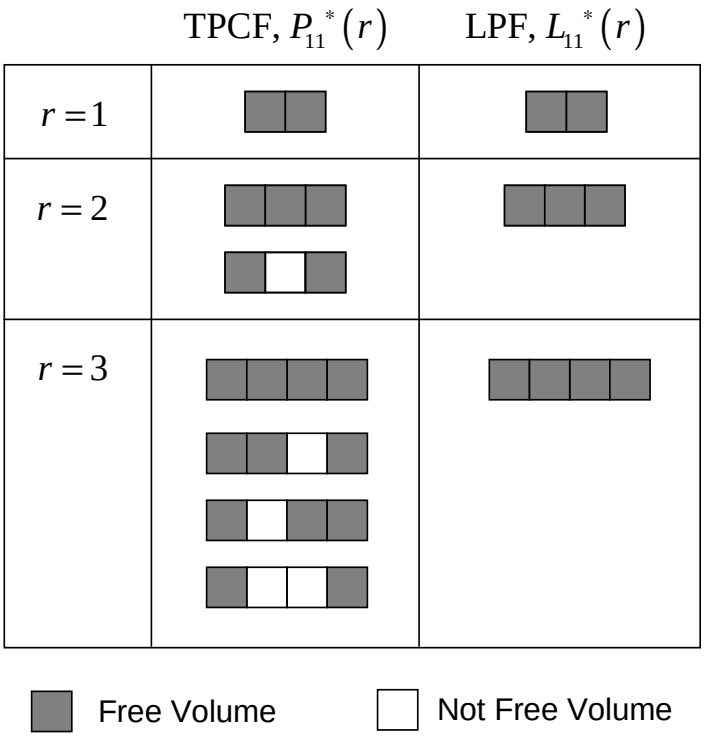


**Figure 5.3:** One-dimensional schematic showing the difference between two-point correlation function $P_{11}^{*}(\mathbf{r}_k)$ and the lineal path function $L_{11}^{*}(\mathbf{r_k})$ for distances of $r = 1, 2, 3$.

volume along directions identical to the TPCF case are of interest, *i.e.*, $L_{11}(\mathbf{r_k})$. Similar to the TPCF, the LPF was normalized by dividing by the volume fraction of free volume, *i.e.*,

$$L_{11}^{*}(\mathbf{r}_k) = \frac{L_{11}(\mathbf{r}_k)}{f_1} \tag{5.4}$$

As with the normalized TPCF $P_{11}^{*}(\mathbf{r}_k)$, the normalized LPF $L_{11}^{*}(\mathbf{r_k}) \rightarrow 1$ as $\mathbf{r}_k \rightarrow \mathbf{0}$. To check the convergence for the two-point statistics, different grid spacings were used for $\Sigma 9$ and $\Sigma 11$ GBs. The same trends in both TPCFs and LPFs were found for grid spacings of $0.05a_0$, $0.025a_0$, and $0.01a_0$ in all directions. Both two-point statistics were used to characterize the spatial arrangement of free volume, because the TPCF represents the *spacing* between free volume points while the LPF represents the *connectivity* of free volume points.

Figure 5.3 is a simple schematic showing the difference between the TPCF $P_{11}^{*}(\mathbf{r}_k)$ and

the LPF $L_{11}^{*}(\mathbf{r_k})$. This schematic contains a 1D representation of two phases that directly corresponds to this chapter; *i.e.*, free volume in gray boxes and occupied sites in white boxes. Figure 5.3 shows the combination of boxes that are accounted for in both the TPCF $P_{11}^{*}(\mathbf{r}_k)$ and LPF $L_{11}^{*}(\mathbf{r_k})$ for distances of $r = 1$, $r = 2$, and $r = 3$. First, notice that as the distance increases, the number of possible combinations for the TPCF increases. Recall that the TPCF does not consider the boxes in between; only the boxes at the end of the line. However, the LPF requires that all boxes along the line belong to a particular phase; therefore, the probability of this occurring decreases with increasing distance. Additionally, this schematic shows that the TPCF represents the *spacing* between free volume points while the LPF represents the *connectivity* of free volume points. This trivial example is the same concept as that used to calculate the two-point statistics $P_{11}^{*}(\mathbf{r}_k)$ and $L_{11}^{*}(\mathbf{r_k})$ for three dimensions.

## *5.3 Results and discussion*

### 5.3.1 Grain boundary structure

After calculating the GB structures, the atoms associated with the GB were identified and characterized as structural units (SUs) using the methodology outlined in Section 2.2.3. Once GB atoms were identified, these atoms were divided into SUs that are consistent with the three favored ⟨110⟩ STGBs for this range [90]; the D SU of the $\Sigma 3\,(111)\,\theta = 109.5^{\circ}$ coherent twin boundary, the E (or E′) SU of the $\Sigma 9\,(221)\,\theta = 141.1^{\circ}$ GB, and the A (or A′) SU of the $\Sigma 1\,(110)\,\theta = 180^{\circ}$ perfect lattice. Notice that all GBs with $\theta < 141.1^{\circ}$ should contain a combination of E SUs and D SUs, while all GBs with $\theta > 141.1^{\circ}$ should contain a combination of A (or A′) and E (or E′) SUs. The convention used for naming SUs is consistent with that of Ref. [90].

Table 5.1 lists 12 STGBs in the ⟨110⟩ tilt axis system in order of increasing misorientation angle within the range $109.5^{\circ} < \theta < 180^{\circ}$. These GBs should contain the E SU based on the structural unit model [148]. Of the 12 GBs listed in Table 5.1, nine of these GB

**Table 5.1:** The misorientation angles and GB plane normals for the twelve GBs with the E structural unit. The structural unit description is given for each of these boundaries along with the publication where each structural image is shown. Note that although all these GBs are calculated, not all structures are shown.

| Misorientation Angle | CSL Designation & GB Plane Normal | Structural Unit Description | Calculated GB Structures |
|---|---|---|---|
| 114.5° | $\Sigma 171\,(11,11,10)$ | $\lvert 9(D)E''.9(D)E''\rvert$ | This work |
| 121.0° | $\Sigma 33\,(554)$ | $\lvert DDDE.DDDE\rvert$ | [72, 90] |
| 126.4° | $\Sigma 123\,(775)$ | $\lvert DDEDE.DDEDE\rvert$ | This work |
| 129.5° | $\Sigma 11\,(332)$ | $\lvert DE.DE\rvert$ | This work, [72, 90] |
| 131.5° | $\Sigma 291\,(11,11,7)$ | $\lvert 3(DE)E.3(DE)E\rvert$ | This work |
| 141.1° | $\Sigma 9\,(221)$ | $\lvert E.E\rvert$ | This work, [90] |
| 144.4° | $\Sigma 267\,(11,11,5)$ | $\lvert 5(E)A.5(E)A\rvert$ | This work |
| 148.4° | $\Sigma 27\,(552)$ | $\lvert EEA.EEA\rvert$ | [90] |
| 153.5° | $\Sigma 19\,(331)$ | $\lvert EA.EA\rvert$ | This work, [90] |
| 160.0° | $\Sigma 33\,(441)$ | $\lvert EAA.EAA\rvert$ | This work, [90] |
| 166.6° | $\Sigma 73\,(661)$ | $\lvert EA'A'.EA'A'\rvert$ | [90] |
| 169.9° | $\Sigma 129\,(881)$ | $\lvert EA'A'A'.EA'A'A'\rvert$ | This work |

structures were calculated and shown in Figs. 5.4, 5.5, and 5.6. These figures are projected 2D views of the 3D atom coordinates around the interface. These structures were chosen to display the evolution of GB structure within the misorientation region $109.5° < \theta < 180°$. The outlined SUs represent one GB period. Additionally, the GB normal and period vectors are given for both crystal lattices on the left-hand side of each structure. The $\left[1\bar{1}0\right]$ tilt axis is into the page for all structures in Figs. 5.4-5.6.

First, notice the $\Sigma 9\,(221)\,\theta = 141.1°$ GB in Fig. 5.4. This is a favored GB, in the sense of Sutton and Vitek [148], within this misorientation range that consists of only E SUs. Therefore, the GB structure for one period is given as $\lvert E.E\rvert$ in Table 5.1, where the bars around the structure denotes one GB period and the dot represents a translation of $a_0/4\left[1\bar{1}0\right]$ along the tilt axis relative to the structure preceding to the period. Now, notice the $\Sigma 11\,(332)\,\theta = 129.5°$ and the $\Sigma 19\,(331)\,\theta = 153.5°$ GBs in Figs. 5.5(c) and 5.6(b), respectively. These GBs both contain either an identical ratio of D:E SUs (for the $\Sigma 11$ GB) or A:E SUs (for the $\Sigma 19$ GB). All three GB structures agree with the $\langle 110\rangle$ STGB structures generated for the low stacking fault energy EAM potential [112] used in Ref. [90]. Additionally, the $\Sigma 11\,(332)\,\theta = 129.5°$ GB structure agrees with the observed

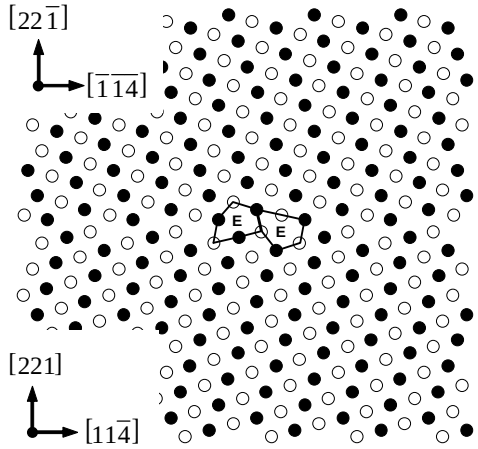


$\Sigma 9\,(221)\,\theta = 141.1^\circ$

**Figure 5.4:** $\Sigma 9$ favored grain boundary structure with the E structural unit in Cu. The structure is viewed along the $\left[1\bar{1}0\right]$ tilt axis; atoms on consecutive $\left(2\bar{2}0\right)$ planes are shown as black and white. The GB normal and period vectors for the lower and upper crystal are shown in the left-hand corner boxes.

structure from HRTEM studies for another low stacking fault energy fcc metal, Ni [211, 248].

To investigate the effect of the ratio of SUs, GB structures with ratios of E SUs to other units less than 1 and greater than 1 are included. The GB structures in Figs. 5.5(d) and 5.6(a) contain a larger ratio of E SUs, while the structures in Figs. 5.5(b) and 5.6(c) contain a smaller ratio of E SUs to the D and A SUs, respectively. Notice that the E SUs in the GB structures in Figs. 5.5(b)-5.5(d) look very similar, while the E SUs in Figs. 5.6(a)-5.6(c) appear more elongated.

Last, the GB structures in Figs. 5.5(a) and 5.6(d) are examples of the GB structure change as the ratio of E SUs per GB period length decreases even further. The structure in Fig. 5.6(d) has elongated E′ SUs with slightly distorted A′ SUs between. However, the E SU of the $\Sigma 171\,(11, 11, 10)\,\theta = 114.5^\circ$ GB is more triangular (in a 2D projected sense) with a dissociated SU that alternates between {111} planes of the adjoining crystals. This distorted E SU was also calculated in Ref. [72] for the $\Sigma 33\,(554)\,\theta = 121.0^\circ$ GB; they

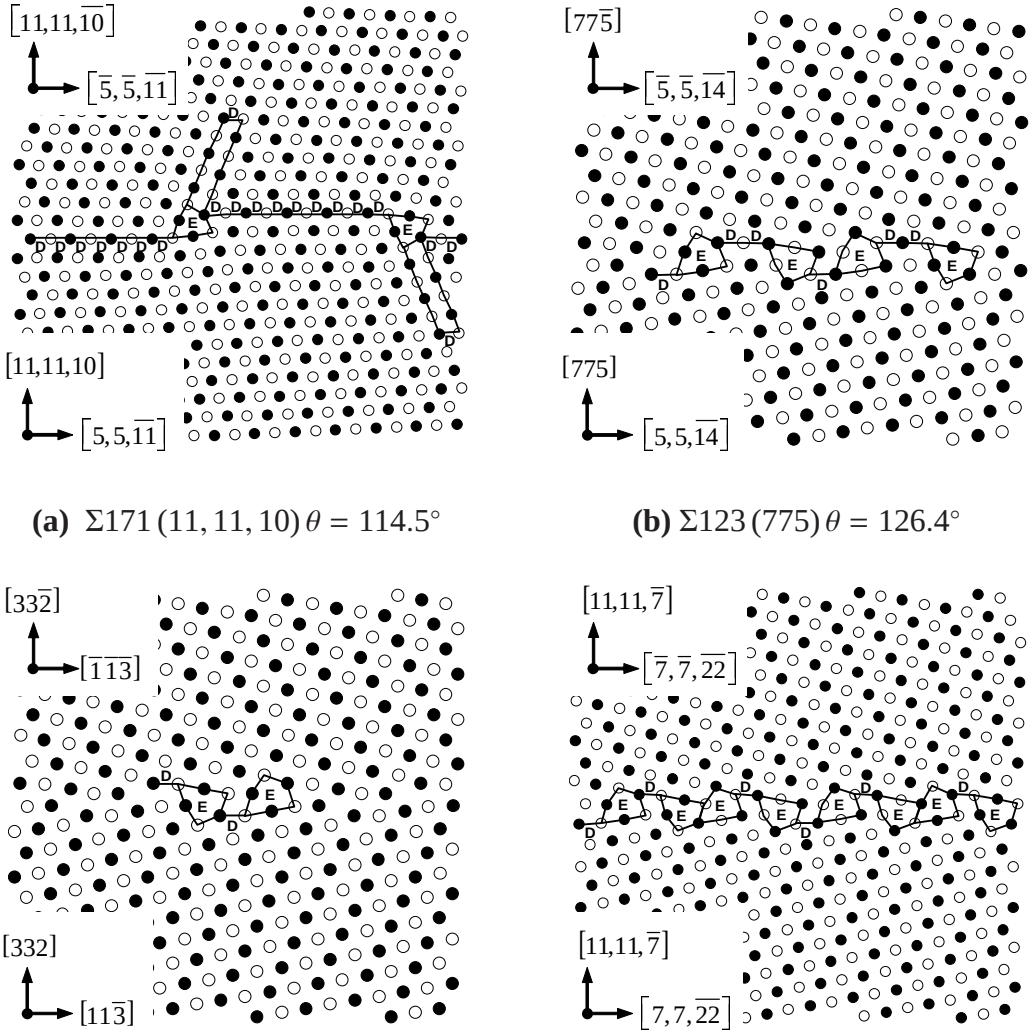


**(a)** $\Sigma 171\,(11,11,10)\,\theta = 114.5°$ **(b)** $\Sigma 123\,(775)\,\theta = 126.4°$

**(c)** $\Sigma 11\,(332)\,\theta = 129.5°$ **(d)** $\Sigma 291\,(11,11,7)\,\theta = 131.5°$

**Figure 5.5:** Four ⟨110⟩ Cu grain boundary structures with the E structural unit with $\theta < 141.1°$. The structures are viewed as in Fig. 5.4.

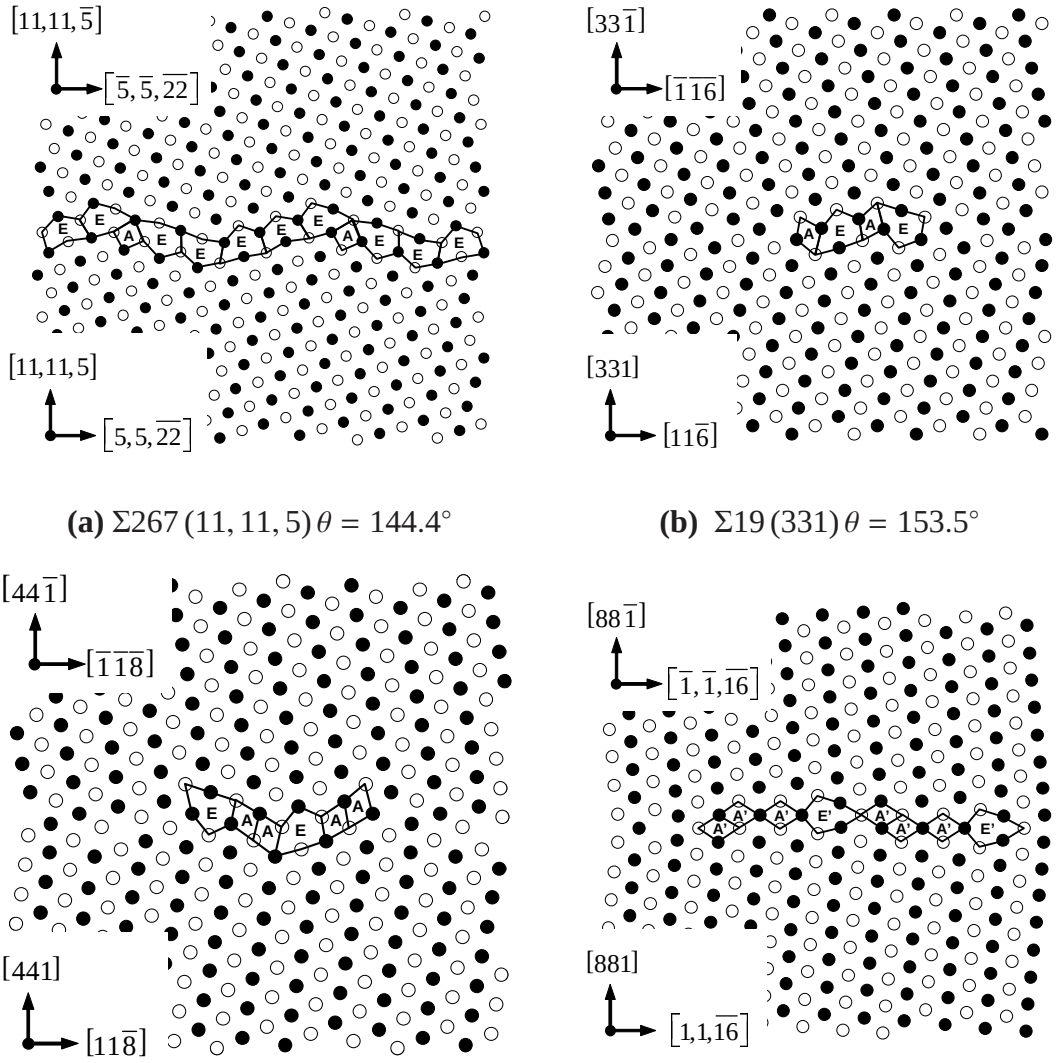


**(a)** $\Sigma 267\,(11,11,5)\,\theta = 144.4°$ **(b)** $\Sigma 19\,(331)\,\theta = 153.5°$

**(c)** $\Sigma 33\,(441)\,\theta = 160.0°$ **(d)** $\Sigma 129\,(881)\,\theta = 169.9°$

**Figure 5.6:** Four ⟨110⟩ Cu grain boundary structures with the E structural unit with $\theta >$ 141.1°. The structures are viewed as in Fig. 5.4.

use E″ to describe this SU because of the attached dissociated ISF. Accordingly, this SU is represented as E" in Table 5.1, as this description correctly follows the structural unit model [148]. Note that this boundary can be equally defined as a *vicinal* boundary to the $\Sigma 3\,(111)\,\theta = 109.5^\circ$ singular boundary (*i.e.*, the coherent twin boundary).

For boundaries with the E SU, as the GB misorientation approaches the $\theta = 109.5^\circ$ coherent twin boundary, the distortion to the E SU causes the dissociation of an intrinsic stacking fault (ISF). The ISF length increases to some extent as the deviation from the coherent twin boundary misorientation angle decreases. This sort of structure is observed experimentally. In particular, a defect structure similar to the E″ SU with a dissociated ISF was observed in HRTEM images in Al [249–251] and Au [252]. A detailed analysis of the observed defect structure in these studies has shown that this defect is a $a_0/3\,\langle 111\rangle$ twin dislocation, also termed a $a_0/3\,\langle 111\rangle$ disconnection. Furthermore, Marquis and Medlin have shown that the $a_0/3\,\langle 111\rangle$ disconnections can relax into two structures: a structure with a dissociated 90° Shockley partial dislocation or a compact core structure. The E″ structure is associated with the former. The emission of the $a_0/6\,\langle 112\rangle$ Shockley partial dislocation is through a reaction of the type $a_0/3\,\langle 111\rangle \rightarrow a_0/6\,\langle 112\rangle + a_0/6\,\langle 110\rangle$ which leaves behind a stair-rod dislocation at the interface. Interestingly, in the current work, the GBs with the E″ SU have alternating 'exterior' $a_0/3\,\langle 111\rangle$ disconnections [252], resulting in a symmetric configuration. Additionally, the E SU appears to be equivalent to the $a_0/3\,\langle 111\rangle$ twin dislocation without the emitted Shockley partial dislocation.

### 5.3.2 Free volume characterization

The free volume per unit GB area, $f_1^*$, defined in Eq. 5.2 was computed using a grid spacing of $0.025a_0$ for numerous ⟨100⟩ and ⟨110⟩ STGBs. Figure 5.7 plots $f_1^*$ as a function of misorientation angle for both ⟨100⟩ and ⟨110⟩ STGBs along with a free volume measure $D_c$, defined in Ref. [1] based on the atomic coordination number (CN), which represents

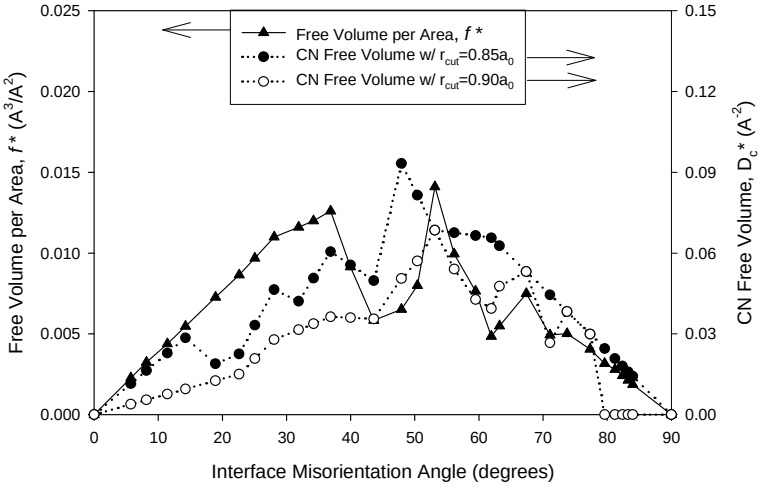


**(a)**

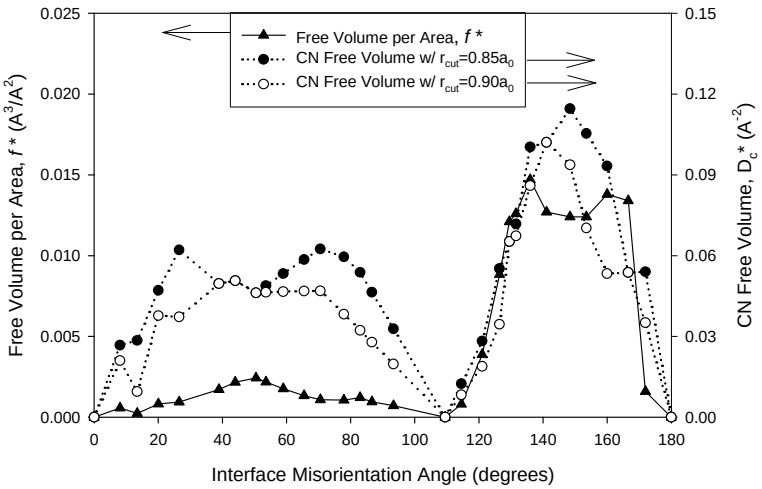


**(b)**

**Figure 5.7:** Free volume for (a) ⟨100⟩ and (b) ⟨110⟩ symmetric tilt grain boundaries as a function of the misorientation angle. The normalized free volume measure $f_1^*$ and the CN-based free volume measure $D_c^*$ are both shown on separate axes.

an interfacial damage parameter. This measure is able to qualitatively capture the differences in damage evolution for dissimilar interfaces and *approximately* correlates to the free volume within the interface [64]. In this work, however, $D_c$ was modified from its original form by normalizing with respect to the GB area $A_{GB}$ instead of number of atoms in the interface region $N'$ , *i.e.*, $D_c^* = (N'/A_{GB})\, D_c$. In this manner, this measure was normalized similarly to $f_1^*$ to facilitate comparison; because $D_c^*$ is unitless in the numerator, it is scaled to compare with $f_1^*$.

Figure 5.7 shows that the $D_c^*$ measure (CN free volume) depends on the cutoff radius $r_cut$ to identify the free volume in the GB; *i.e.*, $r_{cut} = 0.90a_0$ results in slightly lower free volume values than $r_{cut} = 0.85a_0$. This dependence of the cutoff radius causes a CN-based approach to characterize free volume in certain areas differently compared to the grid-based method presented here. For example, notice that both normalized free volume measures $f_1^*$ and $D_c^*$ display the same approximate trend for all misorientation angles for Fig. 5.7(a), but these measures deviate significantly for Fig. 5.7(b). Since the two free volume measures have different units, using a scale factor of $6/\text{Å}^3$ shows that the CN-based measure may overestimate the free volume in $\langle 110 \rangle$ STGBs with $\theta < 109.5°$. While the $\langle 100 \rangle$ STGBs have a similar free volume per unit area, the $\langle 110 \rangle$ STGBs have a very low free volume for $\theta < 109.5°$ and a sharp increase in free volume for $\theta > 109.5°$. This may explain some of the deformation behavior of GBs with $\theta > 109.5°$ in the interface strength model [64]. However, not all $\langle 110 \rangle$ GBs with $\theta > 109.5°$ have a high free volume fraction; the $\Sigma 171\,(11, 11, 10)\,\theta = 114.5°$ GB has a low free volume fraction. This is the GB shown in Fig. 5.5(a) with the E″ SU and associated stacking fault. This indicates that the dissociation of the $a_0/6\,\langle 112 \rangle$ Shockley partial dislocation may not only result in a lower energy GB structure, but also a lower free volume measure.

Recall the sharp decrease in the stress required for dislocation emission for misorientation angles greater than 109.5° in Fig. 5.1. The low volume fraction $f_1^*$ of boundaries *vicinal* to the coherent twin boundary suggest that the overall (one-point) free volume may

not be able to entirely describe the large decrease in stress required for nucleation. For these GBs, the structure is also important to consider, since the intrinsic stacking fault from the E″ SU is caused by a dissociated Shockley partial dislocation.

### 5.3.3 Free volume two-point statistics, TPCF and LPF

The TPCF $P_{11}^{*}(r)$ and LPF $L_{11}^{*}(r)$ were calculated with Eqs. 5.3 and 5.4 for several GBs within the misorientation range $109.5^{\circ} < \theta < 180^{\circ}$. Figure 5.8 shows an example of the TPCF $P_{11}^{*}(r)$ and LPF $L_{11}^{*}(r)$ for the $\Sigma 9\,(221)\,\theta = 141.1^{\circ}$ STGB. Table 5.1 that this GB has a periodic structure composed entirely of E SUs, *i.e.*, $|E.E|$ GB structure. Figure 5.8(a) shows the TPCF $P_{11}^{*}(r)$ as a function of the distance for the $\Sigma 9\,(221)\,\theta = 141.1^{\circ}$ STGB. For small distances, $P_{11}^{*}(r)$ shows the relative spacing between free volume grid points *within* a free volume cluster. However, at large distances the increase in $P_{11}^{*}(r)$ represents the spacing *between* free volume clusters. Notice that for the Z-direction (*i.e.*, tilt axis direction), the spacing between clusters approaches $a_0/2\,\langle 110\rangle$ (2.556 Ångstroms), *i.e.*, every two {220} planes, as expected. In the X-direction (GB period), the spacing between clusters approaches $a_0/2\,\langle 114\rangle$ (7.669 Ångstroms), *i.e.*, half of the GB period for the $\Sigma 9\,(221)\,\theta = 141.1^{\circ}$ GB. The spacing in the Y-direction (GB normal) is not shown; this is merely the spacing between the two periodic grain boundaries in the simulation cell.

Figure 5.8(b) shows the LPF $L_{11}^{*}(r)$ as a function of distance for the X, Y, and Z directions. Unlike the TPCF $P_{11}^{*}(r)$ which refers to the free volume *spacing*, the LPF $L_{11}^{*}(r)$ represents the *connectivity* of the free volume. Notice that $L_{11}^{*}(r)$ is greater in the X and Z directions (*i.e.*, the GB plane directions) than the Y-direction (GB normal). Also, the maximum distance where $L_{11}^{*}(r) \neq 0$ is the maximum length of the free volume clusters in each direction; the free volume clusters have a maximum length of $\sim$ 1 nm in the X and Z directions and a maximum length of $\sim$ 0.4 nm in the Y direction. While the LPFs show that the free volume has approximately the same length dimensions in the GB plane, the TPCFs show that the spacing between the free volume clusters is very different between

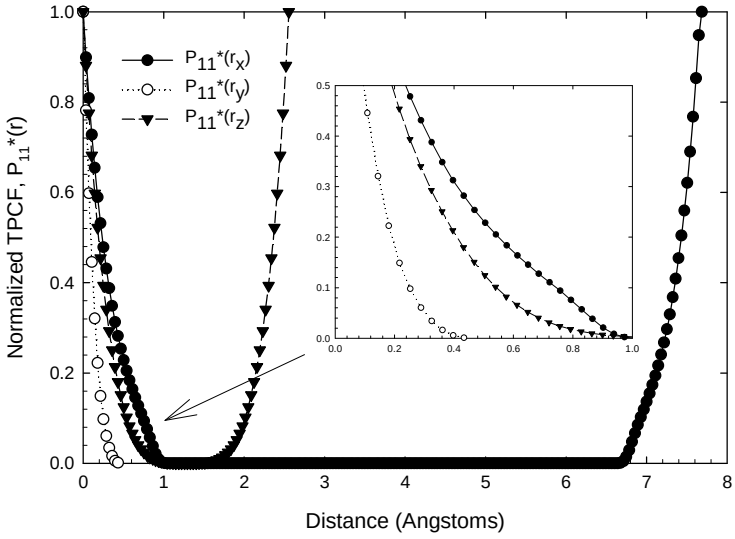


**(a)**

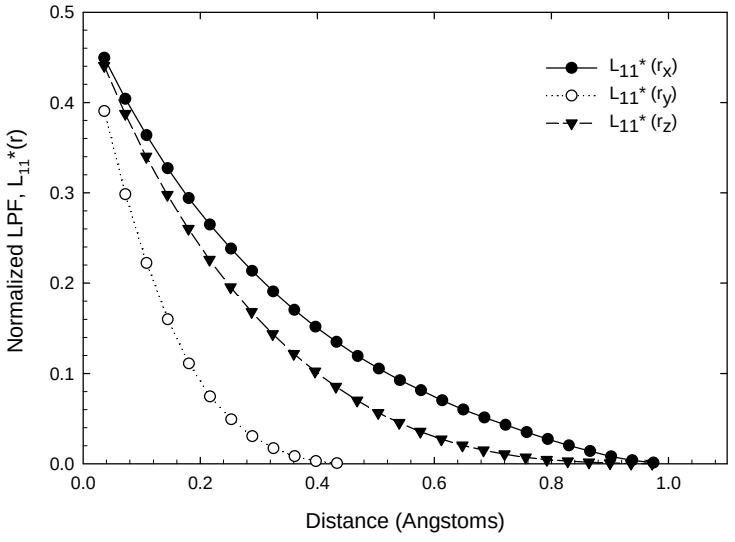


**(b)**

**Figure 5.8:** Normalized (a) TPCF $P^*_{11}(r)$ and (b) LPF $L^*_{11}(r)$ as a function of distance for the $\Sigma 9(221)\theta = 141.1^\circ$ grain boundary.

the two in-plane directions; there is a much smaller spacing between clusters in the Z (tilt axis) direction.

Figure 5.9 shows how several GB structures with misorientation angles $109.5° < \theta < 180°$ affect both the (a) TPCF $P_{11}^{*}(r_z)$ and the (b) LPF $L_{11}^{*}(r_z)$ in the Z (tilt axis) direction. Figure 5.9(a) shows that the free volume TPCF $P_{11}^{*}(r_z)$ increases with increasing misorientation angle within the range $109.5° < \theta < 180°$. As discussed previously, the spacing of the free volume clusters in the Z-direction is $a_0/2\langle 110\rangle$. Figure 5.9(b) shows that the free volume LPF $L_{11}^{*}(r_z)$ also increases with increasing misorientation angle. Note that $L_{11}^{*}(r_z)$ for the $\Sigma 129\,(881)\,\theta = 169.9°$ GB does not approach zero within the periodic length of the Z-direction; this corresponds to a continuous line of free volume from one side of the periodic boundary to the other. The lower limit of 0.0665 means that 6.65% of the free volume points are continuous in the Z-direction for this GB. While an infinite array of free volume points and the violation of the LPF limit, $\lim_{r_z\to\infty} L_{11}^{*}(r_z) = 0$, is an artifact of using periodic boundaries, this illustrates the propensity for GBs within this misorientation range to have interconnected free volume.

The TPCFs and LPFs offer insight into the atomic structure of the E SU over the misorientation angle range of $109.5° < \theta < 141.1°$. Recall the structures of the three STGBs from Fig. 5.9 within this misorientation range. The $\Sigma 9\,(221)\,\theta = 141.1°$ GB consists of only E SUs, while the $\Sigma 11\,(332)\,\theta = 129.5°$ GB has an equal ratio of D and E SUs. First, notice that a 1:1 D to E SU ratio results in very little change to the TPCF $P_{11}^{*}(r_z)$ and the LPF $L_{11}^{*}(r_z)$. This quantitative data is consistent with the qualitative GB structure results; the E SUs appear similar for both the $\Sigma 9\,(221)\,\theta = 141.1°$ and $\Sigma 11\,(332)\,\theta = 129.5°$ GBs. Additional TPCF and LPF results show that the E SU is very similar with respect to free volume for misorientation angles as low as $\theta = 121.0°$ (*i.e.*, the $\Sigma 33\,(554)$ STGB). However, for the lower misorientation angle $\Sigma 171\,(11, 11, 10)\,\theta = 114.5°$ GB, Figs. 5.9(a) and 5.9(b) show that the free volume associated with the E SU (or E", in this case) transforms into a more compact free volume cluster. This is also evident from the GB structure in Fig. 5.5(a).

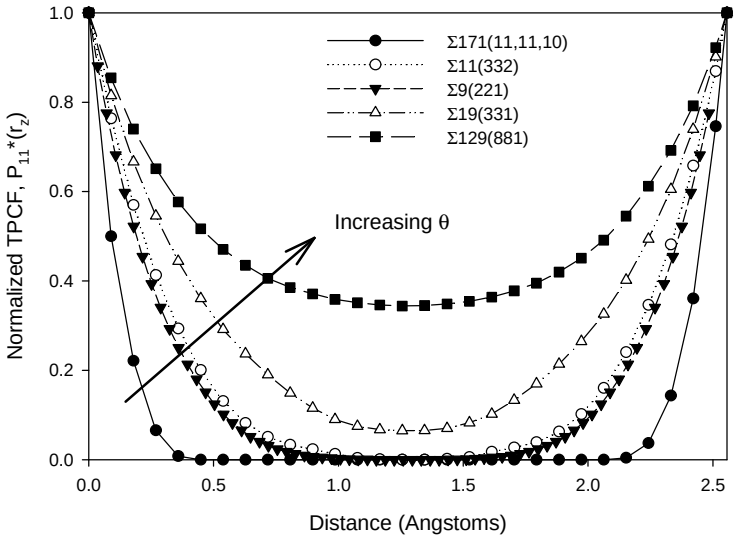


**(a)**

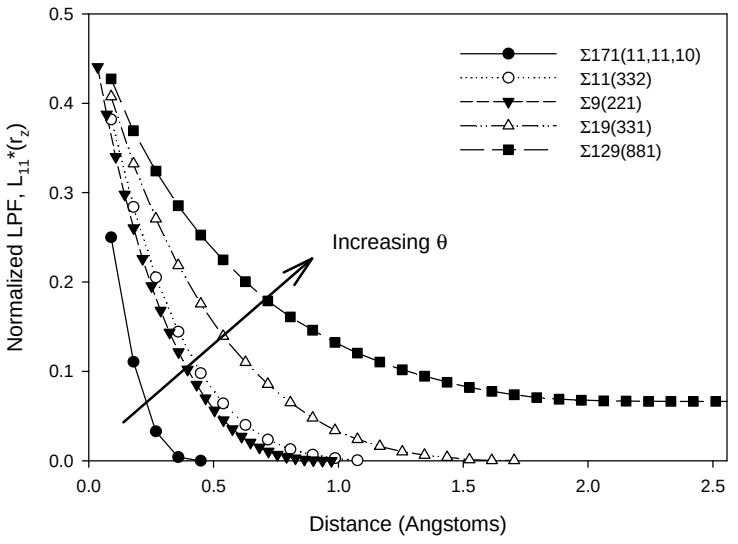


**(b)**

**Figure 5.9:** Normalized (a) TPCF $P_{11}^{*}(r_z)$ and (b) LPF $L_{11}^{*}(r_z)$ as a function of distance in the tilt axis direction for several grain boundaries within the misorientation range $109.5° < \theta < 180°$. Notice that the *spacing* and *connectivity* of the free volume increases with increasing misorientation angle.

From our calculations, this transition of the E to E″ SU occurs when the ratio of D:E SUs exceeds some critical quantity between 3 (*i.e.*, the $\Sigma 33\,(554)\,\theta = 121.0^\circ$ STGB) and 7 (*i.e.*, the $\Sigma 113\,(998)\,\theta = 115.7^\circ$ STGB). Interestingly, this transition of the E SU occurs near the window given by the Brandon criterion [253] for Σ3 STGBs (*i.e.*, 8.7° from the 109.5° Σ3 coherent twin boundary or 118.2°).

The TPCFs and LPFs also offer insight into the atomic structure of the E SU over the misorientation angle range of $141.1^\circ < \theta < 180^\circ$. The $\Sigma 19\,(331)\,\theta = 153.5^\circ$ GB consists of an equal amount of A and E SUs (*i.e.*, 1:1 ratio). However, unlike the 1:1 ratio of D to E SUs, this ratio corresponds to a structural change in the E SU, as evident by the TPCF and LPF in Figs. 5.9(a) and 5.9(b), respectively. This change is also evident in the calculated GB structure; notice that the E SU has elongated slightly compared to the E SU of the $\Sigma 9\,(221)\,\theta = 141.1^\circ$ GB. The elongation of the E SU occurs at a misorientation angle between $141.1^\circ < \theta < 153.5^\circ$. Additional TPCF and LPF data for the $\Sigma 267\,(11, 11, 5)\,\theta = 144.4^\circ$ GB show that this elongation occurs between $141.1^\circ < \theta < 144.4^\circ$. These data suggest that the introduction of the A SU into a boundary of E SUs is associated with a structural change that affects the free volume (*i.e.*, the elongation of the E SU). As noted earlier, the TPCF and LPF for the $\Sigma 129\,(881)\,\theta = 169.9^\circ$ GB show that the changes to the E SU lead to a more connected free volume structure as the misorientation angle increases in this region. Again, it is interesting that this transition to an E SU that is rotated to align with the GB period (*cf.* Fig. 5.6(a)) and contains connected free volume (*cf.* Fig. 5.9(b)) occurs near the window defined by the Brandon criterion [253] (*i.e.*, 15° from the 180° perfect lattice or 165°).

As mentioned for Fig. 5.8, the TPCF in the Z-direction (GB period) gives the spacing between free volume clusters formed from E SUs. Since the A and D SUs are not associated with free volume, the spacing between clusters is equivalent to the spacing between E SUs. As the deviation from the perfect Σ9 misorientation angle increases, the spacing between both E SUs and free volume clusters increases for the misorientation range $109.5^\circ < \theta <$

180°.

### 5.3.4 Visualization of free volume

Figure 5.10 shows a 3D view of the distorted atoms around the interface as well as the free volume for the $\Sigma 9\,(221)\,\theta = 141.1°$ STGB. This is the same boundary that is shown in the 2D projected view of Fig. 5.4. In Fig. 5.10(a), only atoms with a centrosymmetry value above 0.25 are shown. The magnified 2D projected view (above left) shows the relation between the 3D view and the GB SUs. Figure 5.10(b) shows a 3D view of the free volume for this interface. Notice the three-dimensional nature of the free volume. The magnified 2D projected views show the free volume as viewed from the tilt axis direction (below left) and the GB normal direction (below right). The projected view along the GB normal direction allows for visualization of the spacing and connectivity of free volume clusters within the GB plane.

Figure 5.11 shows a projected view of the free volume distribution in the GB plane (*i.e.,* viewed along the GB normal) for the five GBs used for the TPCF and LPF comparisons in Fig. 5.9. First, notice that the smallest overall free volume occurs for the $\Sigma 171\,(11, 11, 10)\,\theta = 114.5°$ GB; recall that this GB exhibits the dissociated E″ SU in Fig. 5.5(a). Second, the minimum free volume spacing in the GB period (x) direction is for the $\Sigma 9\,(221)\,\theta = 141.1°$ GB, as expected. As the number of E SUs per unit length decreases (*i.e.,* the deviation from the perfect Σ9 misorientation angle increases), the spacing between free volume clusters in the GB period direction also decreases. Third, Fig. 5.11 shows that the connectivity of the free volume in the tilt axis direction increases as the misorientation angle increases, as shown in Figs. 5.9(a) and 5.9(b). In fact, the $\Sigma 129\,(881)\,\theta = 169.9°$ GB contains interconnected free volume in the tilt axis direction, which is also evident from the LPF in Fig. 5.9(b). Last, changes in the shape of the free volume within the GB plane corresponds to changes in the atomic structure of the E SU.

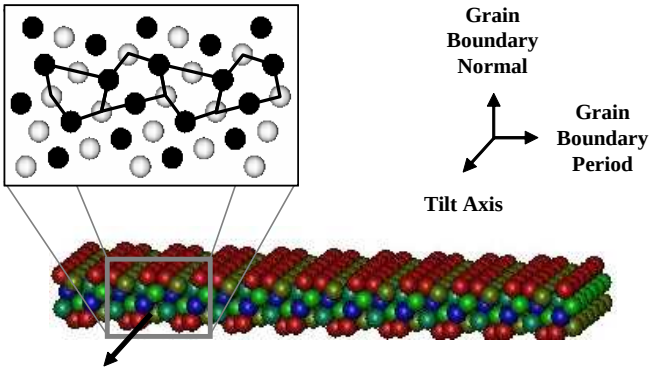


**(a)**

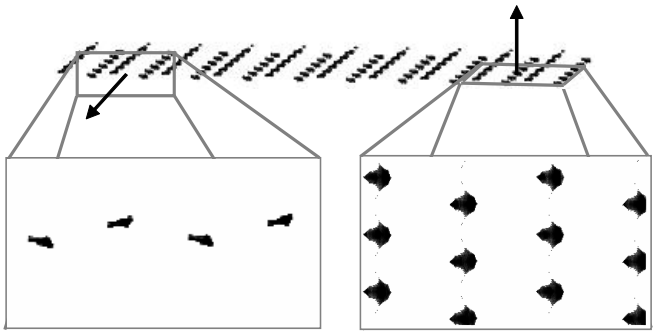

**(b)**

**Figure 5.10:** Three-dimensional view of the (a) non-centrosymmetric atoms at the interface and (b) free volume in the interface for the $\Sigma 9\,(221)\,\theta = 141.1^{\circ}$ GB. The magnified 2D projected views show the structural units (a, above left), and the free volume as viewed from the tilt axis direction (b, below left) and the grain boundary normal (b, below right).

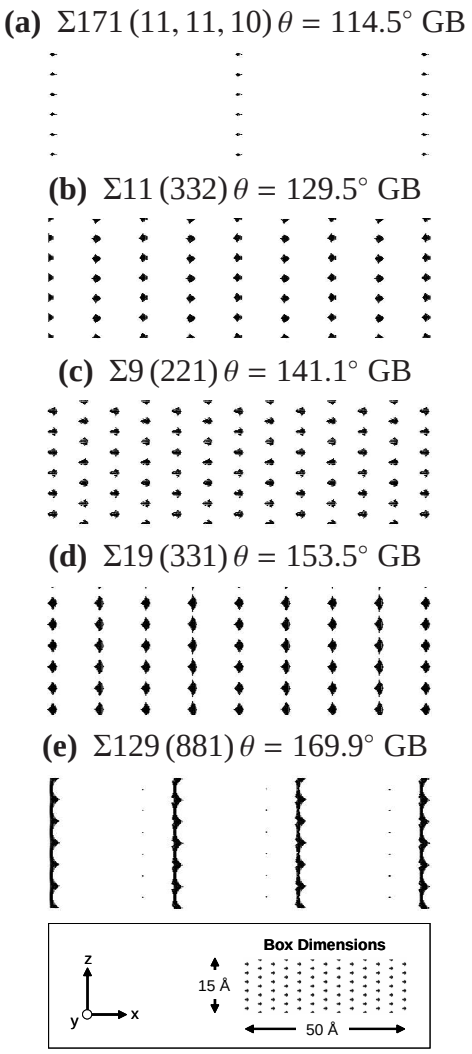


**Figure 5.11:** Two-dimensional projected view of the free volume in the grain boundary plane for five grain boundaries with misorientation angles in the range $109.5° < \theta < 180°$.

### 5.3.5 Role of GB structure and free volume in dislocation nucleation

As discussed in Refs. [64, 77, 97, 139], GB structure and free volume is important to dislocation nucleation and emission under uniaxial tensile load applied perpendicular to the GB. Figure 5.12 plots the normalized volume fraction $f_1^*$ versus the stress required for GB dislocation nucleation and emission for all STGBs in Ref. [64]. The four values corresponding to zero free volume are the 3 single crystal values (*i.e.*, the 0° "grain boundaries") and the coherent twin boundary ($\sigma_{max}$ = 12.4 GPa). Notice that there are two distinct groups: STGBs with the E SU (*i.e.*, ⟨110⟩ STGBs with $\theta > 109.5°$) and all other STGBs. In Fig. 5.12, the lines for these two groups are shown to illustrate the general trends. The trend for the general STGBs is that as the one-point measure of free volume fraction increases, the stress required for dislocation nucleation decreases. Spearot *et al.* [64] have shown that initially the free volume increases in these boundaries until reaching a peak in the CN-based free volume parameter whereby dislocation nucleation occurs. However, for STGBs with the E SU, the stress required for dislocation emission increases only slightly as the free volume increases. This is indicative of different mechanisms of dislocation nucleation between grain boundaries with and without the E SU.

The mechanism whereby a partial dislocation is emitted from a GB has two essential stages for grain boundaries with the E SU: dissociation and nucleation. The first stage is the **dissociation** of partial dislocations from the boundary. The dissociative reaction for the vicinal boundaries to the $\Sigma3\,(111)\,\theta = 109.5°$ boundary are similar to the calculated vicinal reactions by Rittner and Seidman for the misorientation range between the $\Sigma11\,(113)\,\theta = 50.48°$ and $\Sigma3\,(111)\,\theta = 109.5°$ STGBs [90]. The period vector for the $\Sigma171\,(11, 11, 10)\,\theta = 114.5°$ boundary is $a_0\,[5, 5, 11]$; this can be separated into nine and one-half periods of the $\Sigma3\,(111)\,\theta = 109.5°$ GB and half a period of the $\Sigma9\,(221)\,\theta = 141.1°$ GB. This reaction is given by

$$a_0\,[5, 5, 11] = \frac{9}{2} a_0\,[112] + \frac{1}{2} a_0\,[114] \tag{5.5}$$

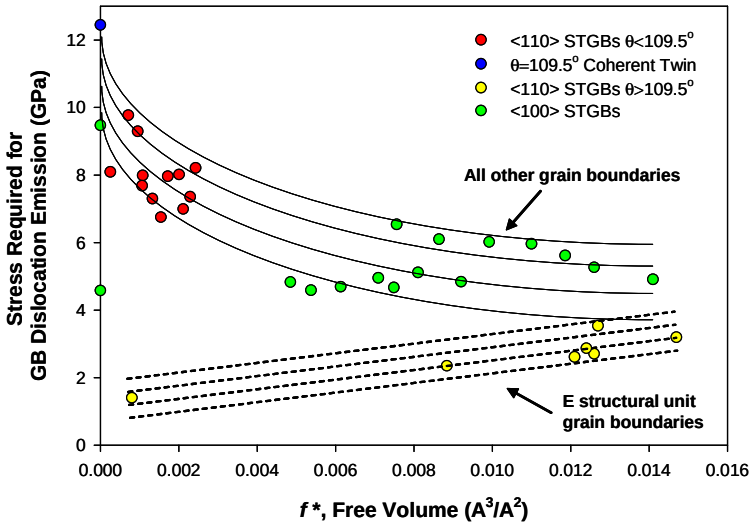


**Figure 5.12:** Free volume measure $f_1^*$ versus the stress required for dislocation nucleation for $\langle 100 \rangle$ and $\langle 110 \rangle$ symmetric tilt grain boundaries. The trend appears entirely different between grain boundaries with and without the E structural unit.

Note that the 9:1 ratio of D:E SUs from Eq. 5.5 is equivalent to the ratio of SUs shown in Fig. 5.5(a); this ratio is correct for all structures calculated within this range. However, in the $\Sigma 171\,(11, 11, 10)\,\theta = 114.5°$ GB, the E SU distorts into E″ SU, also termed an $a_0/3\,\langle 111 \rangle$ disconnection (*cf.* [252]) following the discussion in Sec. 5.3.1. As in Ref. [90], to minimize the distortion of the D SUs, the E″ SU (*i.e.*, the $a_0/3\,\langle 111 \rangle$ disconnection) emits an $a_0/6\,\langle 112 \rangle$ Shockley partial dislocation from the boundary through a reaction of the type

$$\frac{a_0}{3}\langle 111 \rangle = \frac{a_0}{6}\langle 112 \rangle + \frac{a_0}{6}\langle 110 \rangle \tag{5.6}$$

This leaves behind an $a_0/6\,\langle 110 \rangle$ stair-rod dislocation in the boundary as well. Notice that this reaction does not occur for all structures within the range $109.5° < \theta < 141.1°$, only the GB structures vicinal to the coherent twin boundary. The remainder of the GB structures within this range require stress to assist in this reaction. For these remaining boundaries, uniaxial tensile deformation nearly immediately produces a short intrinsic stacking fault,

which is associated with the *dissociated* partial dislocation from this reaction. The combination of the large free volume of the E structural unit and the applied stress enables slip among adjoining {111} planes for the dissociative reaction. This process is very similar to dislocation nucleation in nanocrystalline metals, whereby stress-assisted free volume migration from triple junctions precedes dislocation nucleation [60, 141]. In this work, the free volume inherent to the grain boundary enables the cooperative atomic shuffling that triggers the dissociation of the partial dislocation from the E structural unit. By initiating dislocation dissociation from the boundary, the free volume is vital to emission of partial dislocations from the boundary.

The spatial correlation of free volume with respect to intersecting slip planes may also affect dislocation dissociation and nucleation. For dislocation dissociation to occur from the grain boundary, the cooperative motion of a large number of atoms on a {111} slip plane intersecting the grain boundary is required. It is likely that this depends on the spacing and connectivity of free volume along that slip plane. For instance, an isolated free volume pocket that intersects the slip plane will only allow local atomic shuffling in the few neighboring atoms. However, a large fraction (low spacing and high connectivity) of grain boundary free volume intersecting the slip plane affects a greater number of atoms along the slip plane, enabling the cooperative atomic shuffling required to nucleate dislocations at the boundary. For the boundaries in this work, the two active slip systems (maximum Schmid factor analysis) occur on the same {111} slip plane (coplanar slip), which intersects the boundary along the tilt direction. Thus, the spatial correlation statistics calculated relate to this discussion.

The second required stage is the **nucleation** of partial dislocations at the boundary. For these boundaries, a higher stress is required to *nucleate* the partial dislocation from the dissociated boundary in the form of a dislocation loop (*cf.* [64]). Following Fig. 5.1, the stress required for partial dislocation *nucleation* increases with misorientation angle over

the range studied. The GB structure and free volume influence the stress required for dislocation nucleation in these boundaries by determining the the spacing between *dissociated* partial dislocations, which affects the relative ease of dislocation nucleation from the GB. Further investigation of dislocation nucleation mechanisms will be presented in Chapters 6, 7, and 8.

## *5.4 Summary*

In summary, atomistic simulations of grain boundary structure and free volume in ⟨110⟩ STGBs containing the E structural unit were performed to help explain dislocation nucleation behavior in Spearot *et al.* [64]. The current chapter presents a grid-based method for calculating the free volume whereby both one- and two-point statistics were obtained. Normalized forms for the volume fraction, the two-point correlation functions, and the lineal path functions are introduced so the simulation cell does not skew the 3D statistics calculated for these 3D planar structures. This methodology was then used to calculate free volume statistics in GBs within the misorientation range $109.5° < \theta < 180°$. It was found that the grain boundary structure and distortion of the E structural unit evolves as a function of the misorientation angle and ratio of E structural units in the boundary. Two-point statistics, in the form of two-point correlation functions and lineal path functions, were useful in quantitatively characterizing the spacing *within* and *between* free volume clusters as well as characterizing the *connectivity* of free volume. Last, the grain boundary structure and free volume statistics provide a better understanding of dislocation dissociation and nucleation in these Cu grain boundaries. For citation of the work contained in this chapter, the reader is referred to Ref. [79].

# CHAPTER VI

# DISLOCATION NUCLEATION IN Σ3 ATGBS

Chapter 6 focuses on dislocation nucleation from asymmetric tilt grain boundaries. Atomistic simulations were used to investigate dislocation nucleation from Σ3 asymmetric (inclined) tilt grain boundaries under uniaxial tension applied perpendicular to the boundary. Molecular dynamics was employed based on embedded atom method potentials for Cu and Al at 10 K and 300 K. Results briefly discuss the grain boundary structure and energy from Chapter 3, along with mechanical properties and mechanisms associated with dislocation nucleation from these Σ3 boundaries. The stress and work required for dislocation nucleation were calculated along with elastic stiffness of the bicrystal configurations, exploring the change in response as a function of inclination angle. Analyses of dislocation nucleation mechanisms for asymmetric Σ3 boundaries in Cu show that dislocation nucleation is preceded by dislocation dissociation from the boundary. Then, dislocations preferentially nucleate in only one crystal on the maximum Schmid factor slip plane(s) for that crystal. However, this crystal is not simply predicted based on either the Schmid or non-Schmid factors. The synthesis of these results provides a better understanding of the dislocation nucleation process in these faceted, dissociated grain boundaries.

## *6.1 Introduction*

Grain boundaries (GBs) play a significant role in the properties of polycrystalline materials [154] and dominate responses as grain sizes approach the nanoscale. Interest in nanocrystalline (nc) materials is motivated by the potential improvements in functional properties over coarser grained polycrystals. The mechanical properties of nc materials show numerous advantages over their polycrystalline counterparts, including peak tensile strength and strain rate sensitivity (*e.g.*, [35, 36]), but the mechanisms of deformation are

not as well understood. While some insight into the deformation mechanisms of nc materials was obtained from in situ high resolution transmission electron microscopy (HRTEM) experiments [20, 48, 49], these experiments are often very difficult to perform.

Molecular dynamics (MD) simulations can serve as an effective tool for analyzing dislocation nucleation mechanisms and GB sliding processes in nc face-centered cubic (FCC) materials [25, 50, 51, 53–55, 58, 141, 142]. MD has been utilized to investigate the critical grain size for transition between dislocation emission-mediated and GB-mediated deformation modes, which also corresponds to the peak strength in FCC materials [19] and the breakdown of the classical Hall-Petch relation [31, 32]. Below this critical grain size, MD simulations have shown that GB sliding becomes the dominant deformation mechanism [59], giving rise to grain rotation. Furthermore, Van Swygenhoven *et al*. [54] have shown that GB sliding is triggered by atomic shuffling and stress-assisted free volume migration from triple junctions; the emission of dislocations from GBs was limited. In addition, three-dimensional nanocrystals that undergo grain rotation have also displayed the inverse Hall-Petch response, *i.e.*, the peak stress decreases with decreasing grain size [18, 59]. Above this critical grain size, MD simulations have shown that partial dislocation nucleation from GBs was accompanied by atomic shuffling in the GB [60, 141]. Schiøtz [61] predicted the formation of dislocation pileups at the GB in nc Cu samples with grain sizes above 15-20 nm. MD simulations have shown that nanocrystalline Ni does not emit a trailing partial dislocation even for grain sizes as large as 30 nm, but trailing partial dislocations were observed in nc Al [132] and nc Cu for grain sizes above 15-20 nm. The deformation mechanisms observed in these MD simulations qualitatively agree with limited experimental results.

Dislocation nucleation in MD simulations of 3D nc materials is very complex, though. The combined tilt and twist character of grain boundaries and the inclination of the boundary plane with respect to the tensile axis complicates the analysis of the role of specific GB

structures in nc simulations. Additionally, different boundaries may nucleate and emit dislocations at different stresses in nc simulations; it becomes very difficult to separate out the individual effects of GB structural units on dislocation nucleation. An alternative method is to use bicrystal simulations to study the dislocation nucleation mechanism for specific GBs [97, 139]. For example, Spearot *et al*. [139] have shown how the spacing between dissociated structural units in symmetric tilt grain boundaries (STGBs) impacts dislocation nucleation in Cu and Al. However, while many bicrystal simulations have focused on STGBs, experimental characterization shows that most boundaries in polycrystalline materials are actually asymmetric tilt grain boundaries (ATGBs) [65]. In view of the interest in boundaries with a high density of coincident sites (*i.e.*, $1/\Sigma$) for GB engineering purposes (*cf*. [66, 67]), the $\Sigma 3$ system with a $\langle 110 \rangle$ tilt axis was chosen in this study for two pure FCC metals with significantly different stacking fault energies: Cu and Al. Asymmetric tilt GBs present an interesting case for studying dislocation nucleation behavior because of the faceted structure and dissimilar adjoining crystal orientations with different Schmid factors.

$\Sigma 3$ boundaries present an interesting case for studying dislocation nucleation as well. The most common $\Sigma 3$ GB is the coherent twin boundary. Many experiments have investigated the role of the coherent twin boundary in plastic deformation processes. For example, Couzinià *et al*. [254] used transmission electron microscopy to analyze the reaction process between a Shockley partial dislocation and a $\Sigma 3$ GB. Additionally, introducing coherent twin boundaries with nanoscale spacing (*i.e.*, nanoscale twins) into the grains of polycrystals has been associated with increased strength, ductility, and hardness [172–176]. However, the orientation of the GB plane strongly influences GB properties by determining whether the $\Sigma 3$ boundary is a coherent twin boundary, an incoherent twin boundary, or a $\Sigma 3$ asymmetric tilt grain boundary. Current trends in grain boundary engineering have been to characterize the grain boundary distribution in terms of both misorientation *and* grain

boundary plane (*e.g.*, [164, 165]). In this respect, the grain boundary character of polycrystalline materials can be engineered to enhance their beneficial effects while reducing their detrimental effects, as was first proposed by Watanabe [75].

Additional impetus for using atomistic simulations to investigate inelastic deformation processes is to inform higher scale models, such as continuum or dislocation dynamics models. For example, Warner *et al*. [70] implemented a continuum model for nc Cu informed by quasicontinuum deformation simulations for grain boundaries with different structural units [71, 72]. Additionally, Potirniche *et al*. [73] used molecular dynamics to investigate nanoscale void growth and coalescence in single crystal Ni for potential application to macroscopic constitutive relations. Similarly, dislocation dynamics simulations have been used to model the three-dimensional character of dislocation mechanisms for coupling with continuum finite element models (*e.g.*, modeling planar dislocation boundaries in [74]). As discussed in the current paper, the results of the current study have potential applicability for informing cohesive zone finite element models, dislocation nucleation phenomena in dislocation dynamics models, or continuum constitutive relations (*cf*. [64]).

Therefore, the objective of this paper is to investigate partial dislocation nucleation from Σ3 ATGBs using embedded atom method potentials for both Al and Cu that accurately reflect both stable and unstable stacking fault energies. This paper is organized as follows. Section 6.2 briefly discusses the methodology used for attaining and deforming the Σ3 ATGBs. In Section 6.3, the structure and energy of Σ3 ATGBs is discussed and compared to previous experimental and calculated results. Sections 6.4 and 6.5 concentrate on the mechanical properties and mechanisms associated with dislocation nucleation under a uniaxial tensile stress applied normal to the boundary. For the sake of brevity, in Section 6.5 and further sections, the majority of the focus is given to dislocation nucleation in Cu. Section 6.6 discusses the prediction of the observed preferential nucleation behavior

in Section 6.5 along with a comparison between stresses required for dislocation nucleation in both Cu single crystals and Σ3 ATGBs at 300 K. Finally, results are summarized in Section 6.7.

## *6.2 Bicrystal interface model methodology*

A parallel molecular dynamics code that incorporates domain decomposition was used to deform the Σ3 ATGBs (Warp [69]). In this work, the embedded-atom method [108, 109] potentials for Cu [124] and Al [125] were employed. First, molecular statics calculations were used to locate the minimum energy 0 K structure. The 0 K GB structures and energies obtained prior to equilibration or deformation were presented in Chapter 3 along with available experimental and calculated results for comparison; a brief review of these results is discussed here along with calculations of GB facet (or GB ledge) densities, which relate to dislocation nucleation. Second, the configuration was equilibrated using MD in the isobaric-isothermal (*i.e.*, NPT) ensemble [95] at 0 bar pressure and at the temperature of interest: *i.e.*, 10 K or 300 K. Last, the configuration was deformed in tension applied along a direction perpendicular to the interfaces at a constant strain rate of $10^9$ $s^{-1}$, as in Refs. [97,139]. The deformation details and the modified equations of motion are presented in Chapter 2. For mechanical properties, the system stress was calculated using the virial definition without the kinetic portion [99], as was discussed in Chapter 2.

Figure 6.1 shows a schematic of the 3D periodic computational cell used to investigate the GB dislocation nucleation event during uniaxial tension. As discussed in Chapter 2, this computational cell was previously used to study dislocation nucleation in selected ⟨100⟩ and ⟨110⟩ symmetric tilt GBs [97, 139] and is deemed sufficient to avoid significant effects of periodic boundaries on the 3D dislocation nucleation dynamics. All simulation cells contained Σ3 asymmetric tilt GBs with a $\left[1\bar{1}0\right]$ crystallographic misorientation axis. Appropriate dimensions were used to enforce the 3D boundary conditions.

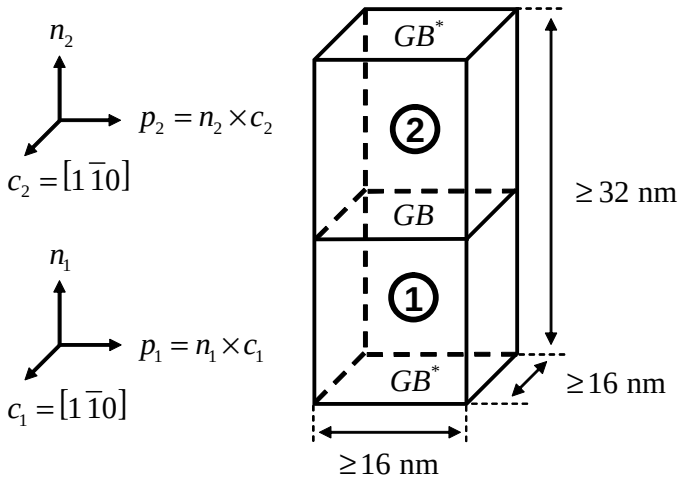


**Figure 6.1:** Schematic of the 3D periodic bicrystal computational cell showing crystal orientation notation. The subscripts denote Crystal 1 and Crystal 2 (circled in the schematic). The tilt axis for both crystals is the $[1\bar{1}0]$ direction. All dimensions are greater than 16 nm.

Table 6.1 lists all 11 Σ3 tilt grain boundaries, including 2 symmetric tilt grain boundaries and 9 asymmetric tilt grain boundaries along with an example of the periodic distances (shown in Fig. 6.1) and number of atoms for Cu. The Σ3 designation denotes that if the two crystal lattices are allowed to overlap, one in every three points is coincident; this occurs for a specific misorientation angle ($\theta$) of 70.53° about the $\left[1\bar{1}0\right]$ axis. This is the misorientation angle for all grain boundaries in Table 6.1. However, the term inclination angle ($\Phi$) is used to define the relative rotation of the GB plane about the tilt axis. The two STGBs in the Σ3 system are the coherent twin boundary (CTB) and the symmetric incoherent twin boundary (SITB); the CTB and SITB are defined as $\Phi$ = 0° and $\Phi$ = 90°, respectively. All other Σ3 boundaries with intermediate inclination angles are ATGBs. The inclination angles and the GB normals in Crystal 1 and Crystal 2 are given in Table 6.1; GBs are subsequently referred to by their inclination angle throughout this work (*e.g.*, $\Phi$ = 35.26° ATGB for the Σ3 $(110)_1$ / $(114)_2$ $\Phi$ = 35.26° ATGB). An important point to remember is that by choosing the Σ3 system, the misorientation across the boundary is identical for all STGBs and ATGBs in Table 6.1 while the GB plane, described by the inclination angle from the CTB about the misorientation axis, is altered. In this respect, the current study examines

**Table 6.1:** The inclination angles and GB normals for the 11 Σ3 boundaries investigated in this study (2 symmetric and 9 asymmetric tilt grain boundaries). As an example of simulation cell size and number of atoms, the periodic distance in all directions are given along with the total number of atoms for Cu. Note that the specified distances follow the bounds given in Fig. 6.1 ($\geq$ 16 nm).

| Type | Inclination Angle, $\Phi$ | GB Normals $(hkl)_1$ / $(hkl)_2$ | $c$ (nm) | $n$ (nm) | $p$ (nm) | Atoms |
|---|---|---|---|---|---|---|
| STGB | 0.00° | $\left(11\bar{1}\right)_1$ / $(111)_2$ | 16.36 | 32.56 | 16.82 | 758,784 |
| ATGB | 10.02° | $\left(33\bar{2}\right)_1$ / $(7,7,10)_2$ | 16.36 | 40.69 | 17.98 | 1,013,120 |
| ATGB | 19.47° | $\left(55\bar{2}\right)_1$ / $(112)_2$ | 16.36 | 37.19 | 16.91 | 865,152 |
| ATGB | 29.50° | $\left(77\bar{1}\right)_1$ / $(113)_2$ | 16.36 | 35.97 | 20.35 | 1,013,760 |
| ATGB | 35.26° | $(110)_1$ / $(114)_2$ | 16.36 | 33.74 | 16.27 | 760,320 |
| ATGB | 43.31° | $(551)_1$ / $(117)_2$ | 16.36 | 36.14 | 18.25 | 913,920 |
| ATGB | 54.74° | $(221)_1$ / $(001)_2$ | 16.36 | 32.54 | 16.87 | 757,504 |
| ATGB | 64.76° | $(554)_1$ / $\left(1,1,\bar{8}\right)_2$ | 16.36 | 35.24 | 16.61 | 807,936 |
| ATGB | 70.53° | $(111)_1$ / $\left(11\bar{5}\right)_2$ | 16.36 | 33.81 | 18.60 | 865,536 |
| ATGB | 79.98° | $(557)_1$ / $\left(11\bar{3}\right)_2$ | 16.36 | 35.97 | 20.35 | 1,004,544 |
| STGB | 90.00° | $(112)_1$ / $\left(11\bar{2}\right)_2$ | 16.36 | 33.65 | 16.28 | 758,784 |

the influence of GB plane on dislocation nucleation by fixing four of the five macroscopic degrees of freedom associated with the interface [255].

Many experiments have investigated the effect of the boundary plane orientation on specific properties in Σ3 ATGBs. For example, the orientation of the GB plane for Σ3 GBs strongly affects properties such as the GB energy [158], GB diffusion [160], or intragranular corrosion resistance [161]. Additional experiments have investigated the distribution of Σ3 boundaries and boundary planes in polycrystals. The recent ability to measure all five independent parameters of interfaces in polycrystals (*cf.* [234]) has allowed for further progress in understanding the mechanisms of grain boundary engineering in various material systems [164, 165, 231, 233]. Much of the focus in grain boundary engineering is on increasing the distribution of Σ3 boundaries in low stacking fault energy materials [66, 67]. In fact, Randle [162, 163] proposed the concept of 'grain boundary plane engineering' to maximize the proportions of desirable grain boundary planes. In line with these experimental studies, the present study aids in understanding how the grain boundary plane affects the mechanical behavior of Σ3 ATGBs.

## *6.3* Σ3 *grain boundary structure and energy*

### 6.3.1 Interfacial energy

The GB energies obtained for 25 Cu Σ3 ATGBs are shown in Fig. 6.2. In Figure 6.2(a), the GB energies are normalized by the surface energy $\gamma_{GB}/\gamma_{Surface}$ to compare the calculated Cu GB energies in this work against experimentally measured and calculated values [158, 159]. The trend between the calculated values from the two studies are in agreement considering that different simulation cells, potentials, and methodologies were used to obtain the minimum energy Cu GB structures. The experimentally measured values from thermal grooving are included along with the experimental error. Notice the larger difference between the calculated and experimental ATGB energies for inclination angles above 70.53°. This region corresponds to a different phase at the GB in Cu, which is termed the 9R phase; the rhombohedral 9R phase is formed from an intrinsic stacking fault on every third plane in an FCC structure. The presence of the 9R phase may explain the larger difference in GB energies in this region. Other potential reasons [158] for the discepancy between calculated and experimental values may be due to the temperature difference (*i.e.*, the experimental values were 1313 K). The higher temperature for the experiment may result in changes to the GB and surface energies; this, in turn, may result in a lower ratio of $\gamma_{GB}/\gamma_{Surface}$. While the magnitude of the calculated energies deviates slightly from experimental energies, the trend between the experimental and calculated values indicates agreement.

Figure 6.2(b) compares calculated GB energy values for Cu with calculated energy values for Al. Notice the two relative minimum GB energies for Cu are at the CTB and at an inclination angle approximately 5-8° from the SITB. For Al, the relative minimum energies are associated with the CTB and the SITB structures. This difference is due to the 9R phase, which is only present in the low stacking fault energy Cu. Now, assuming that the facets corresponding to the CTB and the SITB are energetically independent, *i.e.*, their respective GB energies contribute additively, the equation for GB energy is easily derived for Σ3

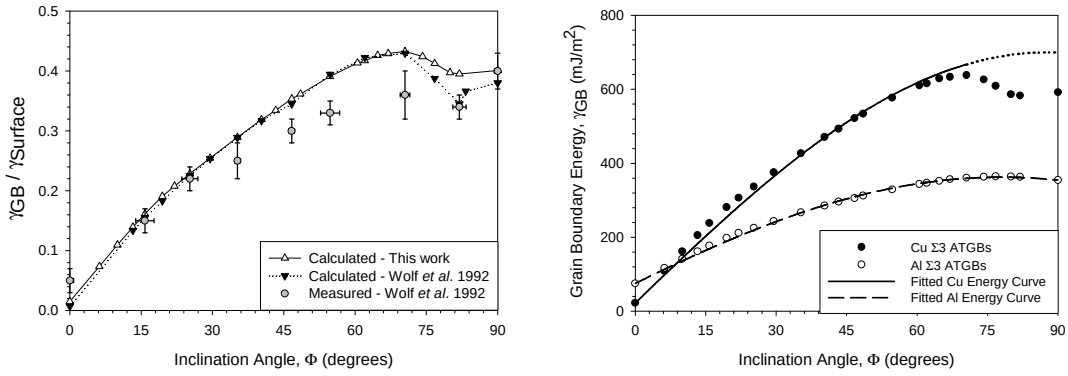


**(a)** **(b)**

**Figure 6.2:** (a) GB energy normalized by surface energy $\gamma_{GB}/\gamma_{Surface}$ as a function of inclination angle for Cu. The values calculated in this work are compared with both calculated and experimental values [158]. (b) GB energy as a function of inclination angle for both Cu and Al. The lines denote the fit according to Eq. 6.1.

ATGBs [158]. First, the ideal relation between the inclination angle $\Phi$ and the lengths of the CTB and SITB facets ($L_{CTB}$ and $L_{SITB}$, respectively) is $\tan(\Phi) = L_{SITB}/L_{CTB}$. Note that this relation holds only if the two faceted segments are perpendicular and the GB structure does not change. From this relation, the Σ3 ATGB energy for an arbitrary inclination angle, $\gamma_\Phi$, is given by

$$\gamma_\Phi = \gamma_{CTB}\cos\Phi + \gamma_{SITB}\sin\Phi \tag{6.1}$$

where $\gamma_{CTB}$ and $\gamma_{SITB}$ correspond to the CTB and SITB energies. This equation is plotted against the calculated GB energies from this study in Fig. 6.2(b). The Cu curve fits the calculated GB energies with constants that correspond to the calculated CTB energy, *i.e.*, $\gamma_{CTB}$ = 22 mJ/m$^2$, and the hypothetical, unrelaxed SITB energy, *i.e.*, $\gamma_{SITB}$ = 700 mJ/m$^2$. The hypothetical, unrelaxed SITB energy is a fitting parameter that corresponds to the energy without the dissociation of GB dislocations [18]. Only energies corresponding to $\Phi < 70.53°$ are used to fit the Cu curve. The values in the 9R phase do not follow this trend for Cu. The Al curve fits the calculated ATGB energies with constants that correspond to the CTB and SITB energies that are calculated from atomistics, *i.e.*, $\gamma_{CTB}$ = 75 mJ/m$^2$ and $\gamma_{SITB}$ = 354 mJ/m$^2$. Interestingly, all Σ3 ATGB energies except those boundaries with the

9R phase follow the ideal relationship in Eq. 6.1, presumably because of the low energy of the CTB.

### 6.3.2 Interface structure

The minimum energy GB structures for the CTB and SITB in Cu are shown in Figs. 6.3(a) and 3(b), respectively. The structures are viewed along the $\left[1\bar{1}0\right]$ tilt axis and the atoms on consecutive $\left(2\bar{2}0\right)$ planes are shown as black and white. The GB normal and period vectors for the lower and upper crystal are shown in the corner boxes on the left-hand side for each GB. Following the notation of [90], the CTB in Fig. 6.3(a) consists of only D structural units (SUs); the GB structure is defined as $|D.D|$ where the period prior to the structural unit signifies the relative translation of structural units by $a_0/4\left[1\bar{1}0\right]$. The SITB, shown in Fig. 6.3(b), consists of exactly one C SU and one D SU; the GB structure is defined as $|DC|$. Notice that the D SU dissociates from the GB in Cu resulting in an intrinsic stacking fault. In terms of dislocations, the D SU is equivalent to a Shockley partial dislocation with edge character (*cf.* [91]) while the C SU is equivalent to a pair of Shockley partial dislocations (*cf.* [213, 214]).

Figure 6.4 shows the structures for Σ3 ATGBs in Cu for three intermediate inclination angles. The two arrows in the upper right corner correspond to the ideal orientation of the CTB and SITB facets based on the inclination angle (also shown). Interestingly, there are two facets for each Σ3 ATGB: one facet corresponds to the SUs of the CTB (*i.e.*, Fig. 6.3(a)) and one facet corresponds to the SUs associated with the SITB (*i.e.*, Fig. 6.3(b)). For example, the $\Phi = 13.26^\circ$ ATGB in Fig. 6.4(a) contains twelve D SUs on the CTB facet for each $|DC|$ SU on the SITB facet. As the inclination angle increases, the ratio of D SUs on the CTB facets to the number of $|DC|$ SUs on the SITB facets decreases, as expected. Additionally, the dissociation of the D SU on the SITB facet transitions from one side of the facet to the other as the inclination angle increases (compare Figs. 6.4(a) and 4(b)). For high inclination angles in Cu (*i.e.*, $\Phi > 70.53^\circ$ as in Fig. 6.4(c)), the D SU

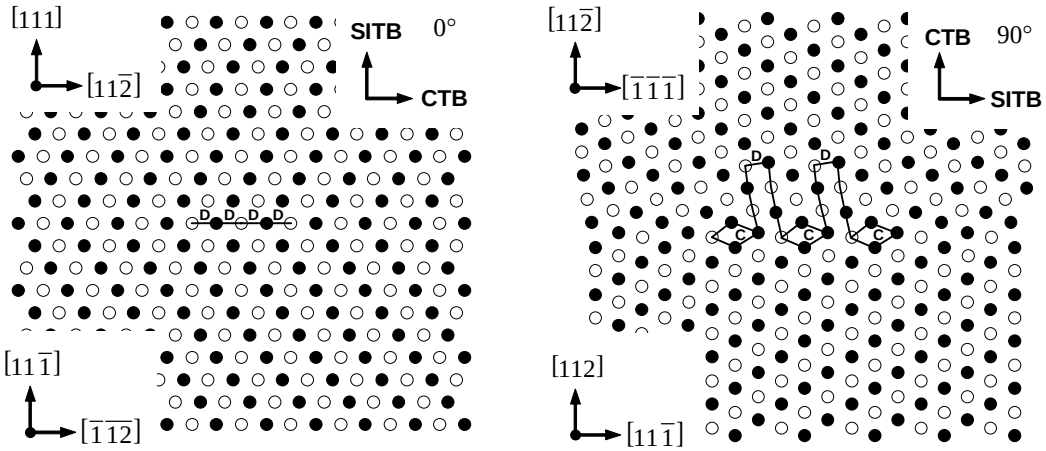


**Figure 6.3:** Σ3 symmetric tilt GB structures in Cu for the (a) Σ3 (111) $\theta = 109.47°$ coherent twin boundary and the (b) Σ3 (112) $\theta = 70.53°$ incoherent twin boundary. The structures are viewed along the $\left[1\bar{1}0\right]$ tilt axis and the atoms on two consecutive $\left(2\bar{2}0\right)$ planes are shown as black and white. The GB normal and period vectors for the lower and upper crystal are shown in the corner boxes on the left side for each GB.

on the SITB facet dissociates further into the adjoining crystal lattice, creating a low angle boundary that delineates the 9R phase (*i.e.*, the repeating intrinsic stacking fault on every third plane). Moreover, the GB structures containing the 9R phase are in agreement with the experimental HRTEM images of low stacking fault energy materials in the literature (*e.g.*, [158, 159, 188]). Last, the Σ3 ATGB structures are very similar between low stacking fault energy Cu and high stacking fault energy Al except that (i) the D SU on the SITB facet dissociates less in Al, and (ii) the 9R phase is not observed in Al. For further information regarding the structure and energy of Σ3 asymmetric tilt grain boundaries, see Chapter 3 or Tschopp and McDowell [76, 78].

The faceted nature of the Σ3 ATGB structure allows the calculation of the number of GB ledges (or steps) per unit length of GB, as shown in Fig. 6.5. In this calculation, a GB ledge is defined as an intersection of two different facets: *i.e.*, in this case, the intersection of a CTB facet and a SITB facet. Also, the unit length is based on the CTB and SITB periods of $p_{CTB} = 1/4\,[112]$ and $p_{SITB} = [111]$, which correspond to the $|D|$ and $|DC|$

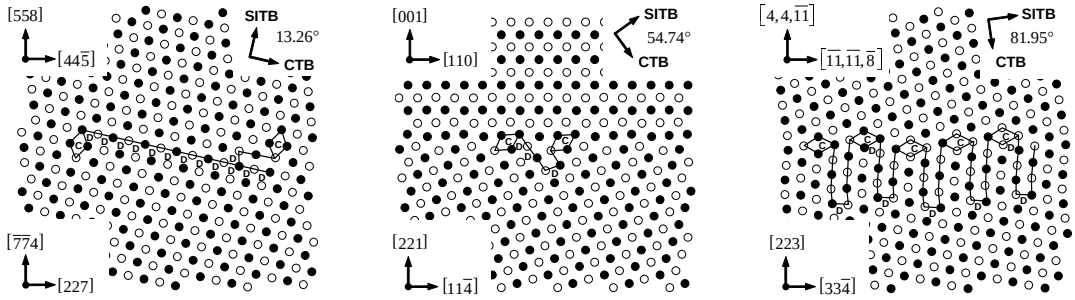


**(a)** **(b)** **(c)**

**Figure 6.4:** Σ3 asymmetric tilt GB structures in Cu for the (a) Φ = 13.26°, (b) Φ = 54.74°, and (c) Φ = 81.95° GBs. The structures are viewed as in Fig. 6.3. The inclination angle is shown in the upper right corner along with the ideal facet locations.

SUs, respectively. This curve is based purely on geometry and does not include the lattice constant, $a_0$, in the length term; this is therefore material independent. The number of |*D*| and |*DC*| SUs per unit GB length are also plotted. The number of minority SUs per unit length dictates the number of GB ledges per unit length; *e.g.*, the number of |*DC*| SUs is equivalent to the number of intersections for inclination angles $\Phi \leq 70.53°$. The $\Phi = 70.53°$ ATGB contains an equal number of |*D*| and |*DC*| SUs and is a transition point in this relationship. Note that the inverse relation of this curve is the spacing between GB ledges for each side of the boundary; the minimum spacing of GB ledges is $\sqrt{27/8}a_0$ (*i.e.*, 6.6 Ångstroms in Cu) for the $\Phi = 70.53°$ ATGB. Knowledge of the faceting, structural unit and dissociative behavior of Σ3 ATGB aids in understanding the mechanisms of dislocation nucleation in these boundaries.

## *6.4 Mechanical response*

### 6.4.1 Stress-strain response for Σ3 asymmetric tilt GBs

The stress-strain curves for Cu and Al under an applied uniaxial tensile strain were calculated at temperatures of 10 K and 300 K for all boundaries in Table 6.1. This results in a total of 44 total curves. Figures 6.6(a) and 6.6(b) show 11 stress-strain curves for Cu Σ3

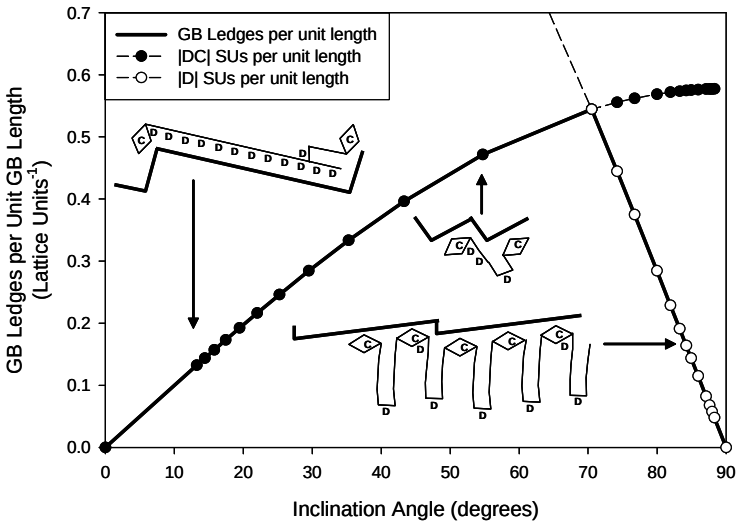


**Figure 6.5:** The change in the number of facet intersections (or GB ledges) per unit GB length as a function of inclination angle for Σ3 asymmetric tilt grain boundaries. This quantity is identical for Cu and Al (*i.e.*, in terms of lattice units). Note that the inverse of this measure is the spacing between the GB ledges. The structural unit images are from Fig. 6.4.

ATGBs at 300 K with inclination angles $\Phi < 45°$ and $\Phi > 45°$, respectively. Since nucleation of the first partial at the GB coincides with the maximum tensile stress, $\sigma^{bc}_{\max}$, the simulations are stopped shortly after reaching the peak stress. Several quantitative parameters were calculated: the elastic stiffness $K^b c$, the maximum tensile stress $\sigma^{bc}_{\max}$, the strain corresponding to that stress $\epsilon^{bc}_{\max}$, and the work per unit volume required for dislocation emission $W^{bc}$, where the superscript *bc* refers the bicrystal configuration.

The definitions for these quantities can be related to force $F_n$ and displacement $\delta_n$ normal to the interface for inclusion in cohesive zone finite element models. The strain is defined as $\epsilon = \delta_n/n$, where $n$ is the initial height of the cell as in Table 6.1 and $\delta_n$ is the conjugate displacement of the overall unit cell. The atomistic stress is defined in Eq. 2.8 of Chapter 2; given the initial grain boundary area, $A_{GB}$, the conjugate force is related by $F_n = \sigma A_{GB}$. The bicrystal elastic stiffness is then given with the relation $K = \sigma/\epsilon = (n/A_{GB})\, F_n/\delta_n$. Last, the work is defined in terms of $F_n$, $\delta_n$, and the volume $V = A_{GB}n$, *i.e.*,

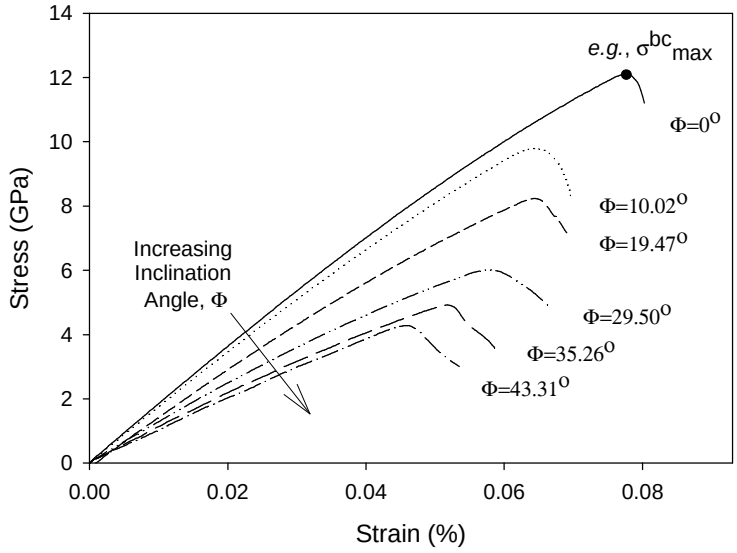


**(a)**

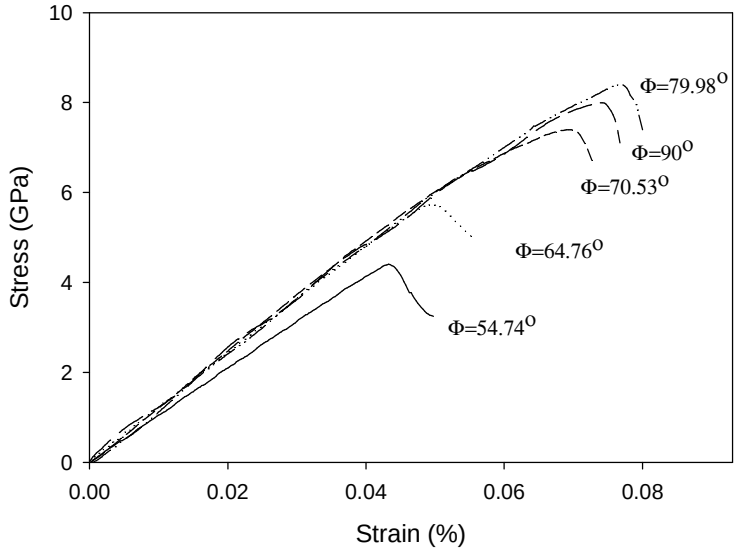


**(b)**

**Figure 6.6:** Stress-strain curves for 11 Σ3 grain boundaries of varying inclination angles at 300 K. The curves are separated according to GBs with inclination angles (a) below 45° and (b) above 45°.

$$W^{bc} = \int_{\epsilon=0}^{\epsilon=\epsilon^{bc}_{\max}} \sigma d\epsilon = \frac{1}{V} \int_{\delta_n=0}^{\delta_n=\delta_{n,\max}} F_n d\delta_n \tag{6.2}$$

where the upper limits of integration, $\epsilon^{bc}_{\max}$ and $\delta_{n,\max}$, correspond to the strain and displacement associated with dislocation nucleation from the boundary. Note that work scales with volume, while the work per unit volume $W^{bc}$ used here remains unchanged for increased distances between GBs ($n$) and increased GB plane dimensions ($c$ and $p$).

The general trends for these quantities are apparent from the stress-strain curves. In Fig. 6.6(a), the elastic stiffness, peak stress, strain at peak stress, and work decreases with increasing inclination angle for $\Phi < 45°$. In Fig. 6.6(b), the elastic stiffness is nearly identical for ATGBs with inclination angles $\Phi \geq 64.76°$. Additionally, the peak stress, strain at peak stress, and work appear very similar for inclination angles in the range $\Phi \geq 70.53°$. While these are indicative of the trends for Cu at 300 K, the trends for the remaining simulations are presented in terms of the peak stress, strain at peak stress, elastic modulus, and work.

### 6.4.2 Stress required for dislocation nucleation

Figure 6.7(a) shows the peak stress values for all simulations. Recall that the peak stress $\sigma^{bc}_{\max}$ is directly related to dislocation nucleation from the GB. First, the stress required for dislocation nucleation changes as a function of inclination angle. The magnitude of the change in stress values is greater as a function of inclination angle in Cu than in Al, though. The highest stress $\sigma^{bc}_{\max}$ for both Al and Cu is at the $\Phi = 0°$ coherent twin boundary. The lowest stress for Cu is at the $\Phi = 43.31°$ GB while the lowest stress in Al is at the $\Phi = 29.50°$ GB; both are boundaries of intermediate inclination angles. The $\Phi = 90°$ incoherent twin boundary is between these values for Cu, and is near the low value in Al. This graph also shows a decrease in $\sigma^{bc}_{\max}$ with increasing temperature, especially near the symmetric twin boundaries ($\Phi = 0°$ and $\Phi = 90°$). The thermal component is expected to

contribute to the dislocation nucleation process via the activation energy and activation volume associated with dislocation nucleation [256]. Of course, the 300 K case is overdriven in terms of kinetics, so in reality the drop of stress may be somewhat more pronounced at low strain rates (on the order of experimental strain rates). For example, at strain rate of 1 $s^{-1}$ the number of atomic vibrations relative to the strain increment is $10^9$ higher than that for a strain rate of $10^9$ $s^{-1}$. However, MD simulations require timestep increments on the order of femtoseconds, which commonly results in strain rates on the order of $10^9$ $s^{-1}$ for calculated dislocation nucleation phenomena. As dislocation nucleation can be aided by thermal fluctuations, the stress required to nucleate dislocations is lower at lower strain rates.

In relation to the stress required for dislocation nucleation, Figure 6.7(b) shows the change in strain at the peak stress for all simulations. Recall that prior to running these simulations, the cell dimensions were tested to verify that the stress and strain values are not significantly affected by the scale of the volume element considered; these can therefore be related to the force and displacement of a GB cohesive separation law.

### 6.4.3 Bicrystal elastic stiffness

Figure 6.7(c) shows the elastic stiffness of the bicrystal pair as a function of inclination angle for the 44 stress-strain curves. The elastic stiffness was computed with a linear regression fit for the equation $\sigma = K\epsilon$ for approximately 40 data points with strains $\epsilon < 0.01$. First, notice the large difference between Cu and Al, as expected. In general, the elastic modulus of Cu ($E_{[100]}$ = 67 GPa and $E_{[111]}$ = 192 GPa) is higher than that of Al ($E_{[100]}$ = 63 GPa and $E_{[111]}$ = 76 GPa) [257]. In addition to the higher elastic modulus values, Cu has a considerably higher degree of elastic anisotropy than Al: $E_{[111]}/E_{[100]}$ = 2.91 for Cu and $E_{[111]}/E_{[100]}$ = 1.20 for Al.

The elastic modulus of each crystal was calculated for uniaxial loading in a given direction $d$ with indices [$hkl$] by [257]

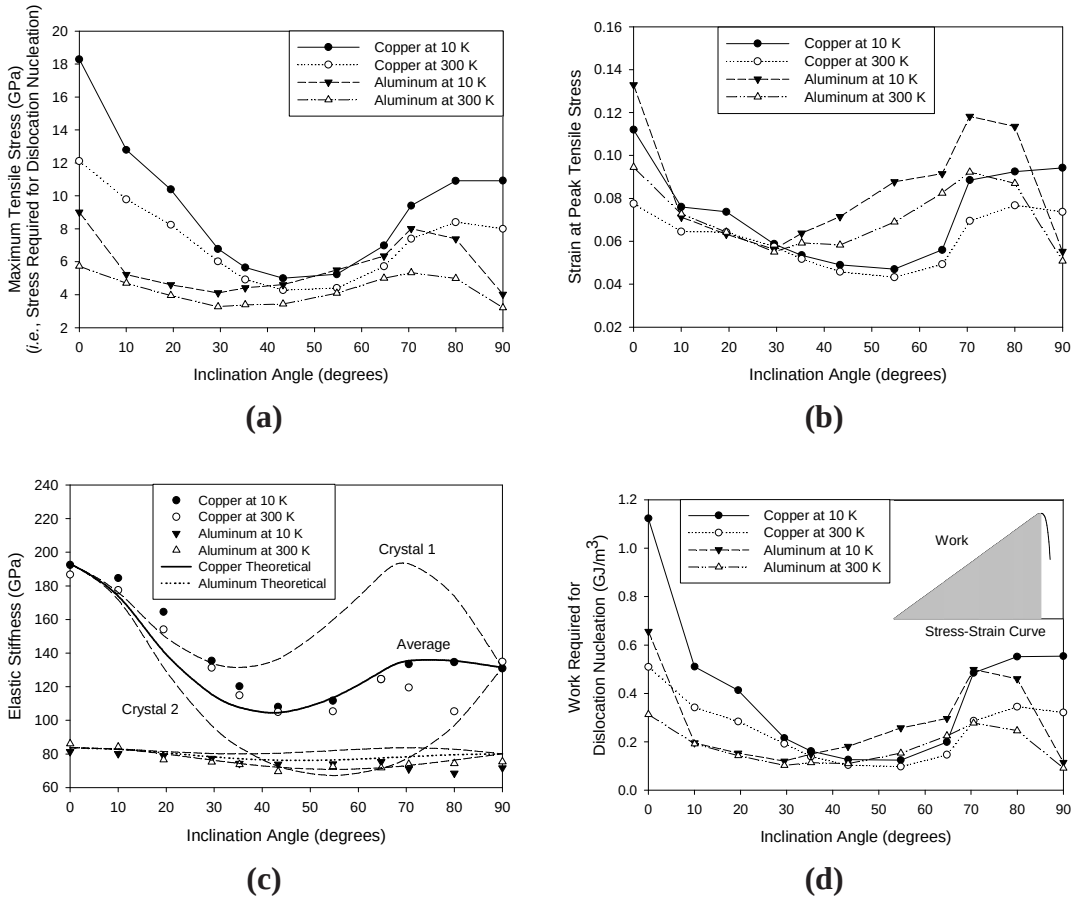


**Figure 6.7:** The change in (a) maximum tensile stress $\sigma^{bc}_{\max}$ (*i.e.*, stress required for dislocation nucleation), (b) strain at peak tensile stress $\epsilon^{bc}_{\max}$, (c) elastic stiffness $K^b c$, and (d) work required for dislocation nucleation $W^{bc}$ as a function of the grain boundary inclination angle. These curves are generated from the stress-strain curves for both Al and Cu at temperatures of 10 K and 300 K.

$$\frac{1}{E_d} = S_{11} + (2S_{12} - 2S_{11} + S_{44}) \frac{\left(k^2l^2 + l^2h^2 + h^2k^2\right)}{(h^2 + k^2 + l^2)} \tag{6.3}$$

In this equation, $S_{ij}$ represents the elastic compliances for a given crystal. By calculating the elastic compliances for a cubic crystal from the elastic moduli $C_{ij}$ given for the Cu and Al EAM potentials [124,125], the elastic modulus for each lattice adjoining the ATGBs was calculated. Since both crystals have equivalent volumes, the bicrystal elastic stiffness can be approximated by averaging the elastic moduli for the two adjoining crystals. The trend lines on Fig. 6.7(c) are the individual elastic modulus for each crystal along with the average elastic stiffness of the assembly as a function of inclination angle. Note that this definition of the elastic stiffness does not account for the effect of the GB. The boundary's influence on the elastic stiffness of the bicrystal increases as the surface-to-volume ratio changes (*i.e.*, the GB has a greater influence in nanocrystalline materials). For the present configuration, though, this effect is negligible and Fig. 6.7(c) shows that the calculated elastic stiffness values are in agreement with predictions obtained by averaging the elastic moduli for the two adjoining crystals, using Eq. 6.3. Moreover, for Cu, the trend for the elastic modulus in Fig. 6.7(c) is very similar to the trend for the peak stress in Fig. 6.7(a); this is not necessarily the case for Al.

### 6.4.4 Work required for dislocation nucleation

Figure 6.7(d) shows the work (Eq. 6.2) as a function of inclination angle for the 44 stress-strain curves. The work values were computed with a multiple segment trapezoidal rule for all stress-strain data points up to the peak stress $\sigma^{bc}_{\max}$. As with the peak stress, the work changes as a function of inclination angle. The largest work value is for the $\Phi = 0^\circ$ coherent twin boundary in both Cu and Al. For most inclination angles, the work required for dislocation nucleation is greater for Cu, but Al requires more work for some inclination angles in the range $43.31^\circ \leq \Phi \leq 70.53^\circ$.

**Table 6.2:** The stress for dislocation nucleation, elastic stiffness, and work for dislocation nucleation are summarized in terms of low values, high values, and the ratio between the high and low values. The ratio of these extreme values reflects the variation of responses with inclination of the boundary plane for both materials and temperatures. Notice the signficant degree of variation of both the stress and work required for dislocation nucleation with the boundary inclination angle.

| | | | Stress for Dislocation Nucleation, $\sigma^{bc}_{\max}$ (GPa) | Elastic Stiffness, $K^{bc}$ (GPa) | Work per Unit Volume, $W^{bc}$ (GJ/m$^3$) |
|---|---|---|---|---|---|
| Al | 10 K | High | 9.00 | 81.25 | 0.66 |
| | | Low | 4.02 | 68.45 | 0.11 |
| | | Ratio | 2.24 | 1.19 | 5.71 |
| | 300 K | High | 5.73 | 86.18 | 0.31 |
| | | Low | 3.21 | 68.02 | 0.09 |
| | | Ratio | 1.78 | 1.27 | 3.44 |
| Cu | 10 K | High | 18.29 | 192.43 | 1.12 |
| | | Low | 4.99 | 107.95 | 0.12 |
| | | Ratio | 3.66 | 1.78 | 9.00 |
| | 300 K | High | 12.11 | 186.70 | 0.51 |
| | | Low | 4.28 | 104.94 | 0.10 |
| | | Ratio | 2.83 | 1.78 | 5.22 |

Table 6.2 categorizes the data for stress required for dislocation nucleation, elastic stiffness, and work for dislocation nucleation in terms of low and high values. Comparison of the ratio between the high and low values shows the dependence on the boundary plane inclination for both materials and temperatures. First, both the stress and work required for dislocation nucleation depend strongly on the inclination angle. Second, notice that the variation of these responses with inclination angle decreases with increasing temperature. Last, the variation of responses with inclination angle is greater in low stacking fault energy Cu than in high stacking fault energy Al. In terms of GB character, all boundaries in this work have the same disorientation angle/axis combination [153]; the only degree of freedom changed is the inclination of the GB plane from the CTB about the misorientation axis. The significant variation of mechanical response with respect to the inclination angle emphasizes the importance of GB plane orientation in characterizing GBs, consistent with recent trends in GB engineering [162, 163, 165, 232].

Figure 6.8(a) shows the correlation between the peak tensile stress and the corresponding strain for both Al and Cu; Fig. 6.8(b) shows the correlation of peak stress and the work required for dislocation nucleation. In Fig. 6.8(a), for an equivalent peak tensile stress, the

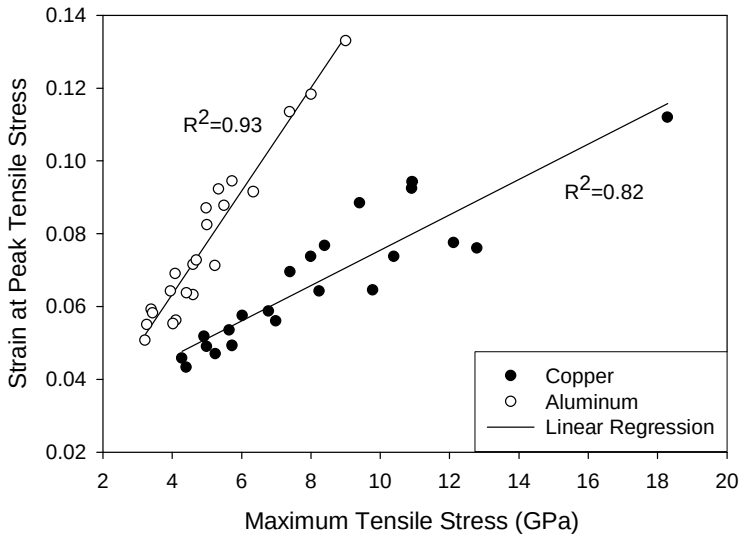


**(a)**

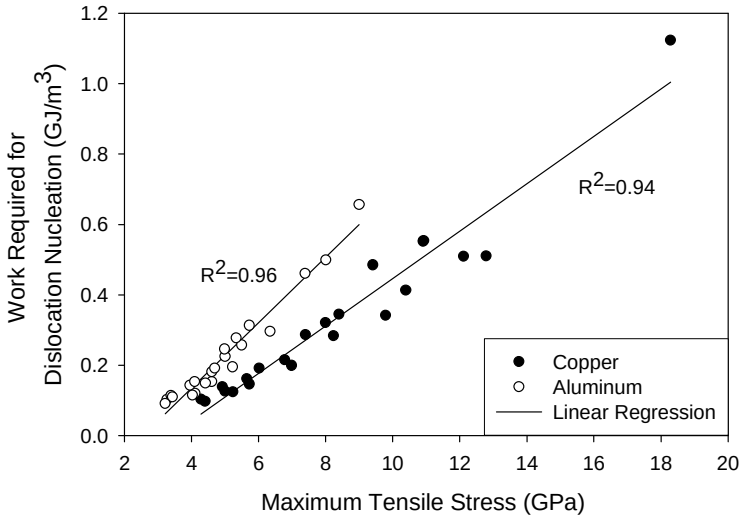


**(b)**

**Figure 6.8:** Correlation between the stress required for dislocation nucleation and (a) the strain at peak tensile stress, as well as (b) work required for dislocation nucleation. The linear regression fit is plotted along with the correlation coefficient. Plot includes both 10 K and 300 K data from Fig. 6.7 for Al and Cu.

strain required to reach that stress is higher for Al than Cu. This is expected based on the lower elastic stiffness of Al. In Fig. 6.8(b), for an equivalent peak stress, the work required for dislocation emission in Al is higher than that of Cu; this is also expected. Interestingly, the data points for Cu and Al are from the stress-strain curves at temperatures of 10 K and 300 K, yet these data fit on the same linear trend line; it is noted that the dynamic strain rates in these analyses may mask nucleation differences at these two temperatures that would be observed at much lower strain rates.

## *6.5 Dislocation nucleation mechanisms*

A full understanding of the dislocation nucleation behavior for Σ3 ATGBs in Cu also requires a discussion of the salient mechanisms. Three distinct mechanisms of dislocation nucleation occur for Σ3 ATGBs, separated into three different regimes of inclination angle: low inclination angles ($\Phi \leq 35.26°$), intermediate inclination angles ($35.26° \leq \Phi \leq 70.53°$), and high inclination angles ($\Phi \geq 70.53°$). The dislocation nucleation mechanisms for Cu Σ3 ATGBs provide similar observations for temperatures of 10 K and 300 K. The present authors have used the 10 K simulations to minimize the thermal component of dislocation nucleation and emission from these boundaries. Recall that all boundaries in this study have identical misorientations and that only the GB plane (*i.e.*, inclination angle) is altered. The following results show that GB plane can heavily influence dislocation nucleation mechanisms as well.

### 6.5.1 Low inclination angles ($\Phi \leq 35.26°$)

At low inclination angles, the boundary is composed of large coherent twin boundary facets separated by smaller incoherent twin boundary facets, as shown in Fig. 6.9(a). Figure 6.9 shows the $\Phi = 10.02°$ Cu ATGB subjected to uniaxial tensile deformation normal to the interface plane at 10 K. In these images, only atoms with a centrosymmetry value greater than 0.25 are shown (*i.e.*, distorted GB atoms, dislocations, and stacking faults). As shown in Fig. 6.9, the X-direction is along the GB normal and the direction of the applied

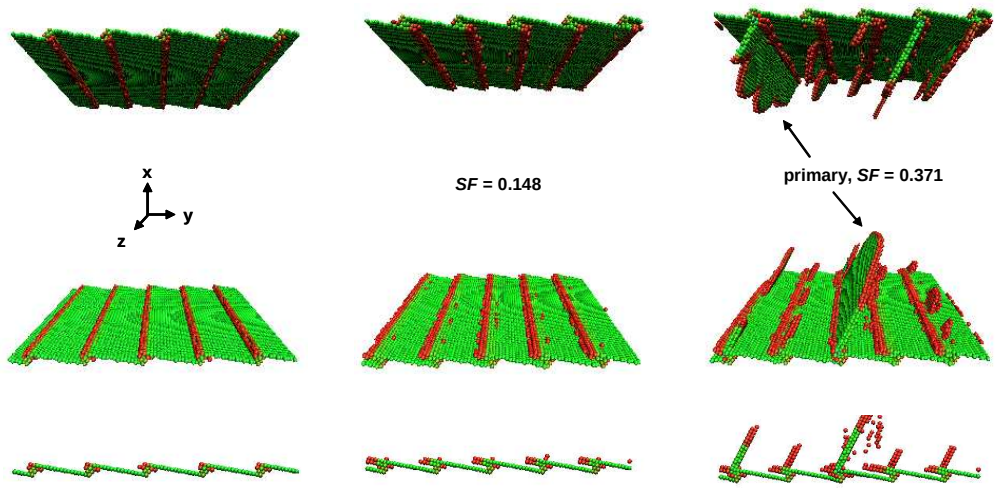


**(a)** $\epsilon = 0.000$ **(b)** $\epsilon = 0.070$ **(c)** $\epsilon = 0.077$

**Figure 6.9:** Uniaxial tensile deformation of the $\Phi = 10.02°$ asymmetric tilt grain boundary in Cu at 10 K. The different views represent (a) the faceted structure prior to deformation, (b) the dissociation of partial dislocations prior to dislocation nucleation, and (c) the nucleation of partial dislocation loops that are emitted into Crystal 1. Only atoms in a non-centrosymmetric environment are shown. The top image is a three-dimensional oblique view and the bottom image is an orthonormal view from the $\left[1\bar{1}0\right]$ direction.

stress, the Y-direction is along the GB period tangent to the interface, and the Z-direction is along the tilt axis. Recall that the crystals adjoining the ATGBs have different lattice orientations. For the images in Fig. 6.9, the two boundaries contain Crystal 1 (upper crystal in Fig. 6.1); Crystal 2 is both above and below these boundaries (*i.e.*, periodic with respect to simulation cell bounds in the X-direction). Last, the images below the three-dimensional views correspond to projections of the lower interface onto the XY-plane, with Z normal to the view. A detailed characterization of the GB structure of the upper boundary in Figs. 6.9(a)-(c) is shown in Figs. 6.10(a)-(c).

Figure 6.9(a) shows an oblique view of the interface after isobaric-isothermal equilibration, but prior to deformation. Notice the ledges formed by the intersection of coherent twin facets with incoherent twin facets, as in Fig. 6.10(a). Figures 6.9(b) and 6.10(b) show that the interface structure evolves prior to dislocation nucleation and emission from the boundary. Specifically, the D structural unit on the incoherent twin facet (*i.e.*, the GB

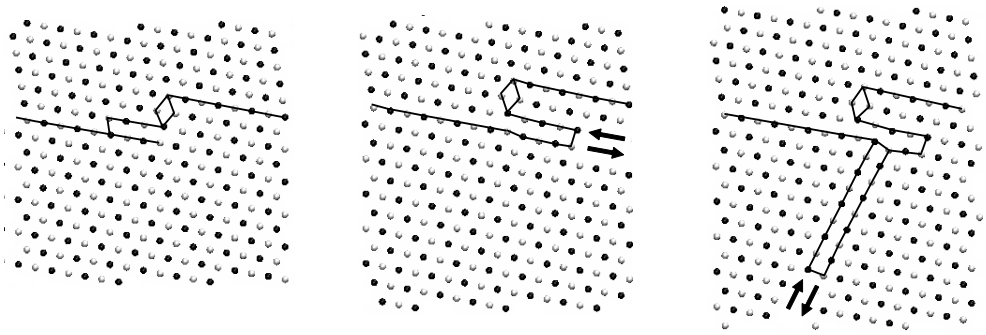

**(a)** **(b)** **(c)**

**Figure 6.10:** Detailed view of the evolution of structure for the $\Phi = 10.02°$ asymmetric tilt grain boundary in Cu at 10 K. The images correspond to the upper boundary in Figs. 6.9(a)-(c). The structures are viewed along the $\left[1\bar{1}0\right]$ tilt axis and the atoms on two consecutive $\left(2\bar{2}0\right)$ planes are shown as black and white. The arrows correspond to the relative shift in atoms compared to their nearest neighbors as measured by the slip vector [107]. Notice that the dislocation nucleates on a different {111} plane than the dissociated glissile partial dislocation.

Shockley partial dislocation) dissociates into crystal lattice 1 on the $\left(11\bar{1}\right)$ plane, leaving an intrinsic stacking fault (ISF). The arrows in Fig. 6.10(b) show the shift (slip) of atoms on the (111) plane relative to their nearest neighbors, as visualized with the slip vector [107]. A Schmid factor analysis [257] of the slip systems in Crystal 1 shows that this is a secondary slip plane for this crystal ($SF^{\max}_{(11\bar{1})} = 0.148$) below all other possible slip planes ($SF^{\max}_{(\bar{1}11)} = SF^{\max}_{(1\bar{1}1)} = 0.223$, $SF^{\max}_{(111)} = 0.371$), where $SF^{\max}_{(hkl)}$ is the maximum Schmid factor for all three slip directions on the ($hkl$) slip plane. Additional tensile strain causes partial edge dislocations to nucleate where the dissociated Shockley partial dislocation intersects the coherent and incoherent twin facets, as shown in Figs. 6.9(c) and 6.10(c). The partial dislocations nucleate as a dislocation loop on the (111) plane with both edge and screw character, unlike the planar dissociation of the GB partial edge dislocations in Fig. 6.9(b). Since the primary slip plane for dislocation nucleation is different from the dissociative plane, the change in slip planes may serve as a nucleation barrier resulting in high peak stresses $\sigma^{bc}_{\max}$ required for dislocation nucleation in low inclination angle Σ3 ATGBs (cf.

Fig. 6.7(a)). Further tensile strain leads to the dislocation loops merging to form a continuous dislocation line as well as propagating further into the lattice. Although not shown, this is also accompanied by a decrease in the length of the dissociated GB Shockley partial and ISF.

Interestingly, upon closer examination of the dislocation nucleation mechanism for this boundary, the dissociated glissile partial dislocation does not cross slip onto the high resolved shear stress slip plane. In fact, a partial dislocation loop homogeneously nucleates on the {111} slip plane near the dissociated D structural unit. This is most likely associated with a local stress concentration near the intersection of the two facets, which may act similarly to a boundary ledge in this respect. Due to the close proximity, the partial dislocation is quickly absorbed into the nearby boundary, giving the appearance of heterogeneous dislocation nucleation. It should be noted that this mechanism requires a very high stress, which may preclude most grain boundaries. The implications of this mechanism on the perfect sink/source concept for grain boundaries is discussed further in Section 8.1.

### 6.5.2 Intermediate inclination angles ($35.26° < \Phi < 70.53°$)

Figure 6.11 shows dislocation nucleation and emission from the $\Phi = 54.74°$ ATGB in Cu at 10 K. The images for Fig. 6.11 are presented in an identical manner to those in Fig. 6.9. The magnified view of the GB structure is also shown in Figs. 6.12(a)-(c). At intermediate inclination angles, the ratio of the length of the coherent twin facet to the incoherent twin facets is around unity (cf. Fig. 6.12(a)). Additionally, the short length of the facets leads to a higher number of facet intersections, or ledges, in the boundary. This is evident from the oblique view of the interface after isobaric-isothermal equilibration in Fig. 6.11(a).

In Figs. 6.11(b) and 6.12(b), prior to dislocation nucleation, the application of a tensile strain perpendicular to the boundary causes the glissile partial dislocations (*i.e.*, D structural units) to further dissociate from the incoherent twin facet into crystal lattice 1 on the

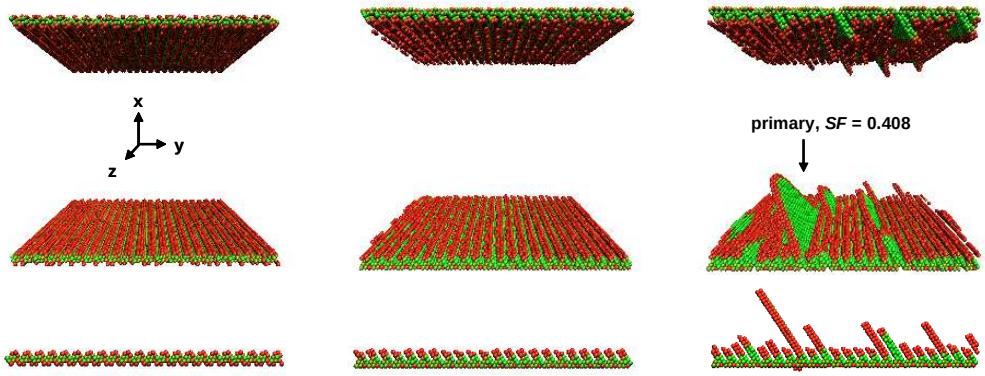


**(a)** $\epsilon = 0.000$ **(b)** $\epsilon = 0.040$ **(c)** $\epsilon = 0.048$

**Figure 6.11:** Uniaxial tensile deformation of the $\Phi = 54.74°$ asymmetric tilt grain boundary in Cu at 10 K. The images are rendered the same as those in Fig. 6.9.

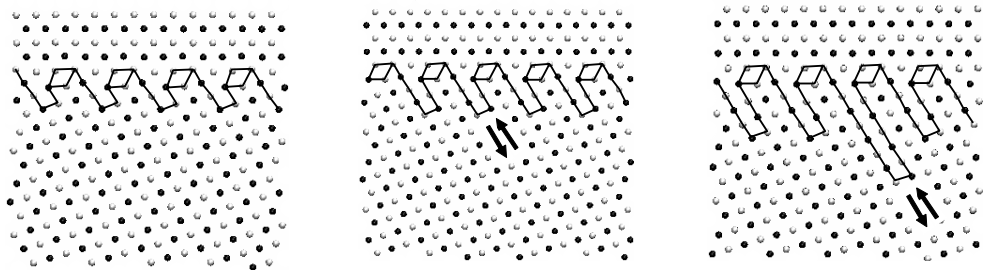

**(a)** **(b)** **(c)**

**Figure 6.12:** Detailed examination of the $\Phi = 54.74°$ asymmetric tilt grain boundary in Cu at 10 K. These images correspond to the upper boundary in Figs. 6.11(a)-(c) and are viewed as in Fig. 6.10. Note that the dislocation nucleates on the same {111} plane as the dissociated glissile partial dislocation.

$\left(11\bar{1}\right)$ plane. This is similar to the pre-nucleation behavior observed at low inclination angles for Σ3 ATGBs. However, for intermediate inclination angles, this is the primary slip plane for Crystal 1 ($SF^{\max}_{\left(11\bar{1}\right)} = 0.408$). Prior to the peak stress, the dissociation is planar, *i.e.*, the dislocations each dissociate an equal distance (approximately) from the boundary. As the stress reaches the peak tensile stress, Figs. 6.11(c) and 6.12(c), the first partial dislocations are nucleated on the $\left(11\bar{1}\right)$ slip plane, the same slip plane onto which partial dislocations dissociated. Notice that not all dissociated partial dislocations are emitted from the boundary; some are retained. The spacing between dissociated structural units may serve as a critical length scale that influences the number of partial dislocations nucleated on the primary slip system. As with the low inclination angle Σ3 ATGBs, the partial dislocations emitted into the lattice are dislocation loops with edge and screw dislocation character and the trailing partial is not observed in Cu. Additionally, since the primary slip plane for dislocation nucleation is the same as the dissociative plane, the barrier for nucleation is lower; this results in low peak stresses $\sigma^{bc}_{\max}$ required for dislocation nucleation in Σ3 ATGBs within this inclination range (cf. Fig. 6.7(a)).

### 6.5.3 High inclination angles ($\Phi \geq 70.53°$)

Figure 6.13 shows dislocation nucleation for the $\Phi = 79.98°$ ATGB in Cu at 10 K. At inclination angles $\Phi \geq 70.53°$, recall that the structure exhibits the 9R phase in Cu, as shown in Fig. 6.4(c). The 9R phase structure in Fig. 6.4(c) is identical to the structure in Fig. 6.13(a), after isobaric-isothermal equilibration, which is rendered using the centrosymmetry parameter as in Figs. 6.9 and 6.11. Figure 6.13(b) shows that the 9R phase structure evolves prior to dislocation nucleation in the $\Phi = 79.98°$ ATGB. Again, tensile strain perpendicular to the boundary causes the dissociation width for the glissile partial dislocations (D structural units) to increase towards crystal lattice 1 on the $\left(11\bar{1}\right)$ plane. This is similar to the pre-nucleation behavior observed at low and intermediate inclination angles for Σ3 ATGBs, but the dissociation width perpendicular to the boundary is larger due to the presence of the

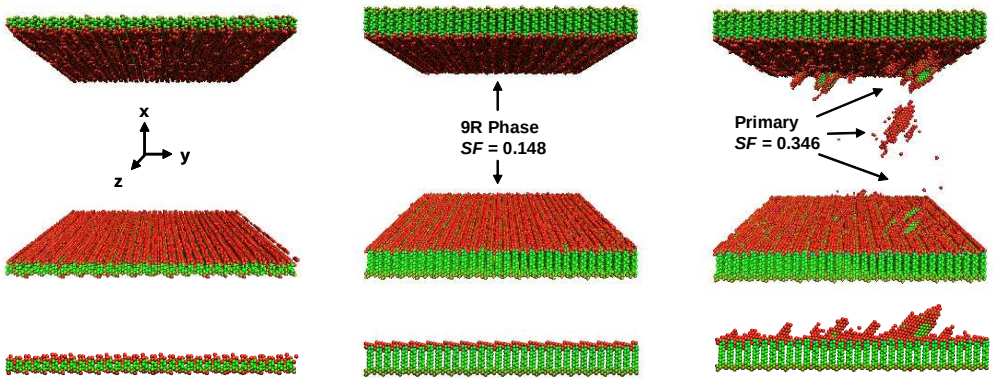


**(a)** $\epsilon = 0.000$ **(b)** $\epsilon = 0.090$ **(c)** $\epsilon = 0.093$

**Figure 6.13:** Uniaxial tensile deformation of the $\Phi = 79.98°$ asymmetric tilt grain boundary in Cu at 10 K. The images are rendered the same as those in Figs. 6.9 and 6.11.

low energy 9R phase.

Figure 6.14 shows images of the 9R phase on the lower boundary just prior to dislocation nucleation in the lattice. This image is rendered similarly to Fig. 6.4, where black and white atoms represent successive $\left(2\bar{2}0\right)$ planes and distorted atoms are identified using the centrosymmetry parameter. In the enlarged view of the boundary (right), the expansion of the 9R phase results from partial dislocations further dissociating from the incoherent twin facet. The 9R phase is clearly visible in this view, with an intrinsic stacking fault on every third $\left(11\bar{1}\right)$ plane, resulting in an ABCBCACAB stacking sequence. Unlike intermediate inclination angles, the dissociation plane is not the primary slip plane for Crystal 1. Schmid factor analyses shows that this is a secondary slip plane ($SF^{\max}_{(11\bar{1})} = 0.148$); the primary slip planes ($SF^{\max}_{(\bar{1}11)} = SF^{\max}_{(1\bar{1}\bar{1})} = 0.346$) have normal vectors that are not orthogonal to the $\left[1\bar{1}0\right]$ tilt axis as in Figs. 6.9-6.11. For high inclination angles, partial dislocations nucleate both at the low angle boundaries *and* within the lattice on the $\left(\bar{1}11\right)$ and $\left(1\bar{1}1\right)$ slip planes; the partials propagate as dislocation loops. Interestingly, the dislocations nucleate nearly simultaneously on both primary slip planes at the nucleation sites. Additionally, the dislocation loop contains a longer intrinsic stacking fault along the direction contained by both slip planes, although this direction has a slightly lower Schmid factor

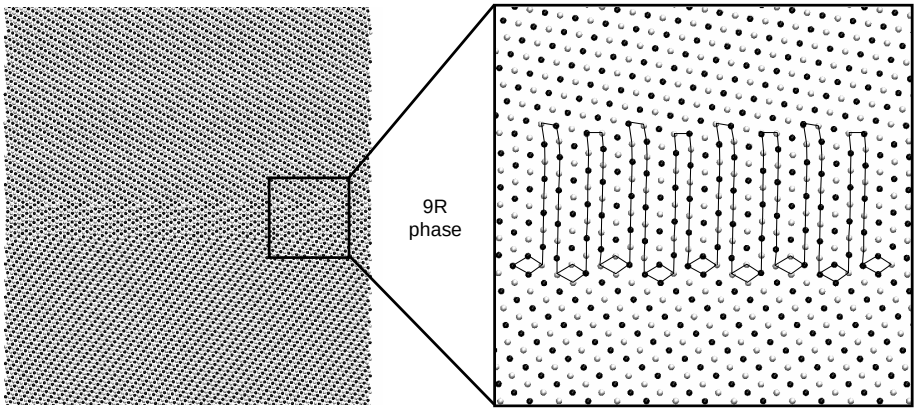


**Figure 6.14:** Detailed images of the structure of the $\Phi = 79.98°$ asymmetric tilt grain boundary in Cu at 10 K. These images show the interface structure just prior to dislocation nucleation. The images are viewed similarly to Figs. 6.3 and 6.4 where black and white atoms represent consecutive $\left(2\bar{2}0\right)$ planes. The magnified view (on right) shows the extended dissociation of the glissile partial dislocation (*i.e.*, D structural unit), which expands the 9R phase.

$(SF_{(\bar{1}11)[110]} = SF_{(1\bar{1}\bar{1})[110]} = 0.289)$.

### 6.5.4 Preferential dislocation nucleation in Cu

Partial dislocations preferentially nucleate into only one crystal lattice; this is characteristic of all Σ3 ATGBs. In fact, all Σ3 ATGBs nucleate partial dislocations into Crystal 1 (see Fig. 1) in this study. This phenomenon is as expected for ATGBs with inclination angles $\Phi < 25.24°$, for which $SF^{\max}_{(hkl)}$ is highest in Crystal 1. However, the preferential dislocation nucleation in Crystal 1 is observed for all ATGBs in this study, despite a higher $SF^{\max}_{(hkl)}$ in Crystal 2 for all inclination angles $\Phi > 25.24°$. This preferred nucleation is in contrast to the dislocation nucleation simulations of Spearot *et al*. [97, 139] for symmetric tilt GBs with ⟨100⟩ and ⟨110⟩ tilt axes. With lattice orientations that are symmetric with respect to the GB plane, Spearot and coworkers have shown that partial dislocations are nucleated and emitted into both lattices once the peak tensile stress is reached. For Σ3 ATGBs, dislocation emission into Crystal 2 only occurs at high strains after excessive dislocation emission severely alters the initial GB structure.

The observation of preferential dislocation nucleation depends on the arrangement of

glissile partial dislocations within the boundary and their character. For all Σ3 ATGBs in this study, the glissile partial dislocation (dissociated D structural unit) dissociates into crystal 1 for the minimized energy grain boundary structure. These dissociated partial dislocations are integral to dislocation nucleation in Σ3 ATGBs. The uniaxial tensile strain merely resolves into stress components acting to overcome the stacking fault energy penalty that restricts glide of these partial dislocation into the lattice. So it seems that the preferential dislocation nucleation event can be traced back to the minimum energy structure. Perhaps the most important question is why does this partial dislocation dissociate into crystal 1 for the minimum energy grain boundary structure? Interestingly, the elastic modulus is higher in crystal 1 for all inclination angles. The local relaxation of the dislocation content of the ATGBs may result in any glissile partial dislocation content dissociating into the adjoining crystal with the higher elastic modulus. The boundary structure, particularly the dissociated glissile partial dislocation, serves as the impetus for dislocation nucleation in Σ3 ATGBs.

## *6.6 Discussion*

Schmid and non-Schmid effects are considered for prediction of the properties and behavior observed in Sections 4-5. Non-Schmid effects have been used to capture the influence of stress components acting on the slip plane in non-glide directions [143, 258, 259]. Previous MD simulations of single crystal and interfaces have indicated that non-Schmid effects play an important role in dislocation nucleation [64]. In fact, Spearot and colleagues show that both Schmid and non-Schmid factors can be incorporated into an interface strength model capable of predicting the dislocation nucleation stress for ⟨100⟩ and ⟨110⟩ Cu STGBs. The calculated and predicted dislocation nucleation stresses are in good agreement for ⟨100⟩ STGBs and ⟨110⟩ STGBs with misorientation angles $\theta < 109.5°$. As in Spearot *et al.* [64], $SF$ projects the uniaxial applied stress into the resolved shear stress on the slip plane in the slip direction (*i.e.*, the conventional Schmid factor), $NF$ projects the uniaxial stress into the

stress **normal** to the slip plane, and $PF$ projects the uniaxial stress into a shear stress acting on the slip plane **perpendicular** to the slip direction (*i.e.*, coslip direction).

Several challenges arise in the formulation of an interface strength model for asymmetric tilt GBs. The ATGBs in this study contain an additional level of complexity relative to the STGBs in the aforementioned study; instead of two identical lattice orientations relative to the GB plane, the bicrystal lattice orientations relative to the ATGB mean boundary plane differ, resulting in different $SF$, $NF$, and $PF$ values for each lattice. Also, while the free volume for ATGBs can be calculated using the same methodology, the faceting of ATGBs adds an additional layer of atomic level complexity because of its impact on dislocation nucleation phenomena. Last, the preferential nucleation of dislocations from ATGBs dictates that the model parameters must have a physical basis. Obviously, using the Schmid and non-Schmid parameters of Crystal 2 to predict the preferential nucleation of dislocations from the ATGB into Crystal 1 is not physically appropriate. Therefore, as a first step towards an interface model for the stress required for dislocation nucleation at Σ3 ATGBs, the present authors investigate the prediction of preferential nucleation in this class of asymmetric boundaries.

### 6.6.1 Schmid and non-Schmid factors

First, the Schmid and non-Schmid effects are investigated to examine their potential utility for understanding the preferential dislocation nucleation. As mentioned previously, the crystal lattices on each side of an ATGB are oriented differently relative to the applied stress direction, resulting in different Schmid and non-Schmid factors. Therefore, dislocation *motion* should be easiest in the lattice with the slip system associated with the highest Schmid factor, since this slip system has the highest resolved shear stress. However, following the results in Section 6.5, dislocation *nucleation* from ATGBs does not necessarily occur on the highest Schmid factor slip system between the two crystals. Figure 6.15(a) shows the maximum Schmid factor for both crystal lattices as a function of the inclination

angle. The vertical lines at $\Phi = 35.26°$ and $\Phi = 54.74°$ correspond to relative minima in the maximum Schmid factor, which corresponds to a transition of active slip systems; the vertical line at $\Phi = 70.53°$ delineates the region where ATGBs contain the 9R phase in Cu. However, contrary to what might be expected from Fig. 6.15(a) based on the Schmid factor, the partial dislocations are nucleated into Crystal 1 for all Σ3 ATGBs in Table 6.1. This observation matches the crystal predicted from the maximum Schmid factors for low inclination angles only (*i.e.*, $\Phi < 25.24°$). Figures 6.15(b) and 6.15(c) show a similar trend for the normal and coslip factors as well; there are Σ3 ATGB inclination angles for which *NF* and *PF* are greater in Crystal 2 than Crystal 1. Consequently, neither the Schmid or non-Schmid factors are useful as a criterion to predict the lattice in which the partial dislocation nucleates. However, the Schmid factor can be used to predict which slip system the dislocation nucleates on, once the crystal is known in which nucleation occurs.

### 6.6.2 Interface stress model

Figure 6.16(a) compares the stress required for dislocation nucleation in Cu Σ3 ATGBs at 300 K with the stress required in Cu single crystals. The Cu single crystals are oriented the same as Crystal 1. The single crystal stress values are calculated using the single crystal maximum tensile stress values required for dislocation nucleation in the 300 K atomistic simulations of Spearot and colleagues [64]. A cubic spline was used to interpolate stress values at intermediate misorientation angles; the data and the cubic spline fit is shown in Fig. 6.16(b). The single crystal stresses represent the *homogeneous* nucleation of dislocations in a defect-free lattice. Therefore, the stress required for *heterogenous* dislocation nucleation from ATGBs should be less than or equal to the crystal with the lowest stress value. First, notice the good agreement between the single crystal and ATGB stress values for low inclination angles ($\Phi \leq 35.26°$). Recall that the low inclination ATGB mechanism shows that the dislocation nucleates on a slip plane different from the plane of dissociation. Interestingly, this phenomenon requires stresses near the level required for homogeneous

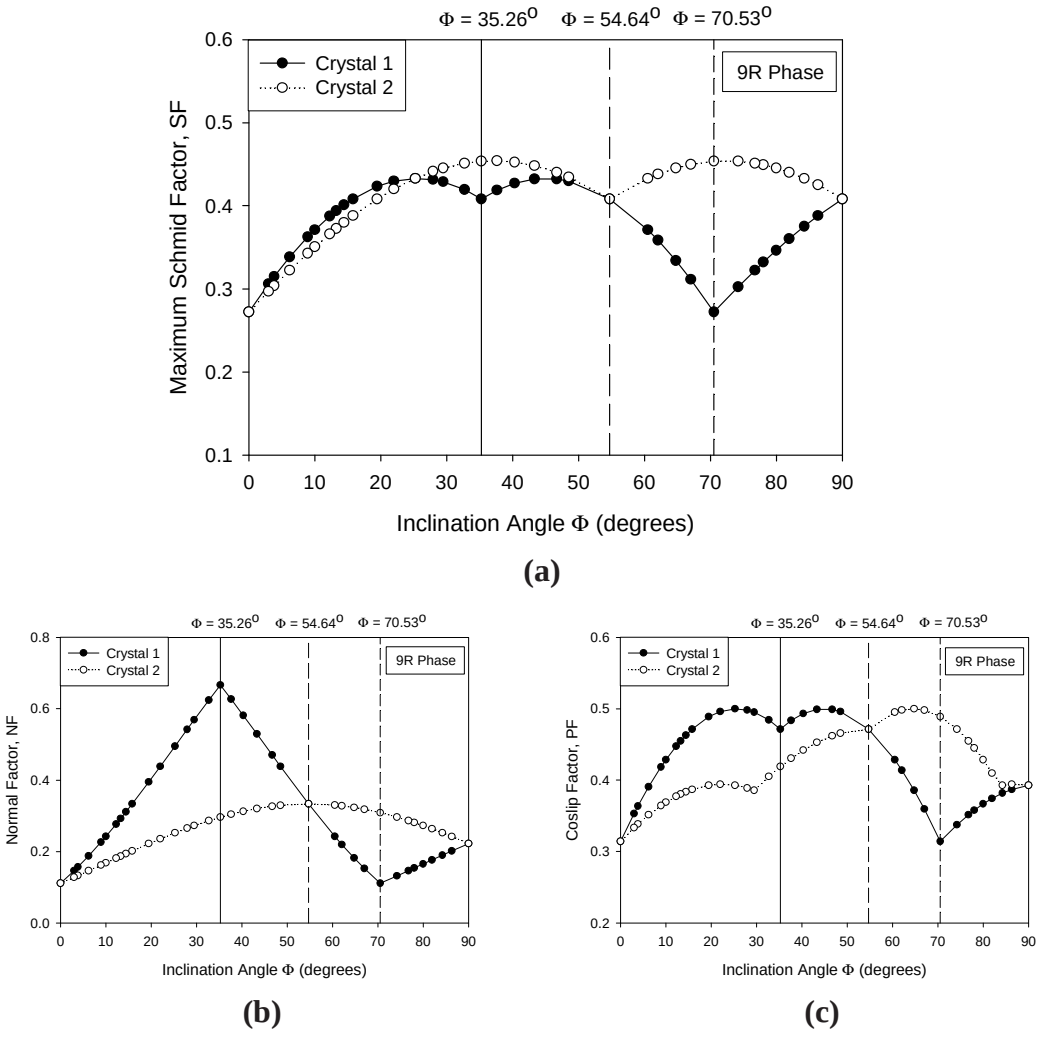


**Figure 6.15:** Change in the (a) Schmid factor $SF$, (b) Normal Factor $NF$, and (c) Coslip Factor $PF$ as a function of grain boundary inclination angle for both Crystal 1 and Crystal 2. These curves are identical for Cu and Al. The 9R phase is only observed in Cu.

nucleation in Crystal 1. Second, the stress required for nucleation in all other ATGBs ($\Phi \geq 43.31°$) is much lower than the stress required for homogeneous nucleation. This difference has been captured in STGBs by considering GB characteristics, such as free volume [64].

The difference between stress values required for *homogeneous* (single crystal) and *heterogeneous* (bicrystal) dislocation nucleation at higher inclination angles in Fig. 6.16(a) may be due to a number of factors; GB free volume and GB faceting are investigated in the current study. First, the initial GB free volume may account for lower stresses required for dislocation emission from the GB. Figure 6.17 uses a grid-based free volume measure $f_1^*$ and a normalized free volume measure $D_c^*$ based on the coordination number (CN) [1] to calculate the change in the free volume as a function of inclination angle for 25 Σ3 ATGBs. The free volume displays a linear trend between the CTB and the SITB for Σ3 ATGBs. This is in agreement with the calculated structural unit images, which show that all Σ3 ATGBs facet into CTB and SITB facets with their respective structural units [260]. The free volume contribution is mainly associated with the C SU for these boundaries. Additionally, the GB ledge density (number of facet intersections) shown in Fig. 6.5 may help to explain the lower stress required for dislocation nucleation. Notice that the number of ledges increase with inclination angle until $\Phi = 70.53°$, at which point the ledge density decreases. Furthermore, since deformation is associated with the D structural unit of the SITB facet, the density of these partial dislocations per unit length is seen to increase with inclination angle over the entire range of ATGBs investigated. However, linear correlations to either the free volume (Fig. 6.17) or GB ledge density (Fig. 6.5) are not able to capture this difference; it may require more complicated nonlinear forms.

In addition to the free volume and faceting of ATGBs, the inclination of the facets with respect to the mean boundary plane may play a role in the decreased stresses required for heterogeneous nucleation of dislocations. As the inclination angle increases (decreases), a higher fraction of the uniaxial stress will resolve into a shear stress component on the

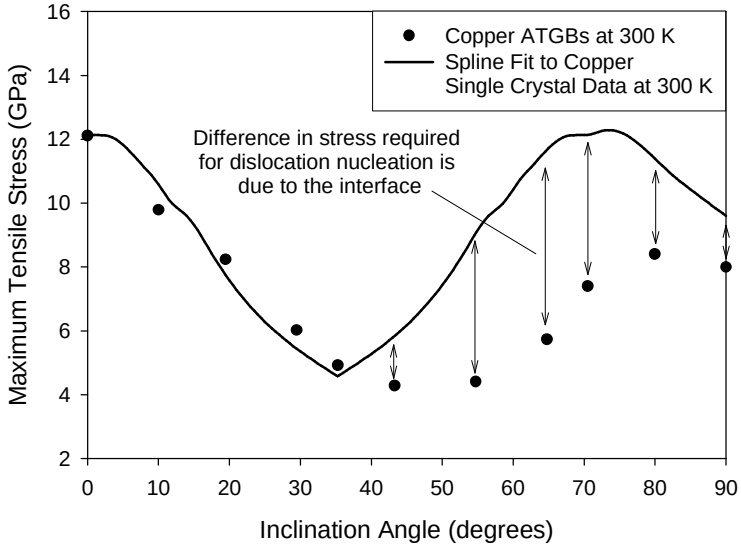


**(a)**

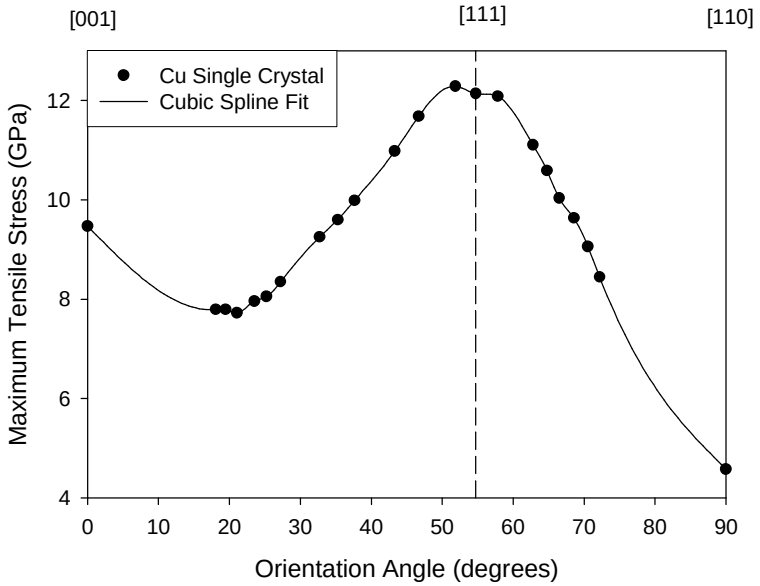


**(b)**

**Figure 6.16:** (a) Comparison between the stress required for dislocation nucleation in Σ3 asymmetric tilt boundaries and single crystals for Cu at 300 K. The difference between the two curves is due to the presence of the interface in the asymmetric boundaries. The single crystal curve in (a) is generated from (b) a cubic spline fit to Cu single crystal data at 300 K [64].

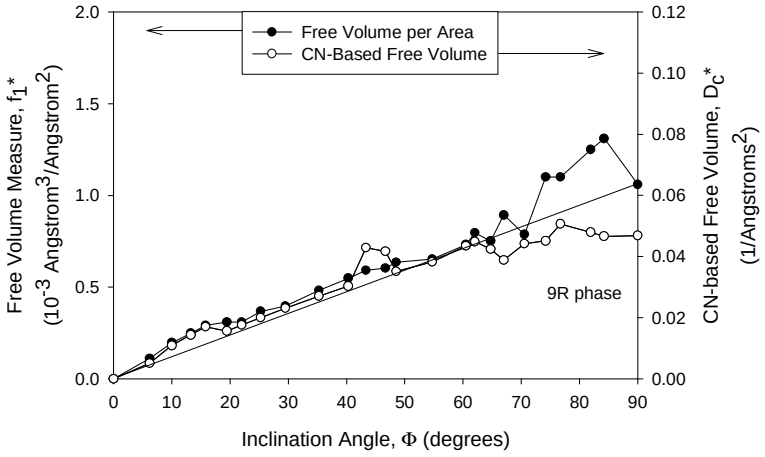


**Figure 6.17:** Free volume as a function of inclination angle for Σ3 asymmetric tilt grain boundaries in Cu. The two free volume measures used display the same linear trend with respect to the free volume, although a scaling factor is required due to the different units. The coordination number (CN) approach is based on a modification from Spearot *et al*. [1].

CTB (SITB) facets. At $\Phi = 45°$, the uniaxial tensile stress resolves equally normal to the facets (tensile) and perpendicular to the facets (shear). Furthermore, the CTB and SITB facets will likely behave differently with respect to the applied shear; *e.g.*, the CTB deforms by twin migration under shear while many other boundaries deform via GB shuffling and partial dislocation nucleation [72]. Moreover, Sansoz and Molinari [71] show that the Σ9 (221) STGB is about 4.5 times weaker in shear than in tension for Cu. Consequently, the inclination of the facets with respect to the mean boundary plane should result in an increased shear component, resulting in a lower tensile stress perpendicular to the mean boundary plane required for dislocation nucleation.

## *6.7 Summary*

In this chapter, atomistic simulations were used to model the nucleation of partial dislocations from Σ3 asymmetric tilt grain boundaries in Cu and Al that exhibited both a faceted and dissociated structure. A total of 11 Σ3 boundaries of varying inclination angle from the coherent twin boundary were considered at temperatures of 10 K and 300 K for Cu and Al. Using an energy minimization procedure, the minimum energy structures and energies

were obtained for the asymmetric boundaries. The calculated grain boundary energies obtained in this work are comparable to previous calculated and experimental energies [158]. The structures show that $\Sigma 3$ asymmetric boundaries facet into coherent twin and incoherent twin boundary facets; likewise, these boundaries contain the structural units associated with these two symmetric tilt boundaries [260]. The intersections of these two facets can be considered as grain boundary ledges or steps and their density can be calculated accordingly. Results show that the mechanical response up to dislocation nucleation for the bicrystal configurations varies significantly as a function of the boundary plane inclination angle. The mechanisms for dislocation nucleation in Cu asymmetric boundaries are decomposed into three regimes with distinctly different behaviors: low ($\Phi \leq 35.26°$), intermediate ($35.26° < \Phi < 70.53°$), and high ($\Phi \leq 70.53°$) inclination angles. Last, preferential dislocation nucleation is observed for $\Sigma 3$ asymmetric tilt grain boundaries, whereby dislocations are only emitted into one of the adjoining crystals from the boundary. For citation of the work contained in this chapter, the reader is referred to Ref. [77].

# CHAPTER VII

# ATOMISTIC SIMULATIONS OF DISLOCATION NUCLEATION IN COPPER GRAIN BOUNDARIES UNDER UNIAXIAL TENSION AND COMPRESSION

Atomistic simulations are used to investigate how grain boundary structure influences dislocation nucleation under uniaxial tension and compression for a specific class of symmetric tilt grain boundaries that contain the E structural unit. After obtaining the minimum energy grain boundary structure, molecular dynamics was employed based on an embedded-atom method potential for Cu at 10 K. Results show several differences in dislocation nucleation with respect to uniaxial tension and compression. First, the average nucleation stress for all ⟨110⟩ STGBs is over three times greater in compression than in tension for both the high strain rate and quasistatic simulations. Second, partial dislocations nucleate from the boundary on the {111} slip plane under uniaxial tension. However, partial and full dislocations nucleate from the boundary on the {100} and {111} slip planes under uniaxial compression. The full dislocation nucleation on the {100} for boundaries with misorientations near the coherent twin boundary is explained through the higher resolved shear stress on the {100} plane compared to the {111} plane. Last, individual dislocation nucleation mechanisms under uniaxial tension and compression are analyzed. For the vicinal twin boundary under tension, the grain boundary partial dislocation is emitted into the lattice on the same {111} plane that it dissociated onto. For compression of the vicinal twin, the 1/3⟨111⟩ disconnection is removed through full dislocation emission on the {100} plane and partial dislocation emission parallel to the coherent twin boundary plane, restoring the boundary to the coherent twin. For the Σ19 boundary, the nearly simultaneous emission of numerous partial dislocations from the boundary result in the formation of the HCP phase.

## *7.1 Introduction*

Much of the recent scientific interest in nanocrystalline materials has regarded the improved functional and mechanical properties as well as the atomic-level mechanisms of plastic deformation in the grain boundaries [9, 10, 13, 14, 16, 18, 19, 21, 24]. In particular, small grain sizes (on the order of 10 nanometers) result in the heterogeneous nucleation and emission of dislocations from the grain boundaries. These deformation mechanisms are confirmed with in-situ transmission electron microscopy (HRTEM) experiments, which have shown grain boundaries emitting partial dislocations that form stacking faults and deformation twins in nc Al and Cu [48, 49]. While some insight into the deformation mechanisms of nc materials has been obtained from in situ HRTEM experiments [20, 48, 49], these experiments are often very difficult to perform. In many cases, atomic simulations of plasticity phenomena actually preceded the experimental observation of the same phenomena. For example, Yamakov and coworkers predicted deformation twinning in aluminum with molecular dynamics simulations [25, 50] prior to the experimental TEM evidence of deformation twinning in nanocrystalline aluminum by Chen and colleagues [10]. The good agreement between calculated and experimentally observed deformation mechanisms motivates using atomistic simulations to examine deformation mechanisms at the nanoscale, as experiments at this scale are often difficult to perform.

Recently, experiments have used nanoindentation techniques (*i.e.*, compression) to test mechanical behavior in materials with small volumes. Uniaxial compression experiments have primarily been used at smaller scales since they do not require gripping the specimen, as with uniaxial tension tests. For example, recent experiments [261–265] have used focused ion beam (FIB) milling to machine a cylindrical column that remains attached to the bulk substrate at one end. After fabricating the columns, a nanoindentor with a flat tip is used to test the plastic response of the column under uniaxial compression. These results have suggested that dislocation nucleation is the rate limiting process at small volumes, **not** dislocation motion. However, there still remain questions about the differences in response

between tension and compression. For example, are there differences in the nucleation stresses for dislocation nucleation between tension and compression? Are there differences in the dislocation nucleation mechanisms? Do dislocations nucleate on the {111} slip plane of maximum resolved shear stress? These research questions provide the motivation for the current work.

As previously mentioned, atomistic simulations can be used to probe the differences in mechanical behavior and mechanisms between tension and compression. Prior literature has focused very little on the effect of uniaxial loading (tension vs. compression) in materials with small volumes. In one recent example, Tschopp and McDowell [80] used atomistic simulations to show an asymmetry in the stress required for homogeneous dislocation nucleation under an applied uniaxial tensile and compressive load. These simulations are applicable to *nucleation* of dislocations in perfect single crystals with no initial dislocation content. For some loading axis orientations, a higher nucleation stress is required in uniaxial compression than tension, and vice versa for other loading axis orientations. This work suggests that the resolved stress normal to the maximum Schmid factor slip plane (on which the dislocation nucleates) may be important for dislocation nucleation. But it is still not known how interfaces affect the nucleation stress asymmetry or the dislocation nucleation mechanisms from grain boundaries. Simulations examining this area may provide insight into the plasticity of nanocrystalline metals and materials at small volumes, such as in the aforementioned FIB machined nano-columns.

To address these questions, nine ⟨110⟩ symmetric tilt grain boundaries with the E structural unit were deformed under uniaxial tension and uniaxial compression applied perpendicular to the boundary until the dislocation nucleation event. To the author's knowledge, this is the first work to investigate the differences in dislocation nucleation from specific grain boundaries under tension and compression. Additionally, this work will compare dislocation nucleation via an applied strain rate with a quasistatic incremental approach. Last, the mechanisms of dislocation nucleation are compared between tension and compression

for a few select boundaries. In low stacking fault energy copper, partial dislocations emit from the grain boundary during tension and full dislocations emit during compression. The slip plane that dislocations nucleate on may be different in tension and compression as well. This highlights the important nature of the resolved stress normal to the dislocation nucleation slip plane. Also, the grain boundary structure (more specifically, the dislocation content and organization within the grain boundary) plays an important role in the dislocation nucleation and emission process.

## *7.2 Methodology*

The grain boundary structures are identical to those described by Tschopp *et al.* [82], and were obtained using a similar methodology to that used for asymmetric tilt grain boundaries in the $\Sigma 3$ system [78] and the $\Sigma 5/\Sigma 9/\Sigma 11/\Sigma 13$ systems [79]. After obtaining the structures with molecular statics (energy minimization), the structures are deformed with a parallel molecular dynamics code (Warp [69]) that incorporates domain decomposition. First, the configuration is equilibrated using MD in the isobaric-isothermal (NPT) ensemble [95] at a pressure of 0 bar and a temperature of 10 K for 10,000 timesteps ($\Delta t$ = 1 fs). Next, the configuration is uniaxially deformed using a constant strain rate of $10^9$ $s^{-1}$ applied perpendicular to the boundary while controlling the lateral boundary motion using a zero stress condition governed by the NPT equations of motion augmented by an additional dampening term, as in Spearot *et al*. [64, 97, 139]. For mechanical properties, the system stress is calculated using the virial definition without the kinetic portion as described in Chapter 2. The stress required for dislocation nucleation is defined as the maximum uniaxial stress. Using Visual Molecular Dynamics (VMD [266]), the centrosymmetry parameter [106] showed that dislocations nucleate at a displacement very close to the maximum tensile stress for all boundaries. The embedded atom method potential for Cu [124] is employed in this study, as stated in Chapter 2. Copper is an ideal FCC material that exhibits weak bond directionality [143], admitting accurate characterization by the non-directional

**Table 7.1:** The misorientation angles, GB plane normal, dimensions, and number of atoms for the nine STGBs in this study.

| Misorientation Angle | CSL Designation & GB Plane Normal | X/Y/Z Dimensions (nm) | Number of Atoms |
|---|---|---|---|
| 114.5° | $\Sigma 171\,(11, 11, 10)$ | 18.91/20.06/16.36 | 1,044,736 |
| 126.4° | $\Sigma 123\,(775)$ | 17.01/20.05/16.36 | 944,640 |
| 129.5° | $\Sigma 11\,(332)$ | 16.79/16.96/16.36 | 786,688 |
| 131.5° | $\Sigma 291\,(11, 11, 7)$ | 17.44/18.50/16.36 | 890,880 |
| 141.1° | $\Sigma 9\,(221)$ | 16.87/16.27/16.36 | 757,504 |
| 144.4° | $\Sigma 267\,(11, 11, 5)$ | 16.71/17.72/16.36 | 818,176 |
| 153.5° | $\Sigma 19\,(331)$ | 17.83/17.33/16.36 | 851,968 |
| 160.0° | $\Sigma 33\,(441)$ | 17.62/16.61/16.36 | 809,472 |
| 169.9° | $\Sigma 129\,(881)$ | 17.42/16.42/16.36 | 789,504 |

nature of the embedded-atom method.

The nine ⟨110⟩ symmetric tilt grain boundaries selected for this study are listed in Table 7.1. Symmetric tilt grain boundaries are typically represented by a misorientation angle/axis combination [153], *i.e.*, the misorientation axis is the ⟨110⟩ axis for all boundaries and the misorientation angle for each boundary is given in Table 7.1. The coincident site lattice (CSL) Σ notation and a grain boundary normal in one of the adjoining lattices are listed, as these are also commonly used to refer to these boundaries. A 3D periodic bicrystal computational cell was used to investigate dislocation nucleation in grain boundaries with the E structural unit. Cell dimensions were chosen to properly enforce the 3D periodic boundary conditions for each orientation, with a minimum length of 16 nm in all directions. This length is chosen to minimize both the effect of periodic boundaries on dislocation nucleation and the number of atoms in the system for computational efficiency. A minimum length of 16 nm or smaller has been employed in previous studies [64, 77, 97, 139], which have found that these cell dimensions are sufficiently large to avoid significant effects of periodic boundaries on the 3D dislocation nucleation dynamics. Table 7.1 lists the initial simulation cell dimensions along with the resulting number of atoms.

A quasistatic approach was also used to deform the bicrystal grain boundary configurations. This approach confirmed that the present results were not significantly influenced by

the large strain rates ($10^9$) used. The quasistatic approach alternated increments of strain and equilibration to achieve deformation that was essentially uninfluenced by the strain rate of the simulations. First, the bicrystal configuration was deformed by a specified strain increment. Then, the configuration is equilibrated at the temperature of interest for 2 ps with a timestep of 1 fs (*i.e.*, 2,000 timesteps). During the equilibration step, the boundary in the loading direction is held fixed and the lateral boundaries are allowed to relax to zero stress through the NPT equations of motion [95]. This approach has been used in non-periodic nanowires [267] and 3D periodic nanocrystalline materials [152] to counter the effects of the high strain rate. However, Leach *et al.* [267] have shown that a quasistatic approach may not show results that differ too far from a high strain rate. This quasistatic approach is investigated for these bicrystal configurations as the results are also relevant to former studies of dislocation nucleation from symmetric and asymmetric tilt grain boundaries [64, 77, 97, 139]. The quasistatic approach was used for five STGBs: three low order CSL boundaries (Σ9, Σ11, and Σ19), the vicinal twin boundary (Σ171), and the low angle boundary vicinal to the Σ1 (110) single crystal configuration (Σ129). All five boundaries were simulated under both uniaxial tension and compression. The dislocation nucleation mechanisms discussed in Section 7.3.2 used the results from the quasistatic approach.

## *7.3 Atomistic simulation results*

### 7.3.1 Nucleation stress for grain boundary dislocations

Figure 7.1 shows the stress-strain curves for the nine ⟨110⟩ STGBs with the E structural unit under uniaxial tension. The curves are arranged in order of increasing misorientation angle, as defined in Table 7.1, with an artificial spacing of 0.01 strain added to separate the curves. In these curves, the stress is calculated through Eq. 2.8 while the strain is defined as $\epsilon = \delta_h/h$, where $h$ is the initial height of the simulation cell and $\delta_h$ is the conjugate displacement of the overall cell. The solid lines were obtained with a $10^9$ strain rate; the symbols

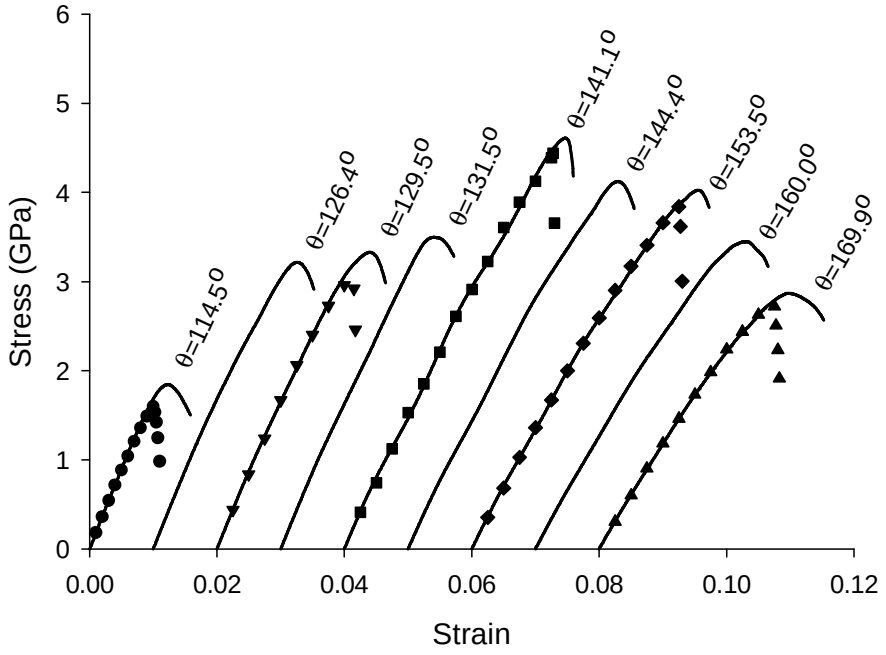


**Figure 7.1:** Stress-strain curves for the symmetric tilt grain boundaries with the E structural unit. The solid line denotes the data obtained with a $10^9$ strain rate and the symbols denote the data obtained with the incremental approach.

were obtained with the incremental quasistatic approach. Interestingly, the stress-strain response is very similar between the $10^9$ strain rate and the quasistatic simulations in terms of elastic stiffness, peak stress and strain corresponding to that stress. It is observed that the quasistatic approach nucleates dislocations at slightly lower stresses, though. Once dislocation nucleation occurs at or near the maximum stress for each grain boundary configuration, the simulations are stopped shortly after this. The stress-strain curves in compression show similar results between the quasistatic and dynamic deformation as well.

Figure 7.2 shows the stress required for dislocation nucleation for the nine $\langle 110 \rangle$ boundaries under an applied uniaxial tensile strain. First, in uniaxial tension, the stress required increases with increasing misorientation angle to the $\Sigma 9\,(221)$ STGB and the stress then decreases with further increases to the misorientation angle. The lowest stresses required for dislocation nucleation occur in grain boundaries with misorientation angles nearest the

$\Sigma 3\,(111)\,\theta = 109.5^\circ$ coherent twin boundary and the $\Sigma 1\,(110)\,\theta = 180^\circ$ perfect lattice. Interestingly, both the $\Sigma 3$ boundary and $\Sigma 1$ single crystal require significantly higher stresses under uniaxial tension (12.4 GPa and 4.6 GPa, respectively). This trend indicates that the presence of the E structural unit, or $a_0/3\,\langle 111\rangle$ disconnection, in a $\langle 110\rangle$ STGB results in a large drop in the nucleation stress. Spearot *et al.* [64] have previously observed this large drop in stress at the $\Sigma 3$ coherent twin boundary, but did not study STGBs with misorientation angles greater than the $\Sigma 9\,(221)$ boundary.

The spacing of the E structural unit plays a definitive role in the nucleation stress under uniaxial tension. The smallest spacing of E structural units is the $\Sigma 9\,(221)\,\theta = 141.1^\circ$ STGB, which is composed of only E structural units. On the other hand, as the misorientation angle approaches either $\Sigma 3\,(111)\,\theta = 109.5^\circ$ coherent twin boundary or the $\Sigma 1\,(110)\,\theta = 180^\circ$ perfect lattice, the spacing between the E structural units increases. Therefore, the nucleation stresses from Fig. 7.2 increase with decreasing spacing between the E structural units.

Figure 7.3 shows the relation between the misorientation angle and the nucleation stress in uniaxial compression. The same correlation between the spacing of the E structural unit and the nucleation stress is not found in compression. In general, the stresses required for dislocation nucleation are greater in compression than in tension. For example, the average nucleation stress for all $\langle 110\rangle$ STGBs is over three times greater in compression than in tension for both the high strain rate (10.8 GPa/3.4 GPa) and quasistatic (9.8 GPa/3.1 GPa) approaches. One potential reason is that the resolved stress normal to the slip system on which the dislocation nucleates is compressive in compression and tensile in tension. Spearot *et al.* [64] and Tschopp *et al.* [81] have found that the resolved stress normal to the slip plane that the dislocation nucleates on is important for dislocation nucleation in single crystal Cu. The compressive resolved normal stress increases the difficulty to nucleate dislocations from the grain boundary.

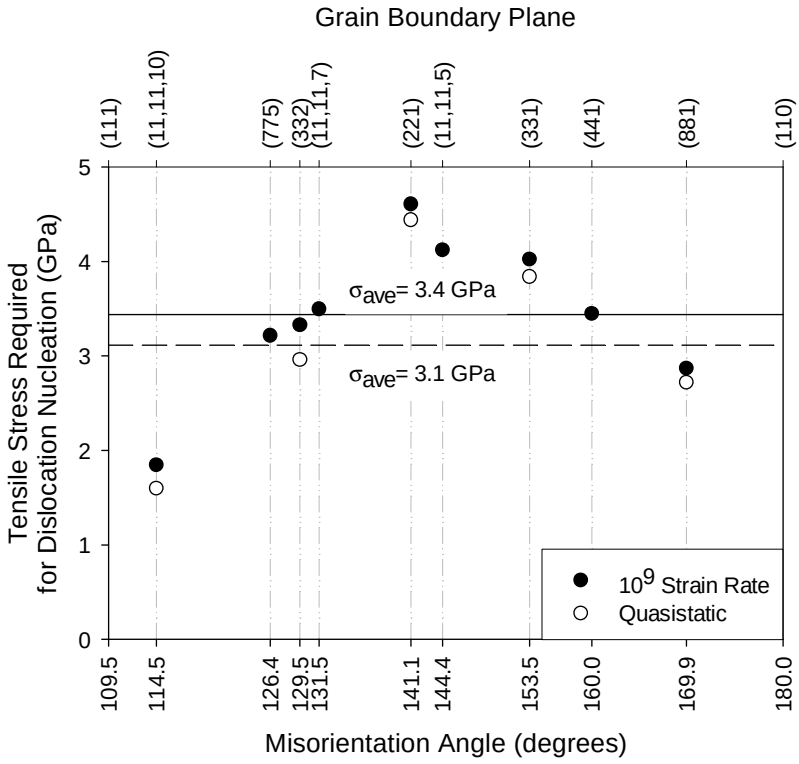


**Figure 7.2:** Stress required for dislocation nucleation for the nine symmetric tilt grain boundaries with the E structural unit in uniaxial tension. The black and dotted horizontal lines represent the average nucleation stress for all STGBs using the $10^9$ strain rate and the quasistatic approach, respectively.

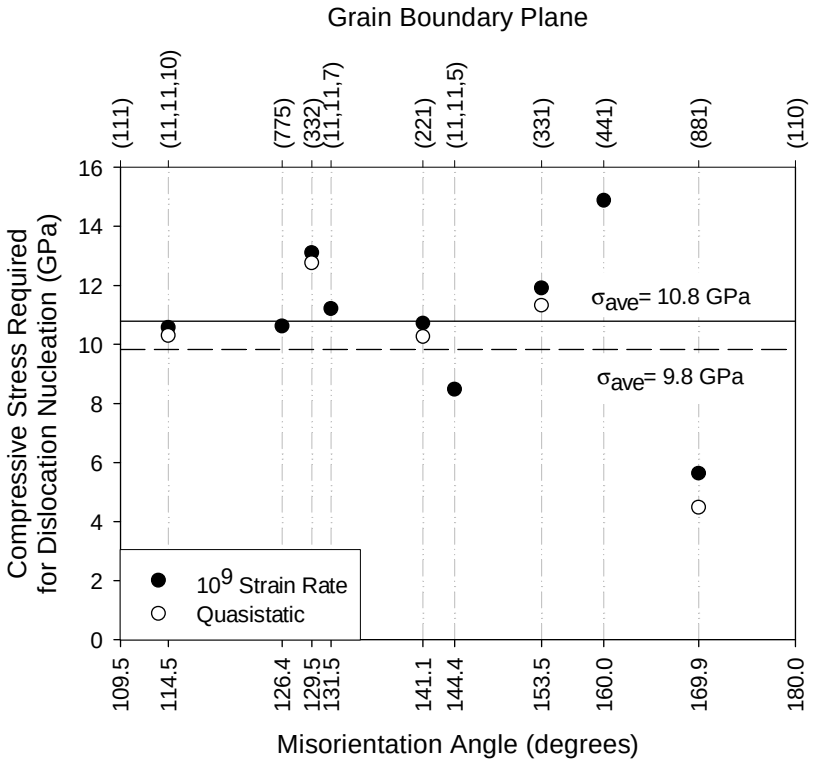


**Figure 7.3:** Stress required for dislocation nucleation for the nine symmetric tilt grain boundaries with the E structural unit in uniaxial compression.

### 7.3.2 Tension-compression asymmetry in dislocation nucleation

The dislocation nucleation mechanism for five ⟨110⟩ symmetric tilt grain boundaries is presented in this subsection. Prior to examining dislocation nucleation, the grain boundary structures will be briefly discussed. Figure 7.4 shows the structure of the four STGBs deformed in uniaxial tension and compression with the quasistatic methodology. The structure of the grain boundary is characterized by structural units (SUs), similar to previous studies [90, 148]. Structural units essentially represent the dislocation or disclination content of the boundary. The $\Sigma 9\,(221)\,\theta = 141.1^\circ$ STGB (not shown) is the favored boundary within this misorientation range and contains only E structural units. The $\Sigma 11\,(332)\,\theta = 129.5^\circ$ and $\Sigma 19\,(331)\,\theta = 153.5^\circ$ STGBs contain either an identical ratio of D:E SUs (for the Σ11 GB) or A:E SUs (for the Σ19 GB). The $\Sigma 171\,(11, 11, 10)\,\theta = 114.5^\circ$ STGB is *vicinal* to the $\Sigma 3\,(111)$ coherent twin boundary and the $\Sigma 129\,(881)\,\theta = 169.9^\circ$ is a low angle boundary near the $\Sigma 1\,(110)$ perfect crystal. For both boundaries, the grain boundary structure is altered as the number of E structural units per unit boundary length decreases; an intrinsic stacking fault (ISF) dissociates from the E structural unit in the Σ171 GB and the E structural unit elongates and becomes centered in the Σ129 GB. Tschopp *et al.* [82] provide further details on how the structure and free volume of STGBs with the E structural unit evolve as a function of the misorientation angle.

Figure 7.5 shows orthonormal two-dimensional images from the three-dimensional simulation cells of the five boundaries just after dislocation nucleation in uniaxial tension. These images are viewed along the $\left[1\bar{1}0\right]$ direction and only atoms in a non-centrosymmetric environment are rendered using a centrosymmetry threshold of 0.25. This allows visualization of the grain boundary atoms, the nucleated dislocations, and the stacking faults within the simulation cell. Only one boundary is shown for each simulation cell. In the lower right hand corner, the two slip planes with normal components orthogonal to the $\left[1\bar{1}0\right]$ tilt axis are shown in each crystal for the Σ19 GB. The solid lines indicate the {111} slip planes with the maximum Schmid factor slip systems in each crystal; the dotted

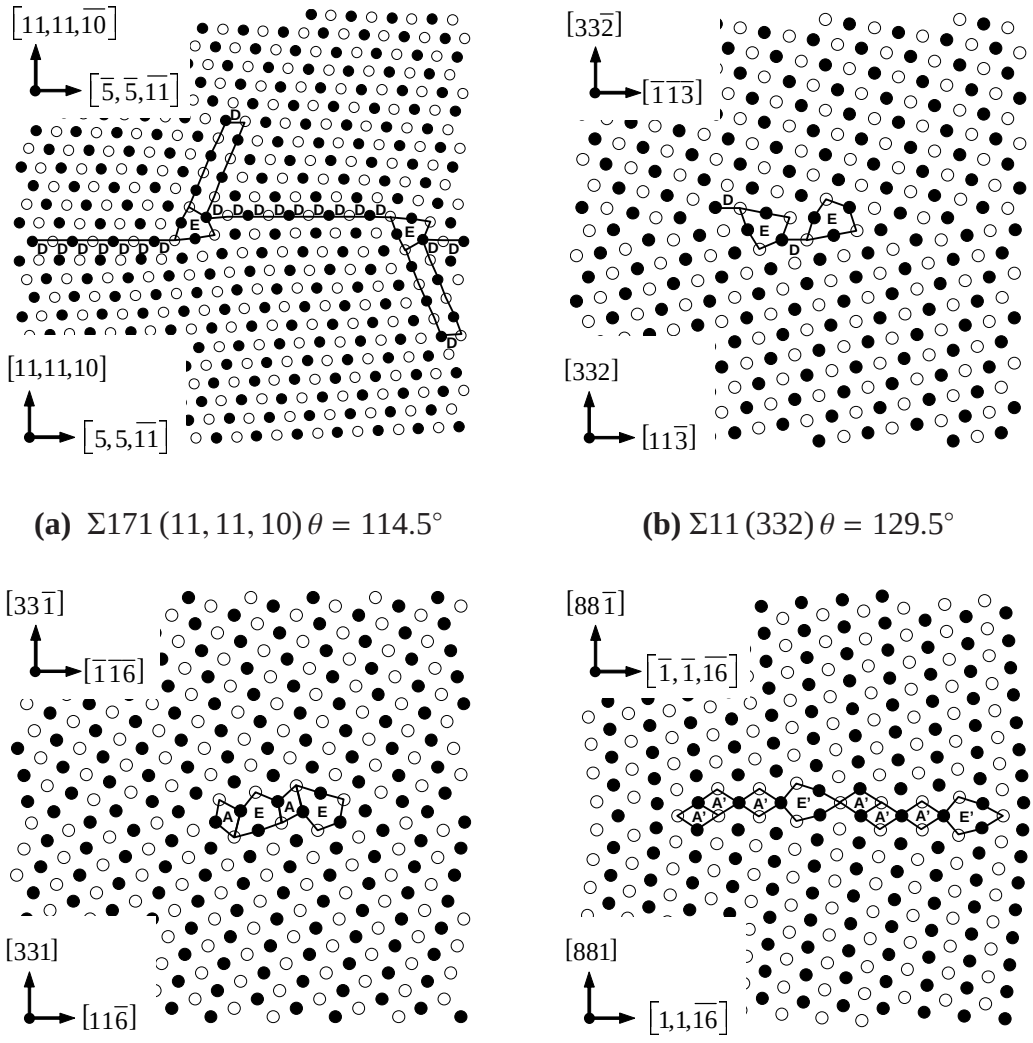


**(a)** $\Sigma 171\,(11,11,10)\,\theta = 114.5°$ **(b)** $\Sigma 11\,(332)\,\theta = 129.5°$

**(c)** $\Sigma 19\,(331)\,\theta = 153.5°$ **(d)** $\Sigma 129\,(881)\,\theta = 169.9°$

**Figure 7.4:** Structural unit description for four symmetric tilt grain boundaries with the E structural unit that are investigated for dislocation nucleation: the $\Sigma 171\,(11,11,10)\,\theta = 114.5°$ GB, the $\Sigma 11\,(332)\,\theta = 129.5°$ GB, the $\Sigma 19\,(331)\,\theta = 153.5°$ GB, and the $\Sigma 129\,(881)\,\theta = 169.9°$ GB. The structures are viewed along the $\left[1\bar{1}0\right]$ tilt axis with atoms on consecutive $\left(2\bar{2}0\right)$ planes shown as black and white. The $\Sigma 9\,(221)\,\theta = 141.1°$ GB, composed of all E structural units, is not shown.

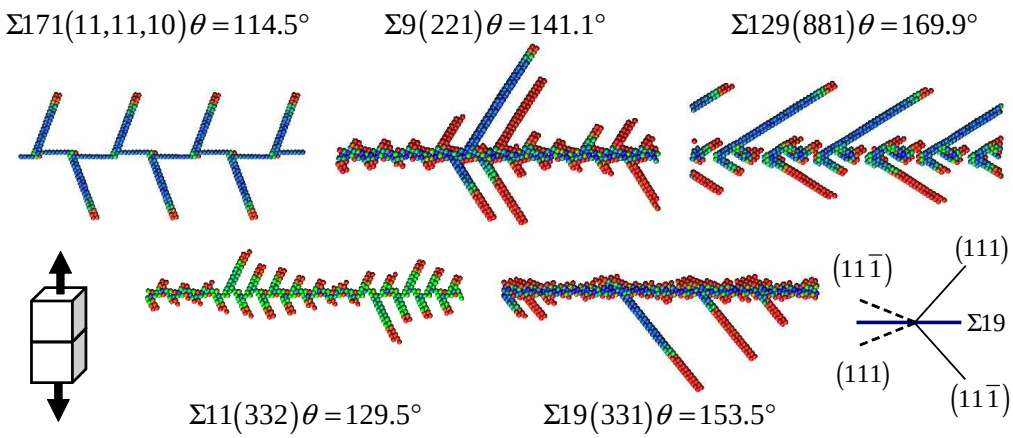


**Figure 7.5:** Dislocation nucleation at five symmetric tilt grain boundaries with the E structural unit under a uniaxial tensile load applied perpendicular to the boundary.

lines indicate the {111} slip planes with a lower resolved shear stress in the slip direction. Only partial dislocations are nucleated from all five boundaries and an intrinsic stacking fault trails the emitted dislocation; no trailing partial dislocation is observed in tension. Moreover, all partial dislocations are nucleated and emitted on the {111} plane with the maximum resolved shear stresses in the slip direction, *i.e.*, the maximum Schmid factors. Since these boundaries are symmetric about the boundary plane, the maximum Schmid factors in both crystal lattices adjoining the boundary are identical. By comparing the Σ171 and the Σ11 boundaries, it can be seen that the spacing between grain boundary dislocations plays a role in their emission from the boundary. For the Σ171 boundary, the large spacing between dislocations results in independent emission events for each grain boundary dislocation, *i.e.*, the nearly identical emission of each dislocation indicates that the individual dislocations are relatively unaffected by the emission of other dislocations. On the other hand, the Σ11 GB has a much smaller spacing between dislocations. The dislocation interactions in this boundary result in the emission of a particular dislocation depending on nearby dislocations and their impact on the local stress state. Spearot *et al.* [139] have also shown that the spacing of certain structural units (GB dislocations) can affect dislocation nucleation.

Figure 7.6 is rendered the same as Figure 7.5 and shows images of the five boundaries just after dislocation nucleation in uniaxial compression. A number of differences are immediately noticeable. First, while nucleation of the leading partial dislocation is often observed in copper, the trailing partial dislocation is also nucleated from most boundaries; an intrinsic stacking fault separates the two $\{111\}\langle 112\rangle$ partial dislocations. The emission of full dislocations is obvious in the $\Sigma 171$ STGB. The circles denote the emission of full dislocations from the $\Sigma 9$ and $\Sigma 129$ GBs as well as just prior to the emission of the trailing partial in the $\Sigma 11$ GB. The $\Sigma 19$ is the only boundary in which full dislocations were not observed. Also notice that when the leading partial dislocation is initially nucleated from the boundary, the intrinsic stacking fault is much larger than after the trailing partial is emitted and the two partials glide away from the boundary. Second, the partial (and full) dislocations are not necessarily nucleated and emitted on the $\{111\}$ plane with the maximum resolved shear stresses in the slip direction, as in uniaxial tension. While dislocation nucleation occurs on the maximum Schmid factor slip system for the $\Sigma 9$ and $\Sigma 19$ boundaries, the $\Sigma 129$ emitted partial and full dislocations on the $\{111\}$ plane with a slightly lower resolved shear stress ($SF = 0.377$ on this plane compared to a Schmid factor of $SF = 0.427$ on the other $\{111\}$ slip plane). Interestingly, the $\Sigma 171$ and $\Sigma 11$ boundaries emit partial and full dislocations on the $\{100\}$ slip plane under uniaxial compression; this will be discussed later.

For the sake of brevity, a detailed look at dislocation nucleation from the $\Sigma 171$ STGB will be discussed for the uniaxial tension and compression simulations. The $\Sigma 171$ GB presents an interesting case because it is a vicinal twin boundary with mirror image $a_0/3\langle 111\rangle$ disconnections that result in a symmetric interface [79]. This boundary also shows emission on the $\{100\}$ slip plane. The dislocation reactions associated with the twin boundary are of particular interest as the coherent twin plays an important role in low stacking fault energy FCC metals. For instance, grain boundary engineering [75] manipulates the grain boundary character distribution to increase the number of boundaries with beneficial properties and decrease the frequency of boundaries with detrimental properties.

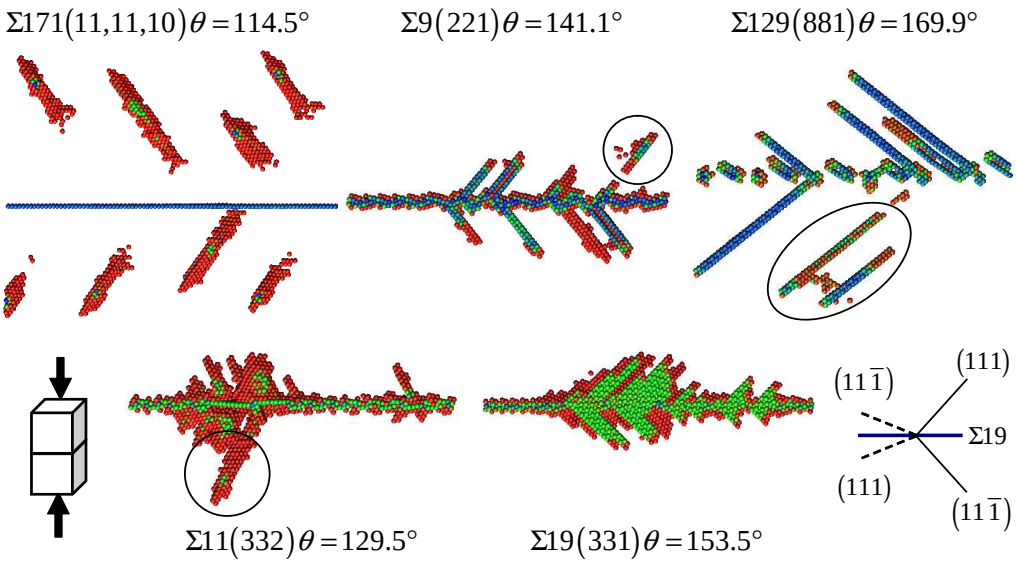


**Figure 7.6:** Dislocation nucleation at five symmetric tilt grain boundaries with the E structural unit under a uniaxial compressive load applied perpendicular to the boundary.

Much of the focus of grain boundary engineering has been on increasing the frequency of the Σ3 coherent twin boundary [66, 67]; this may increase the fraction of vicinal twin boundaries as well. In addition, introducing nanoscale growth twins into ultrafine-grain polycrystals has improved the hardness and flow stress by introducing barriers to dislocation motion [13, 174]. It is anticipated that increasing the distribution of Σ3 coherent twin boundaries will also result in a larger distribution of boundaries vicinal to the coherent twin. Also, dislocation motion and transmission as a function of strain may result in the creation of $a_0/3\langle 111\rangle$ disconnections within the coherent twin boundaries. A second boundary is the Σ19 boundary in uniaxial compression, as the emission of partial dislocations appears to form a new phase at the boundary; this will also be examined.

### 7.3.3 Dislocation nucleation at the vicinal Σ171 coherent twin boundary

Figure 7.7 shows partial dislocation nucleation from the Σ171 vicinal coherent twin. The centrosymmetry parameter is used to identify atoms whose local environment is elastically distorted (bulk crystal lattice) from atoms whose local environment is distorted due to lattice defects, or grain boundary structural units. Figure 7.7(a) shows the boundary structure

after equilibration, but prior to application of the uniaxial tensile load normal to the interface. In terms of structural units, the two triangular shaped regions are defined as distorted E (or E" [72, 79]) structural units with a dissociated D structural unit connected by an intrinsic stacking fault (ISF). This triangular region can also be described as the cores of alternating $a_0/3\langle 111\rangle$ twin dislocations, or $a_0/3\langle 111\rangle$ disconnections, which accommodate the $\approx 5^\circ$ misorientation from the coherent twin boundary and provide a symmetric structure. The dissociated D structural unit can equally be represented as an $a_0/6\langle 112\rangle$ Shockley partial dislocation, following the work of Merkle and Rittner [91]. The $a_0/3\langle 111\rangle$ disconnections has been observed experimentally in HRTEM images in Al [249–251] and Au [252]. The dissociation of the Shockley partial dislocation is through a reaction of the type

$$a_0/3\langle 111\rangle \rightarrow a_0/6\langle 112\rangle + a_0/6\langle 110\rangle \tag{7.1}$$

that leaves behind a stair-rod dislocation at the interface. Figure 7.7(b) shows the boundary structure at the maximum tensile stress, which typically corresponds to dislocation nucleation. In the $\Sigma 171$ boundary, the term dislocation emission seems more appropriate than dislocation nucleation since the peak tensile stress corresponds to the release of the dissociated $a_0/6\langle 112\rangle$ Shockley partial dislocation from the grain boundary into the bulk crystal lattice. The trailing partial is not observed, so an intrinsic stacking fault connects the Shockley partial to the $a_0/6\langle 110\rangle$ stair-rod dislocation lock at the boundary. The Shockley partial is emitted on the maximum Schmid factor (111) and $\left(11\bar{1}\right)$ slip planes in the upper and lower crystal, respectively. The movement of atoms on the {111} slip planes in Fig. 7.7(b) corresponds to the resolved shear stress components (black arrows) acting on the two adjoining {111} slip planes; atomic movement in the tilt axis direction corresponds to the $a_0/6\langle 112\rangle$ partial dislocations. The grain boundary acts a perfect source of dislocations, *i.e.*, the Burgers vector content of the grain boundary is merely reduced by the Burgers vector of the emitted partial dislocation, $b_{before} = b_{after} + b_{dislocation}$.

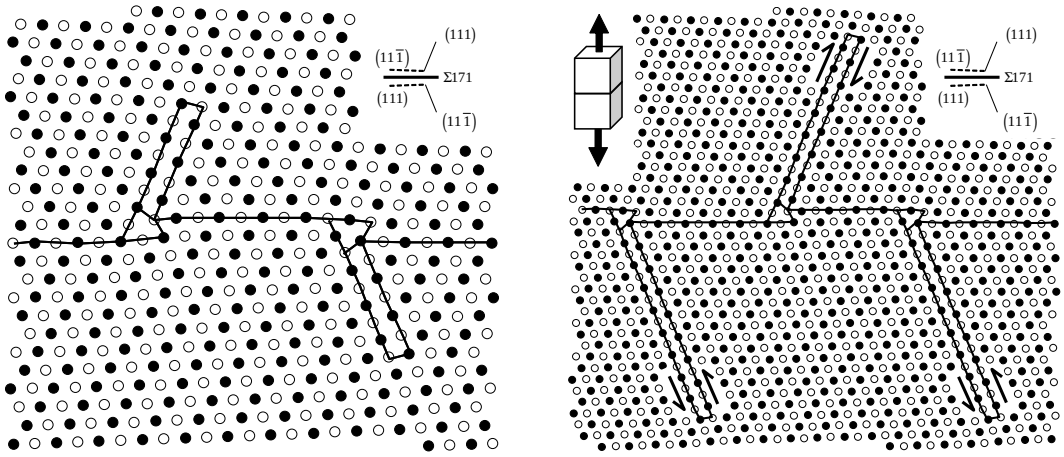


**(a)** **(b)**

**Figure 7.7:** Dislocation emission of a $a_0/6\langle 112\rangle$ Shockley partial dislocation from the $\Sigma 171\,(11, 11, 10)\,\theta = 114.5°$ STGB in Cu under uniaxial tension.

Figure 7.8 shows the evolution of the intrinsic stacking fault length and stress as a function of strain under uniaxial tension. In this plot, the intrinsic stacking fault length is defined in the boundary normal direction based on the atom coordinates of the Shockley partial dislocations on both sides of the two periodic grain boundaries (1 and 2). The partial dislocations were identified with the centrosymmetry parameter. In the undeformed configuration, the intrinsic stacking fault length is approximately 15 Ångstroms from the coherent twin boundary. With increasing elastic strain, the Shockley partial dislocations dissociate further into the bulk crystal lattice, which increases the intrinsic stacking fault length. The peak tensile stress corresponds to dislocation emission and marks a transition in the slopes of the ISF length in Fig. 7.8. Prior to this point, the bulk crystal lattice could dissipate the elastic work without dislocation emission (plasticity). However, at the maximum tensile stress (tensile strain of 1%), the bulk lattice can no longer accommodate the tensile deformation elastically, which enables the emission event.

The dislocation nucleation and emission process is quite different in compression than in tension for the Σ171 STGB vicinal to the coherent twin, as shown in Figs. 7.5 and 7.6. The structure after equilibration is identical to Fig. 7.7(a) with the dissociated $a_0/6\langle 112\rangle$

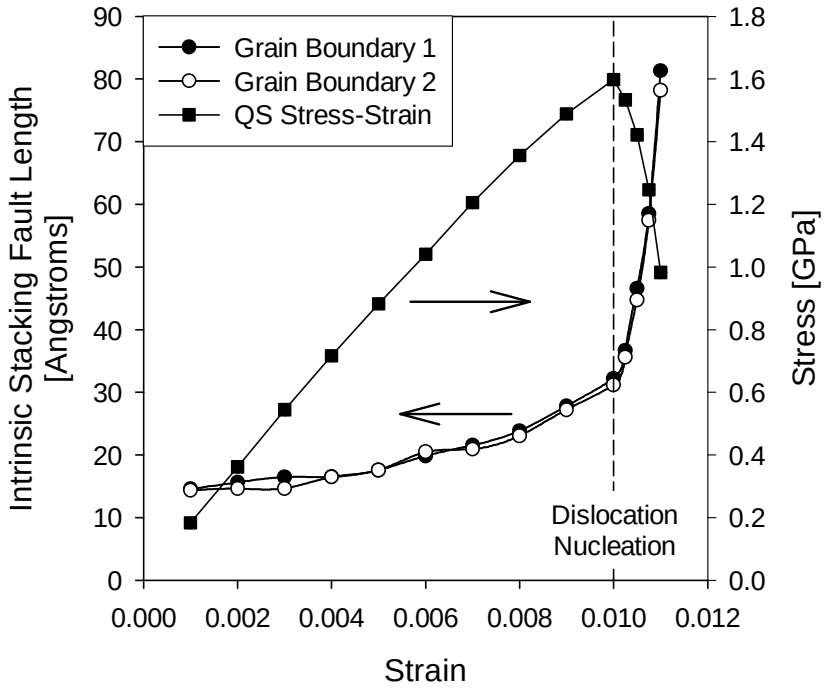


**Figure 7.8:** Intrinsic stacking fault length as a function of tensile strain for the $\Sigma 171\,(11, 11, 10)\,\theta = 114.5°$ STGB in Cu under uniaxial tension.

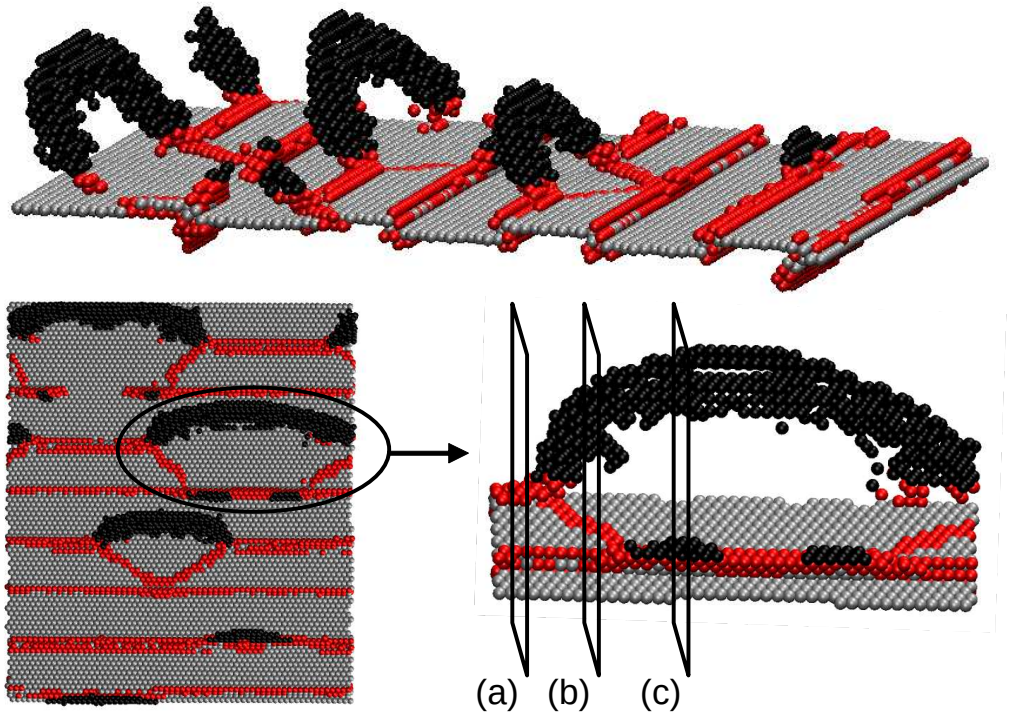


**Figure 7.9:** Dislocation emission of a $a_0/6\langle 110\rangle$ full dislocation on the {001} plane from the $\Sigma 171\,(11, 11, 10)\,\theta = 114.5°$ STGB in Cu under uniaxial compression. Atoms associated with the emitted full dislocation loops and the coherent twin are rendered black and silver, respectively. The remaining atoms along the boundary are rendered red.

Shockley partial and an intrinsic stacking fault. However, tensile deformation applied normal to the interface causes the ISF length to decrease until dislocations are emitted from the $a_0/3\langle 111\rangle$ disconnection at the boundary. Figure 7.9 shows dislocation nucleation at one of the periodic boundaries for the $\Sigma 171$ STGB, where all centrosymmetric atoms are removed. As the full dislocation loops are emitted from the $a_0/3\langle 111\rangle$ disconnection at the boundary, dislocations parallel to the coherent twin boundary plane (red) are also emitted from the $a_0/3\langle 111\rangle$ disconnection. To better interpret the dislocation reactions at the vicinal coherent twin under compression, slices from three locations (a-c, lower right) are analyzed in Fig. 7.10(a)-(c).

Figure 7.10(a) shows that the dissociated Shockley partial dislocations are attracted toward the $a_0/6\langle 110\rangle$ stair-rod dislocation, despite their location on the {111} slip plane

with the maximum resolved shear stress. This is an example of how the dislocation content dictates where the dislocation will nucleate from, not the resolved shear stress. Specifically, the dissociated $a_0/6\langle 112\rangle$ partial dislocation glides in opposite directions in tension and compression because of the interaction between the resolved shear stress on the {111} slip plane and the Burgers vector of the dislocation.

Figure 7.10(b) shows the dislocation loop after emission from one of the $a_0/3\langle 111\rangle$ disconnections. The full dislocation is emitted on the {001} plane and a Burgers circuit identifies that the emitted dislocation is $a_0/2\langle 110\rangle$ dislocation. Unlike dislocations on {111} slip planes in FCC Cu, the dislocation on the {001} causes a highly distorted environment, possibly due to the atypical {001} slip plane. Further explanation regarding dislocation emission on the {001} plane is discussed in Section 7.4. As the dislocation loop is emitted on the {001} plane, a $a_0/6\langle 112\rangle$ Shockley partial dislocation is emitted parallel to the coherent twin boundary plane. Notice that behind the Shockley partial, the $a_0/3\langle 111\rangle$ disconnection is removed and the ordering around the coherent twin boundary is restored. Again, this suggests a reaction like Eq. 7.1, $a_0/3\langle 111\rangle \rightarrow a_0/6\langle 112\rangle + a_0/6\langle 110\rangle$, except where both the Shockley partial and the stair-rod dislocation are emitted from the disconnection. Also notice that the disconnection on the right side of Fig. 7.10(b) is starting to dissociate onto the {001} plane of the lower crystal.

Figure 7.10(c) shows the configuration after the $a_0/6\langle 112\rangle$ Shockley partial dislocation emitted parallel to the interface is absorbed by the $a_0/3\langle 111\rangle$ disconnection on the right. The disconnection now dissociates onto the {111} plane of the upper lattice and the {001} plane of the lower lattice. Figure 7.10(d) shows the emission of a second full dislocation on the {001} plane. Interestingly, the configuration in 7.10(c) could have emitted a dislocation on either the {111} plane or the {001} plane. Since emission on either plane seemed possible, the {001} plane must have a larger driving force for dislocation emission than the {111} plane. The potential influence of resolved stress components on these two slip systems is examined in Section 7.4. While dislocation emission on the {001} plane is unusual,

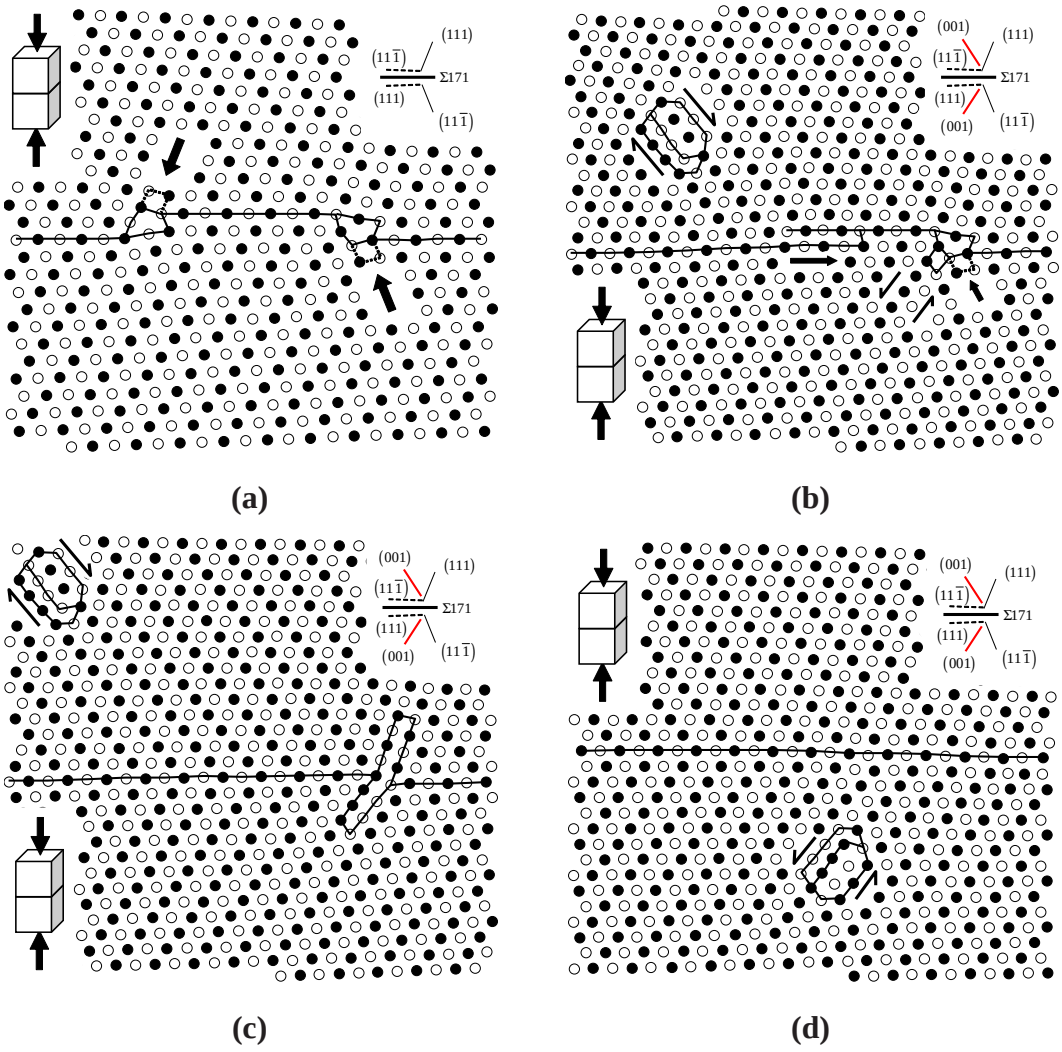


**Figure 7.10:** Dislocation emission of a $a_0/6\langle 110\rangle$ full dislocation from the Σ171 $(11, 11, 10)$ $\theta = 114.5°$ STGB in Cu under uniaxial compression, where atoms on successive {110} planes are colored black and white.

the {100}⟨110⟩ cube slip systems are commonly used to model dislocation behavior at high homologous temperatures and high resolved shear stress in materials such as directionally solidified Ni-base superalloys [268, 269]. Cube slip is most commonly associated with the ⟨111⟩ orientation is these models, in part because of the low resolved shear stress on the {111}⟨110⟩ slip systems near this orientation.

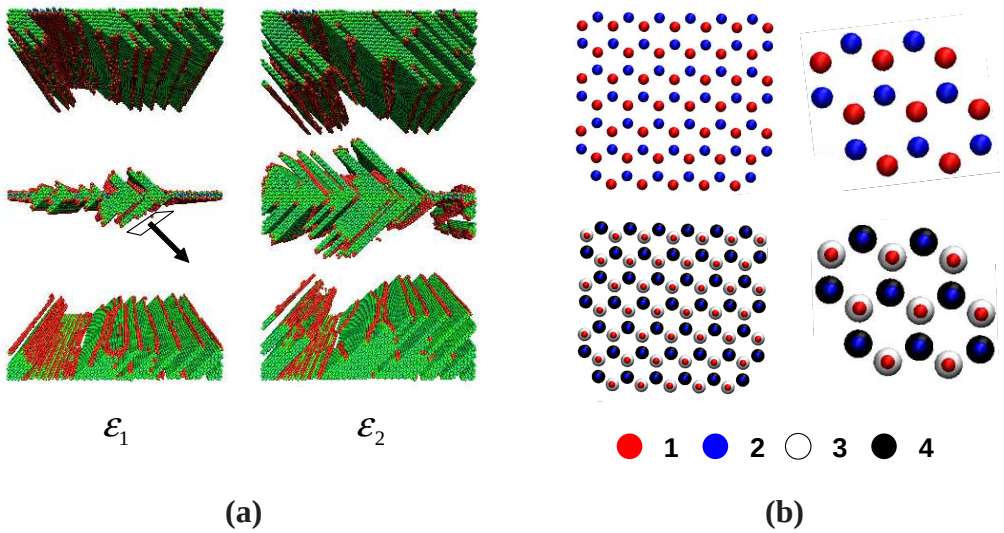


**Figure 7.11:** Dislocation nucleation in the Σ19 symmetric tilt grain boundary in Cu under uniaxial compression. (a) Configurations at two strains, $\epsilon$, after dislocation nucleation has occurred ($\epsilon 1 < \epsilon 2$). (b) Closeup of the stacking arrangement on the {111} slip planes caused by the emission of partial dislocations from the boundary, where atoms on different {111} slip planes are colored differently.

### 7.3.4 Dislocation nucleation at the Σ19 boundary in compression

Figure 7.11 shows dislocation nucleation from the Σ19 (331) grain boundary under uniaxial compression. In the present simulations, one partial dislocation is emitted for every two {111} slip planes intersecting the boundary, leaving behind a stacking fault on every other {111} slip plane, as shown in Fig. 7.11(a) by the green non-centrosymmetric atoms. To analyze the new phase created by the emission of the partial dislocations, Fig. 7.11(b) shows atoms on successive {111} slip planes in this region. The top images show the atoms on two successive {111} slip planes, which is indicative of hexagonal close-packed (HCP) stacking. The bottom images from Fig. 7.11(b) show the atoms on four successive {111} slip planes, where the atom size is decreased on the first two slip planes to facilitate viewing the HCP structure. The atoms on the third (fourth) slip plane correspond to those on the first (second) slip plane, indicating that the HCP phase is created by the emission of partial dislocations under uniaxial compression.

Interestingly, the cooperative emission of partial dislocations from the boundary promotes the formation of the HCP phase in this Cu boundary. To verify that the formation of this phase is not related to the chosen potential, the formulation of the EAM potential must accurately describe the energies of different nonequilibrium structures in Cu. Mishin *et al.* [124] have shown good agreement between the cohesive energies for several nonequilibrium structures (FCC, HCP, 9R, BCC, simple cubic, and diamond) obtained by *ab initio* (local density approximation), tight-binding, and EAM calculations. In fact, Mishin and coworkers [124] state that the agreement is especially good between *ab initio* and their EAM potential for the HCP and 9R structures. The excellent agreement of these energies with *ab initio* calculations helps validate the the HCP structure generated may, in fact, be energetically favorable as a function of compressive deformation in some boundaries. The 9R phase and BCC phase have been experimentally observed at the boundaries by Ernst *et al.* [159, 188] and Schmidt *et al.* [187, 189], respectively. Tschopp *et al.* [77] used atomistic simulations to show expansion of the 9R phase under uniaxial tension with the same Mishin potential. The expansion of the 9R phase has also been observed experimentally in the HRTEM [197], presumably because of the local stress state of the thin foil. These results reinforce that the formation of nonequilibrium crystal structures (9R, HCP, BCC) may be possible at the grain boundary with the appropriate combination of applied loading and grain boundary structure.

## *7.4 Discussion*

The stress required to nucleate dislocations from the ⟨110⟩ STGBs in this study were three times greater in uniaxial compression than tension. The resolved stress components acting upon the slip plane on which the dislocation nucleates may help to explain this difference. Schmid and non-Schmid parameters are often used to describe how the uniaxial tensile or compressive stress projects onto the orthogonal coordinate system located on the active slip system. Following the results of Spearot *et al.* [64], the analysis is restricted to the resolved

shear stress in the slip direction (Schmid factor, $SF$) and the resolved stress normal to the slip plane (normal factor, $NF$). The resolved stress components on the maximum Schmid factor $\{111\}\langle 110\rangle$ slip systems and the $\{001\}\langle 110\rangle$ slip system will be investigated for both uniaxial tension and uniaxial compression.

The affine elastic distortion of the lattice during application of uniaxial stress prior to nucleation is significant in terms of rotation of the slip system and associated co-slip and slip plane normal directions. This work considers how the strain prior to nucleation may influence the resolved stress components in the current (deformed) configuration at the point of nucleation. To do this, the motion of the simulation cell boundaries was used to compute a deformation gradient tensor $\mathbf{F}_{\mathrm{ij}}$, used to map the original orthogonal triad of unit vectors in the slip, co-slip and slip plane normal directions from the undeformed to the deformed configuration. The push-forward transformation

$$d_i^{\alpha *} = \mathbf{F}_{\mathrm{im}} \mathrm{d}_{\mathrm{m}}^{\alpha} \tag{7.2}$$

gives the deformed configuration components $d_i^{\alpha *}$ of these three unit vectors $d^{\alpha}$, $\alpha = 1, 2, 3$ in the initial (undeformed) configuration.

The direction cosines, as used in Ref. [64], can resolve the Cauchy stress onto slip vectors $d^{\alpha}$ in the undeformed configuration. However, the deformed configuration components $d_i^{\alpha *}$ are no longer orthogonal vectors in the current configuration, having undergone stretch and rotation. To provide a meaningful description of the resolved shear stress in the slip direction and the normal stress to the slip plane in the deformed configuration at the point of nucleation, the cross product of the deformed vectors in the slip and co-slip directions (which establish the slip plane tangent) is taken to determine the slip plane normal direction. Then, a vector cross product of this slip plane normal direction with the deformed slip direction vector gives a modified co-slip direction, yielding an orthogonal triad which can describe the projection of the current uniaxial stress onto the slip system through direction cosines. This method preserves the slip direction and slip plane normal as primal

descriptors of the deformed configuration.

Figure 7.12 shows the evolution of the Schmid factor and normal factor at dislocation nucleation with grain boundary misorientation angle. Using the aforementioned method to calculate the resolved stress components in the current (deformed) configuration can illuminate differences that arise from a number of factors: initial vs. deformed, uniaxial tension vs. compression, dynamic strain rate vs. quasistatic, and {111} vs. {001} slip planes. For instance, uniaxial tension and uniaxial compression have different effects on the resolved shear stress and resolved normal stress at dislocation nucleation. In uniaxial tension, the resolved stress parameters $SF$ and $NF$ at dislocation nucleation have decreased on average by 1% and 6%, respectively, from the resolved stress parameters in the initial configuration $SF_0$ and $NF_0$. Uniaxial compression increases $SF$ and $NF$ by 2% and 14%. Note that the resolved stress components change by the same percentage. The resolved stress normal to the {111} slip plane is altered much more by elastic deformation than the resolved shear stress in the slip direction. Since these grain boundaries require the lowest stresses for dislocation nucleation from all ⟨100⟩ and ⟨110⟩ symmetric tilt grain boundaries [64], other grain boundaries may have a significantly larger change in the resolved stress components as a function of elastic deformation prior to dislocation nucleation.

A comparison of the $10^9$ dynamic strain rate with the quasistatic calculations in Fig. 7.12 show that the calculated resolved stress components are not adversely affected by either deformation approach. The dynamic and quasistatic deformation conditions are similar for uniaxial compression as well.

Based on the Schmid factor $SF$ calculated at dislocation nucleation, the critical resolved shear stresses for dislocation nucleation in these boundaries under uniaxial tension are approximately 0.55-1.85 GPa, or $\approx \tau/90$-$\tau/25$ using a shear modulus of $\tau = 48$ GPa. In unaxial compression, the resolved shear stresses are approximately 2.4-6.4 GPa, or $\approx \tau/20$-$\tau/8$ using a shear modulus of $\tau = 48$ GPa. These calculated shear stresses should be interpreted as an upper bound for the critical nucleation stress in these boundaries; impurities or

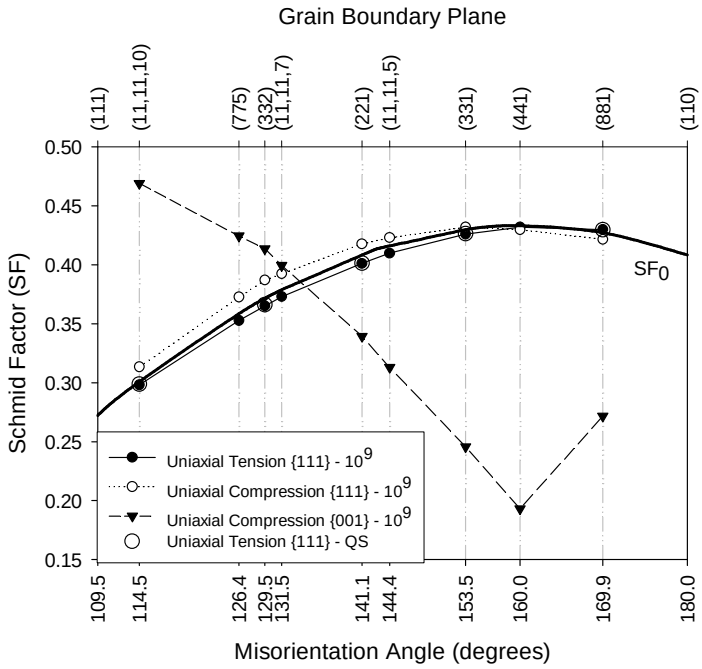


**(a)**

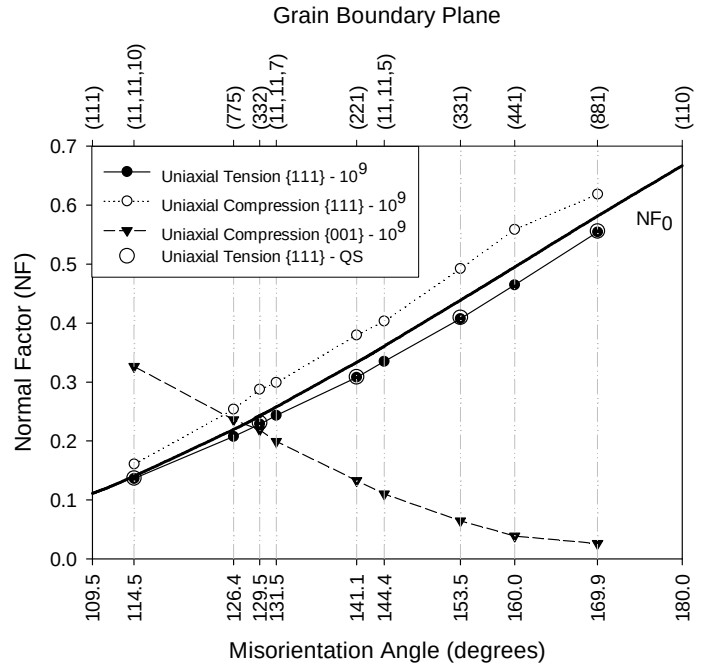


**(b)**

**Figure 7.12:** (a) The change in (a) Schmid factor, $SF$, and (b) normal factor, $NF$, at dislocation nucleation with grain boundary misorientation angle. The legend shows that different symbols are used to distinguish between (a) tension and compression, (b) dynamic strain rate ($10^9$) and quasistatic (QS), and (c) the {111} slip plane and the {001} slip plane. The change in Schmid factor and normal factor prior to deformation are labeled as $SF_0$ and $NF_0$.

vacancies in the boundary are expected to reduce the critical stress required for dislocation nucleation from boundaries.

The resolved stress parameters for the {111} and {001} slip planes in uniaxial compression are also plotted to help explain the observed full dislocation emission on the {111} and {001} slip planes for various misorientation angles (see Fig. 7.6). The {001} slip plane has both a higher resolved shear stress in the [110] slip direction and a higher resolved normal stress for lower misorientation angles within this range, perhaps explaining the observed full dislocation emission on the {001}⟨110⟩ slip system in compression. While this seemingly explains the observed dislocation behavior for compression, the resolved stress components for the {001} slip planes are higher in uniaxial tension as well. The tension-compression asymmetry in dislocation emission behavior may be explained in two ways. First, as discussed earlier, the Burgers vector character of the dislocations that comprise the grain boundary may be influenced differently depending on the sign of the resolved shear stress. Second, while the $NF$ curves in tension and compression are very similar in Fig. 7.12(b), they are in fact opposite in sign. For instance, the resolved normal stress is tensile in uniaxial tension and compressive in uniaxial compression. The full dislocation emission on the {001} plane is most likely due to the combination of the large resolved shear stress on the {001}⟨110⟩ slip system, the dislocation character of the $a_0/3\langle 111\rangle$ disconnection, and the large compressive normal stress on the {001} plane. While grain boundary dislocation character should not be overlooked, since the $\Sigma 9$ STGB emits partial dislocation on the {111} planes in tension and emits full dislocations on the {111} slip planes in compression, the resolved normal stress appears to have the most significant contribution to the emission of the trailing partial dislocation in Cu.

One may ask the question, can the emission of the trailing partial dislocation observed in uniaxial compression, but not in uniaxial tension, provide understanding of how resolved stress components affect grain boundary dislocation reactions in low stacking fault energy FCC nanocrystalline materials? Again, the main difference in how the applied stress is

resolved for uniaxial tension and compression is the stress normal to the slip plane; in tension, this normal stress is tensile, and vice versa. In this study, full dislocation nucleation observed under uniaxial compression implies that a compressive stress normal on the active slip plane may contribute to the nucleation of a second partial dislocation. Conversely, it can also be argued that the tensile stress normal to the slip plane may deter the nucleation of a second partial dislocation; here the latter argument was chosen. This may be explained with the generalized stacking fault (GSF) curve [270, 271] in the ⟨112⟩ direction for an FCC crystal. Zimmerman *et al.* [127] show that the GSF is affected by deformation of the material. They biaxially stretch the lattice by 4% while calculating the GSF curves and find that the unrelaxed $\gamma_{USF}$ of 175 mJ/m$^2$ is reduced to 99 mJ/m$^2$ for the 'deformed and relaxed' simulations. The unstable stacking fault energy ($\gamma_{USF}$) of the GSF curve is associated with the energy barrier for dislocation nucleation [126]. In this sense, the barrier to dislocation nucleation is reduced by the applied deformation. The GSF curve may be similarly affected by the magnitude and directionality of the resolved stress normal to the slip plane, particularly with respect to dislocation nucleation. An analysis [143] of the ideal shear strength of Al and Cu has shown that the hydorstatic pressure has a significant effect on the critical resolved shear stress at the atomic scale; this may also suggest that the normal stress has an equally important role.

Interestingly, several well-known studies on the influence of stacking fault energy on dislocation nucleation in nanocrystalline materials do not consider the effect of loading orientation (tension versus compression). Rather, Yamakov and coworkers [26] proposed a deformation mechanism map that described the transition from dislocation-mediated to grain boundary-mediated plastic deformation based on the equilibrium splitting distance for partials at $\sigma = 0$ and the grain boundary diameter, among other quantities. However, the description for the splitting distance is based solely on the intrinsic stacking fault energy $\gamma_{SF}$, with no dependence on the unstable stacking fault $\gamma_{USF}$. Simulations of nanocrystalline deformation do not support the cross-over of dislocation-based deformation mechanisms

(slip of extended partial dislocations versus perfect slip of full dislocations) with the absolute value of $\gamma_{SF}$. Van Swygenhoven *et al.* [23] noted that extended partial dislocations are observed above and below the predicted cross-over grain size in Cu [18, 19, 59]. Additionally, nc deformation simulations [60, 141] with a Ni potential (higher $\gamma_{SF}$ than Al) only revealed extended partial dislocations for grain sizes as large as 20 nm. In contrast to the deformation mechanism map proposed by Yamakov *et al.*, Van Swygenhoven and coworkers [23] proposed that extended or full dislocation activity should be understood in terms of $\gamma_{sf}/\gamma_{usf}$ and, more importantly, that $\gamma_{SF}$ alone cannot capture the important physics of the nucleation of leading and trailing partial dislocations from grain boundaries. The present simulations suggest that the resolved stress normal to the slip plane may affect the GSF curve and stable/unstable stacking fault energies. In turn, this may significantly influence the nucleation of the trailing partial dislocation in low stacking fault energy materials. Further work exploring how tensile and compressive normal stresses affect the GSF curve may shed some valuable insight into these arguments.

## *7.5 Summary*

In this chapter, atomistic modeling of dislocation nucleation in grain boundaries with the E structural unit was investigated under uniaxial tension and compression using molecular dynamics. Results show several differences in dislocation nucleation with respect to uniaxial tension and compression. First, the average nucleation stress for all ⟨110⟩ STGBs is over three times greater in compression than in tension for both the high strain rate and quasistatic simulations. Second, partial dislocations nucleate from the boundary on the {111} slip plane under uniaxial tension. However, partial and full dislocations nucleate from the boundary on the {100} and {111} slip planes under uniaxial compression. The full dislocation nucleation on the {100} for boundaries with misorientations near the coherent twin boundary is explained through the higher resolved shear stress on the {100} plane compared

to the {111} plane. Last, individual dislocation nucleation mechanisms under uniaxial tension and compression are analyzed. For the vicinal twin boundary under tension, the grain boundary partial dislocation is emitted into the lattice on the same {111} plane that it dissociated onto. For compression of the vicinal twin, the $1/3\langle 111\rangle$ disconnection is removed through full dislocation emission on the {100} plane and partial dislocation emission parallel to the coherent twin boundary plane, restoring the boundary to the coherent twin. For the $\Sigma 19$ boundary, the nearly simultaneous emission of numerous partial dislocations from the boundary result in the formation of the HCP phase. These results show that the resolved stress normal to the slip planes plays an important role in the nucleation of partial dislocations from the grain boundary.

# CHAPTER VIII

# IMPLICATIONS OF DISLOCATION NUCLEATION STUDIES ON HIGHER SCALE MODELS

This chapter provides insight from studies of dislocation nucleation from grain boundaries in this work and discusses potential implications on higher scale models. The structure and nucleation of dislocations at bicrystal boundaries illuminates certain issues pertaining to fundamental understanding of the role of grain boundaries. Here, some important aspects are discussed regarding dislocation nucleation in FCC metals under uniaxial loading applied perpendicular to the boundary plane: (i) dislocation sources or sinks, (ii) tension-compression asymmetry of trailing partial emission in Cu, (iii) the activation energy and volume for grain boundary dislocation nucleation, (iv) the influence of grain boundary free volume on dislocation nucleation, and (v) the influence of grain boundary free volume on dislocation nucleation. This understanding may benefit understanding of behavior of nanocrystalline and polycrystalline FCC metals.

## *8.1 Source/sink concepts based on dislocations*

The perfect source/sink model is based on the assumption of conservation of the net Burgers vector associated with dislocations. In this model, the grain boundary is viewed as having specific dislocation content; when a dislocation is emitted from the grain boundary, the boundary loses the Burgers vector content of the emitted dislocation. This phenomenon has been applied to vacancy content within the grain boundary as well as transmission (absorption and desorption) of dislocations through boundaries [154]. In the latter case, a lattice dislocation is transmitted through the grain boundary, but may leave behind a residual Burgers vector within the boundary, such that the total Burgers content is conserved.

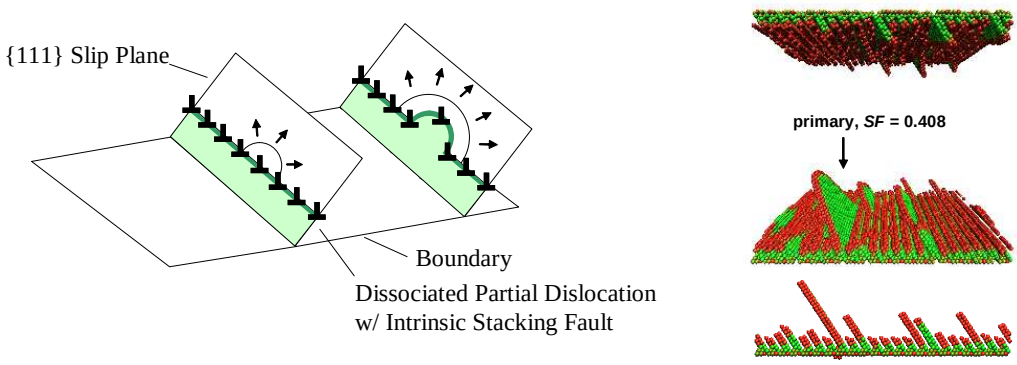


**Figure 8.1:** (a) A schematic showing how dislocations nucleate at boundaries with dissociated partial dislocations on the maximum Schmid factor (111) slip plane. (b) An example of dislocation nucleation for a Σ3 asymmetric tilt grain boundary of intermediate inclination angle.

*Some grain boundaries act as a perfect sink/source for dislocations.* Figure 8.1(a) shows a schematic of dislocation nucleation that occurs when a dissociated partial dislocation at the grain boundary is emitted into the adjoining lattice. For example, for Σ3 asymmetric tilt grain boundaries of intermediate inclination angle, the grain boundary partial dislocation (D structural unit) is dissociated from the boundary on the maximum Schmid factor plane. The dissociation {111} plane is the same {111} plane that the dislocation is emitted into the adjoining lattice onto, as shown in Fig. 8.1(b). In this case, the Burgers vector content of the grain boundary is reduced by the emission of the partial dislocation, *i.e.*, $b_{GB^*} = b_{GB} + b_{dislocation}$ where $b_{GB^*}$, $b_{GB}$, and $b_{dislocation}$ are the GB Burgers vector content before ($*$) and after emission, and the Burgers vector of the emitted partial dislocation, respectively. In this case, the GB Burgers vector after emission is merely reduced by the Burgers vector of the emitted partial dislocation, *i.e.*, $b_{GB} = b_{GB^*} - b_{dislocation}$.

*Other grain boundaries violate the perfect sink/source relationship for dislocations.* That is, for certain boundaries, the Burgers vector content of the grain boundary is not reduced following dislocation nucleation. For example, in the Σ3 asymmetric tilt grain boundary of low inclination angle, the grain boundary dislocation is initially dissociated from the boundary on a {111} slip plane of low resolved shear stress. However, the partial

dislocation prefers nucleation on a {111} slip plane of high resolved shear stress. Upon closer examination, a partial dislocation loop nucleates on the maximum Schmid factor slip plane very near to the facet intersection (or GB ledge), as shown in Fig. 8.2. Because of the proximity to the boundary, the segment of the partial dislocation loop that glides toward the boundary is quickly absorbed, adding Burgers vector content to the boundary. The other half of the loop glides into the lattice, giving the appearance that this dislocation was emitted directly from the boundary. This reaction can also be given as $b_{GB^*} = b_{GB} + b_{dislocation}$, but the Burgers vector content of the boundary is increased by the absorbed dislocation halfloop, *i.e.*, $b_{GB} = b_{GB^*} + b_{halfloop}$.

This is a clear breakdown of the perfect source/sink model if one considers the dislocation to have nucleated from the boundary. However, as Fig. 8.2 shows, the dislocation source visibly lies in the lattice near the intersection of the ATGB facets, and this ledge-like structure is the impetus for the dislocation nucleation event. This event can be thought of as the emission of a single dislocation loop from a Frank-Read type source located near the GB ledge. The size of simulation cell size limits our ability to discern whether these sources emit successive partial loop dislocations under further strain. Atomistic studies of this type offer details of the emission sequence that enhance our understanding of the source/sink nature of boundaries.

Dislocation sources can also lie directly in the interface. This sort of dislocation reaction is depicted in Fig. 8.3(a) with an example of dislocation nucleation from ⟨110⟩ symmetric tilt grain boundaries with dissociated structure from Spearot *et al*. [139] in Fig. 8.3(b). Spearot and coworkers have shown that increasing tensile strain applied perpendicular to the boundary resulted in constriction of the dissociated partial dislocation after which partial dislocations are emitted in another nearby site, producing extrinsic stacking faults, and later intrinsic stacking faults, in both symmetric lattices. In this case, the dislocation source lied directly in the interface, leading to the nucleation of the partial dislocations within the grain boundary. Several partial dislocations were emitted from the

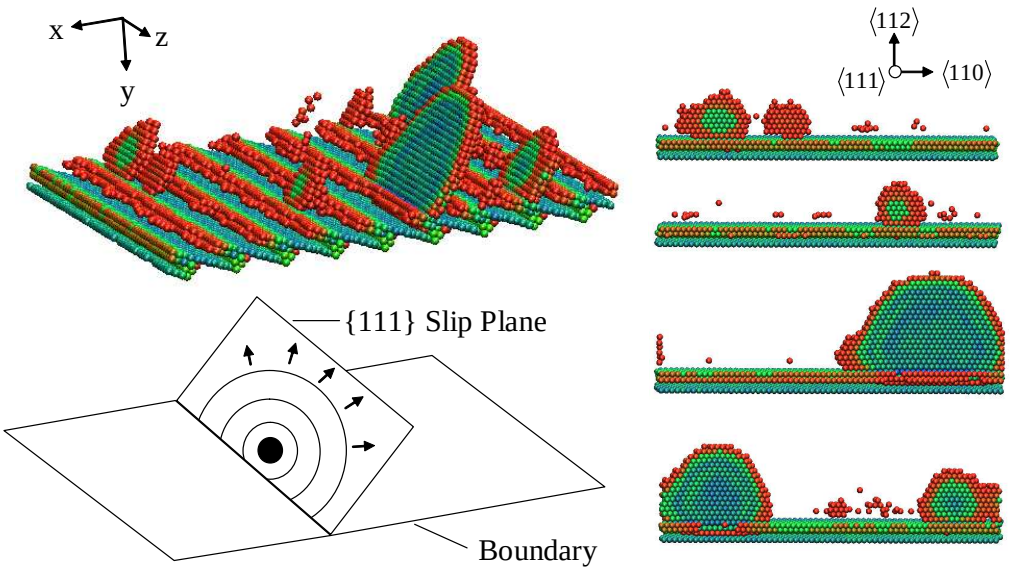


**Figure 8.2:** Dislocation loops nucleate homogeneously in the lattice at a dislocation source nearby the intersection of two boundary facets. A schematic showing the lattice dislocation source activated by deformation (lower left) is shown below an image of dislocation nucleation for the $\Sigma 3\left(55\bar{2}\right)_1 / (112)_2\, \Phi = 19.47°$ ATGB in Cu at 10 K (upper left), as rendered with the centrosymmetry parameter [106]. Slices of the (111) slip plane showing various stages of dislocation loop nucleation are shown to the right.

grain boundary dislocation source and the boundary accommodates their emission through local structural rearrangement near the source. This example also shows a breakdown of a perfect source/sink relationship, if one considers the Burgers content of the boundary to decrease by the Burgers content of the emitted dislocation.

These kinds of complex sequence effects in dislocation nucleation become evident using atomistic simulations. A particularly fruitful area of endeavor is the characterization of Burgers vector content in various general boundaries following nucleation of dislocations, discerning how the residual content is manifested in terms of change of boundary structure, as with the example in Fig. 8.3(b). Moreover, the impact of this evolution on continued nucleation or absorption/desorption reactions is of great interest.

It should also be emphasized that both dislocations and disclinations may be required to describe the lack of closure over a Burgers circuit in a crystal in the relaxed configuration. This is especially important near grain boundaries that have undergone dislocation nucleation or other interactions with dislocations. The associated change in the Burgers circuit at the boundary when a dislocation nucleates may not be feasibly described with a discrete set of partial or full dislocations. In this respect, disclination dipole content may need to be introduced into the boundary during dislocation nucleation to conserve the Burgers vector content. Additionally, Hirth *et al.* introduced the term "disconnection" to describe the Burgers vector content of steps, ledges, and residual dislocations after dislocation transmission reactions [272].

## *8.2 Tension-compression asymmetry in trailing partial emission in Cu*

The issue of partial dislocation versus full dislocation emission from grain boundaries has been the subject of recent interest in models for nanocrystalline materials. Recall that the mechanism of dislocation emission from the grain boundary occurs in several steps. First, a partial dislocation nucleates and is emitted from the grain boundary. Atomistic simulations

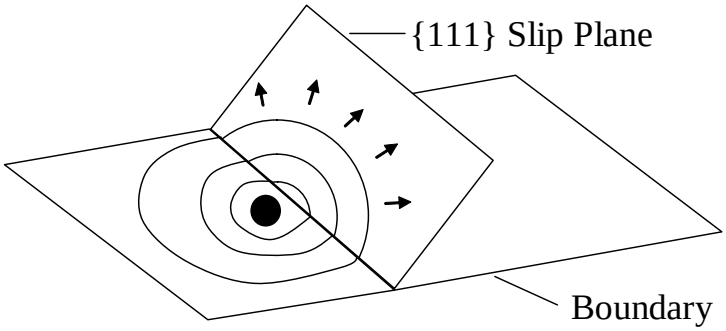


**(a)**

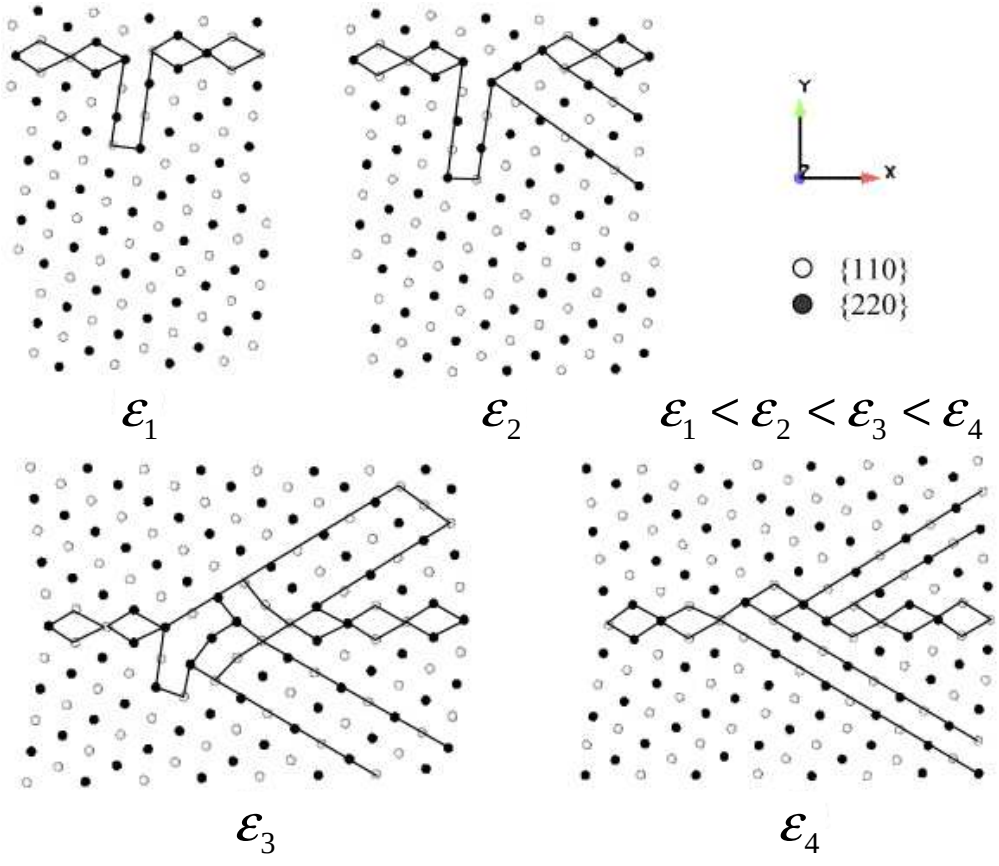


**(b)**

**Figure 8.3:** (a) Dislocation loops nucleate in the grain boundary at a dislocation source. (b) An example of partial dislocations nucleating in a ⟨110⟩ symmetric tilt grain boundary with dissociated structure [139].

have shown that stress-assisted free volume migration leads to the atomic shuffling necessary to form the Burgers vector required to nucleate a partial dislocation from the boundary region [60, 141]. As the leading partial dislocation transects the grain, an intrinsic stacking fault is created behind the partial dislocation. For smaller grain sizes, the leading partial dislocation can be absorbed at the grain boundary on the opposite side of the grain prior to the emission of the trailing partial. For larger grain sizes, the trailing partial dislocation is nucleated from the boundary, restoring the order of the stacking sequence of {111} planes within the lattice and bounding the intrinsic stacking fault.

Developing models or relations with physically-based parameters that give insight to partial versus full dislocation nucleation has received much attention. For example, Yamakov and coworkers [26] proposed a deformation mechanism map that described the transition from dislocation-mediated to grain boundary-mediated plastic deformation based on the equilibrium splitting distance for partials at $\sigma = 0$ and the grain boundary diameter, among other quantities. However, the description for the splitting distance is based solely on the intrinsic stacking fault energy, $\gamma_{SF}$, with no dependence on the unstable stacking fault energy, $\gamma_{USF}$. Simulations of nanocrystalline deformation do not support the cross-over of dislocation-based deformation mechanisms (slip of extended partial dislocations versus perfect slip of full dislocations) based only on the value of $\gamma_{SF}$. Van Swygenhoven *et al.* [23] noted that extended partial dislocations are observed above and below the predicted cross-over grain size in Cu [18, 19, 59]. In addition, nc deformation simulations [60, 141] with a Ni potential (higher $\gamma_{USF}$ than Al) only revealed extended partial dislocations for grain sizes as large as 20 nm. In contrast to the deformation mechanism map proposed by Yamakov and coworkers, Van Swygenhoven *et al*. [23] proposed that extended or full dislocation activity should be understood in terms of $\gamma_{SF}/\gamma_{USF}$ and, more importantly, that $\gamma_{SF}$ alone cannot capture the important physics of the nucleation of leading and trailing partial dislocations from grain boundaries. Along those lines, Asaro and Suresh [273] present a mechanistic model for FCC nanocrystalline metals that employed the ratio $\gamma_{SF}/\gamma_{USF}$ to

predict the emission of the trailing partial dislocation. *However, none of these arguments or models consider the effect of loading orientation (tension versus compression) or the resulting resolved normal stress on the emission of the trailing partial.*

Interestingly, MD simulations in this work have shown a distinctly different behavior of the trailing partial dislocation between uniaxial tension and uniaxial compression for homogeneous and heterogeneous dislocation nucleation from single crystals and grain boundaries, respectively. For homogeneous dislocation nucleation in single crystal Cu, Fig. 8.4 shows that partial dislocation loops containing an intrinsic stacking fault are nucleated in tension and full dislocation loops are nucleated in compression for a single crystal with a [321] loading axis orientation. This phenomenon is commonly observed for multiple crystal orientations around the stereographic triangle.

For heterogeneous dislocation from grain boundaries, symmetric tilt grain boundaries with the E structural unit were deformed under uniaxial tension and compression. Figure 8.4(c) shows the emission of partial dislocations from the $\Sigma171(11, 11, 10)$ vicinal coherent twin boundary under uniaxial tension. Figure Figure 8.4(f) shows the emission of full dislocations from the same boundary under uniaxial compression. Interestingly, the full dislocation is emitted on the {100} slip plane, which has a higher resolved shear stress in the $\langle 110 \rangle$ slip direction than the $\{111\}\langle 110 \rangle$ slip systems. Despite the higher resolved shear stress, dislocation emission on the {100} slip plane is only observed in compression. As with single crystals, the partial (full) dislocation behavior in uniaxial tension (compression) is observed for a wide range of boundary structures across the misorientation range that corresponds to boundaries with the E structural unit. Other grain boundaries have not yet been deformed, but are expected to display similar behavior due to the high compressive resolved normal stress.

The contrast between the nucleation mechanisms under uniaxial tension and compression may shed light on our fundamental understanding of how resolved stresses affect dislocation nucleation in single crystals and grain boundaries. As discussed in Chapter 11

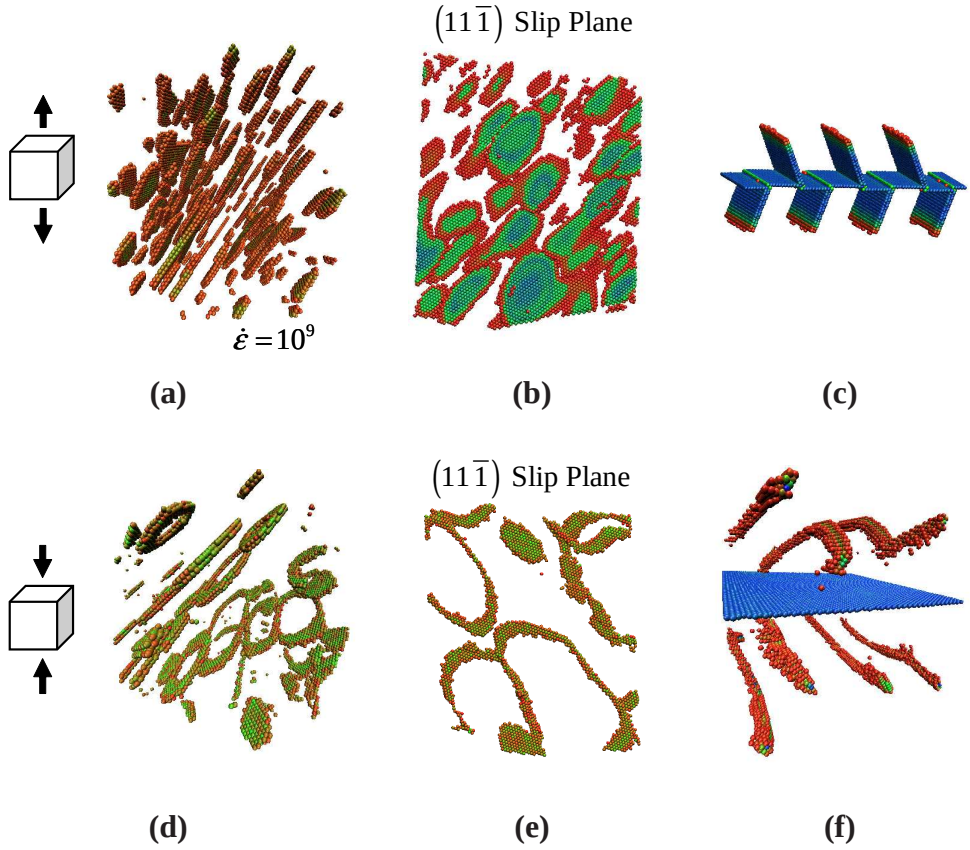


**Figure 8.4:** Dislocation nucleation behavior in uniaxial tension (a-c) and uniaxial compression (d-f) for the (a-b,d-e) [321] single crystal and (c,f) $\Sigma 171\,(11, 11, 10)$ vicinal coherent twin boundary. The emission of the trailing partial dislocation is observed in compression, but not in tension. Images (b) and (e) are slices of the slip plane on which dislocations nucleate.

and depicted in Fig. 11.2, the main difference in how the applied stress is resolved for uniaxial tension and compression is the stress normal to the slip plane; in tension, this normal stress is tensile, and vice versa for compression. Full dislocation nucleation observed under uniaxial compression implies that a compressive stress normal on the active slip plane contributes to the nucleation of the trailing partial dislocation. In contrast, a tensile stress normal to the slip plane may deter the nucleation of a second partial dislocation. This may be explained with the generalized stacking fault (GSF) curve on the {111} slip plane in the ⟨112⟩ direction for an FCC crystal. Zimmerman *et al.* [127] show that the GSF is affected by deformation of the material. They biaxially stretched the lattice by 4% while calculating the GSF curves and found that the unrelaxed $\gamma_{USF}$ of 175 mJ/m$^2$ is reduced to 99 mJ/m$^2$ for the "deformed and relaxed" simulations. The unstable stacking fault energy ($\gamma_{USF}$) of the GSF curve is associated with the energy barrier for dislocation nucleation [126]. In this sense, the barrier to dislocation nucleation is reduced by the applied deformation. The GSF curve may be similarly affected by the magnitude and directionality of the resolved stress normal to the slip plane, particularly with respect to nucleation of the trailing partial dislocation. Indeed this feature of a changing potential energy landscape of grain boundaries under stress renders the prospect of characterizing the activation energies and transition state pathways for various dislocation nucleation events quite challenging from a unit process standpoint.

## *8.3 Activation volumes and energies for grain boundary dislocation nucleation*

The activation volume and the activation energy are important experimentally-measurable scalar quantities that can be used to model the rate and temperature sensitivity of plasticity mechanisms in constitutive relations [256, 273, 274]. The activation energy barrier for nucleation can be overcome with contributions from both mechanical work (applied stress) and thermal energy $k_BT$, where $k_B$ is Boltzmann's constant and $T$ is temperature. The activation volume is that required for the reaction to occur. Asaro and Suresh [273]

have compiled a summary of available data on the effect of grain size on the activation volume in Cu and Ni. They show that the magnitudes of the activation volumes decrease substantially as the material length scale decreases to the nanoscale, in line with other calculated and experimental observations [256, 274–276]. For example, Schuh *et al.* [277] performed nanoindentation experiments on platinum at various temperatures and found activation volumes of $\approx 0.5\ b^3$. Lu *et al.* [174] experimentally measured activation volumes of $\approx 10 - 20\ b^3$ for nano-twinned copper. In addition to measurement of activation energies and activation volumes through experiments, Zhu and coworkers [256] have developed a computational methodology whereby atomistic simulations are used to calculate the activation energy and activation volume and assess the strain rate and temperature sensitivity of dislocation reactions. Here, MD calculations are used to obtain a first-order approximation of the activation energies and volumes for dislocation nucleation from $\Sigma 3$ asymmetric tilt grain boundaries in Cu and Al, as discussed in Chapter 6.

Calculations have shown that there is a significant drop in the stress required to nucleate dislocations from 10 K to 300 K, suggesting that thermal activation plays a role in dislocation nucleation from the grain boundary. The activation volume $\Omega$ and activation energy $Q$ for dislocation nucleation are calculated from a first-order model of stress-dependent activation energy whereby the activation energy linearly depends upon stress $\sigma$, *i.e.*, $Q(\sigma) = Q^* - \sigma\Omega$. In this model, $Q^*$ corresponds to the athermal nucleation energy barrier in the absence of applied stress. The activation energy $Q$ measures the sensitivity of nucleation rate to temperature while the activation volume $\Omega$ measures the sensitivity of nucleation rate to stress. Zhu *et al.* [256] derived a form for the dislocation nucleation stress that takes into account both the temperature and strain-rate dependence. They applied this form to dislocation nucleation at surfaces under a constant strain rate. The same equation was employed to calculate the activation energy and activation volume in this study,

$$\sigma = \frac{Q^*}{\Omega} - \frac{k_B T}{\Omega} ln \frac{k_B T N \nu_0}{E \dot{\epsilon} \Omega} \tag{8.1}$$

In Eq. 8.1, the temperature $T = 300$ K, $N$ is the number of nucleation sites ($N = 50,000$), $\nu_0$ is the jump frequency ($\nu_0 = 3 * 10^{11}\ s^{-1}$), $E$ is the elastic modulus, and $\dot{\epsilon}$ is the applied strain rate ($\dot{\epsilon} = 10^9\ s^{-1}$). The definitions of the terms are given by Zhu and coworkers [274]. The first term $Q^*/\Omega$ is the athermal stress required to nucleate a dislocation from the grain boundary. The pre-factor of the second term $k_B T/\Omega$ reduces the nucleation stress by virtue of thermal fluctuation. In the logarithmic function, the numerator is the rate of energy exchange of the system with the thermal bath and the denominator is the rate of energy delivery into the system through mechanical work; the ratio between these terms determines the relative influence of thermal fluctuations in reducing the nucleation stress.

Several assumptions are made to calculate the activation volume and activation energy. First, the atomic jump frequency ($\nu_0$) is chosen to represent the cooperative atomic motion necessary to form a dislocation, and is on the order of the frequency of free oscillation in Cu [278]. Second, the number of nucleation sites ($N$) represents the approximate number of non-centrosymmetric atoms at the grain boundary. Since these are embedded in the logarithmic term, variation of $N\nu_0$ by several orders of magnitude results in very little change to the activation volume. Third, since the first term in Eq. 8.1 corresponds to the athermal nucleation stress, the calculated nucleation stresses at 10 K were used as an approximate value. The nucleation stresses from all $\Sigma 3$ asymmetric tilt grain boundaries were used to capture the effect of variation in boundary structure and dislocation nucleation mechanisms on the activation energy and volume. Last, the elastic stiffness of the computational cell was calculated using the theoretical values of the two adjoining lattice regions; the effect of elastic anisotropy had little effect on the calculations. Using the nucleation stress values for uniaxial tension at $T = 300$ K, the activation volumes for dislocation nucleation were on the order of $\approx 0.5 - 3\ b^3$ in both Cu and Al, where $b = 0.255$ nm in Cu and $b = 0.286$ nm in Al. Rearranging the first term in Eq. 8.1 such that $Q^* = \sigma\Omega$ gives the athermal activation energy barrier under zero applied stress, which ranges from $\approx 0.8 - 2.4$ eV for

Σ3 asymmetric tilt grain boundaries. Also, using our first order approximation of a linear dependence of activation energy on stress ($Q(\sigma) = Q^* - \sigma\Omega$) the activation energy for dislocation nucleation at 300 K is calculated as $\approx 0.24 - 0.28$ eV. Interestingly, the activation energies at 300 K are roughly the same for all Σ3 boundaries examined, despite the wide range of boundary structures.

Zhu and coworkers [256, 274] have calculated activation volumes and activation energies for heterogeneous dislocation nucleation and dislocation reactions using the climbing image nudged elastic band (CINEB) method. The CINEB method allows for a direct calculation of the activation energy versus stress relationship, without relying on several of the aforementioned assumptions made in the current calculations. Even so, the calculated activation energies are on the order of those computed for side surface nucleation ($Q = 0.64$ eV) and corner nucleation ($Q = 0.1$ eV) from nanopillars [256]. Furthermore, Zhu and coworkers [274] calculated activation energies for dislocation absorption ($Q_{abs} = 0.49$ eV) and dislocation direction transmission ($Q_{trs} = 0.67$ eV) at the coherent twin boundary that are similar to the present molecular dynamics calculations at a strain rate of $10^9$ $s^{-1}$. The similarity of values suggests that the current calculations are a reasonable approximation of the activation volumes and activation energies for dislocation nucleation from Σ3 asymmetric tilt grain boundaries.

The small activation volumes of $0.5 - 3$ $b^3$ promote enhanced temperature sensitivity of dislocation nucleation at grain boundaries and indicate that the atomic volume required for grain boundary dislocation nucleation is similar to the activation volume required for grain boundary shear events, $\Omega = 1$ $b^3$, in another FCC metal, Au [279]. The small activation volumes indicate that at the appropriate stress level, the motion of a few atoms may serve as the impetus for nucleating a dislocation from the boundary. In addition, the small activation volume suggests that the nucleation event is appropriately viewed as a small dislocation loop nucleating at the grain boundary, as shown by our MD calculations in Chapter 6. As the length scales associated with activation volumes are on the order of interatomic spacing,

it is also anticipated that the grain boundary free volume contributes to the driving force for the dislocation nucleation reaction.

## *8.4 Influence of grain boundary free volume on dislocation nucleation*

The extent and distribution of grain boundary free volume may play a significant role in dislocation nucleation. For example, clusters of free volume on boundaries or at triple junctions are on the order of the activation volumes computed in Section 8.3. In addition, the average free volume assists in correlation of the stress required for dislocation nucleation from ⟨100⟩ and ⟨110⟩ symmetric tilt grain boundaries, as discussed in Chapter 9. However, recall that the interface stress model in Chapter 9 was unable to capture the abrupt drop in the stresses required for dislocation nucleation in symmetric tilt grain boundaries with the E structural unit. This particular structural unit is associated with the Σ9 (221) STGB and contains a large amount of free volume compared to other ⟨110⟩ symmetric tilt grain boundaries. Bicrystal simulations can provide insight into the relationship between grain boundary structure, grain boundary free volume, and dislocation nucleation from the boundary. Previous studies have shown that both the amount of free volume within the boundary and the spatial correlation of free volume within the boundary are important factors that play a role in dislocation nucleation [82].

A number of symmetric tilt grain boundaries within the misorientation range $109.47^\circ < \theta < 180^\circ$ were examined in terms of structure and free volume. The free volume was visualized and characterized with spatial correlation functions using a stereologically-based methodology, whereby a grid of points was superimposed in three dimensions over the atomic coordinates and each point was tested against a free volume criterion [82]. This methodology enabled Tschopp *et al.* [82] to show that both the spacing and connectivity of the free volume in the tilt direction increase with increasing misorientation angle over the range $109.47^\circ < \theta < 180^\circ$. In fact, for low angle boundaries near the $180^\circ$ perfect single crystal, the free volume is completely connected in the tilt direction.

The spatial distribution of free volume relates to dislocation nucleation because the free volume enables the cooperative atomic shuffling that triggers the emission of partial dislocations from the grain boundary. Not only is the spatial distribution important, but the spatial distribution of free volume *with respect to intersecting slip planes* may also affect dislocation nucleation. For dislocation nucleation to occur from the grain boundary, the cooperative motion of atoms on a {111} slip plane intersecting the grain boundary is required. It is likely that this depends on the spacing and connectivity of free volume along that slip plane. For example, an isolated free volume pocket that intersects the slip plane will only allow local atomic shuffling in the few neighboring atoms. However, a large fraction of grain boundary free volume intersecting the slip plane affects a greater number of atoms along the slip plane, enabling the cooperative atomic shuffling required to nucleate dislocations at the boundary. Moreover, for the E structural unit boundaries [82], the two active slip systems (maximum Schmid factor analysis) occur on the same {111} slip plane (coplanar slip), which intersects the boundary along the tilt direction. Thus, the spatial correlation statistics of free volume in the tilt direction are essential to the discussion of dislocation nucleation from boundaries with the E structural unit.

# CHAPTER IX

# DISLOCATION NUCLEATION MODEL FOR SINGLE CRYSTALS AND INTERFACES

Chapter 9 is the first chapter to focus on a model to correlate dislocation nucleation stresses calculated from atomistic simulations with continuum parameters related to the resolved stresses. Molecular dynamics (MD) simulations are used to model dislocation nucleation at or near symmetric tilt bicrystal copper interfaces with ⟨100⟩ or ⟨110⟩ misorientation axes. MD simulations indicate that orientation of the opposing lattice regions and the presence of certain structural units are two critical attributes of the interface structure that affect the stress required for dislocation nucleation. Boundaries that contain the E structural unit are found to emit dislocations at comparatively low tensile stress magnitudes. A simple model is proposed to illustrate the impact of interfacial porosity and stresses acting on the slip plane in non-glide directions on tensile interface strength. Accounting for interfacial porosity through an average measure is found to be sufficient to model the tensile strength of boundaries with a ⟨100⟩ misorientation axis and many boundaries with a ⟨110⟩ misorientation axis.

## *9.1 Introduction*

The character and distribution of grain boundary interfaces in polycrystalline metals are known to play a prominent role in many material properties. For example, experimental studies on metallic polycrystalline specimens have indicated that grain boundary structure can effect interface mobility, corrosion, crack nucleation resistance and ductility (*cf.* [65, 280, 281]). Interestingly, many investigations have indicated that there is some correlation between the occurrence of certain coincident site lattice (CSL) [65] boundaries and

particular aspects of material behavior. For example, Lim [280] studied the distribution of cracked and uncracked boundaries during low-cycle fatigue of polycrystalline nickel samples; he found that boundaries with low-order CSL character ($\Sigma 3$ and $\Sigma 5$) did not crack during the deformation process. Uniaxial tensile deformation experiments on polycrystalline copper samples [281] have provided similar conclusions regarding the possible relationship between CSL occurrence and cavitation. Motivated by these experimental findings, grain boundary engineering [155] techniques aim to increase the percentage of 'special' boundaries and to reduce the connectivity of 'random' boundaries, resulting in enhancements in a range of material properties [282–284].

For metallic nanocrystalline materials, the role of grain boundary character and distribution on material properties is amplified due to the increased fraction of atoms that are positioned at or near interfaces. Atomistic simulation serves as a tool to explore potential relationships between interface structure and interfacial failure mechanisms on the nanoscale. For example, Spearot *et al.* used molecular dynamics (MD) simulations to examine the role of interface structure on the nucleation of dislocations from copper [139] and aluminum [97] bicrystal boundaries under uniaxial tension. In copper, they found that the spacing between specific structural units can play a significant role on the character of the nucleated dislocations. Sansoz and Molinari [72] used the quasicontinuum method to study the deformation of tilt bicrystal $\Sigma$ boundaries. Atomic shuffling during shear deformation was correlated to the presence of the E structural unit (cf. [90]) and appeared to be triggered by the free volume inherent to this structural feature. Moreover, Sansoz and Molinari did not find a relationship between maximum shear stress and interface structure over the range of misorientations considered.

In a recent review article, Van Swygenhoven and Weertman [138] emphasized the importance of studies on single interfaces [72,97,139] to explore "particular interesting" grain boundaries in nanocrystalline plasticity. Accordingly, the objective of this work is to utilize MD simulations to study the tensile deformation of bicrystal boundaries in copper with

a range of tilt interface misorientations. MD simulations are used to identify particular features of the interface structure that play an important role in the tensile deformation response. Bicrystal boundaries considered in this work are initially refined using an energy minimization procedure; *i.e.*, all defects that exist at the interface between crystalline regions are a natural consequence of the misorientation across the boundary. Other forms of interfacial defects, such as ledges and disconnections, are not considered in this work.

Based on the MD simulations in this work, a first-order model is proposed to correlate interfacial strength in tension and pertinent characteristics of the interface structure. Here, tensile interfacial strength is regarded as the maximum tensile stress achieved during deformation and is associated with the partial dislocation nucleation event. The proposed model is used to study the relative importance of both interfacial porosity and individual stress components acting on the slip plane in non-glide directions. MD simulations on both single crystal and interface models indicate that non-Schmid effects must be incorporated when formulating a model for dislocation nucleation. This observation is in agreement with *ab initio* calculations of dislocation nucleation in copper and aluminum available in the literature [143, 259, 285]. Furthermore, using an average measure of nanoporosity[1] to characterize the interface structure is sufficient to account for dislocation emission from tilt boundaries with a $\langle 100 \rangle$ misorientation axis and many tilt boundaries with a $\langle 110 \rangle$ misorientation axis. However, for $\langle 110 \rangle$ boundaries which contain the E structural unit, the first-order model fails to capture the complete effect of interface structure on tensile interface strength associated with dislocation nucleation.

## *9.2 Interface model*

The bicrystal interface model used in this work is shown in Figure 9.1(a). MD simulations consider symmetric tilt boundaries in copper formed by rotations around the $\langle 100 \rangle$ or $\langle 110 \rangle$ crystallographic misorientation axes. The specific misorientations studied in this

[1] In this chapter, nanoporosity is used to represent an approximate measure of the free volume of the interface, as defined by a coordination number-based approach in Spearot *et al.* [1].

work are shown on the stereographic orientation triangle in Figure 9.1(b). For boundaries with a [001] misorientation axis, the interface misorientation angle is measured using the [100] direction as the reference (0°). For boundaries with a $\left[1\bar{1}0\right]$ misorientation axis, the interface misorientation angle is measured using the [001] direction as the reference (0°). Copper is modeled using the Mishin *et al.* embedded-atom method (EAM) potential [124]. Periodic boundary conditions are used in all directions; thus, the bicrystal interface model dimensions are defined accordingly to properly enforce this boundary prescription. In total, each bicrystal interface model contains between 450,000 and 750,000 atoms. Note that the use of periodic boundary conditions in the Y-direction introduces a second interface at the periodic border; both interfaces have identical structures. Based on previous MD simulations [97,139], which consider both atomically sharp and dissociated interfaces, the dimensions of the interface models are considered sufficient to study three-dimensional dislocation nucleation at early stages from tilt bicrystal boundaries. In particular, the dimensions of the boundaries in the X- and Z-directions are adequately large to avoid image effects which could suppress dislocation nucleation to specific slip systems. To study dislocation-dislocation or dislocation-interface interactions at advanced stages of deformation, more advanced boundary conditions are necessary to properly handle dislocation image effects related to the periodic boundary conditions [286].

Molecular statics calculations, which employ a nonlinear conjugate gradient method, are used to determine the minimum energy interface configurations. A number of initial 'starting positions' are used to increase the probability that the global minimum energy configuration is attained during this procedure [90]. When available, interface structures are compared with high-resolution transmission electron microscopy images in the literature (*cf.* [287]). After the minimum energy configuration is attained, the interface model is equilibrated using MD in the isobaric-isothermal ensemble [95] at a pressure of 0 bar and a temperature of 300 K. MD simulations are then used to deform each interface model at

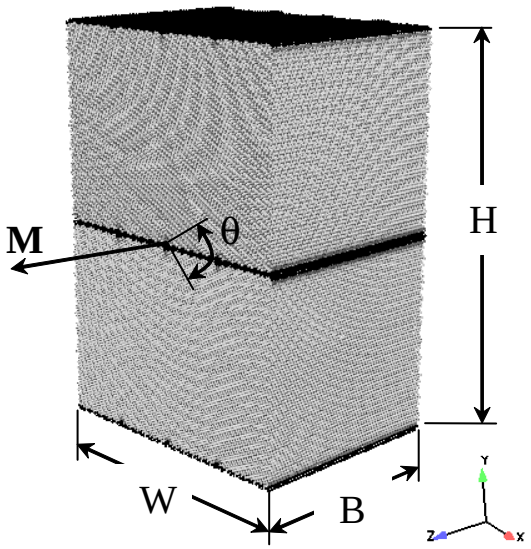


**(a)**

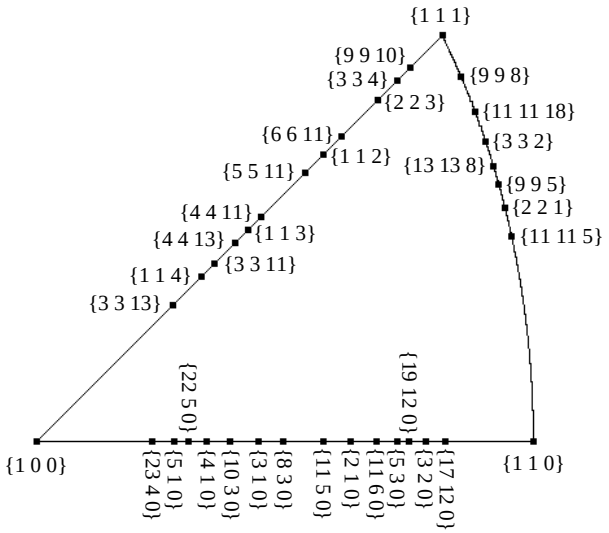


**(b)**

**Figure 9.1:** (a) Bicrystal interface model studied in this work. The interface is created by a symmetric tilt rotation around the ⟨100⟩ or ⟨110⟩ misorientation axis; (b) corresponding boundary misorientations examined.

300 K in uniaxial tension, at a constant strain rate of $10^9$ $s^{-1}$, which is applied in the Y-direction (normal to the interface plane). Deformation is imposed by decoupling the vector which describes the dimensions of the periodic cell from the equations of motion in the loading direction and extending the length of this vector at the prescribed rate during the simulation, as described in Chapter 2. The X- and Z-direction boundaries are specified as stress-free [95].

Mechanical quantities, such as stress [103] and displacement, and a measure of interfacial damage termed 'nanoporosity' [1], are calculated over a defined volume around the interface (interface region); this volume includes the boundary and a portion of the lattice from each crystal. For all interface models (misorientations), the size of the interface region spans the entire model dimensions in the X- and Z-directions. The thickness of the interface region in the Y-direction is identical for all interface models and is equal to 12 lattice constants, centered about the interface. The nanoporosity measure is determined using the atomic coordination number and is regarded as an *approximation* of the average unoccupied volume within the interface region [1]. Calculations in this work show that the nanoporosity measure is capable of identifying relative differences in porosity between dissimilar interfaces; however, since nanoporosity is derived from atomic coordination via an averaging scheme, this measure is not able to portray porosity coalescence at advanced stages of interfacial fracture. Based on its derivation [1], the magnitude of the nanoporosity measure will depend on the thickness of the interface region. However, the qualitative details of nanoporosity evolution are unaffected by the choice of the volume over which the nanoporosity measure is averaged.

## *9.3 Symmetric tilt interfaces: $\langle 100 \rangle$ misorientation Axis*

Figure 9.2(a) shows the tensile stress-displacement response for bicrystal interface models with $\langle 100 \rangle$ tilt axis and misorientations between 19.7° (23, 4, 0) and 41.1° (830). This range encompasses both $\Sigma 5\,(310)\,\theta = 36.9°$ and $\Sigma 13\,(510)\,\theta = 22.6°$ boundaries, which are

two low $\Sigma$ boundaries for the $\langle 100 \rangle$ misorientation axis [65]. Clearly, as the misorientation angle increases, the maximum tensile stress achieved during deformation decreases. Contrary to the experimental evidence discussed in the introduction, the low-order $\Sigma$ boundaries within this misorientation range do not show any special behavior with regard to maximum tensile interface stress. Visual inspection of the MD simulation results indicates that partial dislocations are nucleated from the bicrystal interface at the displacement associated with maximum tensile stress nearly simultaneously on two different slip systems for each misorientation. The activated slip systems in each case are in agreement with those predicted using a Schmid factor analysis [257]. Trailing partial dislocations are not nucleated from the interface during deformation, in agreement with the work of Van Swygenhoven *et al.* [23], who argued that extended partial dislocations are the predominant mode of inelastic failure for nanocrystalline materials that have an unstable to intrinsic stacking fault energy ratio much larger than unity (this ratio is 3.56 in Cu [124]). The spacing between tilt bicrystal interfaces in this work is between 8 and 12 nm (depending on the boundary misorientation and the necessary height of the interface model to enforce periodic boundary conditions), which is on the same order as the nanocrystalline grain sizes studied in previous work by Van Swygenhoven and colleagues (*cf.* [23]). Accordingly, a similar response is expected with regard to the character of the nucleated dislocations in copper.

Nanoporosity evolution during uniaxial tensile deformation is shown in Figure 9.2(b). In general, the nanoporosity measure offers a means to differentiate between interfaces with different misorientations, boundaries with the smallest initial nanoporosity are those with misorientations closest to the low-angle (dislocation) regimes. The nanoporosity measure indicates that the interface evolves prior to the emission of partial dislocations, in qualitative agreement with previous MD simulation work on nanocrystalline samples (*cf.* [138]). Specifically, Figure 9.2(b) shows that maximum nanoporosity occurs at a slightly *smaller* displacement (of the interface region) than that associated with the maximum tensile stress. For high-angle boundaries, like the $\Sigma 5\,(310)\,\theta = 36.9^\circ$ interface, MD simulations indicate

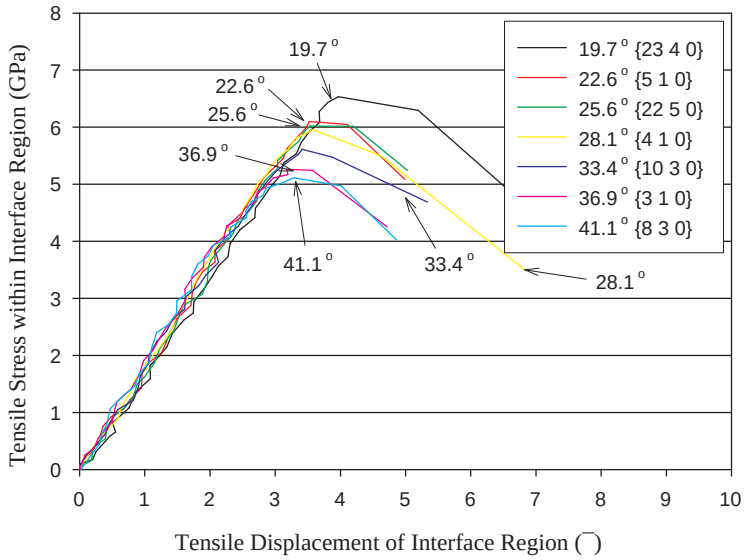


**(a)**

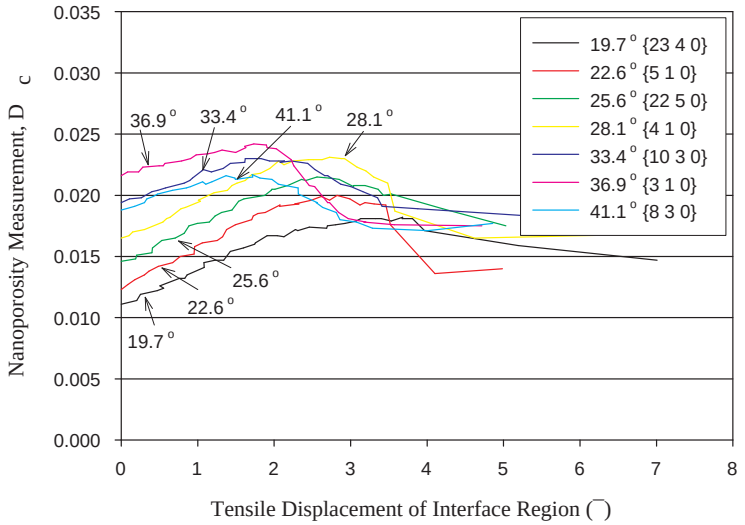


**(b)**

**Figure 9.2:** (a) Stress versus displacement and (b) nanoporosity versus displacement during uniaxial tension of symmetric tilt bicrystal interface models in copper with ⟨100⟩ tilt axis.

that the maximum nanoporosity is associated with the initiation of grain boundary 'coarsening' within the interface region.

This phenomenon is shown in greater detail in Figure 9.3 for the $\Sigma 5\,(310)\,\theta = 36.9^{\circ}$ interface at 300 K. Specifically, Figure 9.3(a) shows a 3D view of the interface model after isobaric-isothermal equilibration (before deformation), Figure 9.3(b) shows a 'projected' view of the initial structure of the interface before deformation, Figure 9.3(c) shows a 3D view of the interface model after the nucleation of the first partial dislocations from the boundary and Figure 9.3(d) shows a close-up projected view of the interface after the dislocation nucleation event. All images are colored based on the centrosymmetry parameter, which is a scalar quantity designed to identify atoms in distorted configurations [106]. Clearly, the thickness of the region that is identified as being distorted by the centrosymmetry parameter increases during uniaxial tensile deformation. Coarsening at the interface distorts the interface structural units in such a way as to increase the local coordination of atoms in the vicinity of the interface. Interface coarsening appears to be more prevalent in materials with low stacking fault energies, as this effect is not observed for the same boundary in aluminum [97]. For low-angle boundaries, coarsening at the interface is less prevalent due to periodic regions of perfect lattice along the interface plane between dislocation cores. Accordingly, the tensile displacement of the interface region associated with maximum nanoporosity and maximum tensile stress nearly coincide for low-angle boundaries.

Figure 9.4 shows the maximum tensile stress achieved during the deformation process and the maximum resolved shear stress (MRSS) in the activated $\{111\}\langle 112\rangle$ slip system as a function of interface misorientation angle. To isolate the influence of lattice orientation on the magnitude of the peak tensile stress, single crystal (SC) calculations are also presented in Figure 9.4 for comparison. The orientation of each SC model is identical to that of the lower lattice region of the corresponding interface model; because the interfaces are of symmetric tilt character, the same geometric slip factors apply to the upper lattice

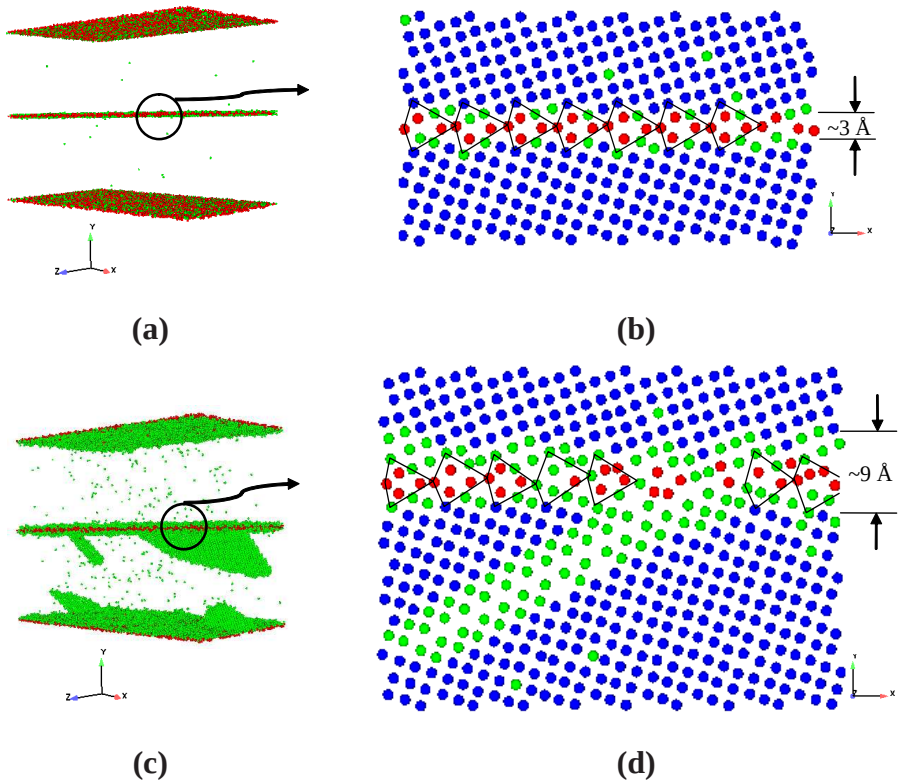


**Figure 9.3:** Detailed view of the $\Sigma 5\,(310)\,\theta = 36.9°$ interface (a) and (b) after isobaric-isothermal equilibration (before dislocation nucleation), (c) and (d) after the nucleation of the first partial dislocation from the interface.

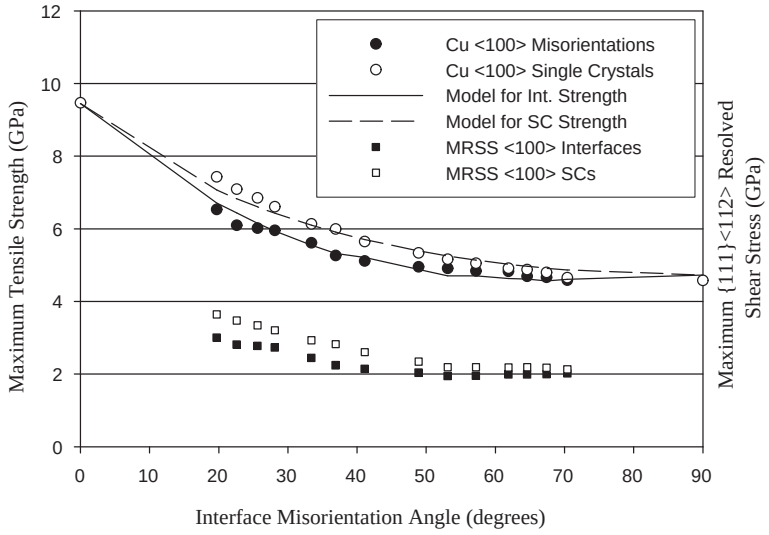


**Figure 9.4:** Maximum tensile stress and maximum resolved shear stress attained during uniaxial tensile deformation as a function of misorientation angle for ⟨100⟩ tilt axis. Single crystal calculations are included for comparison.

region as well. The reference single crystal orientations have the same tilt axis relative to the direction of applied stress, with the same reference values for zero misorientation as the interface models to facilitate a direct comparison. For single crystal models, MD simulations indicate that dislocations are nucleated on the primary slip systems [257] at the uniaxial tensile deformation associated with maximum tensile stress. The range of MRSS magnitudes for SC calculations is consistent with the ideal shear strength of copper computed from *ab initio* calculations [143, 259, 285], indicating that MD with the Mishin *et al.* EAM potential is capable of ascertaining the stress required for dislocation nucleation. Figure 9.4 indicates that the orientation of the lattice with respect to the applied uniaxial tension is important for modeling the tensile strength of tilt interfaces with a ⟨100⟩ misorientation axis. Note that the tensile stress required for dislocation nucleation for single crystal models is greater than that for bicrystal interface models, demonstrating the role of the interface in promoting dislocation nucleation.

## 9.4 Symmetric tilt interfaces: ⟨110⟩ misorientation Axis

Figure 9.5(a) shows the tensile stress-displacement response for copper tilt bicrystal interface models with ⟨110⟩ misorientation axis and interface misorientations between $\Sigma 17\,(334)\,\theta = 93.4°$ and $\Sigma 267\,(11, 11, 5)\,\theta = 144.4°$ STGB. MD simulations indicate that the interface serves as the source for dislocations in all cases except the $\Sigma 3\,(111)\,\theta = 109.5°$ coherent twin boundary. For this interface, dislocations are nucleated homogeneously within each lattice. Accordingly, Figure 9.5(a) shows that the coherent Σ3 boundary has the highest tensile strength compared with the other misorientations considered. This observation may be contrasted with the case of shear in which the coherent Σ3 boundary showed a high propensity to migrate at low applied shear stresses [72]. An abrupt decrease is observed in the tensile strength as the misorientation angle of the interface is increased beyond 109.5°. Interfaces with misorientations greater than 109.5° are different from the other ⟨110⟩ boundaries in two respects: (i) boundaries in this range deform via dislocation nucleation on coplanar slip systems [257] and (ii) visual inspection indicates that boundaries in this range of ⟨110⟩ misorientations contain the E structural unit. Recall that Sansoz and Molinari concluded that boundaries that contained the E structural unit are prone to atomic shuffling when subjected to a shear deformation [72]. In this work, symmetric tilt boundaries with a ⟨110⟩ misorientation axis that contain the E structural unit emit partial dislocations at low applied tensile stresses normal to the interface.

Figure 9.6 shows a projected view of dislocation nucleation from the $\Sigma 9\,(221)\,\theta = 141.1°$ boundary in copper. The initial structure of the Σ9 boundary is composed entirely of E structural units, in agreement with previous work [90]. Deformation occurs in two stages when subjected to a tensile deformation. First, very short intrinsic stacking fault (ISF) facets are nucleated from the interface, as shown in Figure 9.6(b). These facets are emitted on the primary coplanar slip systems. For example, in the lower lattice region the $\left(11\bar{1}\right)$ slip plane is activated with slip occurring in both [101] and [011] directions. Second, extended partial dislocations begin to propagate away from the boundary at the displacement

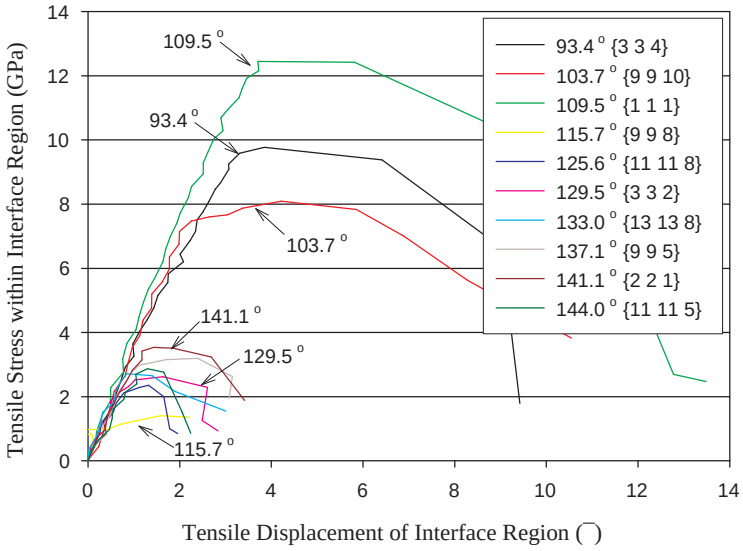


**(a)**

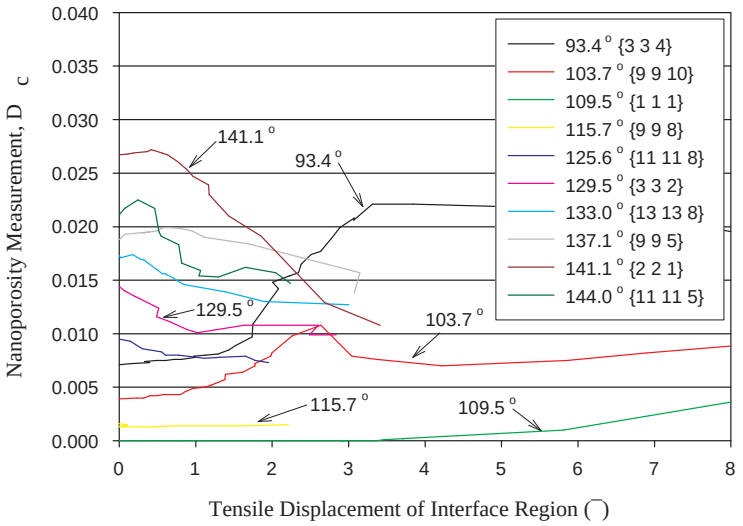


**(b)**

**Figure 9.5:** (a) Stress versus displacement and (b) nanoporosity versus displacement during uniaxial tension of symmetric bicrystal interface models in copper with ⟨110⟩ tilt axis.

associated with maximum tensile interface stress, as shown in Figure 9.6(c). Interestingly, many of the ISF facets remain close to their original length. The trailing partial dislocation is not observed to be emitted from the interface; thus, subsequent dislocation nucleation events (beyond Figure 9.6(c)) will likely be affected by the presence of the trailing partial dislocation at the interface. Analogous to the interface coarsening event observed for some boundaries with a ⟨100⟩ misorientation axis (Figure 9.3), there is some inelastic behavior that occurs at the interface prior to peak tensile stress. This observation is also in qualitative agreement with MD simulations of deformation in nanocrystalline materials, as discrete atomic events (such as shuffling) are often observed at the boundary prior to partial dislocation emission (*cf.* [138]).

Nanoporosity evolution during tensile deformation is shown in Figure 9.5(b). Again, the nanoporosity measure is capable of differentiating between dissimilar groups of boundaries. The $\Sigma 9\,(221)\,\theta = 141.1^\circ$ boundary, which is composed entirely of E structural units, has the highest initial interfacial porosity. For boundaries with misorientations between $\Sigma 113\,(998)\,\theta = 115.7^\circ$ and $\Sigma 9\,(221)\,\theta = 141.1^\circ$, the porosity within the interface region decreases nearly immediately upon application of the tensile deformation. This decrease is associated with the nucleation of the short intrinsic stacking fault facets from the E structural units, as shown in Figure 9.6(b). Similar to the coarsening effect for copper boundaries with ⟨100⟩ misorientation axis, the formation of short ISF facets reduces the free volume along the interface, improving the coordination of atoms at the boundary.

Figure 9.7 shows the maximum tensile stress achieved during uniaxial tension of interface models with a ⟨110⟩ misorientation axis as a function of interface misorientation angle. Again, several single crystal calculations are reported to determine the role of the lattice orientation on the magnitude of the peak tensile stress. Recall, the orientation of each SC model is identical to that of the lower lattice region of the corresponding interface model. These results re-emphasize the abrupt drop in the maximum tensile stress for ⟨110⟩ tilt boundaries with misorientations greater than 109.5°. This drop in tensile strength is

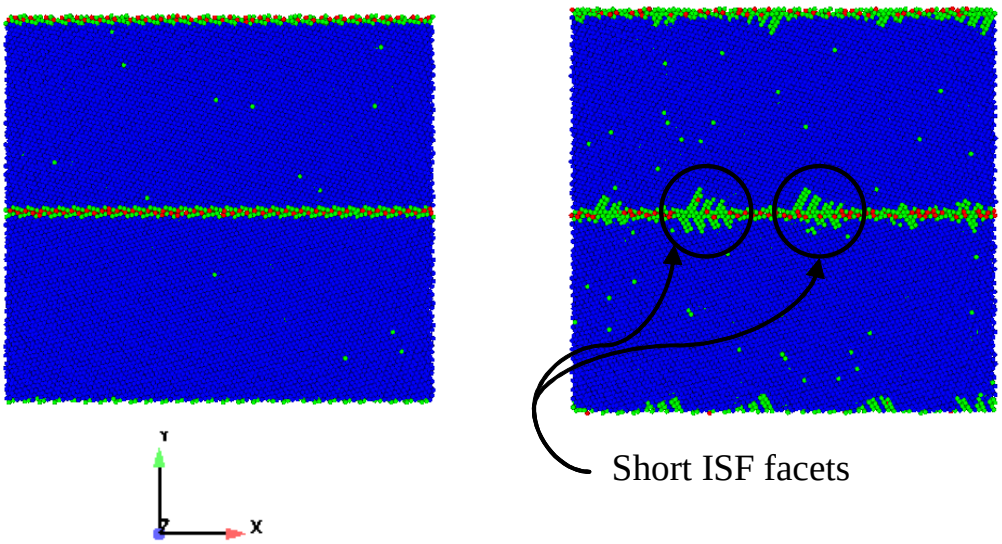


**(a)** **(b)**

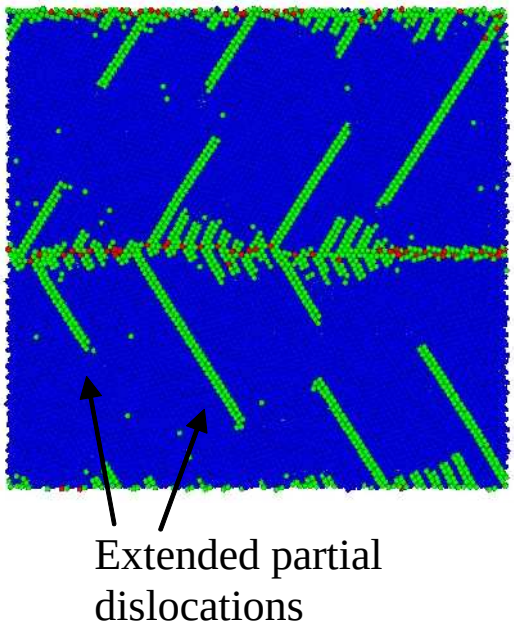


**(c)**

**Figure 9.6:** Projection view of the $\Sigma 9\,(221)\,\theta = 141.1^{\circ}$ interface (a) after isobaric-isothermal equilibration, (b) showing the emission of short ISF facets from the interface and (c) after the nucleation of extended partial dislocations from the interface.

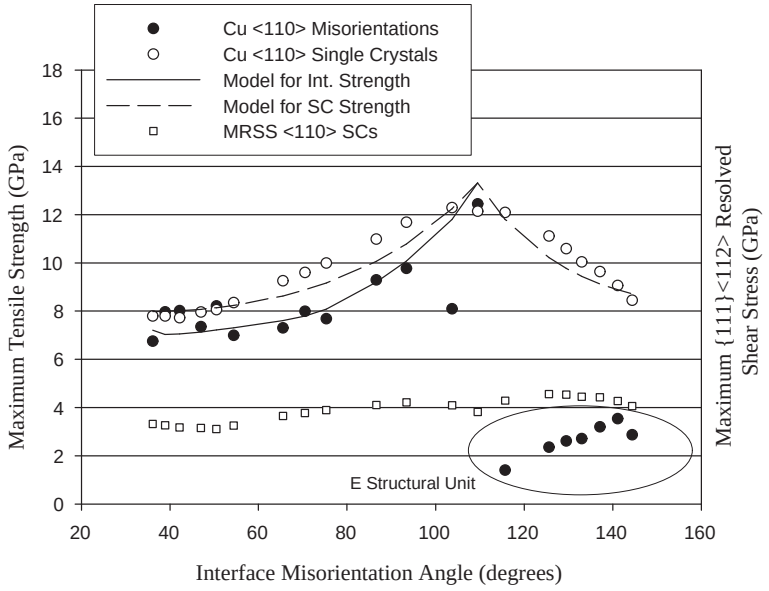


**Figure 9.7:** Maximum tensile stress and maximum resolved shear stress attained during uniaxial tensile deformation for symmetric tilt boundaries as a function of misorientation angle for ⟨110⟩ tilt axis. Single crystal case is included for comparison.

related to the interface structure, as the single crystal calculations do not indicate a discontinuous reduction in the stress required for dislocation emission as the misorientation angle of the interface is increased beyond 109.5°.

## *9.5 Interface strength model*

A simple model is proposed to correlate tensile interface strength, which is associated with the emission of partial dislocations and certain first-order characteristics of the interface structure. The aim of the proposed model is to illustrate the impact of interfacial porosity and non-glide direction stresses on tensile interface strength. This model is developed through the following two step process. First, MD simulation results for uniaxial tensile deformation of single crystal models are used to isolate the influence of lattice orientation on the maximum tensile stress. Figures 9.4 and 9.7 indicate that the partial dislocation *nucleation* process in SC models shows non-Schmid character, as the maximum resolved shear stress varies as a function of orientation. To capture this evolution, non-glide direction

stress components acting on the slip plane must be taken into consideration [143, 259, 285]. For example, the effect of non-Schmid components on dislocation nucleation was studied using *ab initio* calculations by Ogata *et al.* [143]. They found that compressive stresses acting normal to the slip plane can affect the shear stress required for dislocation emission. Accordingly, the relationship

$$\sigma_{max}^{sc} = \frac{\tau_{ideal}}{\mu_s SF + \mu_n NF + \mu_p PF} \tag{9.1}$$

is proposed for *single crystals* subjected to uniaxial tensile stress, where

$$\begin{aligned} SF &= \ell_{y'y}\ell_{x'y} \\ NF &= \ell_{y'y}^2 \\ PF &= \ell_{y'y}\ell_{z'y} \end{aligned} \tag{9.2}$$

Here, $\ell_{ij}$ are the direction cosines relating a coordinate axis fixed to the slip plane ($x'$ is the slip direction, $y'$ is normal to the slip plane and $z'$ lies within the slip plane, perpendicular to the slip direction [257]) to a fixed specimen coordinate system ($x$, $y$ loading direction, and $z$). These direction cosines pertain to the initial (undeformed) configuration of the crystal. Thus, $SF$ projects the uniaxial applied stress into the resolved shear stress acting on the slip plane in the slip direction (the conventional Schmid factor), $NF$ projects the uniaxial stress into the stress normal to the slip plane, and $PF$ projects the uniaxial stress into a shear stress acting on the slip plane perpendicular to the slip direction (coslip direction). The active slip system is defined by the maximum $SF$ among all possible slip systems. In Equation 9.2, the ideal shear strength $\tau_{ideal}$ is defined as the resolved shear stress required for partial dislocation nucleation when all other stress components acting on the slip plane are zero. *Ab initio* calculations by Ogata *et al.* [143] find that $\tau_{ideal} = 2.16$ GPa for copper. The parameters $\mu_s$, $\mu_n$ and $\mu_p$ are positive scalars used to characterize the degree of non-Schmid behavior. Therefore, an increase in any of the coefficients $\mu_s$, $\mu_n$ or $\mu_p$ reduces the predicted peak stress required for dislocation nucleation by increasing the

weight of the corresponding stress component. If $\mu_s = 1$ and $\mu_n = \mu_p = 0$, the proposed model reduces to Schmid's law for single crystal slip, *i.e.*, $\sigma_{max} = \tau_{ideal}/SF$.

The evolution of $SF$, $NF$ and $PF$ as a function of orientation for atomistic models with ⟨100⟩ and ⟨110⟩ tilt axes is shown in Figures 9.8(a) and 9.8(b), respectively. For atomistic models with a ⟨100⟩ tilt axis in Figure 9.8(a), the $SF$ is symmetric about the 45° rotation. Thus, if the tensile stress required for dislocation nucleation showed perfect Schmid behavior, the minimum tensile stress would occur at 45°, while the maximum tensile stress would occur at 0° and 90°. Figure 9.4 clearly shows that the tensile stress required for dislocation nucleation in SC models decreases as the orientation of the lattice increases from 0° to 90°. To capture this response, the stress normal to the slip plane (normal factor, $NF$) must contribute to the maximum tensile stress for dislocation nucleation in single crystal samples. For atomistic models with a ⟨110⟩ tilt axis in Figure 9.8(b), both $SF$ and $NF$ indicate that the maximum tensile stress required for dislocation nucleation should occur at the 109.5° rotation, in agreement with the single crystal MD simulation results presented in Figure 9.7.

Least squares regression is used to determine appropriate values for $\mu_s$, $\mu_n$ and $\mu_p$ for atomistic models with ⟨100⟩ and ⟨110⟩ misorientation axes; these values are shown in Table 9.1. Parameters are fit separately for models with ⟨100⟩ and ⟨110⟩ misorientation axes by minimizing the sum of the squares of the residual error between the calculated peak tensile stress data and the predicted values. The values of the fitting parameters represent the minimum sum of squares for both single crystal and bicrystal calculations; the difference between minimizing the sum of squares separately versus concurrently is negligible. Figures 9.4 and 9.8 show that the proposed relationship (Equation 9.1) correlates well with the MD simulations for uniaxial tension of single crystals rotated at various orientations about ⟨100⟩ and ⟨110⟩ axes, respectively. Apparently, the $NF$ is essential to describe dislocation nucleation in ⟨100⟩ single crystal models, while the maximum tensile stress required for dislocation nucleation in ⟨110⟩ single crystal models correlates more strongly with the $SF$

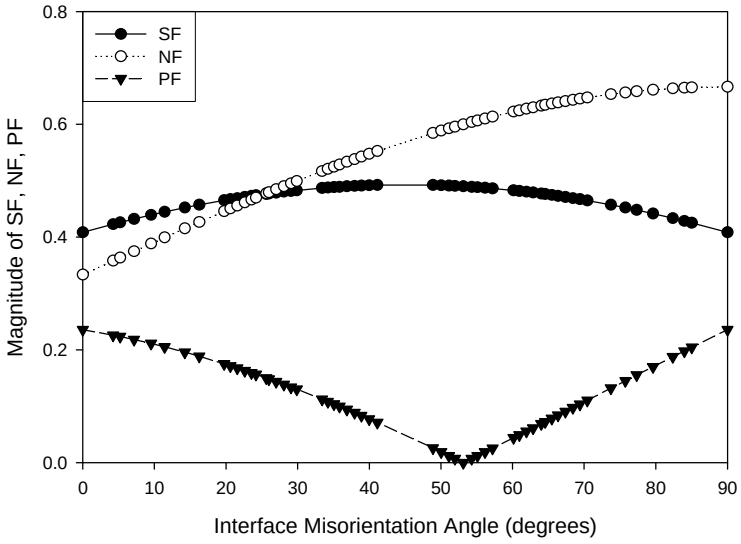


**(a)**

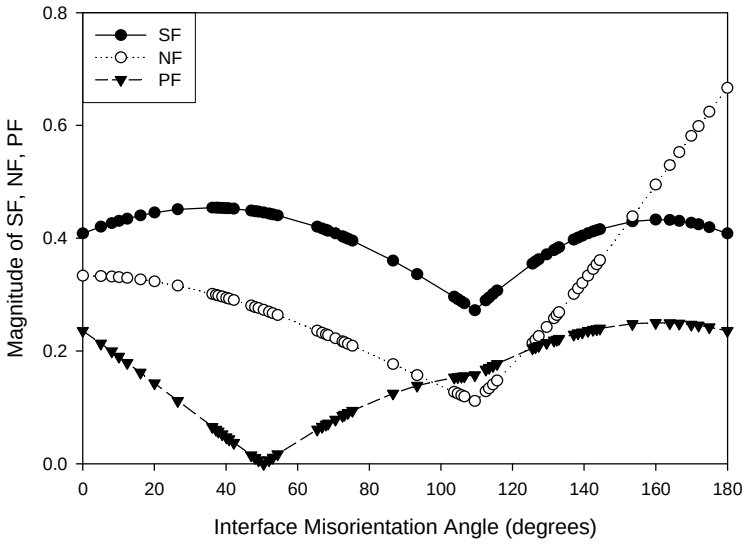


**(b)**

**Figure 9.8:** Evolution of the Schmid factor ($SF$), the normal factor ($NF$) and the coslip factor ($PF$) as a function of the interface misorientation angle for symmetric tilt boundaries with (a) ⟨100⟩ and (b) ⟨110⟩ tilt axes.

**Table 9.1:** Parameters used in the strength model for single crystal and bicrystal interfaces.

| Boundaries | $\tau_{ideal}$ | $\mu_s$ | $\mu_n$ | $\mu_p$ | $\xi$ |
|---|---|---|---|---|---|
| ⟨100⟩ Single Crystal | 2.16 GPa | 0 | 0.69 | 0 | N/A |
| ⟨100⟩ Bicrystal | 2.16 GPa | 0 | 0.69 | 0 | 4.6 |
| ⟨110⟩ Single Crystal | 2.16 GPa | 0.60 | 0 | 0 | N/A |
| ⟨110⟩ Bicrystal $\theta < 109.5^\circ$ | 2.16 GPa | 0.60 | 0 | 0 | 9.3 |

parameter. For example, Figure 9.8(b) shows that for misorientations greater than 109.5°, the $NF$ increases at a much faster rate than the $SF$; this would necessitate that the corresponding SC tensile stress values in Figure 9.7 decrease much more dramatically than those calculated from MD. Finally, for both ⟨100⟩ and ⟨110⟩ tilt axis orientations, the coslip factor $PF$ has minimal effect on the dislocation nucleation stress in SC models. Typically, the non-Schmid parameter $PF$ is used to modify the driving force for cross-slip of screw dislocations in BCC metals (*cf.* [288]).

To further illustrate the relative differences in the roles of $SF$ and $NF$ on dislocation nucleation for uniaxial tension of atomistic models with ⟨100⟩ and ⟨110⟩ misorientation axes, Figures 9.9(a) and 9.9(b) show the magnitudes of $SF$ and $NF$, respectively, against the maximum tensile stress required for dislocation nucleation in single crystal samples. In general, Figure 9.9(a) shows that for small $SF$ values (small resolved shear stress in the direction of slip) the tensile stress required for dislocation nucleation is greater than that at higher $SF$ values. However, for some ⟨100⟩ orientations, the maximum tensile stress values deviate from this general trend, revealing that $SF$ alone is incapable describing the nucleation stress for the ⟨100⟩ case. In Figure 9.9(b), a similar trend is observed; as the $NF$ magnitude increases, the stress required for dislocation nucleation decreases. In other words, an increase in the stress projected normal to the slip plane decreases the applied stress necessary to nucleate dislocations within the crystal lattice; this dependence on the normal stress has been observed using *ab initio* simulations by Ogata *et al.* [143]. Interestingly, the ⟨110⟩ curve displays the same general trend as the ⟨100⟩ data, but is divided

into two regions: $\theta < 109.5°$ and $\theta > 109.5°$. The $\Sigma 3$ coherent twin boundary ($\theta = 109.5°$) separates these two regions, delineating the transition between active slip systems for the two regions. Recall that the two active slip systems for the $\theta < 109.5°$ single crystal orientations occur on different slip planes while the two slip systems for $\theta > 109.5°$ are on the same slip plane (coplanar slip). These data suggest a strong correlation between the stress normal to the slip plane and the dislocation *nucleation* event. However, to correlate $NF$ and the nucleation stress completely clearly requires a more complex formulation that accounts for the relationship between active slip systems.

Once the effect of lattice orientation has been isolated, the second step in the development of the interface strength model is to incorporate a first-order dependence on the inherent GB nanoporosity, $D_c$, via the simple relation

$$\sigma_{max}^{int} = (1 - \xi D_c)\, \sigma_{max}^{sc} \tag{9.3}$$

Here, $\xi$ is an amplification factor, the magnitude of which is dependent on the scale of the selected interface region which is used to compute the average nanoporosity (recall Section 2). This representation considers only the average porosity within a strip around the interface, without regard to its distribution along the interface plane. Here, $D_c$ is the initial nanoporosity [1] inherent to the interface structure. It is computed in the present case from atomistic simulations prior to imposition of tensile deformation (stress). The nanoporosity measure is developed by examining the first-nearest neighbor coordination number of each atom, $Z_1^i$. Of course, atoms in a perfect bulk FCC crystalline arrangement have a first-order coordination number of 12. Atoms with $Z_1^i$ less than that of the bulk crystal are defined as 'damaged' in this methodology. Previous molecular dynamics simulations on nanocrystalline samples [289] have shown that atoms at grain boundaries and triple junctions have a range of coordination numbers, implying the presence of initial porosity within the interface structure. In this work, damaged atoms may be directly attributed to porosity at the interface between crystalline regions (aside from thermal vibrations which have been found

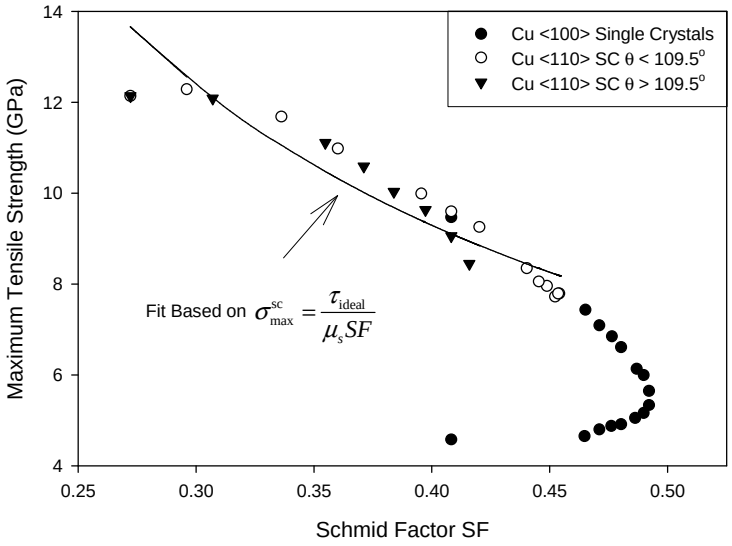


**(a)**

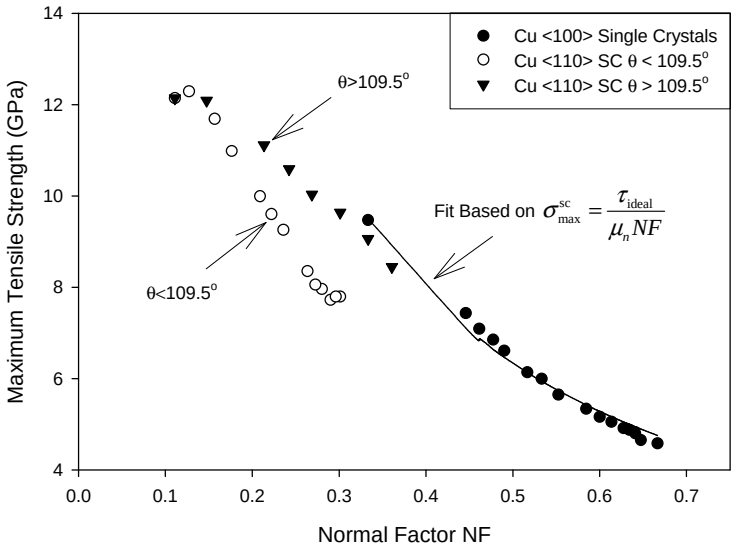


**(b)**

**Figure 9.9:** Single crystal tensile strength for dislocation nucleation as a function of (a) the Schmid factor parameter ($SF$) and (b) the normal factor ($NF$) parameter.

to have a negligible affect on the $D_c$ calculation at 300 K). Using this concept, a damage parameter on a per atom basis is formulated,

$$D^i = 1 - \left\langle \frac{Z_1^i - Z_{1,th}}{Z_{1,ref} - Z_{1,th}} \right\rangle \tag{9.4}$$

In Equation 9.4, $Z_{1,ref}$ is the coordination number associated with a perfect crystalline lattice and $Z_{1,th}$ is the threshold coordination number required for an atom to be considered completely damaged ($D^i = 1$). This threshold value is taken as $Z_{1,th} = 8$ in this work; however, $Z_{1,th}$ may be adjusted to make the calculation of $D^i$ sensitive to different types of interfacial damage. Equation 9.4 allows the i$^t$$h$ atom to have partial damage ($0 \leq D^i \leq 1$) depending on its local environment. Angle brackets define that atoms with $Z_1^i < Z_{1,th}$ have $D^i = 1$ and atoms with $Z_1^i > Z_{1,th}$ have $D^i = 0$. The nanoporosity measure is defined as the average of the point-wise damage parameter over the interface region,

$$D_c = \frac{1}{N'} \left[ \sum_{i=1}^{N'} D^i \right] = \frac{1}{N'} \left[ \sum_{i=1}^{N'} \left( 1 - \left\langle \frac{Z_1^i - Z_{1,th}}{Z_{1,ref} - Z_{1,th}} \right\rangle \right) \right] \tag{9.5}$$

Here, $N'$ is the total number of atoms within the interface region. Numerically, Equation 9.5 may be evaluated at each time step from the atomic positions and requires no *a priori* knowledge of the interface structure or the form of the porosity evolution. In summary, the proposed model for tensile interface strength requires specification of the crystal lattice geometry, the associated non-Schmid parameters $\mu_s$, $\mu_n$ and $\mu_p$, the initial interface nanoporosity, and an amplification factor, $\xi$. Further development of a relationship relating the crystal lattice geometry with nanoporosity would allow the calculation of the tensile stress required for interfacial dislocation nucleation using only continuum quantities and the aforementioned non-Schmid parameters.

The interface strength model (Equation 9.3) is then fit to the computed peak tensile stress values for interface models with $\langle 100 \rangle$ and $\langle 110 \rangle$ misorientation axes (the value of the amplification parameter is included in Table 9.1). The amplification factor $\xi$ is regarded as an additional fitting parameter that is required in Equation 9.3 to predict the peak tensile

interface stress values. The least-squares regression fit for the interface models with ⟨100⟩ and ⟨110⟩ misorientation axes uses the same non-Schmid parameters $\mu_s$, $\mu_n$ and $\mu_p$ that were calculated using the single crystal data. Figure 9.4 shows that the proposed relationship is capable of capturing the influence of interface structure on the maximum tensile stress for bicrystal interfaces with a ⟨100⟩ misorientation axis. For these boundaries, the role of the interface misorientation on dislocation nucleation is effectively captured through the averaged description of the interfacial porosity. Figure 9.7 shows that the proposed relationship works well for boundaries with a ⟨110⟩ misorientation axis and $\theta < 109.5°$. However, MD simulation results indicate that the proposed first-order model is not universally applicable, as this model is unable to capture the significant drop in the maximum tensile stress for symmetric boundaries which include the E structural unit ($\theta > 109.5°$).

In order to address a greater range of interface misorientations for the ⟨110⟩ tilt axis, two solutions are currently being pursued to enhance the interface strength model. First, a higher-order formulation may be proposed, which includes a dependence on the *gradient* of nanoporosity within the interface region. It is possible that localized 'pockets' of porosity, characteristic of interfaces with the E structural unit, result in high stress concentrations that contribute to the drop in tensile strength by promoting dislocation nucleation. Second, the amplification factor for the nanoporosity measure may be posed as a function of the distribution of specific structural elements. This modification acknowledges that dissimilar interface features can contribute differently to the dislocation nucleation process. For example, Van Swygenhoven *et al*. have observed that stress concentrations at ledges and triple junctions in nanocrystalline samples can promote dislocation nucleation [53]. In our work, the natural alignment of certain structural units with respect to the primary slip systems appears to render certain interface features particularly susceptible to dislocation nucleation. For these boundaries, the tensile interface strength computed from MD simulations is probably closer to the Peierls-Nabarro stress (the applied stress required to overcome the lattice resistance to the movement of the interfacial dislocations).

Although not considered in this work, temperature will also affect the peak stress required for dislocation nucleation. For example, Schiøtz *et al.* reported stress-strain data over a wide range of temperatures for nanocrystalline copper samples with grain size between 3 and 13 nm [59]. They observed a clear softening effect in the tensile stress-strain response as the temperature was increased from 0 K to 1200 K. In this work, all MD simulations are performed at 300 K; thus temperature dependence is not included in Equations 9.1 and 9.3. One possible method to incorporate temperature is to formulate a multiplicative temperature dependent function, $f(T)$, and to present the interface tensile strength relation as, $\sigma_{max}^{int} = f(T)(1 - \xi D_c)\sigma_{max}^{sc}$. Of course, $f(T = 300K) = 1$ would give the results in the present study. Indeed, preliminary MD simulations which compare the peak tensile stress values at 10 K and 300 K show that the magnitude of $f(T)$ changes with interface misorientation; this indicates that thermal activation influences dissimilar interfaces differently with respect to dislocation nucleation. We leave consideration of the form of $f(T)$ to future work, although it is clear from Schiøtz *et al.* [59] that this form is nonlinear.

## *9.6 Summary*

In this chapter, molecular dynamics simulations are used to model nucleation of dislocations at or near symmetric tilt interfaces in copper with ⟨100⟩ and ⟨110⟩ misorientation axes. The aim of this work is to (i) identify particular features of the interface structure that play an important role in the tensile deformation response and (ii) propose a simple first-order model to illustrate the influence of interfacial porosity and stresses in non-glide directions on interfacial strength in tension. Aside from the coherent $\Sigma 3\,(111)\,\theta = 109.5^\circ$ boundary, no increase in tensile strength (or other special behavior) is observed at boundaries with low-order CSL character. For all other models, failure in uniaxial tension occurs by way of partial dislocation nucleation from the bicrystal interface. The partial dislocation nucleation event may be accompanied by structural rearrangement prior to emission (coarsening or the emission of short stacking fault facets) that locally improves the coherency of the

interface. MD simulations indicate that the orientation of the opposing lattice regions relative to the applied stress and the presence of certain structural units are two critical features of the interface structure that affect the tensile interface strength. Specifically, boundaries that contain the E structural unit nucleate dislocations at low applied tensile stresses. MD simulations on both single crystal and interface models indicate that non-Schmid effects must be incorporated when formulating a model for dislocation nucleation. Specifically, the stress normal to the slip plane is found to play a significant role in the dislocation nucleation event for boundaries with the ⟨100⟩ misorientation axis. Last, accounting for interfacial porosity through an average measure based on coordination number is found to be sufficient to model the tensile strength of boundaries with the ⟨100⟩ tilt axis and many boundaries with the ⟨110⟩ tilt axis. However, for ⟨110⟩ boundaries that contain the E structural unit, it is likely that a higher-order model must be invoked that includes the effect of porosity gradients or more detailed information concerning the relationship between structural unit configuration and slip system orientation. For citation of the work contained in this chapter, the reader is referred to Ref. [64].

# CHAPTER X

# ATOMISTIC SIMULATIONS OF HOMOGENEOUS DISLOCATION NUCLEATION IN SINGLE CRYSTAL COPPER

Chapter 10 describes a second generation model to correlate dislocation nucleation stresses calculated from atomistic simulations with continuum parameters related to the resolved stresses. Molecular dynamics simulations are used to investigate how the stress required for homogeneous nucleation of partial dislocations in single crystal copper under uniaxial tension changes as a function of crystallographic orientation. An embedded-atom method potential for Cu is employed at temperatures of 10 K and 300 K. Results indicate that non-Schmid parameters are required to describe dislocation nucleation for certain single crystal orientations. Specifically, the stereographic triangle can be divided into two regions: a region where dislocation nucleation is dominated by the conventional Schmid factor (the resolved shear stress in the direction of slip) and a region where dislocation nucleation is dominated by the normal factor (the resolved stress normal to the slip plane). A continuum relationship that incorporates Schmid and non-Schmid terms to correlate the stress required for dislocation nucleation over all tensile axis orientations within the stereographic triangle is presented. The significance of this work is that simulation results are cast into an atomistically inspired continuum formulation for partial dislocation loop nucleation in FCC single crystals.

## *10.1 Introduction*

Dislocation motion in face-centered cubic (FCC) single crystals is well-known to be governed by the critically resolved shear stress via Schmid's law [215]. However, the factors that control dislocation nucleation are not as well understood as dislocation motion in FCC

crystals.

Rice [126] proposed using the unstable stacking fault energy as a criterion for predicting heterogeneous dislocation nucleation from a crack tip. In his work, the unstable stacking fault energy acts as an energetic barrier for nucleating dislocations (ductile response) that competes with Griffith cleavage (brittle response) at a crack tip. More recent simulations have focused on the atomic mechanisms associated with dislocation nucleation. Spearot and colleagues used bicrystal atomistic simulations to show that grain boundary structural units play an important role in the mechanisms of dislocation nucleation from specific symmetric tilt grain boundaries in Cu [139] and Al [97]. Van Swygenhoven and coworkers also used atomistic simulations to show that grain boundary ledges and triple junctions play an important role in dislocation nucleation and propagation in nanocrystalline materials (*cf.*, [53]). Such simulations help identify the role of grain boundary structure and the underlying nanocrystalline grain boundary network, respectively, on *heterogeneous* dislocation nucleation.

Improved understanding of how dislocations nucleate *homogeneously* within a perfect single crystal is also relevant. For example, nanoindentation simulations, which have been used to explain experimentally observed nanoindentation behavior (*e.g.*, [290–292]), showed that homogeneous dislocation nucleation occurs beneath the indented free surface [106, 107, 293] due to the localized stress state. Moreover, atomistic simulations have been used to analyze the effect of non-glide stress components in FCC [143] and BCC [294] metals to understand how local stress conditions may influence homogeneous dislocation nucleation. Homogeneous nucleation becomes increasingly important as scales of materials or applications approach tens to hundreds of nanometers, and the probability of finding heterogeneous sources decreases. One of the challenges in the characterization of homogeneous dislocation nucleation is the definition of a criterion in continuum models that accurately describes the mechanical conditions that lead to dislocation nucleation (*e.g.*, [295–298]).

The ability to predict homogeneous dislocation nucleation in single crystals due to the localized stress state has potential impact on discrete dislocation dynamics simulations [299–301]. In this computational approach, the deformation of a crystalline material is often modeled by introducing dislocations into the material through Frank-Read sources and tracking the movement of each dislocation segment as a function of the applied stress. A criterion which is capable of predicting dislocation nucleation via the localized stress state would extend the applicability of dislocation dynamics simulations to problems where Frank-Read sources are not the dominant dislocation nucleation mechanism, such as in length scales approaching the nanoscale.

This work utilizes atomistic simulations to examine homogeneous dislocation nucleation in single crystals with the goal of casting the atomistic results in terms of continuum parameters, specifically with regard to the resolved stress components onto the primary slip plane(s). Previous work by the present authors on dislocation nucleation in single crystals has examined the influence of the interface on the nucleation stress [64] and the tension-compression asymmetry of dislocation nucleation in single crystals [80]. Spearot and coworkers [64] examined orientations on the exterior of the stereographic triangle at 300K to contrast with bicrystal calculations of dislocation nucleation. Conversely, the current chapter also examines orientations on the interior of the stereographic triangle, aiming to capture the dependence of dislocation nucleation for all possible single crystal orientations under uniaxial tension. Tschopp and McDowell [80] examined the tension-compression asymmetry in homogeneous dislocation nucleation in single crystal copper and found certain regions of the stereographic triangle that require a higher stress in compression than in tension (*e.g.*, [110] and [111]), and vice versa ([100]). The current chapter provides more detail than Ref. [80] by examining how homogeneous dislocation nucleation in single crystal copper under uniaxial tension depends on loading orientation, temperature, and the Schmid and non-Schmid stresses. In contrast to prior studies of the effect of non-glide

stress components (*i.e.*, confining pressure and compressive normal stresses) on dislocation nucleation by other authors (*e.g.*, [143, 294]), this work examines the dependence of homogeneous dislocation nucleation on the orientation of the uniaxial tensile axis. In this manner, the applied uniaxial tensile stress resolves onto the primary slip system(s), creating stress components in the direction of slip, in the direction normal to the slip plane, and in a direction orthogonal to the first two directions. Furthermore, in the present simulations the normal stress on the slip plane is tensile instead of compressive. Therefore, the objective of this work is to investigate how both the tensile axis orientation *and* the stress components resolved onto the active slip systems affect *homogeneous* dislocation nucleation in FCC Cu. Results show that homogeneous dislocation nucleation in FCC Cu single crystals can depend on the magnitude of both the resolved shear stress in the direction of slip and the resolved tensile stress normal to the slip plane. This increased understanding of the dislocation nucleation process is then used to formulate a continuum relationship that accounts for the dependence of dislocation nucleation on the uniaxial tensile axis orientation.

## *10.2 Simulation methodology*

A parallel molecular dynamics code (Warp [69]) that incorporates domain decomposition is used to deform the single crystal atomistic models. In this work, the embedded-atom method [108, 109] potentials for Cu [124] was employed for the aforementioned reasons in Chapter 2. First, the configuration is equilibrated using MD in the isobaric-isothermal (NPT) ensemble [95] at a pressure of 0 bar and a temperature of either 10 K or 300 K for 10 ps. Next, the configuration is deformed in uniaxial tension at a constant strain rate of $10^9$ $s^{-1}$ with a stress-free condition for the other two boundaries, as in Refs. [97, 139]. The deformation details and the modified equations of motion are presented in Chapter 2. For mechanical properties, the system stress was calculated using the virial definition without the kinetic portion [99], as was discussed in Chapter 2.

The **stress required for dislocation nucleation** is defined as the maximum uniaxial

tensile stress. Visualization of selected tensile axis orientations with the centrosymmetry parameter [106] have shown that dislocations are nucleated at a displacement very close to the maximum tensile stress for all single crystal models. In some cases, dislocations appeared to nucleate slightly before the maximum tensile stress is reached (< 1.0% below the maximum tensile stress). However, in light of the difficulty of visually ascertaining exactly when the dislocation nucleates (*i.e.*, how many spatially clustered, distorted atoms on the slip plane constitute a dislocation?), the maximum tensile stress provides an accurate indication of the stress required to homogeneously nucleate a dislocation in a single crystal. Visualization of the nucleated partial dislocations confirmed that the activated slip system(s) for all tensile orientations is (are) in agreement with that (those) predicted via a Schmid factor analysis [257].

A 3D periodic computational cell is used to investigate *homogeneous* dislocation nucleation in single crystal Cu under uniaxial tension at a constant strain rate. Cell dimensions are chosen to properly enforce the 3D periodic boundary conditions for each orientation, with a minimum length of 16 nm in all directions. This length is chosen to minimize both the effect of periodic boundaries on dislocation nucleation and the number of atoms in the system for computational efficiency. Although not explicitly shown in this work, simulations investigating the effect of the periodic length (2, 4, 8, 12, 16, and 24 nm lengths) validate that the stress required for dislocation nucleation is essentially unaffected by further increases in the size of the simulation cell (*i.e.*, an error of $\leq$ 0.8% for the maximum tensile stress of a $16^3$ nm$^3$ cell when compared to a $24^3$ nm$^3$ cell with a [321] tensile axis at 300 K). This minimum periodic length results in cells with sizes ranging from 352,800 to 842,400 atoms ([310] and [751] orientations, respectively). Therefore, the $16^3$ nm$^3$ cell size is deemed sufficient to avoid significant effects of periodic boundaries on the 3D dislocation nucleation dynamics.

Figure 10.1 shows the tensile axis for the 47 crystallographic orientations examined in this work, within the basic stereographic triangle with [100], [110], and [111] vertices.

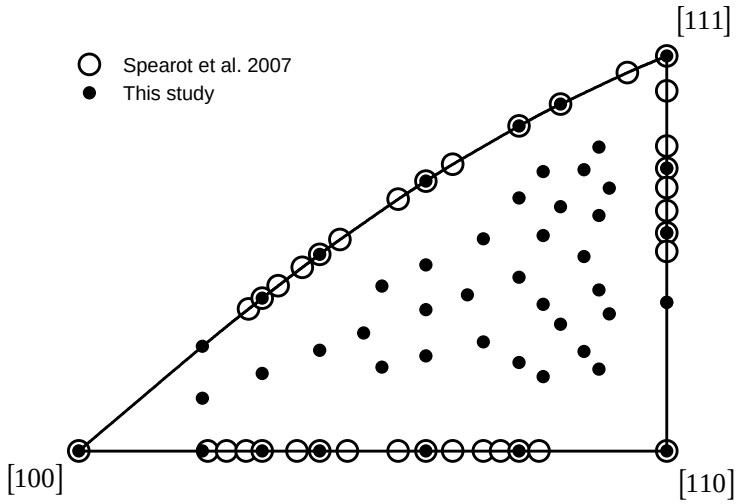


**Figure 10.1:** Stereographic triangle showing the 47 crystallographic orientations for which dislocation nucleation was investigated. Also included are the nucleation stresses from 20 tensile loading orientations from Spearot *et al.* [64]. Each direction denotes the uniaxial tensile axis for the corresponding single crystal deformation simulation.

Each single crystal model is deformed under uniaxial tension at temperatures of either 10 K or 300 K to examine the effect of temperature on the dislocation nucleation stress. The crystallographic orientations and calculated stress values required for dislocation nucleation at 10 K and 300 K are listed in Tables 10.1 and 10.2. For the 300 K case, the dislocation nucleation stress values for an additional 20 crystal orientations along the exterior of the stereographic triangle are used from Spearot *et al.* [64]. The axes of the stereographic triangle represent the latitude $\theta$ and longitude $\phi$ of the tensile axis, where $\theta = \{0°, 45°\}$ and $\phi = \{0°, 35.26°\}$; this coordinate system is employed for plotting the computational results for each orientation on the stereographic triangle. The expected slip system (maximum Schmid factor) is the $\left(11\bar{1}\right)[101]$ slip system for all tensile axis orientations on the interior of the [100]-[110]-[111] triangle. Note that all the interior tensile axis orientations deform via single slip on the $\left(11\bar{1}\right)[101]$ slip system, while all tensile axis orientations on the boundary of the stereographic triangle have at least two active slip systems. If the tensile axis is on the [100]-[111] boundary, the *conjugate* slip system is the $\left(1\bar{1}1\right)[110]$ system. If the tensile axis is on the [100]-[110] boundary, the *critical* slip system is the $(111)\left[10\bar{1}\right]$

system. If the tensile axis is on the [110]-[111] boundary, the *coplanar* slip system is the $\left(1\bar{1}1\right)$[011] system. The [110], [111], and [100] vertices have 4, 6, and 8 active slip systems, respectively, which may have conjugate, critical, and coplanar slip system arrangements.

Figure 10.2 shows images of dislocation nucleation for several loading orientations: [110], [111], [221], and [321]. These images show multiple dislocations at different stages of their formation. Dislocations are rendered by using a cutoff in the centrosymmetry parameter [106] to show only the atoms in a local non-centrosymmetric environment. First, the collective motion of several atoms along the active slip system(s) begins nucleation. Then, the cooperative atomic shuffling of these atoms nucleates a partial dislocation loop within the single crystal, where the exterior of the dislocation loop is the partial dislocation core that bounds an intrinsic stacking fault in the lattice. Thus, the nucleated dislocations have both edge and screw dislocation character. Multiple dislocations are nucleated within the crystal lattice at very similar strains at 10K, which causes dislocation loop interactions as the dislocation loops propagate throughout the crystal. However, these interactions occur after the stress required for dislocation nucleation has been obtained. Examination of the calculated partial dislocation loops indicates that dislocations nucleate on the maximum Schmid factor slip system(s). Figure 10.2 shows that the quadruple slip [110] (Figure 10.2(a)) and octahedral slip [111] (Figure 10.2(b)) orientations have partial dislocation loops on two and three {111} slip planes, respectively. Only partial dislocation loops on one {111} slip plane are observed for the single-slip [321] (Figure 10.2(d)) and double slip [221] (Figure 10.2(c)) orientation, which agrees with the predicted slip systems. Recall that the [221] orientation is a coplanar slip system, *i.e.*, both slip directions are on the same slip plane. Other loading orientations show a similar response with respect to the expected slip systems.

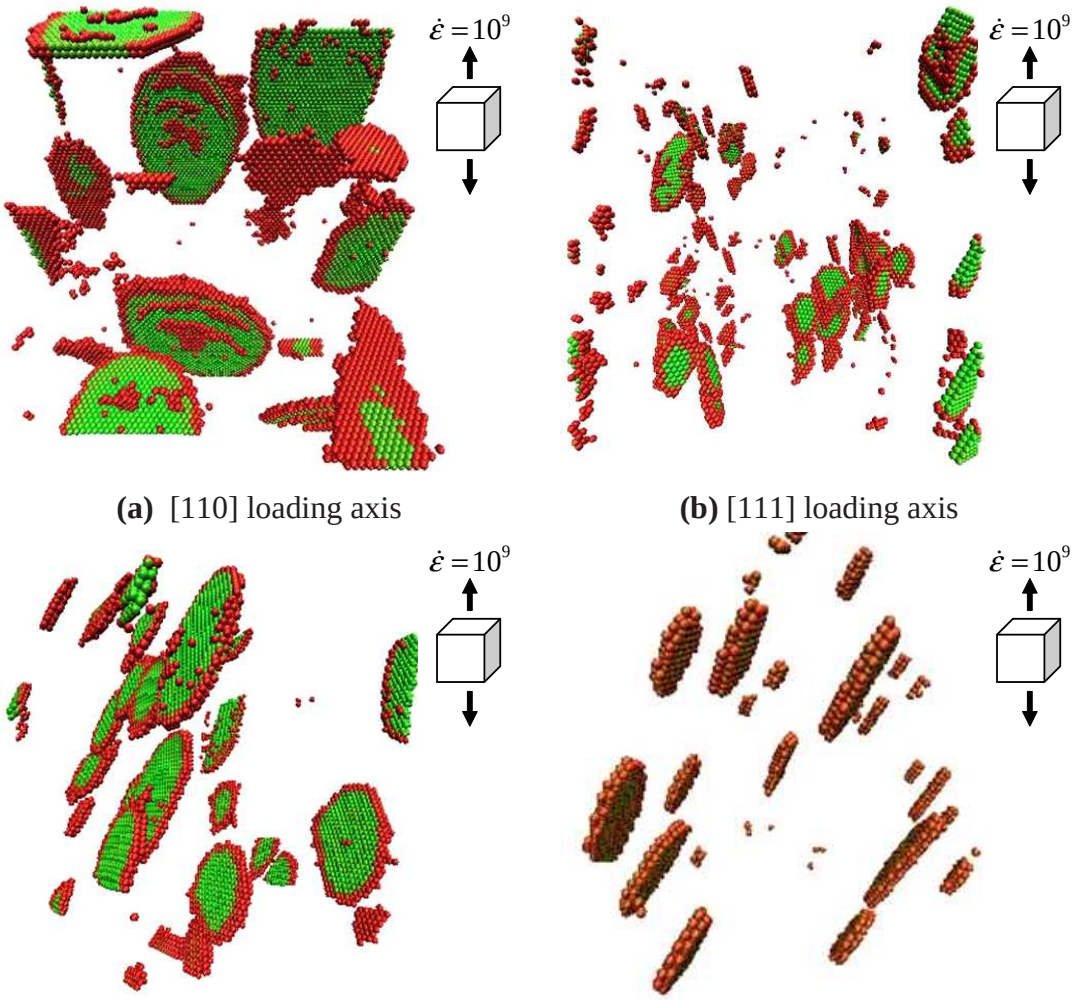


**(a)** [110] loading axis **(b)** [111] loading axis

**(c)** [221] loading axis **(d)** [321] loading axis

**Figure 10.2:** Homogeneous dislocation nucleation for (a) [110], (b) [111], (c) [221], and (d) [321] loading orientations in single crystal Cu at 10 K. Only atoms in a local non-centrosymmetric environment are shown.

**Table 10.1:** List of the 30 crystallographic orientations on the interior of the stereographic triangle examined in this work. Also listed is the calculated stress required for dislocation nucleation at 10 K and 300 K.

| Crystal Orientation | Stress (GPa) 10 K | Stress (GPa) 300 K | Crystal Orientation | Stress (GPa) 10 K | Stress (GPa) 300 K |
|---|---|---|---|---|---|
| [321] | 11.60 | 8.52 | [651] | 7.68 | 6.02 |
| [421] | 10.46 | 7.84 | [652] | 11.00 | 7.81 |
| [431] | 9.75 | 7.22 | [653] | 13.86 | 9.88 |
| [432] | 14.02 | 9.82 | [654] | 15.86 | 11.14 |
| [521] | 9.81 | 7.55 | [731] | 9.17 | 6.99 |
| [531] | 9.43 | 7.18 | [732] | 10.60 | 7.98 |
| [532] | 12.56 | 9.01 | [742] | 11.00 | 8.09 |
| [541] | 8.49 | 6.55 | [751] | 7.70 | 5.95 |
| [542] | 12.37 | 8.92 | [752] | 10.59 | 7.81 |
| [543] | 15.31 | 10.61 | [753] | 12.90 | 9.27 |
| [621] | 9.55 | 7.33 | [754] | 14.87 | 10.44 |
| [631] | 9.28 | 6.89 | [762] | 9.94 | 7.41 |
| [632] | 11.43 | 8.42 | [764] | 14.84 | 10.38 |
| [641] | 8.45 | 6.47 | [821] | 9.61 | 7.47 |
| [643] | 13.82 | 9.98 | [12, 2, 1] | 10.14 | 8.36 |

**Table 10.2:** List of the 17 crystallographic orientations on the exterior of the stereographic triangle examined in this work. Also listed is the calculated stress required for dislocation nucleation at 10 K and 300 K.

| Crystal Orientation | Stress (GPa) 10 K | Stress (GPa) 300 K | Crystal Orientation | Stress (GPa) 10 K | Stress (GPa) 300 K |
|---|---|---|---|---|---|
| [100] | 11.26 | 9.12 | [322] | 15.40 | 10.63 |
| [110] | 5.57 | 4.23 | [331] | 9.74 | 7.20 |
| [111] | 18.21 | 11.79 | [332] | 15.43 | 10.24 |
| [210] | 6.66 | 4.81 | [410] | 9.18 | 6.26 |
| [211] | 13.00 | 9.25 | [411] | 9.63 | 7.44 |
| [221] | 12.75 | 8.71 | [433] | 16.61 | 11.33 |
| [310] | 8.07 | 5.65 | [610] | 10.37 | 7.54 |
| [311] | 10.33 | 7.70 | [611] | 9.71 | 8.00 |
| [320] | 5.96 | 4.45 | | | |

## *10.3 Results and discussion*

### 10.3.1 Schmid and non-Schmid effects

The glide of dislocations in FCC crystals is commonly observed to obey Schmid's law. However, other crystal structures have displayed 'non-Schmid' dislocation behavior [302, 303], whereby dislocation motion exhibits a strong dependence on resolved stress components in directions other than the slip direction. For dislocation nucleation, Ogata *et al.* [143] used *ab initio* calculations to show that compressive stress components acting normal to the slip plane can affect the critical resolved shear stress in Cu and Al, indicating that non-Schmid terms may be required for dislocation *nucleation*. In addition, previous MD calculations [64] showed that the maximum resolved shear stress varies as a function of the tensile axis, reinforcing that non-Schmid terms are required. Consequently, Spearot and colleagues [64] proposed the following relationship for single crystals subjected to uniaxial tensile stress, *i.e.*,

$$\sigma_{max}^{sc} = \frac{\tau_{ideal}}{\mu_s SF + \mu_n NF + \mu_p PF} \tag{10.1}$$

where,

$$\begin{aligned} SF &= \ell_{y'y}\ell_{x'y} \\ NF &= \ell_{y'y}^2 \\ PF &= \ell_{y'y}\ell_{z'y} \end{aligned} \tag{10.2}$$

Here, $\ell_{ij}$ are the direction cosines relating a coordinate axis fixed to the primary slip plane ($x'$ is the slip direction, $y'$ is normal to the slip plane and $z'$ lies within the slip plane, perpendicular to the slip direction [257]) to a fixed specimen coordinate system ($x$, $y$ loading direction, and $z$). These direction cosines pertain to the initial (undeformed) configuration of the crystal. Thus, $SF$ projects the uniaxial applied stress into the resolved shear stress on the slip plane in the direction of the slip direction (the conventional Schmid factor), $NF$ projects the uniaxial stress into a stress **normal** to the slip plane, and $PF$

projects the uniaxial stress into a shear stress acting on the slip plane **perpendicular** to the slip direction (coslip direction). The active slip system(s) for each tensile axis is defined by the maximum $SF$ value(s) among all possible slip systems. The ideal shear strength $\tau_{ideal}$ is defined as the resolved shear stress required for partial dislocation nucleation when all other stress components acting on the slip plane are zero. *Ab initio* calculations find that $\tau_{ideal} = 2.16$ GPa for Cu [143]. The parameters $\mu_s$, $\mu_n$, and $\mu_p$ are positive scalars used to characterize the degree of non-Schmid behavior. Therefore, an increase in any of the coefficients $\mu_s$, $\mu_n$, and $\mu_p$ reduces the predicted stress required for dislocation nucleation by increasing the weight of the corresponding stress component. If $\mu_s = 1$ and $\mu_n = \mu_p = 0$, Eq. 10.1 reduces to Schmid's law for single crystal slip, *i.e.*, $\sigma_{max} = \tau_{ideal}/SF$. In this work, the applicability of the relationship in Eq. 10.1 to the entire stereographic triangle will be re-evaluated.

Figure 10.3 shows how the Schmid factor ($SF$) and the normal factor ($NF$) change as a function of the crystal orientation with respect to the tensile axis. The maximum $SF = 0.5$, occurs in the interior of the stereographic triangle, while the maximum $NF = 0.666$, occurs for the [110] direction. The minimum Schmid factor, $SF = 0.272$, and normal factor, $NF = 0.111$, occur for the [111] orientation. MD simulations in this work show that dislocation nucleation can be correlated to specific regions within the stereographic triangle where the $SF$ is greater than the $NF$, or vice versa. The orientation dependence of $SF$ and $NF$ play an important role in the homogeneous dislocation nucleation process.

The coslip factor ($PF$) is not included in Figure 10.3; an analysis of the Schmid and non-Schmid components for FCC Cu shows that the coslip factor has essentially no effect (*i.e.*, $\mu_p = 0$) on the stress required for dislocation nucleation [64]. Typically, the non-Schmid parameter $PF$ is used to modify the driving force for cross-slip of screw dislocations in body-centered cubic metals (*cf.*, [288]).

The stress required for dislocation nucleation is calculated for all tensile axis orientations examined in this work. Figure 10.4 shows contour plots of the stress required for

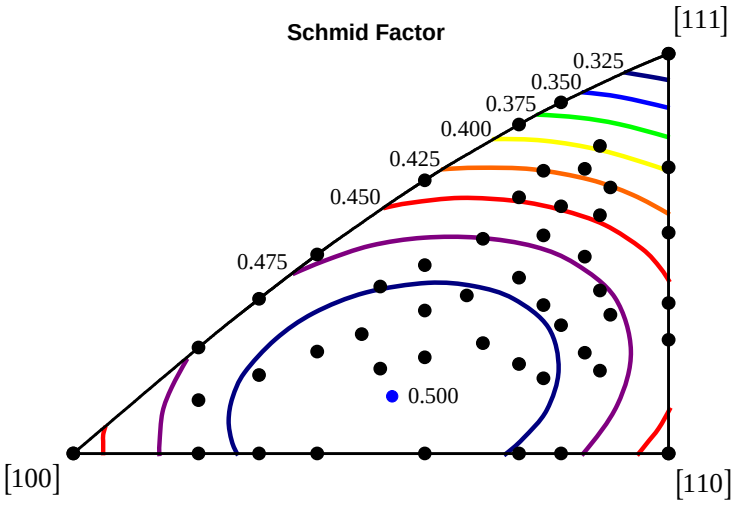


**(a)**

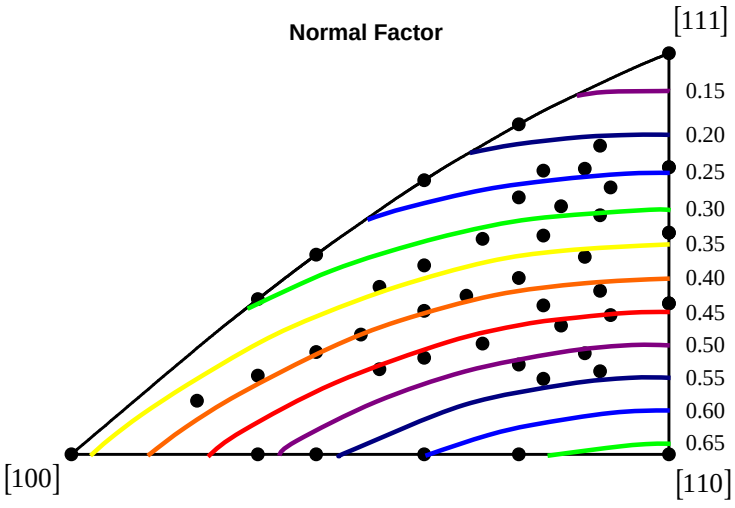


**(b)**

**Figure 10.3:** Orientation dependence of the (a) Schmid factor ($SF$) and (b) normal factor ($NF$) for FCC crystals.

dislocation nucleation as a function of the tensile axis orientation on the stereographic triangle at 10 K and 300 K, respectively. All intermediate tensile axis orientations in the stereographic triangle are obtained through linear interpolation. For both temperatures, the [111] axis requires the largest stress for dislocation nucleation while the [110] axis requires the lowest stress for dislocation nucleation. Moreover, the stress contours between 10 K and 300 K appear very similar, other than the magnitude of the nucleation stresses. Note that the stress along the [100]-[110] boundary is relatively unchanged near the [110] vertice of the stereographic triangle; this trend is similar to the normal factor contour in Figure 10.3(b). All other stress contours for Fig. 10.4(a) and 10.4(b) appear similar to the Schmid factor contours in Figure 10.3(a).

To illustrate the relative differences in the role of the $SF$ and $NF$ terms in dislocation nucleation process for uniaxial loading, Figs. 10.5(a) and 10.5(b) show the magnitudes of $SF$ and $NF$, respectively, against the maximum tensile stress required for dislocation nucleation in single crystals at 300 K. In general, Figure 10.5(a) shows that the tensile stress required for dislocation nucleation decreases as the magnitude of $SF$ increases (*i.e.*, as the resolved shear stress in the direction of slip increases). However, several orientations deviate from this trend, revealing that $SF$ alone is not capable of capturing all aspects of the dislocation nucleation process. In Figure 10.5(b), a similar trend is observed; as the magnitude of $NF$ increases (*i.e.*, as the resolved stress normal to the slip plane increases), the stress required for dislocation nucleation decreases. The peak stress values in Figs. 10.5(a) and 10.5(b) are separated into orientations where single slip is predicted (interior of stereographic triangle) and those where multiple slip systems are expected (exterior of stereographic triangle). Interestingly, for a similar magnitude of $SF$, a higher stress for dislocation nucleation is found for tensile axis orientations for which single slip is expected. A similar trend is not observed for $NF$.

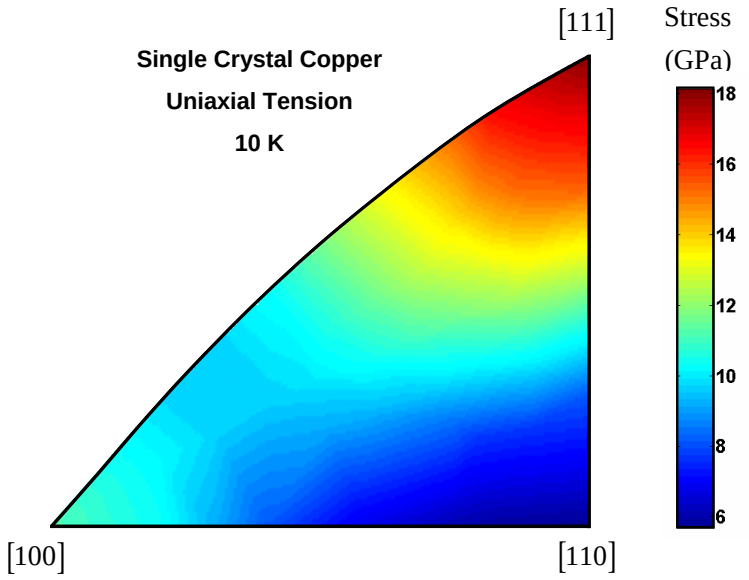


**(a)**

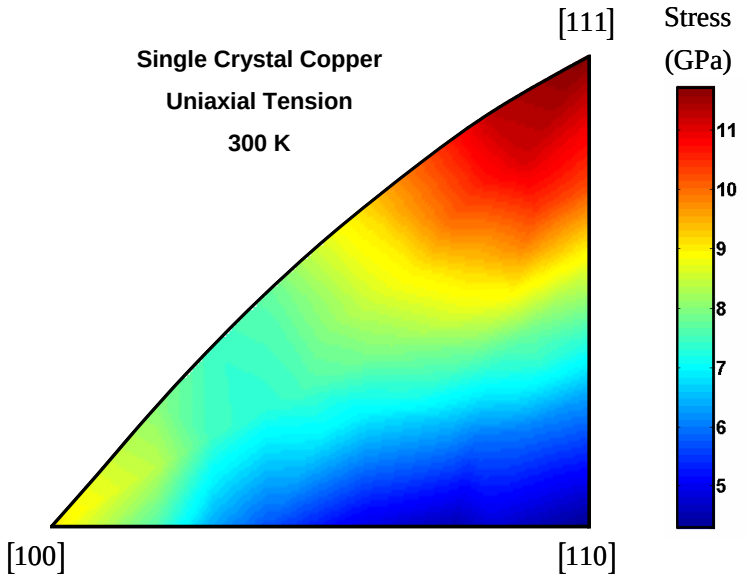


**(b)**

**Figure 10.4:** Tensile stress required for homogeneous dislocation nucleation as a function of tensile axis orientation for single crystal models at (a) 10 K and (b) 300 K.

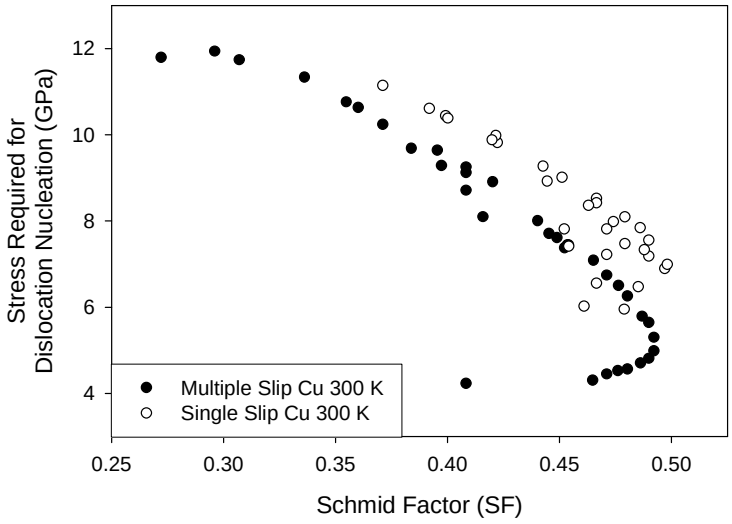


**(a)**

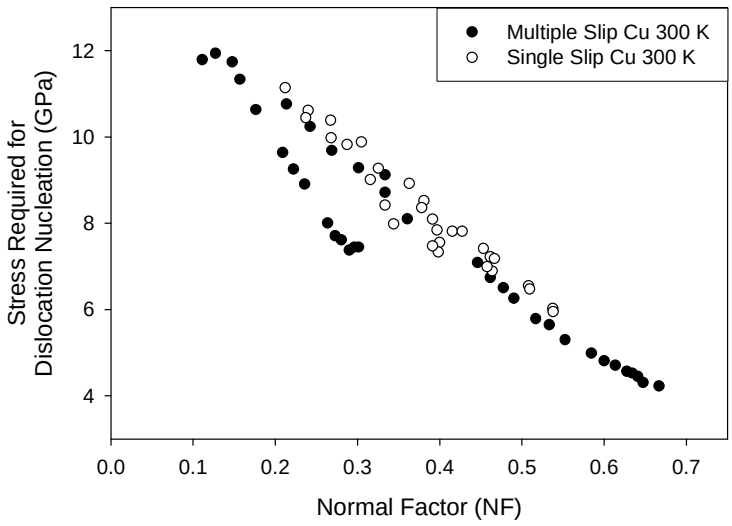


**(b)**

**Figure 10.5:** Tensile stress required for homogeneous dislocation nucleation as a function of (a) Schmid factor ($SF$) and (b) normal factor ($NF$) at 300 K. Black and white symbols denote multiple slip or single slip orientations, respectively.

### 10.3.2 Temperature effect

The influence of temperature on the stress required for dislocation nucleation in single crystal Cu is investigated in Figs. 10.6(a) and 10.6(b) as a function of $SF$ and $NF$, respectively. As expected, the peak stress decreases with increasing temperature; *i.e.*, thermal energy aids the dislocation nucleation process. In Figure 10.6, arrows illustrate the difference in the stress required for dislocation nucleation between the two temperatures for the [100], [110], and [111] tensile axis orientations. The [111] axis shows the largest difference in the peak stress magnitude with respect to temperature, while the [110] axis shows the smallest difference. Clearly, thermal energy affects the magnitude of the stress required for dislocation nucleation differently depending on the tensile axis of the single crystal configuration.

Figure 10.7 shows the percent decrease in the dislocation nucleation stress at 300 K relative to that at 10 K as a function of the stress required for dislocation nucleation at 10 K. Data in Figure 10.7 shows that tensile axis orientations with a higher dislocation nucleation threshold stress at 10 K are more adversely affected by increases in temperature. This trend is quite strong for single crystal models with orientations on the interior of the stereographic triangle (single slip regime). The trend is less apparent for tensile axis orientations along the exterior of the stereographic triangle (multiple slip regime), possibly due to an interaction between the temperature and the nature of the multiple active slip systems (conjugate vs. critical vs. coplanar). Interestingly, the observed trend correlates well with respect to $NF$, *i.e.*, tensile axis orientations with a higher $NF$ component have a greater percentage decrease in the dislocation nucleation stress with increasing temperature, which is apparent from Figure 10.6(b).

### 10.3.3 Model for homogeneous dislocation nucleation in single crystal Cu

A modified model is proposed to correlate the stress required for dislocation nucleation using both $SF$ and $NF$. The aim of this model is to isolate the influence of lattice orientation with respect to the uniaxial tensile axis on the homogeneous dislocation nucleation

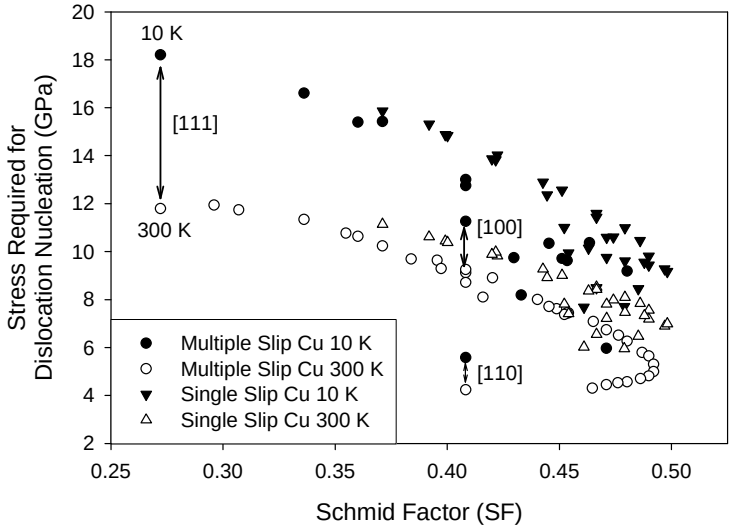


**(a)**

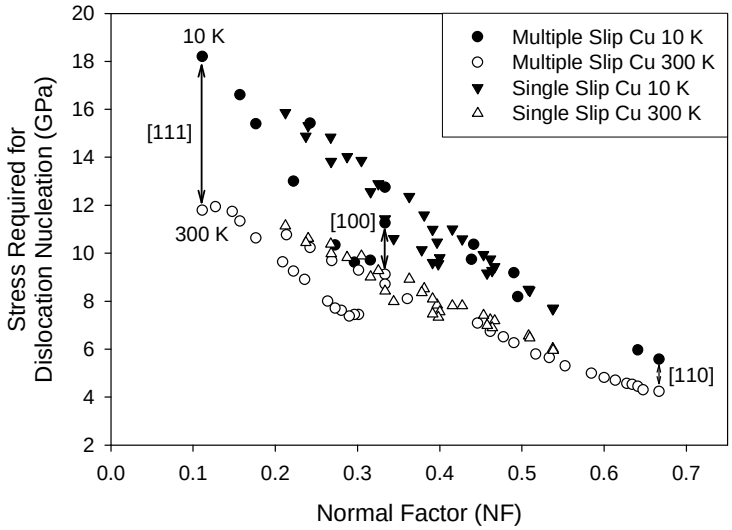


**(b)**

**Figure 10.6:** Tensile stress required for homogeneous dislocation nucleation as a function of (a) Schmid factor ($SF$) and (b) normal factor ($NF$) at 10 K and 300 K. Arrows illustrate the difference in dislocation nucleation stress between 10 K and 300 K for [100], [110], and [111] tensile axis orientations.

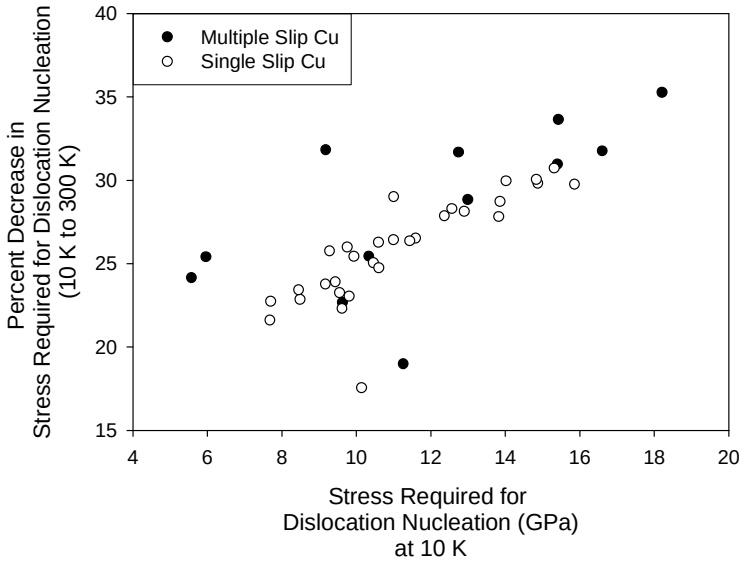


**Figure 10.7:** Percent decrease in the dislocation nucleation stress at 300 K as a function of the stress required for dislocation nucleation at 10 K. Black and white symbols denote multiple slip or single slip orientations, respectively.

event. Recall that the relationship given in Eq. 10.1 is unable to capture the effect on dislocation nucleation stress for all orientations. Spearot and colleagues [64] used different values of $\mu_s$, $\mu_n$, and $\mu_p$ in Eq. 10.1 to correlate the stress required for dislocation nucleation along the [100]-[110], [100]-[111], and [110]-[111] boundaries of the stereographic triangle. They find that the [100]-[110] boundary correlates best with $NF$ and the [100]-[111] boundary correlates best with $SF$, indicating that there are two regions within the stereographic triangle whereby dislocation nucleation is driven by different resolved stresses: a $SF$-dominated region and an $NF$-dominated region. Furthermore, these models are only applied to specific orientations along the exterior of the stereographic triangle.

The aforementioned model in Eq. 10.1 is modified to capture the stress required for dislocation nucleation from all orientations within the stereographic triangle as well as the transition between the $NF$-dominated dislocation nucleation along the [100]-[110] boundary to the $SF$-dominated dislocation nucleation along the [100]-[111] boundary. The following criterion is used to identify the transition between these two regions within the

stereographic triangle, *i.e.*,

$$\sigma_{max}^{sc} = \begin{cases} \frac{\tau_{ideal}}{\mu_{s,1}SF+\mu_{n,1}NF}, & \text{if } \mu_{s,1}SF + \mu_{n,1}NF \geq \mu_{s,2}SF + \mu_{n,2}NF, \\ \frac{\tau_{ideal}}{\mu_{s,2}SF+\mu_{n,2}NF}, & \text{if } \mu_{s,1}SF + \mu_{n,1}NF < \mu_{s,2}SF + \mu_{n,2}NF, \end{cases} \tag{10.3}$$

where $\mu_{s,i}$ and $\mu_{n,i}$ are fitting coefficients for the Schmid factor and normal factor; $i = 1$ corresponds to the $SF$-dominated dislocation nucleation region and $i = 2$ corresponds to the $NF$-dominated dislocation nucleation region. This equation is formulated to allow a mild dependence on $NF$ in an $SF$-dominated region, and vice versa. The use of the fitting parameters within the criterion acts as additional constraint ($\tau_{ideal}/\mu_{s,1}SF + \mu_{n,1}NF = \tau_{ideal}/\mu_{s,2}SF + \mu_{n,2}NF$ when $\mu_{s,1}SF + \mu_{n,1}NF = \mu_{s,2}SF + \mu_{n,2}NF$) that forces a first order transition between the $SF$ and $NF$-dominated regions.

Least squares regression is then used to determine the appropriate values of $\mu_{s,1}$, $\mu_{n,1}$, $\mu_{s,2}$, and $\mu_{n,2}$ based on the data for homogeneous dislocation nucleation in single crystal Cu. The tensile axis of each crystal orientation, Schmid and normal factors, and peak stress required for dislocation nucleation are listed in Tables 10.1 and 10.2; these values are used for the proposed model. The parameters for Eq. 10.3 at 10 K and 300 K are listed in Table 10.3. These parameters are obtained by minimizing the sum of squares of the residual error between the calculated stress data and the predicted values. Interestingly, by forcing $\mu_{s,i} \geq 0$ and $\mu_{n,i} \geq 0$, the minimum sum of squares shows that the normal factor $NF$ has no influence ($\mu_{n,1} = 0$ at 10 K and 300 K) in the $SF$-dominated dislocation nucleation region, while the Schmid factor $SF$ has minimal influence ($\mu_{s,2} = 0$ at 10 K and $\mu_{s,2} = 0.037$ at 300 K) on dislocation nucleation in the $NF$-dominated region. Consequently, if the small dependence of $\mu_{s,2}$ at 300 K is neglected, Eq. 10.3 can be reduced further, *i.e.*,

$$\sigma_{max}^{sc} = \begin{cases} \frac{\tau_{ideal}}{\mu_{s,1}SF}, & \text{if } \mu_{s,1}SF \geq \mu_{n,2}NF, \\ \frac{\tau_{ideal}}{\mu_{n,2}NF}, & \text{if } \mu_{s,1}SF < \mu_{n,2}NF. \end{cases} \tag{10.4}$$

While Eq. 10.4 represents a simplified version of Eq. 10.3, the parameters from Table 10.3

**Table 10.3:** Parameters used in the model for homogeneous dislocation nucleation stress (Eq. 10.3) in single crystals at both 10 K and 300 K.

| Temperature | $\tau_{ideal}$ | $SF$-dominated region | | $NF$-dominated region | |
|---|---|---|---|---|---|
| (K) | (GPa) | $\mu_{s,1}$ | $\mu_{n,1}$ | $\mu_{s,2}$ | $\mu_{n,2}$ |
| 10 K | 2.16 | 0.574 | 0.000 | 0.000 | 0.693 |
| 300 K | 2.16 | 0.396 | 0.000 | 0.037 | 0.473 |

are used with Eq. 10.3 for the remaining discussion in this section.

Figures 10.8(a) and 10.8(b) show that the proposed relationship (Eq. 10.3) correlates well with the MD simulations for uniaxial loading of crystals with tensile axis orientations along the exterior of the stereographic triangle at 300 K. Dislocation nucleation for tensile axis orientations along the [100]-[110] boundary (Figure 10.8(a)) is entirely driven by resolved stress normal to the slip plane (the normal factor), while dislocation nucleation along the [100]-[111] boundary (Figure 10.8(b)) is entirely driven by the resolved shear stress in the direction of slip (the Schmid factor). The proposed model is also able to capture the transition between the $SF$-dominated response to $NF$-dominated response along the [110]-[111] boundary in Figure 10.8(b), unlike the first-generation single crystal model [64]. There is a slight difference in the fitting parameters for the two models in Fig. 10.8(b) that results from the interior orientations of the stereographic triangle in this study. Note that both models overestimate the stress at the [111] corner of the stereographic triangle. Recall that Figure 10.5(a) shows a slight decrease in the stress required for dislocation nucleation (for similar $SF$ values) if the single crystal is oriented such that multiple slip systems are active.

Finally, to show the agreement of the proposed relationship with all stresses for dislocation nucleation in the stereographic triangle, Figure 10.9 compares the predicted values from Eq. 10.3 using parameters from Table 10.3 against the calculated stresses required for dislocation nucleation from MD simulations. The correlation coefficients ($R^2$) for 10 K and 300 K are $R^2 = 0.886$ and $R^2 = 0.920$, indicating good agreement between the predicted and calculated stress magnitudes.

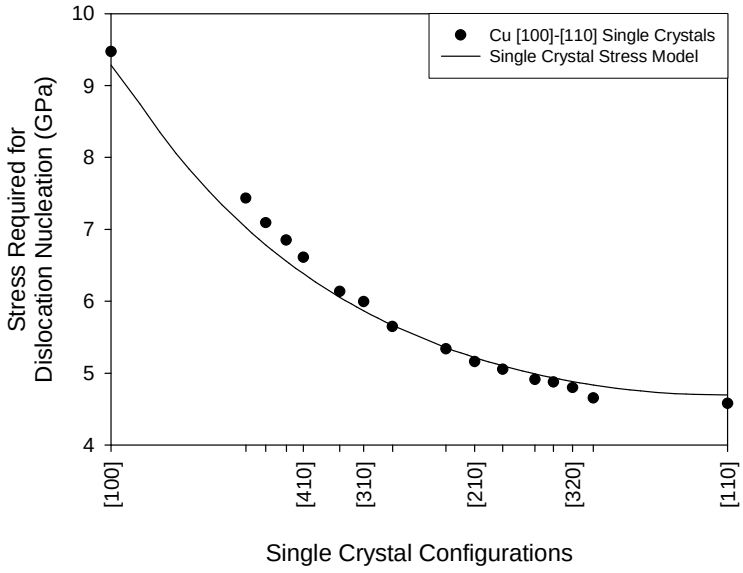


**(a)**

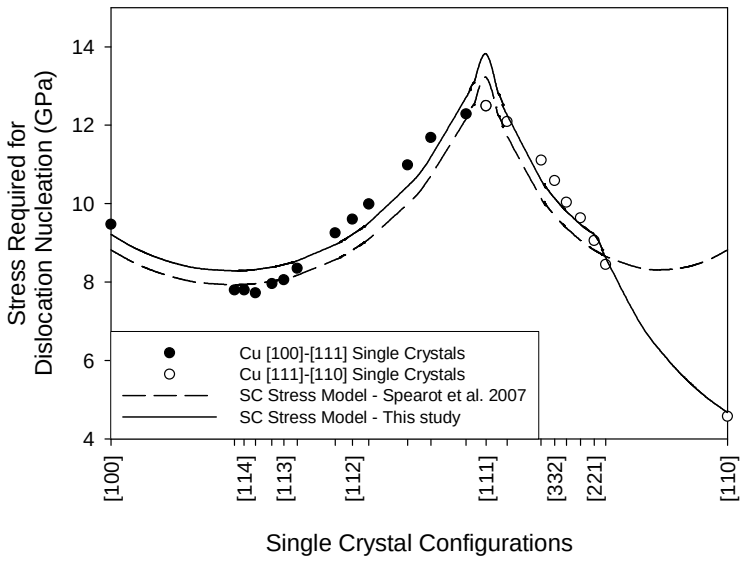


**(b)**

**Figure 10.8:** Tensile stress required for homogeneous dislocation nucleation as a function of the tensile axis orientation for the (a) [100]-[110] boundary and (b) [100]-[111]/[111]-[110] boundaries. Data points represent calculated stress values from MD simulations. Two trend lines are shown in (b): the solid line is the dislocation nucleation stress relationship given in Eq. 10.3 and the dotted line is the trend line from Spearot *et al.* [64].

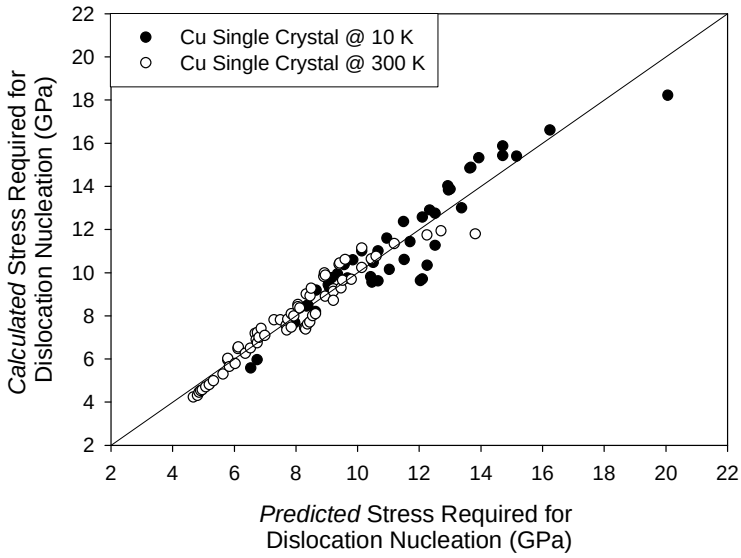


**Figure 10.9:** The predicted stress values required for dislocation nucleation (Eq. 10.3) versus the calculated stress values from the atomistic simulations for all tensile axis orientations at 10 K and 300 K. Deviation of any data points from the line denotes the relative error between the calculated values and Eq. 10.3.

Since homogeneous dislocation nucleation in single crystals follows the relationship in Eq. 10.3, this implies that a tension-shear coupling exists between the resolved tensile stress normal to the slip plane and the resolved shear stress in the direction of slip. For instance, dislocation nucleation cannot be predicted based solely on the magnitude of the Schmid stress or the non-Schmid stress; both resolved stress components are necessary for the inequality governing Eq. 10.3. Future work will investigate the tension-shear coupling in homogeneous dislocation nucleation along with the development of a 'yield' surface for dislocation nucleation in single crystals under uniaxial loading.

In addition to the application of Eq. 10.3 to homogeneous dislocation nucleation, this formulation also has the potential to be applied to heterogeneous dislocation nucleation. Recent simulations by Spearot and colleagues [64] examined the correlation between the stress required for dislocation nucleation from ⟨100⟩ and ⟨110⟩ symmetric tilt grain boundaries using the crystallographic orientations of the adjacent lattices ($SF$ and $NF$) and a measure of the interface free volume, termed nanoporosity. The first step in the development of

the interface strength model required an understanding of the influence of lattice orientation on *homogeneous* dislocation nucleation in single crystals. Accordingly, Eq. 10.3 has a wider range of applicability and can be applied to all single crystal tensile axis orientations instead of Eq. 10.1 [64]. The second step in the interface strength model involved the modification of the homogeneous dislocation nucleation stress for dislocation nucleation due to the presence of a heterogeneous defect (grain boundary interface). In a similar manner, the homogeneous dislocation nucleation stress in the current work can provide a form whereby the influence of other heterogeneous defects (*e.g.*, vacancies, impurities, free surfaces) on dislocation nucleation can be ascertained.

## *10.4 Summary*

In this chapter, atomistic simulations were used to investigate how the stress required for homogeneous nucleation of partial dislocations in single crystal copper under uniaxial tension changes as a function of crystallographic orientation. Molecular dynamics was employed based on an embedded-atom method potential for Cu at 10 K and 300 K. Results indicated that non-Schmid parameters are required to describe dislocation nucleation for certain single crystal orientations. Specifically, it is found that the stereographic triangle can be divided into two regions: a region where dislocation nucleation is dominated by the conventional Schmid factor (the resolved shear stress in the direction of slip) and a region where dislocation nucleation is dominated by the normal factor (the resolved stress normal to the slip plane). A continuum relationship that incorporates Schmid and non-Schmid terms to correlate the stress required for dislocation nucleation over all tensile axis orientations within the stereographic triangle was presented. The significance of this work is that simulation results are cast into an atomistically inspired continuum formulation for partial dislocation loop nucleation in FCC single crystal copper. For citation of the work contained in this chapter, the reader is referred to Ref. [81].

# CHAPTER XI

# INFLUENCE OF SINGLE CRYSTAL ORIENTATION ON HOMOGENEOUS DISLOCATION NUCLEATION UNDER UNIAXIAL LOADING

The chapter investigates homogeneous dislocation nucleation from single crystal copper. Atomistic simulations are used to investigate how the stress required for homogeneous nucleation of partial dislocations in single crystal copper under uniaxial loading changes as a function of crystallographic orientation. Molecular dynamics is employed based on an embedded-atom method potential for Cu at 10 K and 300 K. Results indicate that non-Schmid parameters are important for describing the calculated dislocation nucleation behavior for single crystal orientations under tension and compression. A continuum relationship is presented that incorporates Schmid and non-Schmid terms to correlate the nucleation stress over all tensile axis orientations within the stereographic triangle. Simulations investigating the temperature dependence of homogeneous dislocation nucleation yield activation volumes of ≈0.5-2 $b^3$ and activation energies of ≈0.30 eV. For uniaxial compression, full dislocation loop nucleation is observed, in contrast to uniaxial tension. One of the main differences between uniaxial tension and compression is how the applied stress is resolved normal to the slip plane on which dislocations nucleate — in tension, this normal stress is tensile, and in compression, it is compressive. Last, the tension-compression asymmetry is examined as a function of loading axis orientation. Orientations with a high resolved stress normal to the slip plane on which dislocations nucleate have a larger tension-compression asymmetry with respect to dislocation nucleation than those orientations with a low resolved normal stress. The significance of this research is that the resolved stress normal to the slip plane on which dislocations nucleate plays an important

role in partial (and full) dislocation loop nucleation in FCC Cu single crystals.

## *11.1 Introduction*

Dislocation motion in face-centered cubic (FCC) single crystals is well-known to be governed by the critical resolved shear stress via Schmid's law [215]. However, the factors that control dislocation nucleation in FCC crystals are not as well understood as dislocation motion. Specifically, the influence of the loading axis orientation and the loading directionality (tension versus compression) on dislocation nucleation has not been extensively investigated in FCC single crystals.

Rice [126] proposed using the unstable stacking fault energy as a criterion for predicting heterogeneous dislocation nucleation from a crack tip. In his work, the unstable stacking fault energy acts as an energetic barrier for nucleating dislocations (ductile response) that competes with Griffith cleavage (brittle response). More recent simulations have focused on the atomic mechanisms associated with dislocation nucleation due to the interest in plasticity of structures at the nanoscale, *e.g.*, nanocrystalline materials and nanowires, to name a few. Spearot and colleagues used bicrystal atomistic simulations to show that grain boundary structural units play an important role in the mechanisms of dislocation nucleation from specific symmetric tilt grain boundaries in Cu [139] and Al [97]. Van Swygenhoven and coworkers also used atomistic simulations to show that grain boundary ledges and triple junctions play an important role in dislocation nucleation and propagation in nanocrystalline materials (*cf.,* [53]). Such simulations help identify the role of grain boundary structure and the underlying nanocrystalline grain boundary network, respectively, on *heterogeneous* dislocation nucleation.

Improved understanding of how dislocations nucleate *homogeneously* within a perfect single crystal is also relevant. For example, nanoindentation simulations, which have been used to explain experimentally observed nanoindentation behavior (*e.g.*, [290–292]),

have shown that homogeneous dislocation nucleation occurs beneath the indented free surface [106, 107, 293] due to the localized stress state. Moreover, atomistic simulations have been used to analyze the effect of non-glide stress components in FCC [143] and BCC [294] metals to understand how local stress conditions may influence homogeneous dislocation nucleation. Homogeneous nucleation becomes increasingly important as scales of materials or applications approach tens to hundreds of nanometers, and the probability of finding heterogeneous sources decreases. One of the challenges in the characterization of homogeneous dislocation nucleation is the definition of criteria in continuum models that accurately describe the mechanical conditions that lead to dislocation nucleation (*e.g.*, [295–298]).

The ability to predict homogeneous dislocation nucleation in single crystals has potential impact on discrete dislocation dynamics simulations [299–301], in which the deformation of a crystalline material is often modeled by introducing dislocations into the material through Frank-Read sources and tracking the movement of each dislocation segment as a function of the applied stress. A criterion which is capable of predicting dislocation nucleation via the localized stress state would extend the applicability of dislocation dynamics simulations to problems where Frank-Read sources are not the dominant dislocation nucleation mechanism, for example in length scales approaching the nanoscale.

This work utilizes atomistic simulations to help understand how the resolved stress components on the primary slip plane(s) impact homogeneous dislocation nucleation in FCC Cu single crystals. In contrast to prior studies of the effect of non-glide stress components (*i.e.*, confining pressure and compressive normal stresses) on dislocation nucleation (*e.g.*, [143, 294]), this work examines the dependence of homogeneous dislocation nucleation on the orientation of the uniaxial loading axis relative to the crystal system under both compression and tension. In this manner, the applied uniaxial stress resolves onto the primary slip system(s), creating three main stress components acting upon the slip plane on which the dislocation nucleates:

- A resolved stress normal to the {111} slip plane,
- A resolved shear stress upon the {111} slip plane in the slip direction, and
- A resolved shear stress upon the {111} slip plane perpendicular to the slip direction.

Therefore, in the present simulations the normal stress on the slip plane is both tensile (for uniaxial tension) and compressive (for uniaxial compression), which can aid in the analysis of how the normal stress affects dislocation nucleation.

The non-Schmid stresses, particularly the resolved normal stress, play an important role in plasticity in other material systems. Qin and Bassani [304] have shown that the non-Schmid stresses are necessary to characterize slip in the intermetallic $Ni_3Al$ system. Ito and Vitek [303] have shown that non-Schmid stresses impact the motion of screw dislocations and the critical resolved shear stress in body-centered cubic (BCC) metals. Lund and Schuh [305] have shown that yield in metallic glasses has a significant dependence upon pressure or the normal stress, analogous to the case of granular materials. Used successfully in modeling nucleation and growth of small fatigue cracks under multiaxial strain states, the Fatemi-Socie parameter [306] combines the maximum plastic shear strain amplitude with the modifying influence of normal stress acting on the associated plane to predict mean stress effects. It is particularly interesting to note that while normal stress effects are often used in mesoscopic or macroscopic constitutive theories of plasticity and damage, the resolved normal stress also has a fundamental role in atomic scale nucleation of dislocations in FCC metals.

Therefore, the objective of this work is to investigate how the loading axis orientation *and* the stress components resolved onto the active slip systems affect *homogeneous* dislocation nucleation in FCC Cu. Results show that homogeneous dislocation nucleation in FCC Cu single crystals can depend on the magnitude of both the resolved shear stress in the slip direction and the resolved tensile stress normal to the slip plane. The distinctly different dislocation nucleation behavior under tension and compression is attributed to the

resolved stress normal to the slip plane. Methodically analyzing the role of loading axis orientation and directionality in FCC single crystals can help our understanding of how resolved stresses impact dislocation nucleation processes.

## *11.2 Methodology*

A parallel molecular dynamics code (Warp [69]) that incorporates domain decomposition is used to deform the single crystal atomistic models. After generating the atom positions in the desired crystallographic orientation, the configuration is equilibrated using MD in the isobaric-isothermal (NPT) ensemble at a pressure of 0 bar and a temperature of either 10 K or 300 K for 10 ps. The configuration is then deformed in uniaxial tension at a constant strain rate of $10^9$ $s^{-1}$ with a stress-free condition for the other two simulation cell boundaries [97, 139]. Spearot *et al*. [97] implemented these boundary conditions by decoupling the boundary in the loading direction from the Melchionna *et al*. [95] NPT equations of motion. Therefore, the motion of the boundary is prescribed in the loading direction while the two orthogonal boundaries are controlled through the NPT equations.

Recall from Chapter 2 that the original NPT equations were modified by adding an additional dampening term to the evolution of the isobaric friction coefficient parameter $\eta$ [89], *i.e.*,

$$\dot{\eta} = \frac{\nu_P^2}{Nk_BT_{ext}} V\left(\sigma\left(\mathbf{t}\right) - \mathbf{P}_{\text{ext}}\mathbf{I}\right) - \gamma\eta \tag{11.1}$$

where $\sigma\left(\mathrm{t}\right)$ is the instantaneous stress tensor, $\mathbf{P}_{\text{ext}}$ is the externally applied pressure, $N$ is the total number of atoms in the system, $k_B$ is Boltzmann's constant, $\mathrm{T}_{\text{ext}}$ is the external temperature, and $\nu_P$ is the barostating rate. The isobaric damping constant $\gamma$ reduces pressure fluctuations acting upon the cell boundaries. This additional damping term $\gamma\eta$ [89] modifies the original Melchionna *et al*. equations. The lateral boundaries are specified as stress-free ($P_{ext} = 0$) and controlled through Eq. 11.1, while the boundary in the loading direction is specified. Boundary conditions with appropriate damping terms are essential to dislocation

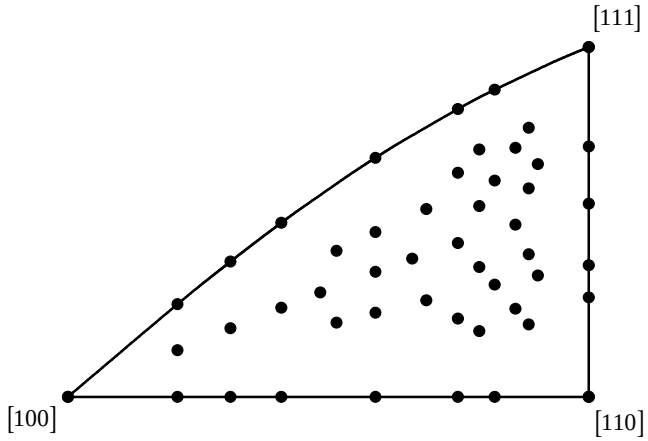


**Figure 11.1:** Stereographic triangle showing the 49 crystallographic orientations investigated for dislocation nucleation. Each direction denotes the uniaxial loading axis for the corresponding single crystal deformation simulation.

nucleation within a three-dimensional (3D) periodic configuration, since improper motion of the periodic boundaries may falsely affect dislocation nucleation.

For mechanical properties, the system stress was calculated using the virial definition without the kinetic portion [99], as was discussed in Chapter 2. An embedded-atom method [108, 109] potential for Cu [124] is employed in this study for reasons outlined in Chapter 2.

Figure 11.1 shows the loading axis for the 49 crystallographic orientations examined in this work, within the basic stereographic triangle with [100], [110], and [111] vertices. Each single crystal model is deformed under uniaxial tension and compression at temperatures of 10 K and 300 K to examine the effect of loading directionality and temperature on dislocation nucleation. The crystallographic orientations and calculated stress values required for dislocation nucleation under uniaxial compression at 10 K and 300 K are listed in Table 11.1; the values under uniaxial tension can be found elsewhere [81]. For uniaxial tension at 300 K, the dislocation nucleation stress values for an additional 20 crystal orientations along the exterior of the stereographic triangle are used from Spearot *et al.* [64].

The axes of the stereographic triangle represent the latitude $\theta$ and longitude $\phi$ of the loading axis, where $\theta = \{0°, 45°\}$ and $\phi = \{0°, 35.26°\}$; this coordinate system is employed for plotting the computational results for each orientation on the stereographic triangle. The expected slip system (maximum Schmid factor) is the $\left(11\bar{1}\right)[101]$ slip system for all tensile axis orientations on the interior of the [100]-[110]-[111] triangle. Note that all the interior tensile axis orientations deform via single slip nucleation on the $\left(11\bar{1}\right)[101]$ slip system, while all axis orientations on the boundary of the stereographic triangle have at least two active slip systems. If the tensile axis is on the [100]-[111] boundary, the *conjugate* slip system is the $\left(1\bar{1}1\right)[110]$ system. If the tensile axis is on the [100]-[110] boundary, the *critical* slip system is the $(111)\left[10\bar{1}\right]$ system. If the loading axis is on the [110]-[111] boundary, the *coplanar* slip system is the $\left(11\bar{1}\right)[011]$ system. The [110], [111], and [100] vertices have 4, 6, and 8 active slip systems, respectively, which may have conjugate, critical, and coplanar slip system arrangements.

## *11.3 Atomistic simulation results*

### 11.3.1 Schmid and non-Schmid dependence

The glide of dislocations in FCC crystals is commonly observed to obey Schmid's law. However, other crystal structures have displayed 'non-Schmid' dislocation behavior [302, 303], whereby dislocation motion exhibits a strong dependence on resolved stress components in directions other than the slip direction. For dislocation nucleation, Ogata *et al.* [143] used *ab initio* calculations to show that compressive stress components acting normal to the slip plane can affect the critical resolved shear stress in Cu and Al, indicating that non-Schmid terms may be required for dislocation *nucleation*. In addition, previous MD calculations examining dislocation nucleation in single crystals and grain boundaries by Spearot *et al.* [64] have shown that the maximum resolved shear stress varies as a function of the tensile axis, reinforcing that non-Schmid terms are required. Consequently, Spearot and colleagues [64] proposed the following relationship for single crystals subjected to

**Table 11.1:** List of the 49 crystallographic orientations examined in this work. Also listed is the calculated stress required for dislocation nucleation under uniaxial compression at 10 K and 300 K.

| Crystal Orientation | Stress (GPa) 10 K | Stress (GPa) 300 K | Crystal Orientation | Stress (GPa) 10 K | Stress (GPa) 300 K |
|---|---|---|---|---|---|
| [100] | 4.82 | 3.71 | [542] | 19.01 | 14.42 |
| [110] | 17.82 | 15.58 | [543] | 19.57 | 15.40 |
| [111] | 24.39 | 19.47 | [610] | 7.41 | 5.72 |
| [210] | 17.76 | 14.51 | [611] | 8.20 | 6.50 |
| [211] | 15.88 | 12.80 | [621] | 12.86 | 9.32 |
| [221] | 18.57 | 15.48 | [631] | 17.06 | 12.25 |
| [310] | 14.88 | 10.53 | [632] | 15.31 | 11.71 |
| [311] | 12.48 | 9.97 | [641] | 18.19 | 14.48 |
| [320] | 18.02 | 15.34 | [643] | 17.66 | 13.92 |
| [321] | 17.91 | 13.63 | [651] | 18.48 | 15.52 |
| [322] | 19.04 | 15.07 | [652] | 19.05 | 14.55 |
| [331] | 18.43 | 15.43 | [653] | 19.48 | 14.66 |
| [332] | 19.52 | 16.17 | [654] | 18.90 | 15.90 |
| [410] | 11.03 | 7.86 | [731] | 16.11 | 11.08 |
| [411] | 10.48 | 8.48 | [732] | 14.08 | 10.69 |
| [421] | 15.85 | 11.80 | [742] | 17.03 | 12.84 |
| [430] | 18.32 | 15.64 | [751] | 18.27 | 15.02 |
| [431] | 18.63 | 14.78 | [752] | 18.41 | 13.82 |
| [432] | 18.76 | 14.32 | [753] | 17.93 | 13.97 |
| [433] | 20.55 | 16.61 | [754] | 17.94 | 14.75 |
| [441] | 18.28 | 15.50 | [762] | 18.93 | 15.33 |
| [521] | 14.33 | 10.52 | [764] | 19.95 | 15.42 |
| [531] | 17.87 | 13.68 | [821] | 10.52 | 7.70 |
| [532] | 16.79 | 12.76 | [12, 2, 1] | 7.87 | 5.88 |
| [541] | 18.58 | 15.01 | | | |

uniaxial tensile stress, *i.e.*,

$$\sigma_{max}^{sc} = \frac{\tau_{ideal}}{\mu_s SF + \mu_n NF + \mu_p PF} \tag{11.2}$$

where,

$$\begin{aligned} SF &= \ell_{y'y}\ell_{x'y} \\ NF &= \ell_{y'y}^2 \\ PF &= \ell_{y'y}\ell_{z'y} \end{aligned} \tag{11.3}$$

Here, $\ell_{ij}$ are the direction cosines relating a coordinate axis fixed to the primary slip plane ($x'$ is the slip direction, $y'$ is normal to the slip plane and $z'$ lies within the slip plane, perpendicular to the slip direction [257]) to a fixed specimen coordinate system ($x$, $y$ uniaxial loading direction, and $z$). Thus, $SF$ projects the uniaxial applied stress into the resolved shear stress on the {111} slip plane in the slip direction (the conventional Schmid factor), $NF$ projects the uniaxial stress into a component **normal** to the {111} slip plane, and $PF$ projects the uniaxial stress into a shear stress acting on the {111} slip plane **perpendicular** to the slip direction (coslip direction). The active slip system(s) for each loading axis is(are) defined by the maximum $SF$ value(s) among all possible slip systems. Figure 11.2 shows a schematic of how the uniaxial tensile stress, $\sigma_{11}$, is resolved into stress components acting on the active {111}⟨110⟩ slip system given the above definitions for the Schmid and non-Schmid parameters. When $\sigma_{11}$ in Fig. 11.2 reaches $\sigma_{\max}^{sc}$, dislocation nucleation occurs in the single crystal configuration.

In Eq. 11.2, the ideal shear strength $\tau_{ideal}$ is defined as the resolved shear stress in the slip direction required for partial dislocation nucleation when all other stress components acting on the slip plane are zero. *Ab initio* calculations find that $\tau_{ideal} = 2.16$ GPa for Cu [143]. The parameters $\mu_n$ and $\mu_p$ are positive scalars that characterize the degree of non-Schmid behavior; $\mu_s$ characterizes the degree of Schmid behavior. Therefore, an increase in either $\mu_s$, $\mu_n$, or $\mu_p$ reduces the predicted nucleation stress by increasing the weight of

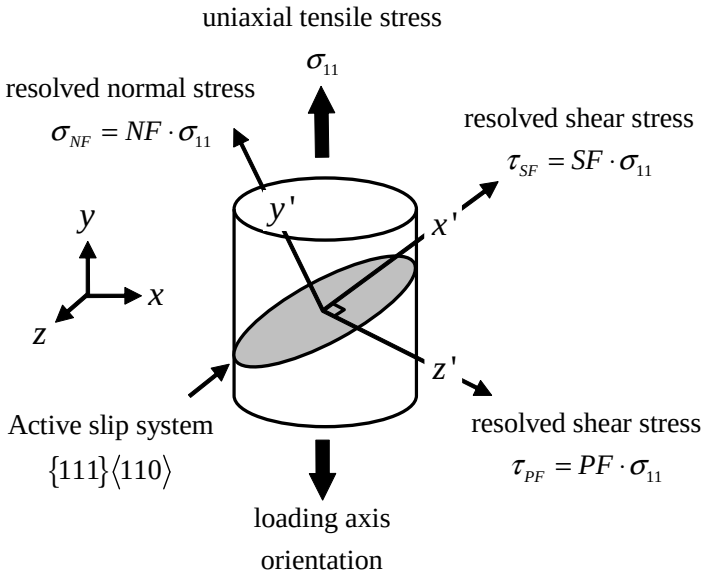


**Figure 11.2:** Schematic showing how the uniaxial tensile stress, $\sigma_{11}$, resolves into different stress components acting upon the active $\{111\}\langle 110\rangle$ slip system. The resolved shear stress in the slip direction, $\tau_{SF}$ the resolved shear stress perpendicular to the slip direction, $\tau_{PF}$, and the resolved normal stress, $\sigma_{NF}$, are all related to $\sigma_{11}$ through the Schmid and non-Schmid parameters $SF$, $PF$, and $NF$, respectively.

the corresponding stress component. Assuming that $\tau_{ideal} = 2.16$ GPa for the Mishin Cu potential used, if $\mu_s = 1$ and $\mu_n = \mu_p = 0$, Eq. 11.2 reduces to Schmid's law for single crystal slip, *i.e.*, $\sigma_{max} = \tau_{ideal}/SF$. In this work, the applicability of the relationship in Eq. 11.2 to the entire stereographic triangle for uniaxial compression will be evaluated. Tschopp *et al.* [81] have correlated the dislocation nucleation stresses for uniaxial tension with all 49 orientations in a modified form of Eq. 11.2; this will be briefly discussed later as well.

Figure 11.3 shows how the Schmid factor ($SF$) and the normal factor ($NF$) change as a function of the crystal orientation with respect to the tensile axis. The maximum $SF = 0.5$, occurs in the interior of the stereographic triangle, while the maximum $NF = 0.666$, occurs for the [110] direction. The minimum Schmid factor, $SF = 0.272$, and normal factor, $NF = 0.111$, occur for the [111] orientation. MD simulations in this work show that dislocation nucleation can be correlated to specific regions within the stereographic triangle where the $SF$ is greater than the $NF$, or vice versa. The orientation dependence of $SF$ and $NF$ play an important role in the homogeneous dislocation nucleation process. The coslip factor ($PF$) is included in Fig. 11.3. However, an analysis of the Schmid and non-Schmid components for FCC Cu has shown that the coslip factor has essentially no effect (*i.e.*, $\mu_p = 0$) on the nucleation stress [64]. The coslip factor resolves the shear stress in the $\langle 112 \rangle$ direction on the $\{111\}$ slip plane. Typically, the non-Schmid parameter $PF$ is used to modify the driving force for cross-slip of screw dislocations in body-centered cubic metals (*cf.*, [288]).

### 11.3.2 Elastic lattice distortion

The affine elastic distortion of the lattice during application of uniaxial stress prior to nucleation is significant in terms of rotation of the slip system and associated co-slip and slip plane normal directions. Here the influence of the strain to nucleation on the resolved stress components in the current (deformed) configuration are considered at the precise point of

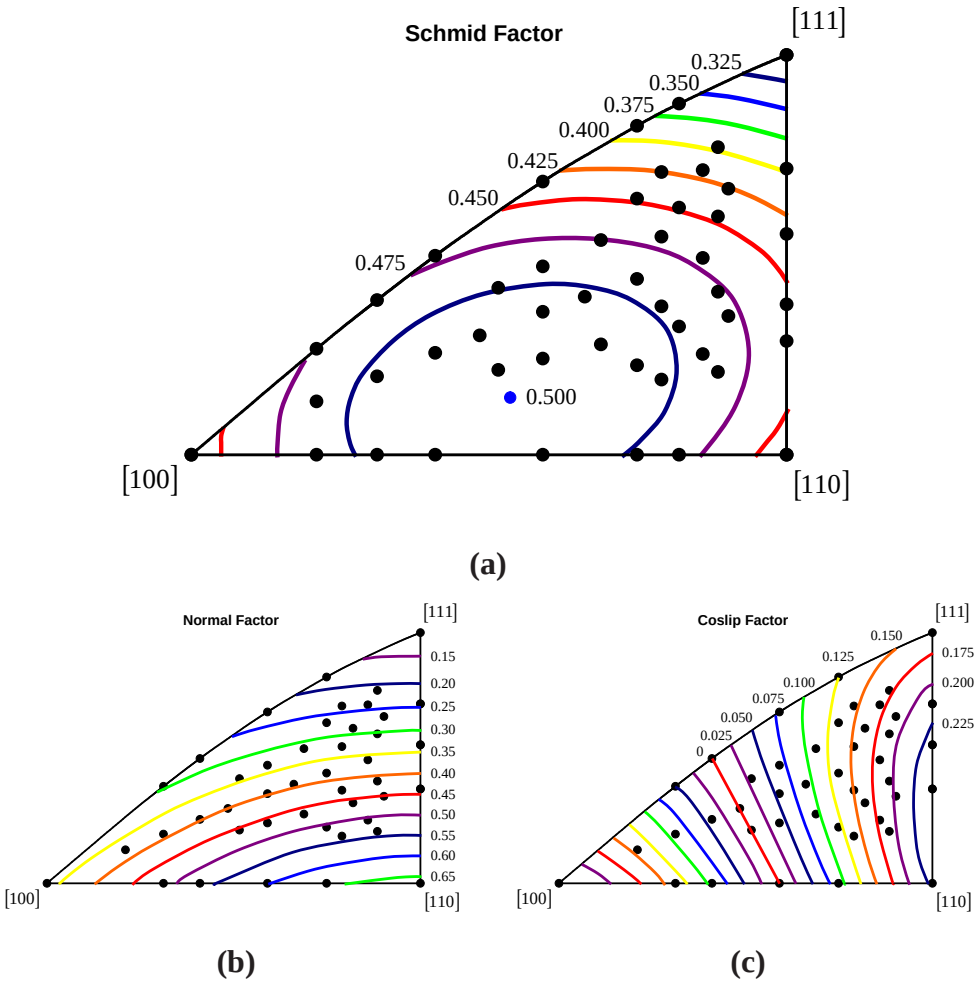


**Figure 11.3:** Orientation dependence of the (a) Schmid factor ($SF$), (b) normal factor ($NF$), and (b) coslip factor ($PF$) for FCC crystals.

nucleation, since simulation results show high strains (6-14%) are required for dislocation nucleation. To do this, the motion of the simulation cell boundaries was used to compute a deformation gradient tensor $\mathbf{F}_{\mathrm{ij}}$, used to map the original orthogonal triad of unit vectors in the slip, co-slip and slip plane normal directions from the undeformed to the deformed configuration. The push-forward transformation

$$d_i^{\alpha *} = \mathbf{F}_{\mathrm{im}} \mathrm{d}_{\mathrm{m}}^{\alpha} \tag{11.4}$$

gives the deformed configuration components $d_i^{\alpha^*}$ of the three unit vectors in the initial (undeformed) configuration $d^{\alpha}$, $\alpha = x, y, z$. Components of both vectors in both configurations are expressed with respect to the global Cartesian coordinates shown in Fig. 11.2.

It is noted that they are no longer orthogonal vectors in the current configuration, having undergone stretch and rotation. The direction cosines $\ell_{ij}$ used in Eq. 11.3 pertain to the resolution of Cauchy stress onto slip vectors in the undeformed configuration. To provide a meaningful description of the resolved shear stress in the slip direction and the normal stress to the slip plane in the deformed configuration at the point of nucleation, the cross product of the deformed vectors in the slip and co-slip directions (which establish the slip plane tangent) is taken to determine the slip plane normal direction. Then, a vector cross product of this slip plane normal direction with the deformed slip direction vector gives a modified co-slip direction, yielding an orthogonal triad which is then normalized to a set of unit vectors for defining an updated set of direction cosines in Eq. 11.3. In so doing, the slip direction and slip plane normal are preserved as primal descriptors. Next, the differences in using this rotated basis is compared to the original undeformed basis of slip, co-slip and slip plane normal directions in Eq. 11.3.

Figure 11.4 examines the evolution of the resolved stress parameters $SF$ and $NF$ as a function of strain for the 12 $\{111\}\langle 110\rangle$ slip systems for the [321] orientation under uniaxial tension at 10 K. The temperature of 10 K requires larger strains for dislocation nucleation than the simulations at 300 K and therefore represents the upper bound for slip system

rotation. The maximum Schmid factor $\left(11\bar{1}\right)[101]$ slip system in the undeformed configuration has the highest $SF$ value throughout uniaxial loading in tension. Even for large strain deformation (10% strain), the increase in $SF$ on an individual slip system is not enough for another slip system to become the favored slip system, *i.e.*, a higher $SF$ than the $\left(11\bar{1}\right)[101]$ slip system. The magnitude and direction of the change in $SF$ indicates that homogeneous elastic deformation affects the evolution of the resolved stresses differently among $\{111\}\langle 110\rangle$ different slip systems. For example, the $SF$ values range from increasing by 10% to decreasing by 9% at dislocation nucleation. The differences in the evolution of $SF$ is due to a combination of the decreasing inclination of the slip direction and the increasing inclination of the slip plane normal with respect to the loading axis. For the $NF$ plot, only four curves are needed for the four $\{111\}$ slip planes. The $NF$ values decrease with increasing strain for all slip systems due to the increasing angle between the slip plane normal and the loading axis. The active slip plane has only the second highest resolved normal stress, yet dislocations nucleate on this slip plane. This emphasizes an important point. Despite the dependence of many aspects of dislocation nucleation on the normal stress in the current work, the resolved normal stress discussed is associated with the maximum Schmid factor slip system. A high normal stress in the absence of a high shear stress is insufficient for nucleating dislocations on that slip plane.

The evolution of the resolved stress parameters $SF$ and $NF$ were investigated as a function of strain for four orientations ([100], [110], [111], and [321]) under uniaxial tension and compression at 10 K. Figure 11.5 shows a plot of the evolution of $SF$ and $NF$ as a function of strain under uniaxial tension and compression. Only the maximum Schmid factor $\left(11\bar{1}\right)[101]$ slip system is shown in Fig. 11.5. The black arrows point to the strain associated with the peak stress (*i.e.*, the first dislocation nucleates). The normal factor decreased(increased) as function of strain in uniaxial tension(compression) for all four crystal orientations. There is some anisotropy in the evolution of the Schmid factor as a function of elastic deformation for the four crystal orientations. Specifically, the Schmid factor for

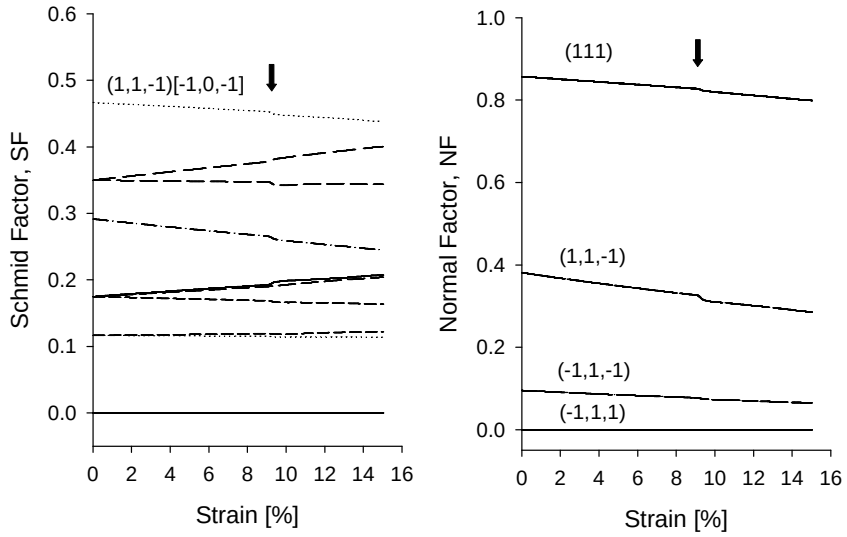


**Figure 11.4:** The change in the resolved stress parameters, $SF$ and $NF$, as a function of strain for all 12 $\{111\}\langle 110\rangle$ slip systems for the [321] orientation under uniaxial tension. The arrows denote the strain associated with dislocation nucleation.

the [100], [111], and [321] decreased in tension and increased in compression. However, $SF$ for the [110] orientation increased in uniaxial tension and decreased in uniaxial compression. Unlike these other orientations, the slip direction and slip normal rotate towards an inclination angle of 45° from the loading axis in tension and rotate away in compression. The different evolution of $SF$ may contribute to anisotropy in dislocation nucleation behavior.

For some orientations in Fig. 11.5, there is a visible step in the $SF/NF$ curves, while the other orientations only show the step upon higher resolution of the axis scale (see inset for the [111] orientation in Fig. 11.5(b)). When the first dislocation nucleates, there is a rapid expansion or contraction of the lateral boundaries to accommodate the nucleation and propagation of the dislocation, causing a step in the first derivative of the lengths of the lateral boundaries with respect to the applied strain. Since the simulation cell boundary lengths $h_i$ are used to calculate the deformation gradient $\tilde{F}_{ij}$, this ends up causing the small steps observed in the $SF/NF$ curves in Fig. 11.5. Once dislocations nucleate within the single crystals, the assumption of homogeneous elastic deformation is no longer valid.

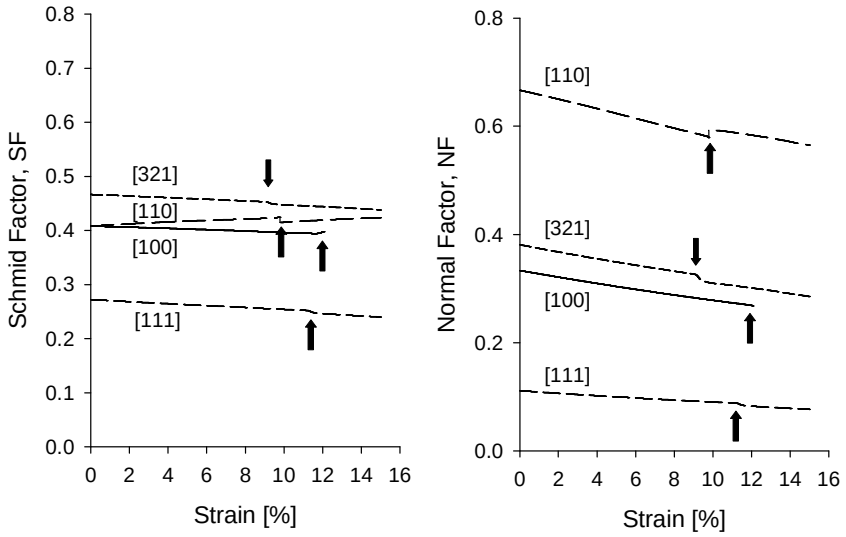


**(a)**

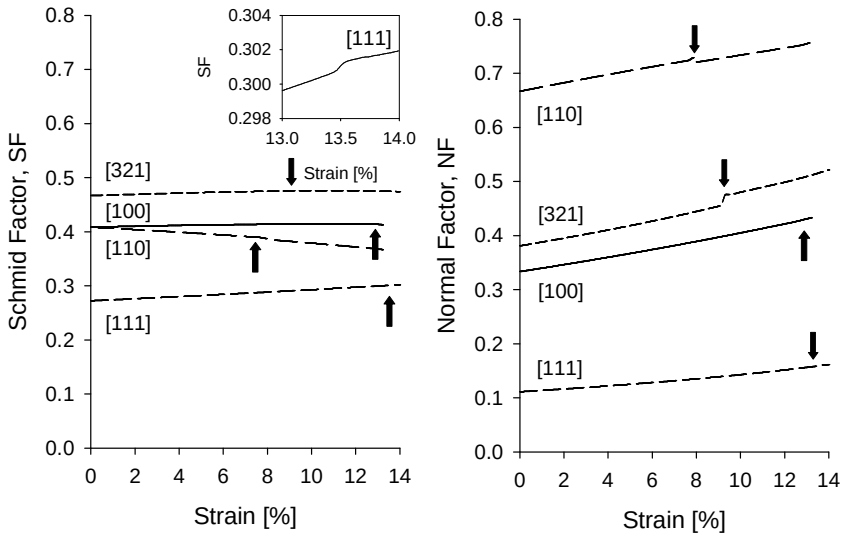


**(b)**

**Figure 11.5:** The change in the resolved stress parameters, $SF$ and $NF$, as a function of strain for four orientations ([100], [110], [111], and [321]) under (a) uniaxial tension and (b) uniaxial compression.

This methodology was applied to all crystal orientations around the stereographic triangle to find the approximate increase in the resolved stress parameters $SF$ and $NF$ at the strain associated with dislocation nucleation. Figure 11.6 compares $SF$ and $NF$ in the initial configuration (referred to as $SF_0$ and $NF_0$) versus $SF$ and $NF$ in the deformed configuration. The slope of a linear regression fit of the data with a zero intercept gives the total percent increase or decrease of the resolved stress components on the slip system at dislocation nucleation. In uniaxial tension at 10 K, $SF$ and $NF$ *decreased* by an average of 2.5% and 14.2%, respectively. In uniaxial compression at 10 K, $SF$ and $NF$ *increased* by an average of 1.5% and 16.8%, respectively. The changes in the resolved shear stress in the slip direction (*i.e.*, $SF$) as a function of elastic deformation are minimal compared to the changes in the resolved stress normal to the slip plane ($NF$). Moreover, on average, the resolved stresses evolve differently in tension and compression, *i.e.*, in tension the resolved stress components decrease and vice versa. This may contribute to the tension-compression asymmetry observed for dislocation nucleation [80], which is also discussed in Section 11.3.2.3. However, while the evolution of resolved stress components under tension and compression may partly explain the calculated tension-compression asymmetry, the magnitude changes are still small relative to the sign change for the resolved normal stress (tensile in tension, compressive in compression). For example, for the [321] orientation at 10 K, the change in the resolved shear stress due to lattice rotation is $\Delta\tau_{SF} = 4.7 - 4.6 = 0.1$ GPa in tension and $\Delta\tau_{SF} = 8.4 - 8.5 = -0.1$ GPa in compression. However, the difference in the resolved normal stress between tension and compression is $\Delta\sigma_{NF} = 11.5$ GPa at dislocation nucleation ($\Delta\sigma_{NF} = 10.7$ GPa based on the geometry of the undeformed lattice), considerably more pronounced than the change in the resolved shear stress.

This methodology is used in the following subsections to investigate the effect of the evolving resolved stress components on the {111} slip plane on homogeneous dislocation

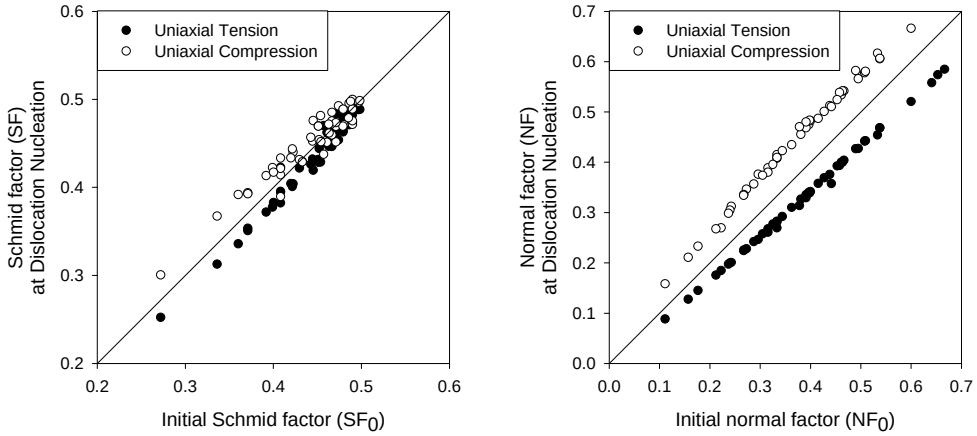


**Figure 11.6:** Comparison of the resolved stress parameters, (a) $SF$ and (b) $NF$, in the initial configuration versus the deformed configuration at dislocation nucleation for uniaxial tension and compression. All single crystal configurations at 10 K are shown.

nucleation. Moreover, Section 11.3.2.4 examines the effect of the resolved stress parameters at dislocation nucleation on previous single crystal models that predict the stress required for homogeneous dislocation nucleation [64, 81]. Spearot *et al.* [64] used a model for homogeneous dislocation nucleation in single crystals to isolate the influence of the lattice on heterogeneous dislocation nucleation from ⟨100⟩ and ⟨110⟩ symmetric tilt grain boundaries in copper.

#### *11.3.2.1 Uniaxial tension at 10 K*

The nucleation stress is calculated for all tensile axis orientations examined in this work. Figure 11.7(a) shows a contour plot of the nucleation stress as a function of the tensile axis orientation on the stereographic triangle at 10 K. All intermediate tensile axis orientations in the stereographic triangle are obtained through linear interpolation. The [111] axis requires the largest tensile stress for dislocation nucleation while the [110] axis requires the lowest tensile stress for dislocation nucleation. The stress along the [100]-[110] boundary is relatively unchanged near the [110] vertice of the stereographic triangle; this trend is similar to the normal factor contour in Fig. 11.3(b). All other regions of the contour plot in

Fig. 11.7(a) appear similar to the Schmid factor contours in Fig. 11.3(a).

Copper has a large degree of elastic anisotropy as a function of the loading axis orientation. For example, the elastic modulus in the [111] orientation ($E_{[111]}$ = 192 GPa) is nearly three times greater than in the [100] orientation ($E_{[100]}$ = 63 GPa) [257]. Figure 11.7(b) normalizes the nucleation stress by dividing by the elastic modulus for each single crystal loading orientation. The elastic modulus of each crystal was calculated for uniaxial loading in a given direction [*hkl*] by

$$\frac{1}{E_{[hkl]}} = S_{11} + (2S_{12} - 2S_{11} + S_{44}) \frac{\left(k^2l^2 + l^2h^2 + h^2k^2\right)}{(h^2 + k^2 + l^2)} \tag{11.5}$$

where $S_{ij}$ represents the elastic compliances for a given crystal, which were calculated from the elastic moduli $C_{ij}$ given for the Cu EAM potential [124]. The normalized stress, $\sigma/E_{[hkl]}$, differs from the stress contours in Fig. 11.7(a). The low elastic modulus of the [100] orientation results in the highest normalized stress ($\sigma/E_{[100]}$ = 0.168), while the low stress required for dislocation in the [110] orientation yields the lowest normalized stress, $\sigma/E_{[110]}$ = 0.042. In comparison, the high nucleation stress in the [111] orientation is offset by the high elastic modulus, resulting in an intermediate value of $\sigma/E_{[111]}$ = 0.094. The elastic modulus calculated by Eq. 11.5 is for the initial configuration only; note that the stress-strain curves in section 11.3.3 show that the elastic modulus evolves with elastic strain up to the dislocation nucleation event. Section 11.3.4 examines the dislocation nucleation mechanisms, which may be affected by the elastic response that results from the loading orientation.

To illustrate the relative differences in the role of the $SF$ and $NF$ terms in dislocation nucleation process for uniaxial loading, Figs. 11.8(a) and 11.8(b) show the magnitudes of $SF$ and $NF$, respectively, against the maximum tensile nucleation stress in single crystals at 10 K. In general, Fig. 11.8(a) shows that the tensile nucleation stress decreases as the magnitude of $SF$ increases (*i.e.*, as the resolved shear stress in the slip direction increases). However, several orientations deviate from this trend, revealing that $SF$ alone is

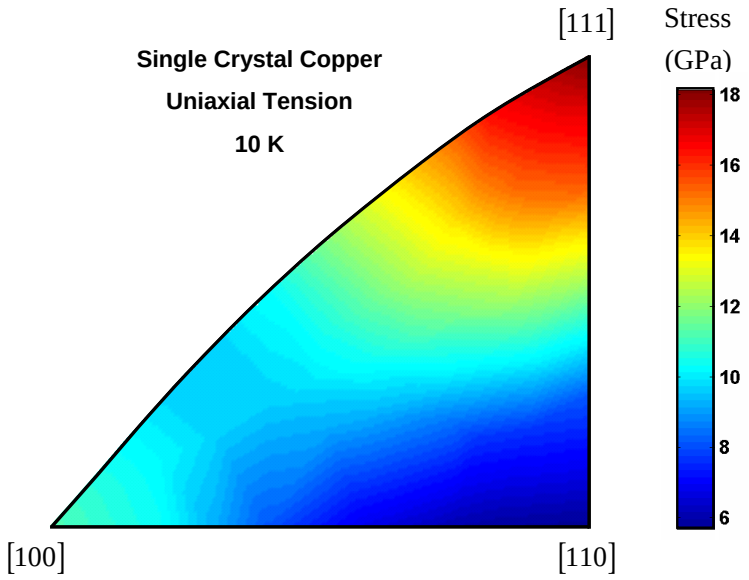


**(a)**

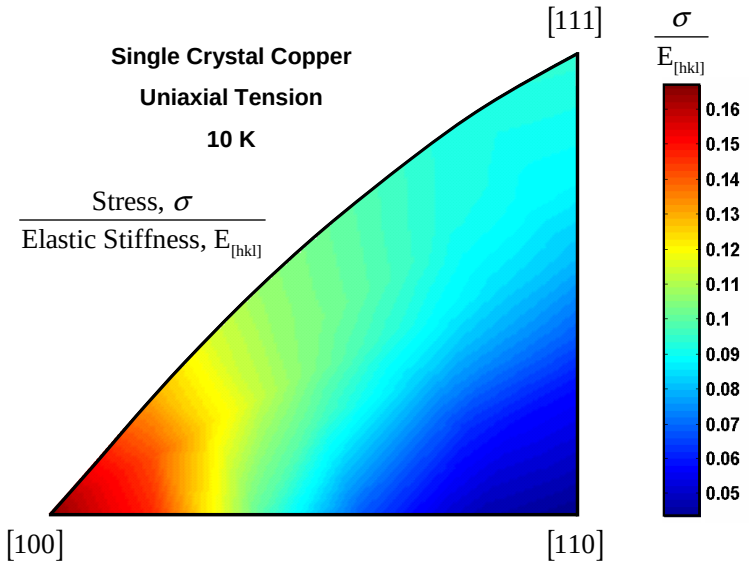


**(b)**

**Figure 11.7:** Contour plots of (a) the tensile stress required for homogeneous dislocation nucleation and (b) the tensile stress normalized by the elastic stiffness, $\sigma/E_{[hkl]}$, as a function of loading axis orientation for single crystal models at 10 K.

not capable of capturing all aspects of the dislocation nucleation process. In Fig. 11.8(b), a similar trend is observed; as the magnitude of $NF$ increases (*i.e.*, as the resolved stress normal to the slip plane increases), the nucleation stress decreases. The peak stress values in Figs. 11.8(a) and 11.8(b) are separated into orientations where single slip is predicted (interior of stereographic triangle) and those where multiple slip systems are expected (exterior of stereographic triangle). Interestingly, for a similar magnitude of $SF$, a higher stress for dislocation nucleation is found for tensile axis orientations for which single slip is expected. In other words, a lower resolved shear stress in the slip direction is required for crystal orientations with multiple active slip systems. A similar trend is not observed for $NF$.

#### *11.3.2.2 Uniaxial compression at 10 K*

The nucleation stress was also calculated for all compressive axis orientations. Figure 11.9(a) shows a contour plot of the nucleation stress as a function of the compressive axis orientation on the stereographic triangle at 10 K. As with Fig. 11.7, the stresses for all intermediate axis orientations in the stereographic triangle were obtained using linear interpolation. The [111] axis requires the largest compressive stress for dislocation nucleation while the [100] axis requires the lowest compressive stress for dislocation nucleation. There is a large change in dislocation nucleation stress along the [100]-[110] and [100]-[111] boundaries compared to the relatively unchanged [110]-[111] boundary.

Figure 11.9(b) normalizes the nucleation stress in a similar manner as Fig. 11.7(b), dividing by the elastic modulus (Eq. 11.5. As with Fig. 11.7(b), when the stress is normalized by the elastic modulus, the [111] orientation has an intermediate normalized stress, $\sigma/E_{[111]} = 0.126$, compared to the [100] and [110] orientations with $\sigma/E_{[100]} = 0.072$ and $\sigma/E_{[110]} = 0.136$, respectively. Interestingly, in uniaxial compression, the nucleation stress increases with increasing elastic modulus in the loading direction with a much more defined trend than in tension, in which the lowest nucleation stress occurs at the intermediate

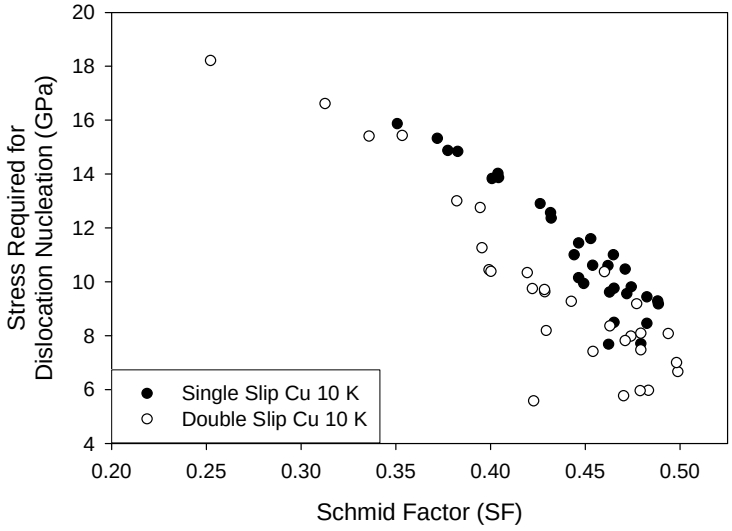


**(a)**

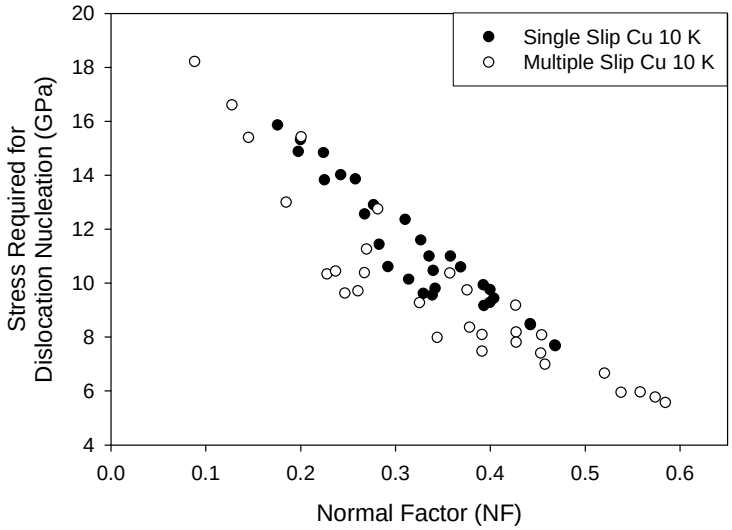


**(b)**

**Figure 11.8:** Tensile stress required for homogeneous dislocation nucleation as a function of (a) Schmid factor ($SF$) and (b) normal factor ($NF$) at 10 K. Black and white symbols denote single slip or multiple slip orientations, respectively.

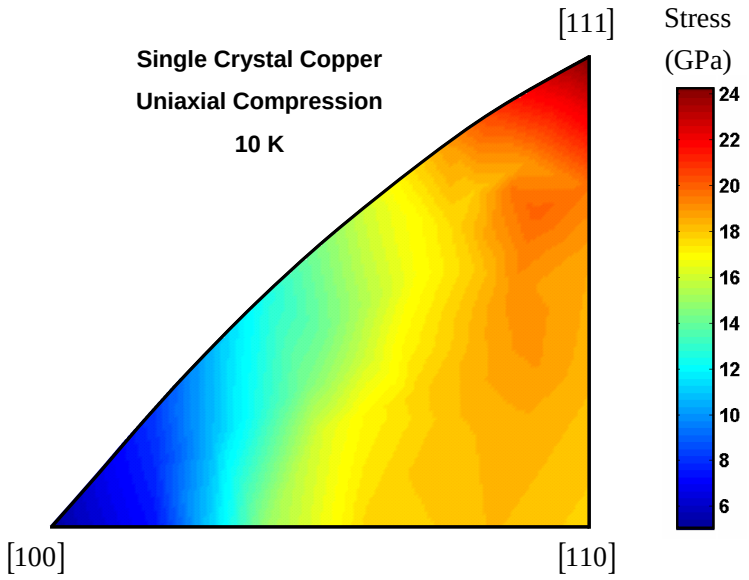


**(a)**

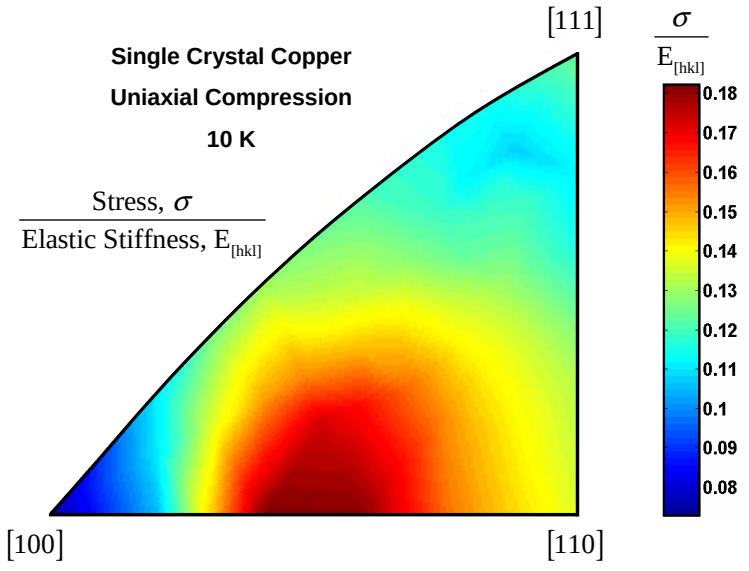


**(b)**

**Figure 11.9:** Contour plots of (a) the compressive stress required for homogeneous dislocation nucleation and (b) the compressive stress normalized by the elastic stiffness, $\sigma/E_{[hkl]}$, as a function of loading axis orientation for single crystal models at 10 K.

elastic modulus of the [110] direction.

As with the uniaxial tension configurations, Figs. 11.10(a) and 11.10(b) show the magnitudes of $SF$ and $NF$, respectively, against the maximum compressive nucleation stress in single crystal Cu at 10 K. Unlike Fig. 11.8 for uniaxial tension, no clear trend exists between $SF$ or $NF$ and the nucleation stress in uniaxial compression. While the highest stress (the [111] direction) has the lowest values of $SF$ and $NF$, the lowest stress (the [100] direction) has intermediate values of $SF$ and $NF$. Additionally, there is a large amount of variability in the calculated stresses versus $SF/NF$ in Fig. 11.10 compared to the uniaxial tension simulations. *The lack of a trend in this relationship suggests that dislocation nucleation under uniaxial compression may require a different form than in tension*. The peak stresses in Figs. 11.10(a) and 11.10(b) are separated into orientations where single slip is predicted (interior of stereographic triangle) and those where multiple slip systems are expected (exterior of stereographic triangle). Interestingly, multiple slip axis orientations seem to bound the single slip axis orientations.

#### *11.3.2.3 Tension-compression asymmetry at 10 K*

At the nanoscale, plastic deformation behavior of FCC crystals has exhibited a tension-compression asymmetry in various materials, *e.g.*, nanowires and nanocrystalline materials. Atomistic simulations are often used to analyze this tension-compression asymmetry. For example, Diao *et al.* [307] have shown that the yield strength asymmetry in Au nanowires for the [100] and [111] orientations is due to surface-induced internal stresses. Tomar and Zhou [308] related the yield strength asymmetry in nanocrystalline $\alpha$-$Fe_2O_3$-FCC Al composites to differences in grain boundary sliding behavior. Lund *et al.* [309, 310] have shown that nanocrystalline Ni has higher yield and flow stresses in compression than in tension (both uniaxial and biaxial simulations); these results suggest a similar atomic-level mechanism controls yield in both FCC Ni and metallic glasses [305]. Cheng *et al.* [291]

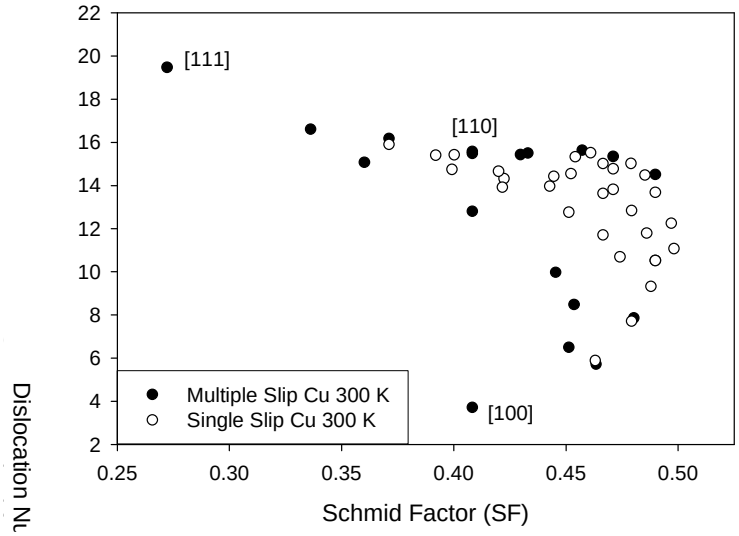


**(a)**

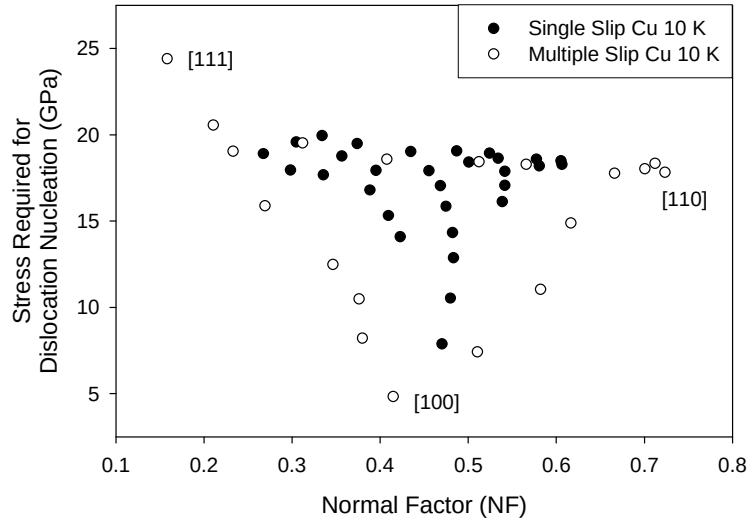


**(b)**

**Figure 11.10:** Compressive stress required for homogeneous dislocation nucleation as a function of (a) Schmid factor ($SF$) and (b) normal factor ($NF$) at 10 K. Black and white symbols denote multiple slip or single slip orientations, respectively.

propose a pressure-dependent analytical model that predicts the observed tension/compression asymmetry of the yield strength in nanocrystalline Cu, Al, and BCC Fe. Consequently, as the material length scale decreases to the nanoscale, tension-compression asymmetry is expected. While these studies focused on inelastic deformation due to heterogeneities at the nanoscale, the influence of crystal orientation on dislocation nucleation in the *absence* of heterogeneities is also vital to a full understanding of inelasticity at the nanoscale.

Figure 11.11 shows the ratio of the stress required for homogeneous dislocation nucleation under compression to that in tension as a function of the loading axis orientation of single crystal copper. A ratio greater(less) than unity signifies that homogeneous dislocation nucleation requires a higher(lower) stress in compression than in tension. Most orientations within the stereographic triangle require a higher stress in uniaxial *compression* to nucleate dislocations; the [110] axis has the largest ratio of 3.20 at 10 K(17.82 GPa in compression/5.57 GPa in tension). The [110] orientation also has the highest $NF$ value of all orientations ($NF = 0.58$ in tension and $NF = 0.72$ in compression). Interestingly, not all orientations require a higher stress in compression. Figure 11.11 also shows that some axis orientations require a greater stress in uniaxial *tension* than uniaxial compression. Specifically, the [100] axis has the lowest ratio of 0.43 (4.82 GPa/11.26 GPa), showing a much greater propensity to homogeneously nucleate partial dislocations under an applied uniaxial compressive stress. As the material length scale decreases to the nanoscale, a tension-compression asymmetry is expected. Therefore, the current MD simulations, which show a tension-compression asymmetry of dislocation nucleation in single crystals, agrees with previous simulations and analytical models that have shown a tension-compression asymmetry in the yield stress for nanocrystalline FCC metals [291, 309], metallic glasses [305], and nanocrystalline $\alpha$-$Fe_2O_3$-FCC Al composites [308].

Figure 11.12 shows the tension-compression asymmetry (ratio of the stress required for homogeneous dislocation nucleation under compression to that in tension) as a function of (a) the Schmid factor and (b) the normal factor in the initial configuration at 10 K. The

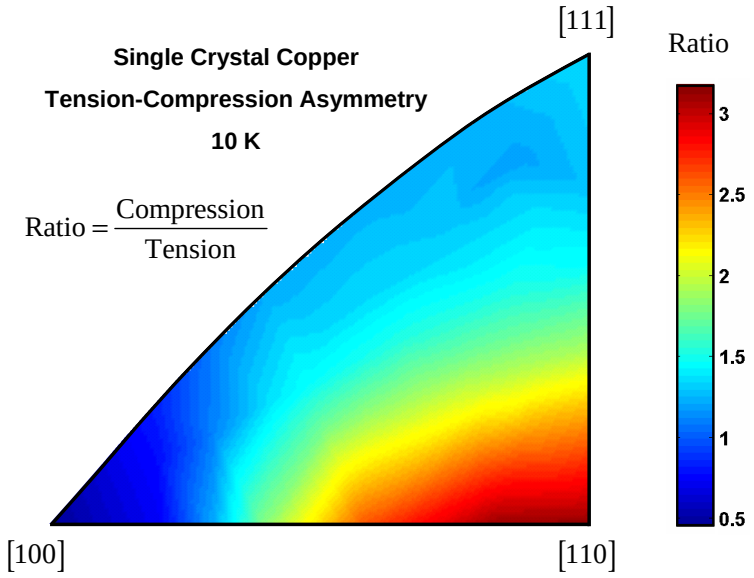


**Figure 11.11:** The tension-compression asymmetry for homogeneous dislocation nucleation in single crystals as a function of the loading axis orientation at 300 K. The tension-compression asymmetry is rendered by plotting the ratio of the stress required for homogeneous dislocation nucleation in uniaxial compression to that in uniaxial tension.

initial configuration was used because $SF$ and $NF$ are different at dislocation nucleation in tension and compression. No clear trend exists between the tension-compression asymmetry and the Schmid factor. However, the tension-compression asymmetry increases for high $NF_0$ values ($NF_0 > 0.5$), which may help describe the fundamental mechanism for this asymmetric behavior.

Figure 11.13 shows how the uniaxial tensile and compressive stresses are resolved into stress components acting upon the active $\{111\}\langle 110\rangle$ slip system. The main difference between the two loading cases is that the resolved normal stress to the slip plane is tensile in uniaxial tension and compressive in uniaxial compression. Also recall that the elastic lattice distortion results in $NF$ evolving differently in tension and compression.

Figure 11.13(c) shows that the tensile normal stress acts to increase the interplanar spacing between {111} planes, which may allow easier nucleation of the partial dislocation loop by lowering the resistance to slip on adjoining {111} planes. Additionally, in uniaxial

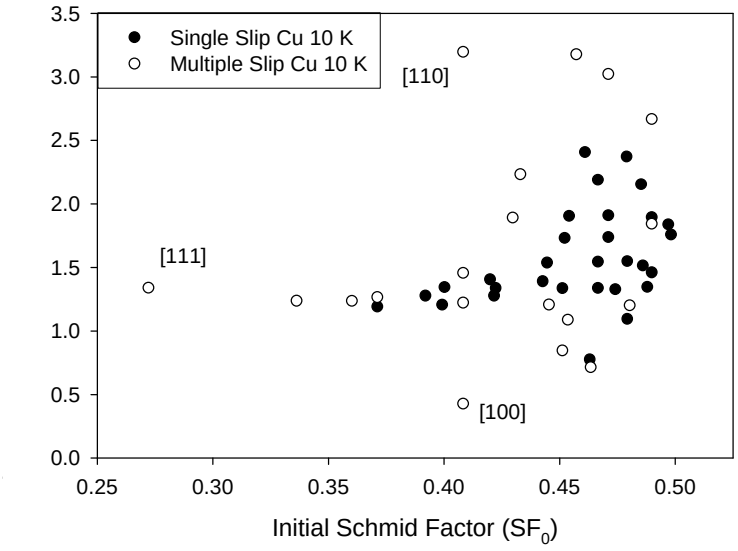


**(a)**

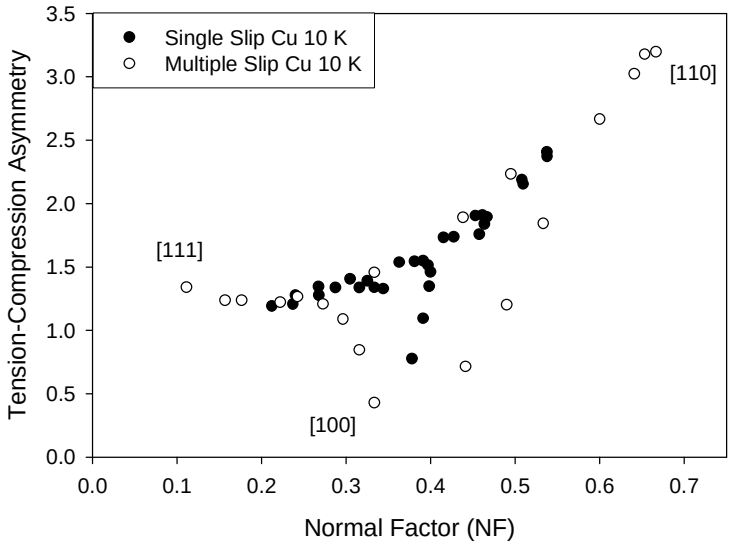


**(b)**

**Figure 11.12:** The tension-compression asymmetry for homogeneous dislocation nucleation as a function of (a) Schmid factor ($SF_0$) and (b) normal factor ($NF_0$) in the initial configuration at 10 K. Black and white symbols denote single and multiple slip lattice orientations.

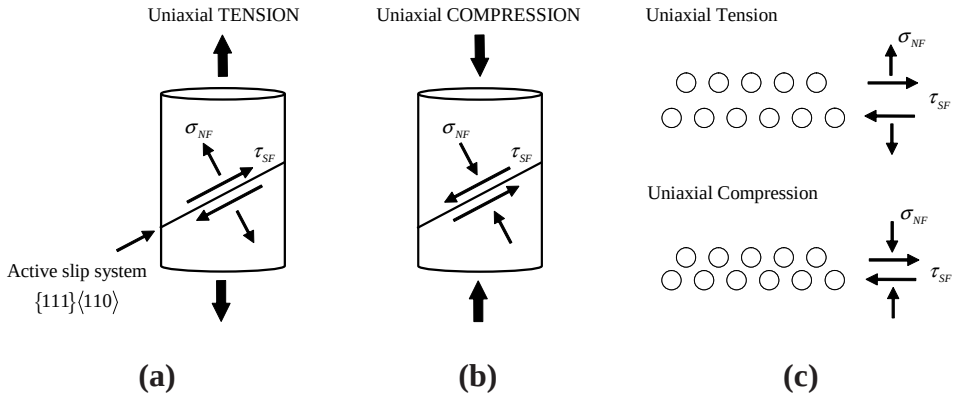


**Figure 11.13:** Schematic showing the differences in resolved stresses on the active slip plane for (a) uniaxial tension and (b) uniaxial compression. At the atomic scale (c), the different directionality of the resolved normal stresses results in forces acting on the spacing of {111} planes, which may prove beneficial or detrimental to dislocation loop nucleation in single crystals depending on the loading.

compression, the compressive normal stress acts to decrease the interplanar spacing between {111} planes, which may effectively increase the interatomic "friction" to slip along these planes. Therefore, since the [110] orientation has the largest normal factor, it is expected that this orientation should also have the largest tension-compression asymmetry, as is shown in Fig. 11.12(b). Moreover, by examining the orientation dependence of the normal factor (Fig. 11.3(b)), it is expected that large tension-compression asymmetries in the dislocation nucleation stress should exist around the [110] orientation with contours skewed towards the [100] orientation, as is observed in Fig. 11.11. While this simple description of how the resolved normal stress affects dislocation nucleation agrees with the calculated results from most loading axis orientations, it does not agree with all orientations (specifically, near the [100] axis), indicating that there may be additional factors contributing to the tension-compression asymmetry in these regions. The [100] orientation has a much lower stress for dislocation nucleation in compression than tension, which may indicate a different dislocation nucleation mechanism; this is examined further in Section 11.3.4. Additionally, there is a tension-compression asymmetry in the elastic response of the [100] and [110] orientation that is briefly discussed in Section 11.3.3.

#### *11.3.2.4 Model for homogeneous dislocation nucleation in single crystals*

The aforementioned first generation single crystal model in Eq. 11.2 [64] was modified to capture the nucleation stress from *all* orientations within the stereographic triangle [81]. This model is also able to capture the transition between the $NF$-dominated dislocation nucleation along the [100]-[110] boundary to the $SF$-dominated dislocation nucleation along the [100]-[111] boundary identified by Spearot and colleagues [64]. The following criterion was used to identify the transition between these two regions within the stereographic triangle, *i.e.*,

$$\sigma_{max}^{sc} = \begin{cases} \frac{\tau_{ideal}}{\mu_{s,1}SF+\mu_{n,1}NF}, & \text{if } \mu_{s,1}SF + \mu_{n,1}NF \geq \mu_{s,2}SF + \mu_{n,2}NF, \\ \frac{\tau_{ideal}}{\mu_{s,2}SF+\mu_{n,2}NF}, & \text{if } \mu_{s,1}SF + \mu_{n,1}NF < \mu_{s,2}SF + \mu_{n,2}NF, \end{cases} \tag{11.6}$$

where $\mu_{s,i}$ and $\mu_{n,i}$ are fitting coefficients for the Schmid factor and normal factor; $i = 1$ corresponds to the $SF$-dominated dislocation nucleation region and $i = 2$ corresponds to the $NF$-dominated dislocation nucleation region. This equation was formulated to allow a mild dependence on $NF$ in an $SF$-dominated region, and vice versa. The use of the fitting parameters within the criterion acts as additional constraint ($\tau_{ideal}/\mu_{s,1}SF + \mu_{n,1}NF = \tau_{ideal}/\mu_{s,2}SF + \mu_{n,2}NF$ when $\mu_{s,1}SF + \mu_{n,1}NF = \mu_{s,2}SF + \mu_{n,2}NF$) that forces a first order transition between the $SF$ and $NF$-dominated regions.

Tschopp *et al*. [81] employed least squares regression to determine the appropriate fitting coefficients for Eq. 11.6: $\mu_{s,1} = 0.574$, $\mu_{n,1} = 0.000$, $\mu_{s,2} = 0.000$, and $\mu_{n,2} = 0.693$ at 10 K. Interestingly, in Cu at 10 K, the normal factor $NF$ has no influence ($\mu_{n,1} = 0$) in the $SF$-dominated dislocation nucleation region, while the Schmid factor $SF$ has no influence ($\mu_{s,2} = 0$) on dislocation nucleation in the $NF$-dominated region. Consequently, Eq. 11.6 can be reduced further, *i.e.*,

$$\sigma_{max}^{sc} = \begin{cases} \frac{\tau_{ideal}}{\mu_{s,1}SF}, & \text{if } \mu_{s,1}SF \geq \mu_{n,2}NF, \\ \frac{\tau_{ideal}}{\mu_{n,2}NF}, & \text{if } \mu_{s,1}SF < \mu_{n,2}NF. \end{cases} \tag{11.7}$$

This equation indicates that the critical component necessary for dislocation nucleation in single crystals under uniaxial tension is either the resolved shear stress in the slip direction *or* the resolved normal stress to the slip plane in which the dislocation nucleates, depending on their magnitudes. Recall that this second generation model for the stress required for homogeneous dislocation nucleation is based on the resolved stress parameters in the initial configuration, though.

The $SF$ and $NF$ values in the deformed configuration corresponding to dislocation nucleation were fit to Eq. 11.6 to evaluate the change in the model with more accurate resolved stress parameters. Least squares nonlinear regression fit to Eq. 11.6 results in $\mu_{s,1} = 0.426$ and $\mu_{n,2} = 0.583$ with $\mu_{n,1} = \mu_{s,2} = 0.000$, which is mainly influenced by the large decrease of $NF$ under uniaxial tension. The fitting parameters for Eq. 11.6 are in line with those based off of the initial $SF$ and $NF$. While a fit to Eq. 11.6 with the resolved stress parameters at dislocation nucleation may be more appropriate, this required atomistic information to calculate the elastic deformation gradient in this work. In this respect, the resolved stress parameters $SF$ and $NF$ from the initial single crystal configuration give a relatively good approximation of the resolved stress components required for dislocation nucleation, noting that the largest change at the onset of plasticity is in the resolved stress normal to the slip plane on which the dislocation nucleates.

A model correlating the calculated dislocation nucleation stresses in uniaxial compression for single crystals with the resolved stress components on the active slip plane(s) was also investigated. Equations 11.2 and 11.6 were used along with a nonlinear regression to find the appropriate fitting parameters: $\mu_s$, $\mu_n$, $\mu_p$, *etc*. However, a satisfactory fit to the calculated values could not be obtained. While Figure 11.9 shows that the dislocation nucleation stress clearly trends with the compressive loading orientation, the form of this relation is different than in tension. As noted earlier, the compressive stress normal to the active slip plane(s) in uniaxial compression has a much different role in dislocation nucleation than the tensile stress normal to the active slip plane in uniaxial tension. However,

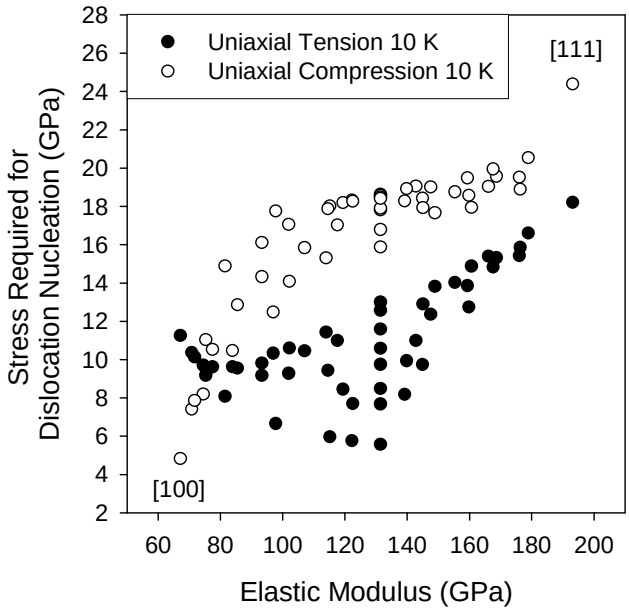


**Figure 11.14:** The tension-compression asymmetry for homogeneous dislocation nucleation as a function of (a) Schmid factor ($SF_0$) and (b) normal factor ($NF_0$) in the initial configuration at 10 K. Black and white symbols denote single and multiple slip lattice orientations.

as briefly mentioned, the initial elastic modulus appears to correlate fairly well with the compressive nucleation stress. Figure 11.14 shows the homogeneous nucleation stress as a function of the initial elastic modulus for uniaxial tension and compression. For tension, no direct correlation exists. For compression, the nucleation stress increases with increasing elastic modulus of the single crystal orientation. Note that Fig. 11.14 also shows a larger asymmetry in the nucleation stress as the elastic modulus decreases toward the orientation with the lowest elastic modulus ([100]). Further work is required to understand the phenomenological form of dislocation nucleation stress during uniaxial compression and to explain the observed correlation with the elastic modulus in compression.

In addition to the application of Eq. 11.6 to homogeneous dislocation nucleation in single crystals, this formulation also has the potential to be applied to heterogeneous dislocation nucleation. Recent simulations by Spearot and colleagues [64] examined the correlation between the nucleation stress from ⟨100⟩ and ⟨110⟩ symmetric tilt grain boundaries

using the crystallographic orientations of the adjacent lattices ($SF$ and $NF$) and a measure of the interface free volume, termed nanoporosity. The first step in the development of the interface strength model required an understanding of the influence of lattice orientation on *homogeneous* dislocation nucleation in single crystals. Accordingly, Eq. 11.6 has a wider range of applicability and can be applied to all single crystal tensile axis orientations instead of Eq. 11.2 [64]. The second step in the interface strength model involved the modification of the homogeneous dislocation nucleation stress for dislocation nucleation due to the presence of a heterogeneous defect (grain boundary interface). In a similar manner, the homogeneous dislocation nucleation stress in the current work can provide a form whereby the influence of other heterogeneous defects (*e.g.*, vacancies, impurities, free surfaces) on dislocation nucleation can be ascertained.

### 11.3.3 Temperature dependence of dislocation nucleation

This section examines the relation between the results obtained at 10 K and 300 K. Previous discussion focused solely on results at 10 K. The influence of temperature on the tensile nucleation stress in single crystal Cu is investigated in Figs. 11.15(a) and 11.15(b) as a function of $SF_0$ and $NF_0$, respectively. As expected, the peak stress decreases with increasing temperature; *i.e.*, thermal energy aids the dislocation nucleation process. In Fig. 11.15, arrows illustrate the difference in the nucleation stress between the two temperatures for the [100], [110], and [111] tensile axis orientations. The [111] axis shows the largest difference in the peak stress magnitude with respect to temperature, while the [110] axis shows the smallest difference. Clearly, thermal energy affects the magnitude of the nucleation stress differently depending on the tensile axis of the single crystal configuration.

Figure 11.16 shows the percent decrease in the dislocation nucleation stress at 300 K relative to that at 10 K as a function of the nucleation stress at 10 K. Data in Fig. 11.16 show that tensile axis orientations with a higher dislocation nucleation threshold stress at 10 K are more adversely affected by increases in temperature. This trend is quite strong for

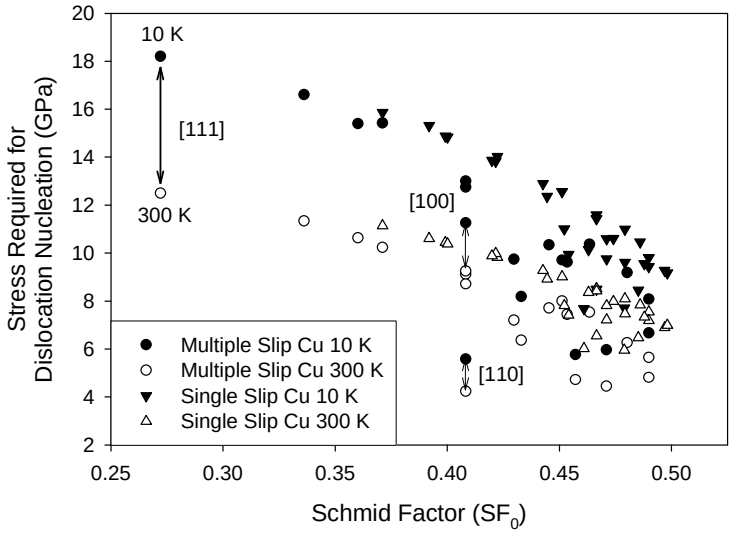


**(a)**

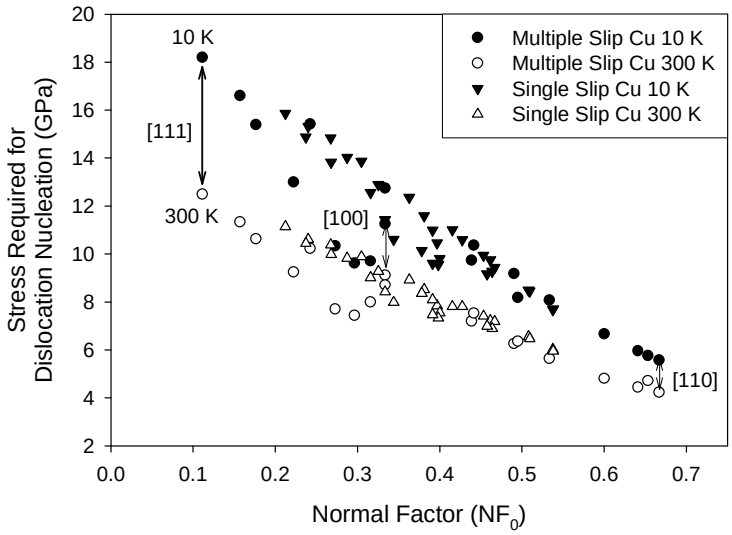


**(b)**

**Figure 11.15:** Tensile stress required for homogeneous dislocation nucleation as a function of (a) Schmid factor ($SF$) and (b) normal factor ($NF$) at 10 K and 300 K. Arrows illustrate the difference in dislocation nucleation stress between 10 K and 300 K for [100], [110], and [111] tensile axis orientations.

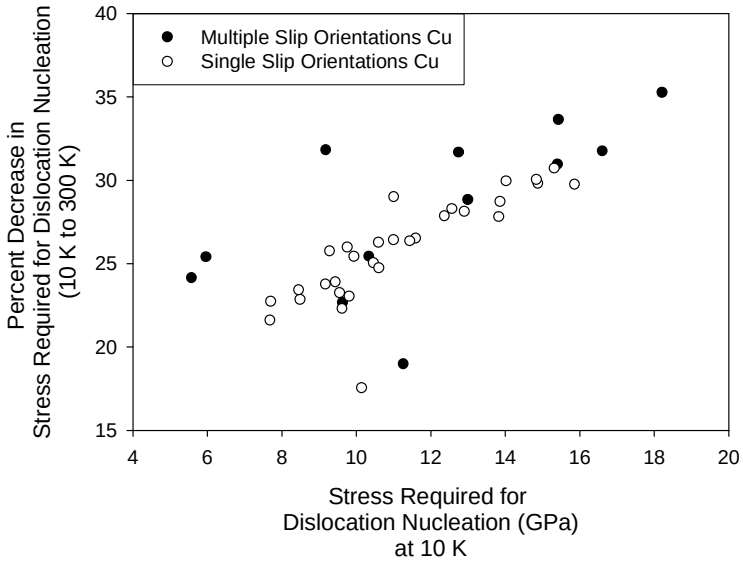


**Figure 11.16:** Percent decrease in the dislocation nucleation stress at 300 K as a function of the nucleation stress at 10 K. Black and white symbols denote multiple slip or single slip orientations, respectively.

single crystal models with orientations on the interior of the stereographic triangle (single slip regime). The trend is less apparent from Fig. 11.16 for tensile axis orientations along the exterior of the stereographic triangle (multiple slip regime), possibly due to an interaction between the temperature and the nature of the multiple active slip systems (conjugate vs. critical vs. coplanar). Interestingly, the observed trend correlates well with respect to $NF$, *i.e.*, tensile axis orientations with a higher $NF$ component have a greater percentage decrease in the dislocation nucleation stress with increasing temperature, which is apparent from Fig. 11.15(b).

While the analysis to this point has focused on the differences in the effect of temperature on the stress required for nucleation in uniaxial tension, there are many similarities in the responses as well. Figure 11.17(a) shows a graph of the stresses required for dislocation nucleation under uniaxial tension and compression at 10 K and 300 K with a fit linear regression line that has a zero intercept. For uniaxial tension, a correlation coefficient of $R^2 = 0.95$ indicates that, on average, the dislocation nucleation stresses at 10 K

and 300 K are related by a temperature-dependent ratio, *i.e.*, $\sigma_{300K} = 0.72\sigma_{10K}$, which is not very sensitive to the loading orientation axis. Figure 11.16 indicates that some of the deviation involved with this temperature-dependent constant may be due to orientations with multiple active slip systems. A similar analysis of both the compressive nucleation stress (also in Fig. 11.17(a)) and the tension-compression ratio (Fig. 11.17(b)) at the two temperatures also gives correlation coefficients of $R^2 = 0.96$ and $R^2 = 0.97$, respectively. The temperature-dependent ratios for the compressive nucleation stress and the tension-compression ratio are 0.79 and 1.07, respectively. These ratios suggest that temperature has a slightly larger influence in tension ($\Delta_{avg} = 28\%$ decrease) than compression ($\Delta_{avg} = 21\%$ decrease) and temperature has a relatively minor effect ($\Delta_{avg} = 7\%$ increase) on the tension-compression ratio.

#### *11.3.3.1 Activation energy and activation volume associated with dislocation nucleation*

Since the stress required to homogeneously nucleate dislocations at 10 K and 300 K is related by a constant, this suggests that thermal activation plays a similar role in homogeneous nucleation in single crystal Cu as in heterogeneous dislocation nucleation (*e.g.*, surfaces or defects). The activation volume $\Omega$ and activation energy $Q$ for homogeneous nucleation are calculated from a first-order model of stress-dependent activation energy whereby the activation energy linearly depends upon stress $\sigma$, *i.e.*, $Q(\sigma) = Q^* - \sigma\Omega$. In this model, $Q^*$ corresponds to the nucleation energy barrier in the absence of applied stress. The activation energy $Q$ measures the sensitivity of nucleation rate to temperature while the activation volume $\Omega$ measures the sensitivity of nucleation rate to stress.

Zhu *et al*. [274] derived a form for the nucleation stress that takes into account both the temperature and strain-rate dependence. They applied this form to dislocation nucleation at surfaces under a constant strain rate. The same equation is employed to calculate the activation energy and activation volume in this study, *i.e.*,

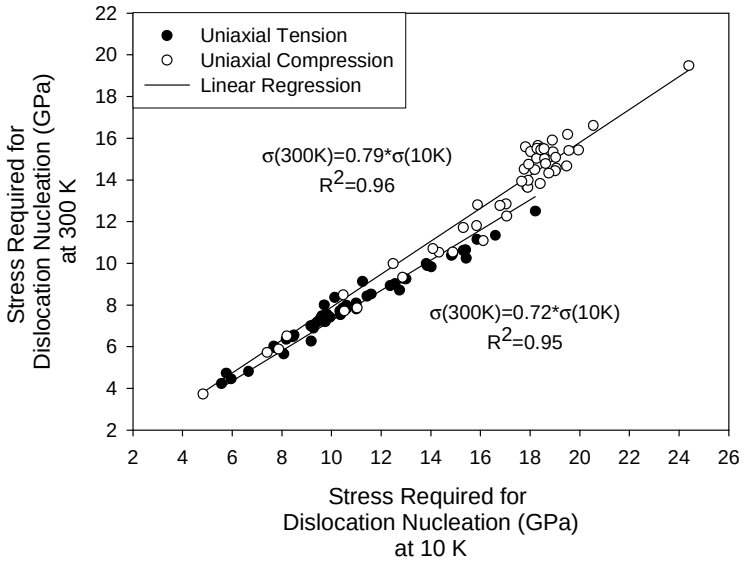


**(a)**

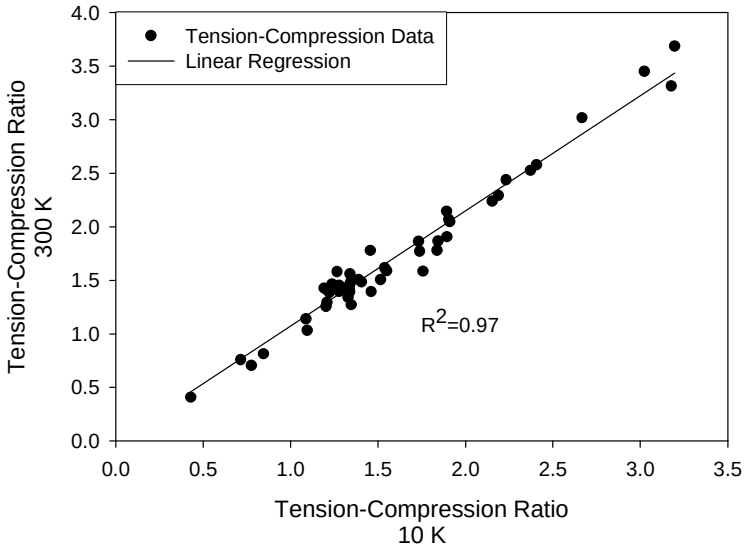


**(b)**

**Figure 11.17:** Comparison of (a) the nucleation stress and (b) the tension-compression ratio at 10 K and 300 K. A linear regression line with a zero intercept is also shown along with the correlation coefficient, $R^2$.

$$\sigma = \frac{Q^*}{\Omega} - \frac{k_B T}{\Omega} ln \frac{k_B T N \nu_0}{E \dot{\epsilon} \Omega} \tag{11.8}$$

In Eq. 11.8, $k_B$ is Boltzmann's constant, $T$ is temperature ($T = 300$ K), $N$ is the number of nucleation sites ($N = 500,000$), $\nu_0$ is the jump frequency ($\nu_0 = 3 * 10^{11}\ s^{-1}$), $E$ is the elastic modulus, and $\dot{\epsilon}$ is the applied strain rate ($\dot{\epsilon} = 10^9\ s^{-1}$). The definitions of the terms are given by Zhu and coworkers [274]. The first term $Q^*/\Omega$ is the athermal stress required to nucleate a dislocation within the single crystal. The pre-factor of the second term $k_B T/\Omega$ reduces the nucleation stress by virtue of thermal fluctuation. In the logarithmic function, the numerator is the rate of energy exchange of the system with the thermal bath and the denominator is the rate of energy delivery into the system through mechanical work; the ratio between these terms determines the relative influence of thermal fluctuations in reducing the nucleation stress.

Several assumptions were made to calculate the activation volume and activation energy. First, the atomic jump frequency ($\nu_0$) chosen represents the cooperative atomic motion necessary to form a dislocation, and is on the order of the frequency of free oscillation in copper [278]. Second, the number of nucleation sites ($N$) chosen represents the approximate number of atoms in the system. Since these are embedded in the logarithmic term, variation of $N\nu_0$ by several orders of magnitude results in very little change to the activation volume. Third, since the first term in Eq. 11.8 corresponds to the athermal nucleation stress, the calculated nucleation stresses at 10 K are used as an approximate value. The nucleation stresses from multiple orientations were used to capture the effect of the orientation-dependent variation in the nucleation stress on the activation volume. Last, the initial elastic moduli (Eq. 11.5) for multiple orientations were used to determine the effect of elastic anisotropy on the calculations; this had little effect. Using the nucleation stress values for uniaxial tension at $T = 300$ K, the activation volumes for homogeneous dislocation nucleation were on the order of 0.5-2 $b^3$. Rearranging the first term in Eq. 11.8, *i.e.*, $Q^* = \sigma\Omega$, gives the activation energy barrier under zero applied stress. However, using

**Table 11.2:** Activation energies and volumes for [100], [110], [111], and [321] oriented single crystals.

| Loading Orientation | $\sigma_{300K}$ (GPa) | $E_{[hkl]}$ (GPa) | $\Omega$ ($b^3$) | $Q^*$ (eV) | $Q$ (eV) |
|---|---|---|---|---|---|
| [100] | 9.5 | 67.1 | 1.63 | 1.92 | 0.30 |
| [110] | 4.2 | 131.4 | 2.17 | 1.26 | 0.30 |
| [111] | 12.5 | 193.1 | 0.55 | 1.05 | 0.33 |
| [321] | 8.6 | 131.4 | 1.02 | 1.23 | 0.32 |

our first order approximation of a linear dependence of activation energy on stress, *i.e.*, $Q(\sigma) = Q^* - \sigma\Omega$, the activation energy for homogeneous dislocation nucleation at 300 K can be calculated. For example, the [100], [110], [111], and [321] orientations have calculated activation volumes of $\Omega$ = 1.63, 2.17, 0.55, and 1.02 $m^3$, respectively, and calculated activation energies of $Q$ = 0.30, 0.30, 0.33, and 0.32 eV, respectively. These values and others are summarized in Table 11.2. Interestingly, the activation energies at 300 K are roughly the same for all orientations examined. Since the activation volume is defined as $\Omega \equiv -dQ/d\sigma$, changes in the nucleation stress as a function of loading orientation slightly affect the calculated values of $\Omega$. Small activation volumes of 0.5-2 $b^3$ promote enhanced temperature sensitivity of homogeneous dislocation nucleation in single crystal simulations.

Conversely, Zhu and coworkers [256, 274] have calculated activation volumes and activation energies for heterogeneous dislocation nucleation and dislocation reactions using the climbing image nudged elastic band (CINEB) method. The CINEB method allows for a direct calculation of the activation energy vs stress relationship, without relying on several of the aforementioned assumptions made in the current calculations. Even so, the calculated activation energies for homogeneous dislocation nucleation in the present study are on the order of those computed for side surface nucleation ($Q$ = 0.64 eV) and corner nucleation ($Q$ = 0.1 eV) from nanopillars [274]. Moreover, Zhu and coworkers [256] calculated activation energies for dislocation absorption ($Q_{abs}$ = 0.49 eV) and dislocation direction transmission ($Q_{trs}$ = 0.67 eV) at the coherent twin boundary that are similar to the present

molecular dynamics calculations at a strain rate of $10^9$ $s^{-1}$. The similarity of values suggests that the current calculations are a reasonable approximation of the activation volumes and activation energies for homogeneous dislocation nucleation in pure Cu single crystals.

The calculated activation energies does seem to contrast with some former studies on the activation energies required for homogeneous dislocation nucleation, though. For instance, Xu and Argon used a continuum description of dislocations to determine an activation energy of 16 eV in Cu at a shear stress half of the ideal shear stress [311, 312]. This suggests that thermal motion should have no effect on the nucleation of dislocation loops in perfect crystals. In fact, due to the high activation energies for homogeneous dislocation nucleation [311, 312], Gutkin and Ovidko [313] have proposed that the dislocation loops nucleate by a special mechanism in nanocrystalline materials, whereby the Burgers vector of the dislocation loop gradually increases from zero with the increasing size of the dislocation loop; they show this to be energetically favorable in nanocrystalline materials.

The activation energies and activation volumes for dislocation nucleation in single crystals can be measured from nanoindentation experiments. While these values can be measured, there is some debate as to whether this is the result of homogeneous or heterogeneous nucleation. Numerous atomistic simulations of nanoindentation of perfect single crystals have shown that dislocations nucleate homogeneously beneath the indenter (*e.g.*, [106, 107, 314]). Schuh *et al.* [277] measured activation volumes of $\approx 0.5\ b^3$ and activation energies of $\approx 0.28$ eV associated with nanoindentation experiments on platinum at various temperatures. However, homogeneous dislocation loop nucleation is expected to have larger activation volumes [277, 315], corresponding to the cooperative process of atomic motion. These low activation volumes suggested that homogeneous dislocation nucleation was not likely the case. Rather, heterogeneous dislocation nucleation from pre-existing point defects, such as vacancies, were more likely.

On the other hand, the current study suggests that dislocation nucleation is in fact sensitive to temperature fluctuations (atomic vibration) and has low activation volumes. The

low activation volumes indicate that at the appropriate stress level, the motion of a few atoms may serve as the impetus for nucleating the dislocation loop. Zuo *et al.* [316] used atomistic simulations of $Ni_3Al$ to show that dislocation nucleation occurs when one atom reaches a critical displacement relative to its neighbors under the influence of temperature and stress. In previous studies, Spearot *et al.* [64] have shown that the dislocation nucleation stresses for some symmetric tilt grain boundaries are very similar to the stresses required for homogeneous dislocation nucleation in a single crystal with identical lattice orientation. These simulations were performed at the same temperature and strain rate, so very few parameters within Eq. 11.8 would change between the single crystal and bicrystal deformation simulations. This results in similar calculated activation energies and volumes for both heterogeneous and homogeneous dislocation nucleation. The simulations suggest that while heterogeneities offer an additional driving force for dislocation nucleation, in some cases this may not result in a significant deviation from the driving force for homogeneous dislocation nucleation in the corresponding defect-free single crystal lattice.

#### *11.3.3.2 Temperature dependence of dislocation nucleation*

To further examine the temperature dependence of dislocation nucleation in single crystals, Figure 11.18 plots the stress-strain response for four loading orientations under uniaxial tension and compression as a function of several temperatures: 10, 100, 200, 300, 400, 500, 600, and 700 K. In these graphs, the tensile stress is positive while the compressive stress is negative. The strain is defined as $\epsilon = \delta_h/h$, where $h$ is the initial height of the cell in the loading direction and $\delta_h$ is the conjugate displacement of the overall unit cell. The four loading orientations correspond to the three corners of the stereographic triangle (*i.e.*, [100], [110], and [111]) and an interior orientation ([321]). The tension-compression asymmetry in dislocation nucleation as a function of temperature is evident from Fig. 11.18, *i.e.*, the peak stress is very different for some orientations. Interestingly, the strain associated with dislocation nucleation also differs between tension and compression. The effect of

temperature on the peak stress and strain can be observed from Fig. 11.18. For instance, temperature greatly affects the stress for some orientations (*e.g.*, [111]) and less so in other orientations (*e.g.*, [110] in tension). The temperature may also affect the same orientation differently in tension than in compression. For example, the strain required for dislocation nucleation is greatly affected by temperature for the [110] orientation in uniaxial tension, but it is not affected as much in compression by comparison.

The strain at dislocation nucleation in Fig. 11.18 may be very different in terms of magnitudes for (i) tension and compression, or for (ii) different crystallographic orientations, which will influence the magnitudes of the resolved stress components. The parameters $SF$ and $NF$ were calculated from the initial crystal orientation in order to give an approximate description of how the uniaxial loads resolve into stress components acting on the active slip systems. However, as deformation occurs, the active slip systems will rotate with the lattice creating slightly different resolved stresses on the slip systems. The magnitude that the slip systems rotate just prior to dislocation nucleation will depend on the strain corresponding to the peak stress. The rotation is not necessarily negligible as the strain to nucleation is on the order of 10%. Therefore, the influence of lattice rotation on the resolved stress components is investigated further in Section 11.3.2.

Lattice rotation may also explain the nonlinear elastic effect observed for the [100] and [110] orientations in Figs. 11.18(a) and (b), respectively. For example, the change in the stress as a function of strain increases for the [100] orientation in tension and the [110] orientation in compression. On the other hand, there is a pronounced decrease in the stress as a function of strain for the [100] orientation in compression and the [110] orientation in tension, despite the fact that no dislocations have nucleated yet. This tension-compression asymmetry in elastic response for the [100] and [110] orientations is in line with Fig. 11.11, which shows that these two orientations are the extreme values of the tension-compression asymmetry for the stresses required for dislocation nucleation. Moreover, the normalized stress ($\sigma/E_{[hkl]}$) contour plots in Figs. 11.7(b) and 11.9(b) also show that the [100] and

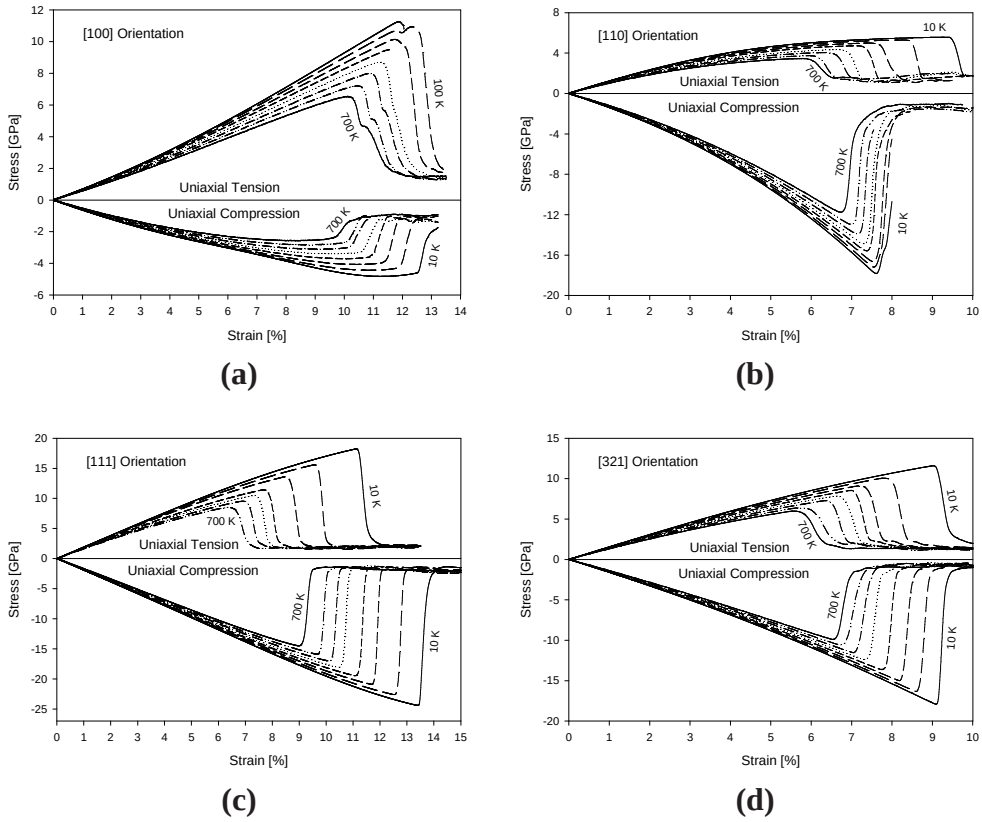


**Figure 11.18:** Stress-strain curves for uniaxial loading in the (a) [100], (b) [110], (c) [111], and (d) [321] orientations at multiple temperatures: 10, 100, 200, 300, 400, 500, 600, and 700 K. The outer stress strain curves are labeled with the temperature and all other stress-strain curves follow in order of temperature.

[110] orientations are the extreme values of $\sigma/E_{[hkl]}$. On the other hand, the [111] and [321] orientations do not exhibit this nonlinearity nearly to the extent of the [100] and [110] orientations.

The nucleation stress was extracted from Fig. 11.18 and is shown in Fig. 11.19(a) for uniaxial tension and compression. In agreement with the earlier findings in tension at temperatures of 10 K and 300 K, the decrease in the nucleation stress at an elevated temperature depends on the magnitude of the *athermal* nucleation stress (or at 10 K, in this work). Temperature had a much greater effect on orientations that required a higher stress at 10 K to nucleate dislocations. This was true for both uniaxial tension and compression. The lines for the uniaxial tension nucleation stresses were generated using Eq. 11.8 with

the activation volume as a fitting parameter for each orientation, *i.e.*, the activation volume is assumed constant for all temperatures. Least squares regression gives activation volumes of 0.7-3.0 $b^3$ for the four orientations, in line with the previously calculated activation volumes at 300 K. However, the trend lines generated using a constant activation volume do not capture the nonlinear behavior of the stress-temperature relationship (*e.g.*, see data for the [111] orientation). A slight temperature dependence of the activation volume may be required to capture this relationship with Eq. 11.8. Figure 11.19(b) shows the tension-compression ratio as a function of temperature for these four loading orientations. The tension-compression ratio is relatively unaffected by temperature in comparison to the stresses required for dislocation nucleation in Fig. 11.19(a). The nucleation stress scales similarly with respect to temperature in both uniaxial tension and compression. This implies that the activation volumes and activation energies are similar in tension and compression for a given crystal orientation.

### 11.3.4 Dislocation nucleation mechanisms and slip system analysis

#### *11.3.4.1 Dislocation activity in uniaxial tension*

Figure 11.20 shows images following dislocation nucleation under uniaxial tension at 10 K for several loading orientations: [110], [111], [221], and [321]. These images show multiple dislocations at different stages of their formation. Dislocations are rendered by using a cutoff in the centrosymmetry parameter [106] to show only the atoms in a local non-centrosymmetric environment. First, the collective motion of several atoms along the active slip system(s) begins nucleation. Then, the cooperative atomic shuffling of these atoms nucleates a partial dislocation loop within the single crystal, where the exterior of the dislocation loop is the partial dislocation core that bounds an intrinsic stacking fault in the lattice. Thus, the nucleated dislocations have both edge and screw dislocation character. Multiple dislocations are nucleated within the crystal lattice at very similar strains at 10 K, which causes dislocation loop interactions as the dislocation loops propagate throughout

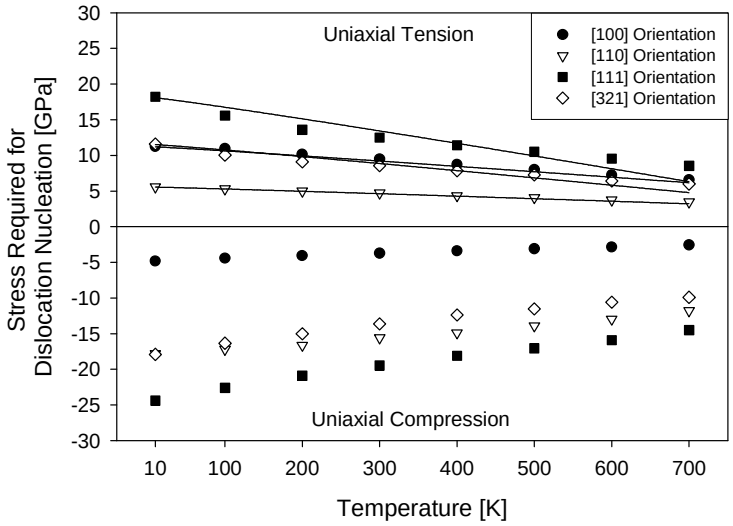


**(a)**

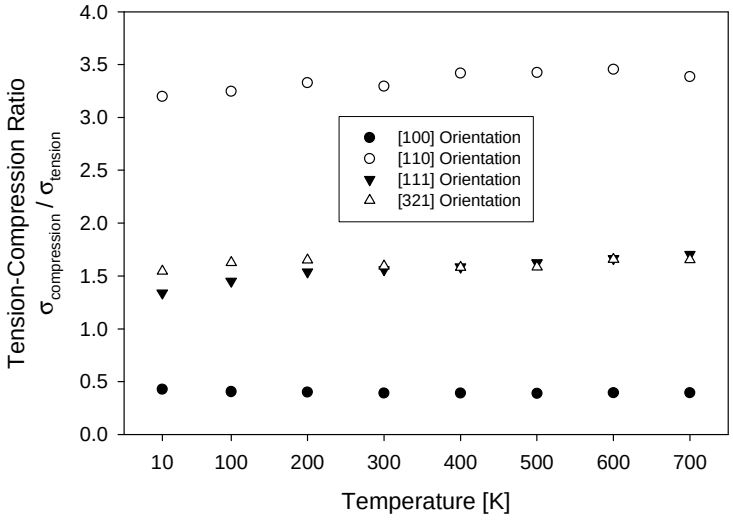


**(b)**

**Figure 11.19:** The temperature influence on (a) the uniaxial tensile and compressive stresses required for dislocation nucleation and (b) the tension-compression ratio, $\sigma_{compression}/\sigma_{tension}$. The four orientations correspond to those in Fig. 11.18.

the crystal. However, these interactions occur after the nucleation stress has been obtained. Examination of the partial dislocation loops indicates that dislocations nucleate on slip planes with the highest resolved stress components. Fig. 11.20 shows that the quadruple slip [110] (Fig. 11.20(a)) and octahedral slip [111] (Fig. 11.20(b)) orientations have partial dislocation loops on two and three {111} slip planes, respectively. Only partial dislocation loops on one {111} slip plane are observed for the single-slip [321] (Fig. 11.20(d)) and double slip [221] (Fig. 11.20(c)) orientation, which agrees with the predicted slip systems. Recall that the [221] orientation is a coplanar slip system, *i.e.*, both ⟨110⟩ slip directions are on the same slip plane. The inset shows isolated dislocation loops on the $\left(11\bar{1}\right)$ slip plane for each crystal; for the three orientations along the [110]-[111] boundary of the stereographic triangle, the dislocation loop expands more rapidly in the [112] partial slip direction. The [321] orientation expands more rapidly in a ⟨110⟩ slip direction, similar to the [210] and [211] orientations (not shown). The asymmetric dislocation loop expansion is the consequence of differing resolved shear stresses in the ⟨110⟩ and ⟨112⟩ directions on the {111} slip planes. Last, temperature does not appear to affect the calculated dislocation mechanism; partial dislocation loops are also observed at 300 K.

#### *11.3.4.2 Dislocation activity in uniaxial compression*

Dislocation nucleation in uniaxial compression shows several differences from that in tension, particularly at 300 K. For the 10 K simulations, partial dislocation loops are nucleated in compression, similar to those nucleated in tension. However, seven loading orientations from various locations around the stereographic triangle — [100], [110], [111], [210], [211], [221], and [321] — were examined at 300 K. Five of these orientations nucleated full dislocation loops, while the other two orientations ([100] and [110]) nucleated partial dislocation loops similar to those at 10 K. This emphasizes the role of thermal activation in the nucleation of the second partial. Dislocation nucleation for these orientations at 300 K is analyzed further in the following paragraphs.

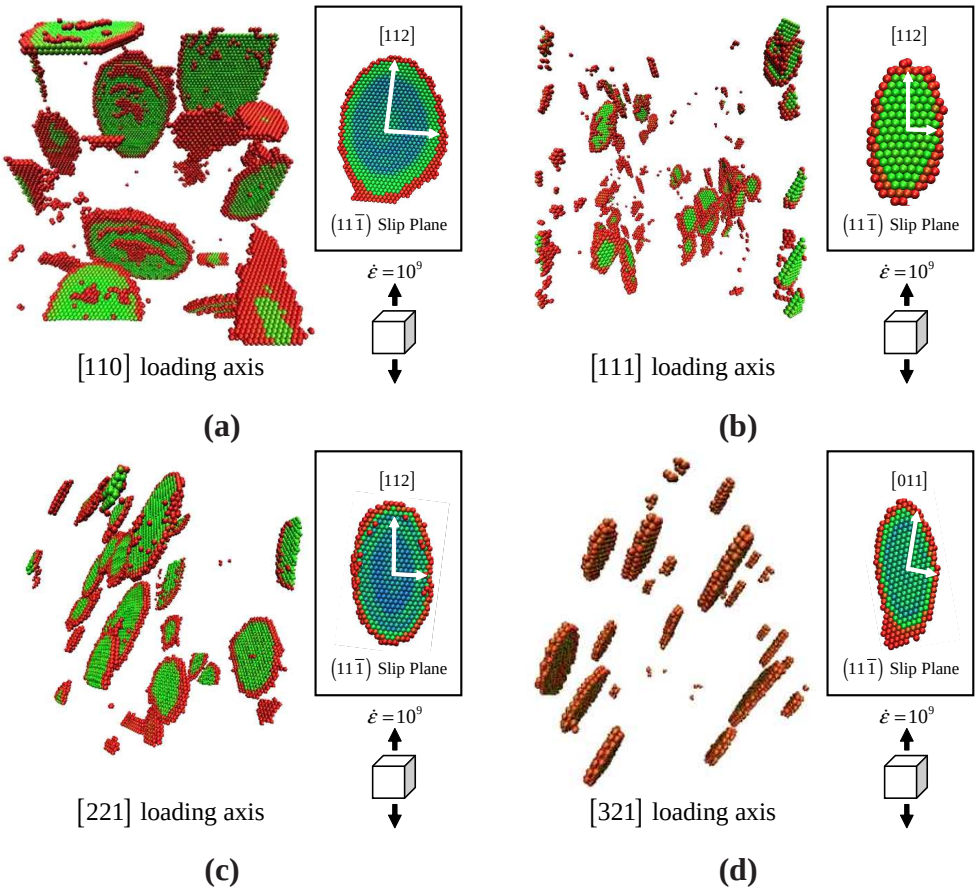


**Figure 11.20:** Homogeneous dislocation nucleation for (a) [110], (b) [111], (c) [221], and (d) [321] loading orientations in single crystal Cu at 10 K under uniaxial tension. Only atoms in a local non-centrosymmetric environment are shown. The inset in the upper right corner shows an isolated dislocation loop on the $\left(11\bar{1}\right)$ slip plane.

Figure 11.21 shows images of dislocation nucleation under uniaxial compression at 300 K for five loading orientations: [111], [210], [211], [221], and [321]. These images are rendered in a similar manner to Fig. 11.20 to show multiple dislocation loops, at different stages of their formation, for each loading orientation. In contrast to uniaxial tension, the dislocations nucleate as full dislocation loops in uniaxial compression for many loading axis orientations. That is, each dislocation loop is the result of two partial dislocations: an initial Shockley partial dislocation and a trailing Shockley partial dislocation. The intrinsic stacking fault separating the two partials can be observed in Fig. 11.21 as well. Examination of the calculated partial dislocation loops indicates that dislocations nucleate on the maximum Schmid factor slip planes. Figures 11.21(c) and (d) show the dislocation loops at two slightly different strain levels; Fig. 11.21(d) is at a higher strain than Fig. 11.21(c). Interestingly, there appears to be an evolution to the nucleation of a full dislocation loop in uniaxial compression.

Figure 11.22 shows different stages of evolution for dislocation loops under an applied uniaxial compressive stress. As with uniaxial tension, the collective motion of several atoms along the active slip system(s) marks the onset of nucleation. Then, the cooperative atomic shuffling of these atoms nucleates a partial dislocation loop within the single crystal as shown in Fig. 11.22(a), where the exterior of the dislocation loop is the partial dislocation core that bounds an intrinsic stacking fault in the lattice. This is similar to how dislocation loops nucleate in uniaxial tension. However, unlike in uniaxial tension, the second trailing partial dislocation is nucleated at the center of the partial dislocation loop as shown in Fig. 11.22(b). At this point, the width of the stacking fault is wider than at subsequent strains. Figures 11.22(c) and (d) show the full dislocation loop as it expands under an increasing compressive strain. The separation distance between the two partial dislocations (*i.e.*, the stacking fault width) has decreased. Notice that the width of the stacking fault depends on the location on the dislocation loop; this corresponds to portions of the dislocation loop with edge and screw dislocation character. By equating the attractive force

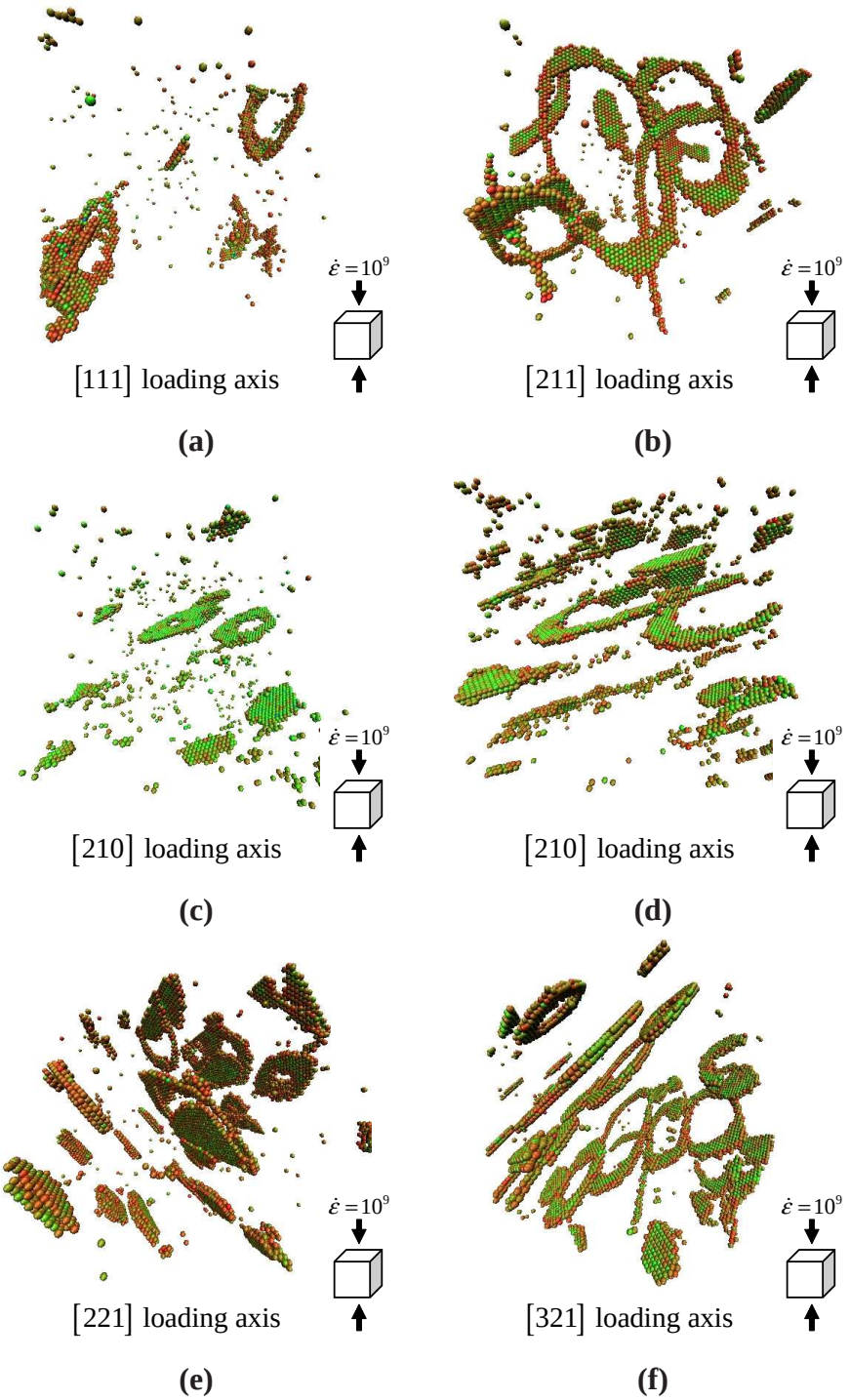


**Figure 11.21:** Homogeneous dislocation nucleation for (a) [111], (b) [211], (c-d) [210], (e) [221], and (f) [321] loading orientations in single crystal Cu at 300 K under uniaxial compression. Only atoms in a local non-centrosymmetric environment are shown. Slightly different stages of dislocation nucleation are shown for the [210] orientation in (c) and (d).

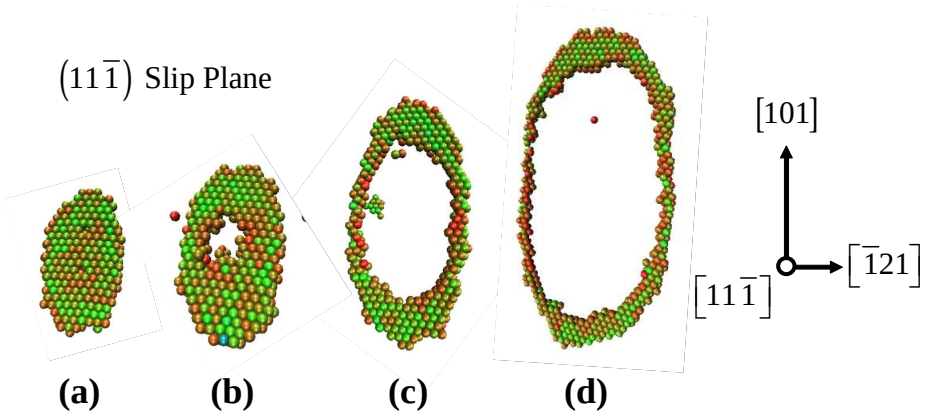


**Figure 11.22:** Evolution of dislocation loop nucleation for [321] loading orientation in single crystal Cu at 300 K under uniaxial compression. The dislocation loops are viewed from the direction normal to the slip plane, *i.e.*, the $[11\bar{1}]$ direction. The coordinate system is shown to the right. The Burger vector is in the [101] direction.

due to the stacking fault energy and the repulsive elastic force of the two partials, Hirth and Lothe ( [215], p. 315-316) calculate that the ratio of *equilibrium* separations for two Shockley partials of edge and screw character is 7:3 (the edge orientation exceeds that for a screw orientation). In the present case, the separation distance of the edge segment with Burgers vector in the [101] direction is greater than the screw segment. The separation distance from Ref. [215] is for equilibrium between two infinite partial dislocations (not dislocation loops) and does not account for either the influence of the resolved stresses or the motion of the dislocations (dynamics), but the agreement with the present results is still good. The dislocation loop also expands non-uniformly with the edge dislocation segment moving at a slightly higher rate than the edge dislocation segment. This non-uniform expansion is likely due to the much higher resolved shear stress in the $\langle 110 \rangle$ slip direction.

One may ask the question, can the calculated behavior in single crystals promote understanding in configurations with heterogeneities, such as grain boundaries and free surfaces? To this end, the calculated dislocation loop behavior for these orientations is also compared with bicrystal grain boundary dislocation nucleation simulations and nanocrystalline deformation simulations. It is frequently observed that partial dislocations are emitted from the

grain boundary and absorbed into the opposite boundary without the trailing partial being emitted (*e.g.*, in bicrystal Cu [64] or nanocrystalline Cu simulations [18,19,59]). However, relatively few simulations in the literature focus on the deformation of copper in compression. Bringa *et al.* [7] show the presence of full dislocation emission in nanocrystalline copper simulations under compressive shock loading. Moreover, in Chapter 7, bicrystal MD simulations calculate full dislocation nucleation and emission from a vicinal twin boundary and other [110] symmetric tilt grain boundaries in Cu under a compressive strain rate of $10^9$ $s^{-1}$. Additionally, nanowire deformation simulations of Park *et al.* [317] show that slip by full dislocation emission for single crystal FCC nanowires with ⟨100⟩ and ⟨110⟩ orientations is only calculated in compression. These studies indicate that the present calculated dislocation behavior for single crystals in tension and compression may also improve understanding about plasticity in FCC lattices with heterogeneities as well.

#### *11.3.4.3 Anomalous dislocation activity in uniaxial compression*

While many single crystal orientations nucleate a full dislocation loop under uniaxial compression, the [100] and [110] orientations display quite different dislocation behavior. Dislocation nucleation for the [100] axis orientation in compression is similar to that in tension, as shown in Figure 11.23. Notice that no trailing partial dislocation is nucleated for the [100] orientation, so the exterior of the loop is an $a_0/6\langle 112\rangle$ partial dislocation. Relating to the resolved stresses, the [100] orientation has a normal factor value of $NF = 0.333$, but due to the low applied nucleation stress, the resolved stress normal to the slip plane is $\sigma_{NF} = -1.24$ GPa at 300 K. This is the lowest compressive normal stress for all orientations in uniaxial compression, implying that the nucleation of the second trailing partial dislocation may be related to the magnitude of the resolved normal stress ($\sigma_{NF}$) in uniaxial compression.

On the other hand, the dislocation nucleation behavior for the [110] axis orientation is much different in compression than in tension. Figure 11.24 shows dislocation nucleation

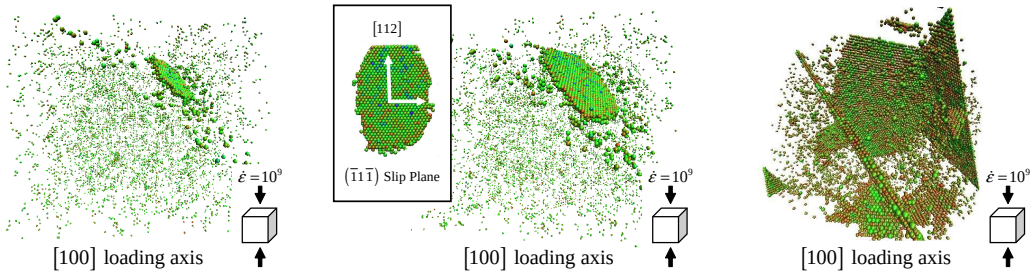


**(a)** **(b)** **(c)**

**Figure 11.23:** Homogeneous dislocation nucleation for the [100] loading orientation in single crystal Cu at 300 K under uniaxial compression.

in the [110] orientation for three strains (a-c) as viewed along the $\left[1\bar{1}0\right]$ direction (into the page). Figures 11.24(d-f) show an orthonormal view of a 1-nm slice taken from parts (a-c). At first glance, there appears to be a noticeable absence of dislocation line defects within the single crystal. Instead, there appears to be a noticeable band of atoms (perpendicular to the loading axis) in a non-centrosymmetric environment that widens in the compressive axis direction with increasing strain. This seems to agree with the observations of Park and coworkers [317], who observed a similar sort of plastic deformation behavior in Ni nanowires with a ⟨110⟩ axis and {111} side surfaces. However, upon closer examination of the slices in Figs. 11.24(d-f), this band behavior is actually due to short segments of dislocations on the {111} and $\left\{11\bar{1}\right\}$ slip planes. Possible factors that contribute to this behavior include:

1. The available slip planes may contribute to this behavior. The $\left\{1\bar{1}1\right\}$ and $\left\{1\bar{1}\bar{1}\right\}$ slip planes are rendered inactive since the resolved shear stress (and resolved normal stress) is zero for these planes (*i.e.*, these planes contain the [110] loading orientation). The only possible slip planes for dislocation nucleation and motion are the two active slip planes: {111} and $\left\{11\bar{1}\right\}$. This crystallographic situation only arises in ⟨110⟩ orientations.

2. The resolved stresses on the slip planes may also contribute to this behavior. The normal factor ($NF = 0.666$), the ratio of the normal factor to the Schmid factor

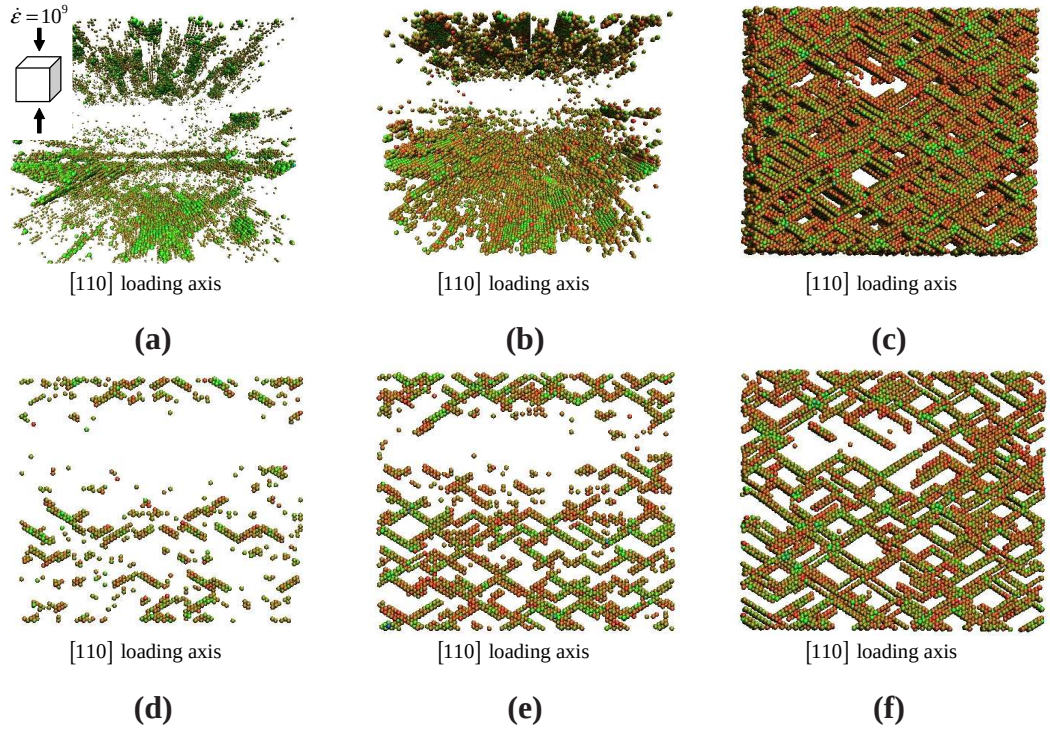


**Figure 11.24:** Homogeneous dislocation nucleation for the [110] loading orientation in single crystal Cu at 300 K under uniaxial compression. The loading direction shown in (a) is consistent for all orientations.

($NF/SF = 1.633$), and the resolved normal stress ($\sigma_{NF} = -10.39$ GPa at 300 K) are highest for the [110] orientation.

Figure 11.25 shows the resolved shear stress $\tau_{SF}$ and resolved normal stress $\sigma_{NF}$ for all single crystal orientations at 300 K. The magnitudes of the resolved stress components are much higher in compression than in tension. In particular, the resolved stress normal to the maximum Schmid factor slip plane is much higher in compression. Unlike most orientations in compression, the [100] and [110] orientations nucleate partial dislocations similar to in tension and are pointed out with arrows. Notice that these orientations have the lowest and highest $\sigma_{NF}$ values, perhaps explaining their behavior. Not all orientations were examined for the dislocation nucleation mechanism, so it is not precisely known where plastic deformation transitions from a partial dislocation to a full dislocation mechanism. Some orientations near the [100] and [110] may exhibit similar dislocation behavior.

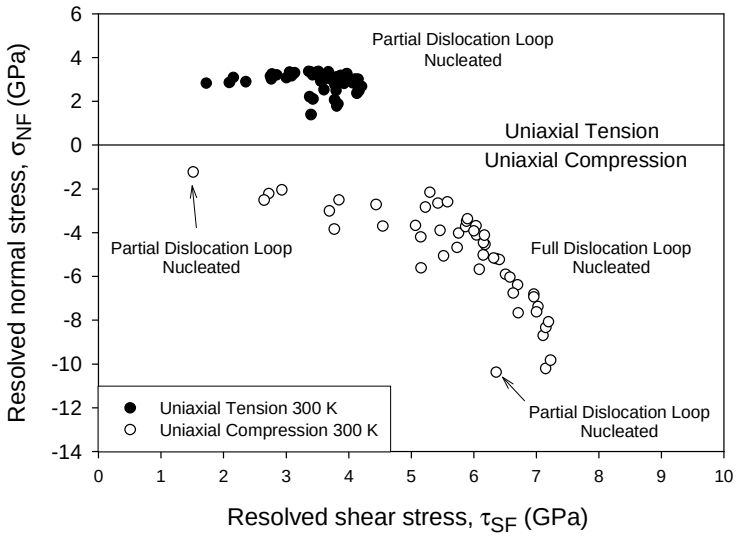


**Figure 11.25:** Resolved shear stress $\tau_{SF}$ and resolved normal stress $\sigma_{NF}$ associated with homogeneous dislocation nucleation for all single crystal orientations under uniaxial tension and compression at 300 K. The [100] and [110] orientations nucleated partial dislocations, while all other orientations examined in uniaxial compression nucleated full dislocation loops.

#### *11.3.4.4 Resolved stresses, stacking fault energies and dislocation activity*

The contrast between the nucleation mechanisms under uniaxial tension and compression sheds light on our fundamental understanding of how resolved stresses affect dislocation loop nucleation in single crystals. As discussed in Section 11.3.2.3 and depicted in Fig. 11.13, the main difference in how the applied stress is resolved for uniaxial tension and compression is the stress normal to the slip plane; in tension, this normal stress is tensile, and vice versa. Full dislocation nucleation observed under uniaxial compression implies that a compressive stress normal on the active slip plane may (i) contribute to the nucleation of a second partial dislocation, and (ii) may exert an additional attractive force between the two partial dislocations, both of which are observed in Fig. 11.21. In contrast, a tensile stress normal to the slip plane may deter the nucleation of a second partial dislocation and possibly exert an additional repulsive force between the two partial dislocations. This may be explained with the generalized stacking fault (GSF) curve [270, 271] in the $\langle 112 \rangle$

direction for an FCC crystal. Zimmerman *et al.* [127] show that the GSF is affected by deformation of the material. They biaxially stretch the lattice by 4% while calculating the GSF curves and find that the unrelaxed $\gamma_{USF}$ value[1] of 175 mJ/m$^2$ is reduced to 99 mJ/m$^2$ for the 'deformed and relaxed' simulations. In this sense, the barrier to dislocation nucleation is reduced by the applied deformation. The GSF curve may be similarly affected by the magnitude and directionality of the resolved stress normal to the slip plane, particularly with respect to dislocation nucleation.

Interestingly, several well-known studies on the influence of stacking fault energy on dislocation nucleation in nanocrystalline materials do not consider the effect of loading orientation (tension versus compression). Rather, Yamakov and coworkers [26] proposed a deformation mechanism map that described the transition from dislocation-mediated to grain boundary-mediated plastic deformation based on the equilibrium splitting distance for partials at $\sigma = 0$ and the grain boundary diameter, among other quantities. However, the description for the splitting distance is based solely on the intrinsic stacking fault energy, $\gamma_{SF}$, with no dependence on the unstable stacking fault energy, $\gamma_{USF}$. Simulations of nanocrystalline deformation do not support the cross-over of dislocation-based deformation mechanisms (slip of extended partial dislocations versus perfect slip of full dislocations) based only on the value of $\gamma_{SF}$. Van Swygenhoven *et al.* [23] noted that extended partial dislocations are observed above and below the predicted cross-over grain size in Cu [18, 19, 59]. Additionally, nc deformation simulations [60, 141] with a Ni potential (higher $\gamma_{SF}$ than Al) only revealed extended partial dislocations for grain sizes as large as 20 nm. In contrast to the deformation mechanism map proposed by Yamakov *et al.*, Van Swygenhoven and coworkers [23] proposed that extended or full dislocation activity should be understood in terms of $\gamma_{sf}/\gamma_{usf}$ and, more importantly, that $\gamma_{SF}$ alone cannot capture the important physics of the nucleation of leading and trailing partial dislocations from grain

[1]Recall that the unstable stacking fault energy ($\gamma_{USF}$) of the GSF curve is associated with the energy barrier for dislocation nucleation [126].

boundaries. Although only single crystal atomistic simulations, the present simulations show that the loading orientation, and the resolved stress normal to the slip plane, may affect the GSF curve as discussed in the preceding paragraph. Further work exploring how both compressive *and* tensile normal stresses affect the GSF curve would shed valuable insight into these arguments.

## *11.4 Summary*

In this chapter, atomistic modeling of *homogeneous* dislocation nucleation in Cu single crystals was investigated under uniaxial tension and compression using molecular dynamics with the Mishin EAM potential [124]. Atomistic simulations are used to investigate how the stress required for homogeneous nucleation of partial dislocations in single crystal copper under uniaxial loading changes as a function of crystallographic orientation. Results indicate that non-Schmid parameters are important for describing the calculated dislocation nucleation behavior for single crystal orientations under tension and compression. A continuum relationship is presented that incorporates Schmid and non-Schmid terms to correlate the nucleation stress over all tensile axis orientations within the stereographic triangle. Simulations investigating the temperature dependence of homogeneous dislocation nucleation yield activation volumes of ≈0.5-2 $b^3$ and activation energies of ≈0.30 eV. For uniaxial compression, full dislocation loop nucleation is observed, in contrast to uniaxial tension. One of the main differences between uniaxial tension and compression is how the applied stress is resolved normal to the slip plane on which dislocations nucleate — in tension, this normal stress is tensile, and in compression, it is compressive. Last, the tension-compression asymmetry is examined as a function of loading axis orientation. Orientations with a high resolved stress normal to the slip plane on which dislocations nucleate have a larger tension-compression asymmetry with respect to dislocation nucleation than those orientations with a low resolved normal stress. The significance of this research is that the resolved stress normal to the slip plane on which dislocations nucleate plays an

important role in partial (and full) dislocation loop nucleation in FCC Cu single crystals.

# CHAPTER XII

# CONCLUSIONS AND RECOMMENDATIONS

## *12.1 Overview*

This dissertation has addressed dislocation nucleation in single crystals and grain boundaries in FCC Cu and Al. The subject is of considerable importance given the interest in the plasticity nanocrystalline materials. The work presented here has focused on understanding the role of the grain boundary structure and single crystal orientation in the nucleation and emission of dislocations from grain boundaries. This effort necessitated the development and implementation of computational tools for performing simulations and analyzing the results. A number of independent studies were required to gain a better understanding of how dislocations nucleate at atomic scales, including:

- Structure and energies of $\Sigma 3$ asymmetric tilt grain boundaries
- Structure and energies of low order CSL asymmetric tilt grain boundaries
- Structure and free volume of symmetric tilt grain boundaries with the E structural unit
- Dislocation nucleation from $\Sigma 3$ asymmetric tilt grain boundaries
- Atomistic simulations of dislocation nucleation under uniaxial tension and compression
- Implications of Dislocation Nucleation Studies on Higher Scale Models
- Tensile strength of $\langle 100 \rangle$ and $\langle 110 \rangle$ symmetric tilt bicrystal interfaces
- Atomistic simulations of homogeneous dislocation nucleation in single crystal copper

- Influence of crystal orientation on homogeneous dislocation nucleation under uniaxial loading

Consequently, the chapters in this dissertation systematically address the computational methodologies used, the results found, and the analyses performed on the aforementioned topics. It is clear that each of these topics is addressed by the work presented in this dissertation. The synthesis of knowledge from all these aspects of dislocation nucleation from grain boundaries. The significant contributions of this work are summarized in the following sections, which are organized by chapters.

## *12.2 Structures and energies of* $\Sigma 3$ *ATGBs*

In Chapter 3, atomistic simulations are used to investigate the energy and structure of symmetric and asymmetric $\Sigma 3$ $\langle 110 \rangle$ tilt grain boundaries. A nonlinear conjugate gradient algorithm was employed along with an embedded atom method potential for Cu and Al to generate the equilibrium 0 K grain boundary structures. A total of 25 $\langle 110 \rangle$ grain boundary structures were explored to identify the various equilibrium and metastable structures. Simulation results show that the $\Sigma 3$ asymmetric tilt grain boundaries in the $\langle 110 \rangle$ system are composed of only structural units of the two $\Sigma 3$ symmetric tilt grain boundaries. The energies for the $\Sigma 3$ grain boundaries are similar to previous experimental and calculated grain boundary energies. A structural unit and faceting model for $\Sigma 3$ asymmetric tilt grain boundaries fits all of the calculated asymmetric grain boundary structures. The significance of these results is that the structural unit and facet description of all $\Sigma 3$ asymmetric tilt grain boundaries may be predicted from the structural units of the $\Sigma 3$ coherent twin and incoherent twin boundaries for both Cu and Al.

The conclusions from this chapter are as follows:

1. The GB energy values obtained using the current methodology are in agreement with previous calculated and experimentally obtained GB energies. For Cu, two relative energy minima were calculated: the CTB and the $\Sigma 3(223)_1/(4,4,\bar{1}1)_2\Phi = 81.95^\circ$

ATGB. An excellent fit to the Al Σ3 ATGB energies was obtained with an equation that requires only the CTB and SITB energies. This same equation fails to capture the dissociated D SUs that create the 9R phase in Cu.

2. The structure of Σ3 asymmetric tilt grain boundaries for both Cu and Al is composed of CTB and SITB atomistic facets. As such, the only SUs present for all Σ3 ATGBs are the D SU on the CTB facet and the $|DC|$ SUs on the SITB facet. Additionally, even though Cu exhibits the 9R phase, the SU description for all Σ3 ATGBs is equivalent for Cu and Al. The higher SFE of Cu causes the GB SUs to rotate from their ideal location to reduce the GB energy and presumably allow for further dissociation of the D SU on the SITB facet. It is also observed that the 9R phase is formed from this dissociated D SU on the SITB facet. The width of the intrinsic stacking fault created by the dissociated D SU evolves as a function of the inclination angle. The dissociation width is affected by the orientation of the surrounding lattices as well as the rotation of the C SU and the D SU on the CTB facet.

3. A model of the structural unit and microfaceting description for Σ3 asymmetric tilt grain boundaries predicts the SU description for all Σ3 ATGBs calculated in this study, both in Cu and Al. The significance of this description is that it only requires the SU description for the two Σ3 STGBs and a coincidence plot.

## *12.3 Structures and energies for low order CSL ATGBs*

In Chapter 4, atomistic simulations were used to explore the structure and energy of several low order CSL ATGB systems (Σ5, Σ9, Σ11, and Σ13) about the ⟨100⟩ and ⟨110⟩ tilt axes. The Σ5 and Σ13 systems with a boundary plane rotated about the ⟨100⟩ misorientation axis were examined along with the Σ9 and Σ11 systems rotated about the ⟨110⟩ misorientation axis. Asymmetric tilt grain boundary energies were calculated as a function of inclination angle and compared with an energy relationship based on faceting into the two symmetric tilt grain boundaries in each system. One finding is that asymmetric tilt boundaries with

low index normals do not necessarily have lower energies than boundaries with similar inclination angles, contrary to previous studies. Further analysis of grain boundary structures provides insight into the asymmetric tilt grain boundary energy. The Σ5 and Σ13 systems in the ⟨100⟩ system agree with the aforementioned energy relationship; structures confirm that these asymmetric boundaries facet into the symmetric tilt boundaries. The Σ9 and Σ11 systems in the ⟨110⟩ system deviate from the idealized energy relationship. As the boundary inclination angle increases towards the Σ9 (221) and Σ11 (332) symmetric tilt boundaries, the minimum energy asymmetric boundary structures contain low index {111} and {110} planes bounding the interface region.

The conclusions from this chapter are as follows:

1. The Σ5 and Σ13 asymmetric tilt grain boundaries about the ⟨100⟩ tilt axis facet into their corresponding symmetric tilt grain boundaries. The grain boundary energy relationship as a function of inclination angle (Fig. 4.3) closely follows a geometrically-based energy relationship for ideal faceting into symmetric tilt grain boundaries (Eq. 4.2). On the other hand, the deviation of the Σ9 and Σ11 grain boundary energies (Fig. 4.4) from Eq. 4.2 indicates that these systems may not ideally facet into the symmetric tilt grain boundaries. The Σ9 asymmetric boundaries deviate greatest from this relationship. The deviation from this relationship is caused by a combination of the anisotropy of energies for the Σ9 symmetric tilt grain boundaries as well as the inclination angle separating the two symmetric boundaries, $\alpha$, which is dependent on the tilt axis. It is noted that the ⟨100⟩ boundaries have a much lower value of $\alpha$ ($\alpha = 45°$) while the Σ3 and Σ11 have a much larger degree of anisotropy in the symmetric tilt boundary energies due to the low energies of the Σ3 coherent twin and Σ11 (113) boundaries.

2. Examination of the calculated grain boundary structures for both the Σ5 and Σ13 asymmetric tilt grain boundaries in Cu (Figs. 4.7 and 4.8) shows that the asymmetric

boundaries facet into the corresponding structural units of the Σ5 and Σ13 symmetric tilt grain boundaries, respectively. This agrees with the trend of the calculated boundary energies.

3. The Σ9 and Σ11 asymmetric tilt grain boundaries about the ⟨110⟩ tilt axis have a more complicated structure and faceting description than the ⟨100⟩ asymmetric boundaries. Examination of the calculated Σ11 asymmetric boundary structures in Al (Fig. 4.9) confirms that many of these boundaries do not facet into the corresponding symmetric boundaries. The $\Sigma 11\,(225)_1\,(441)_2$ asymmetric boundary does facet into the structural units of the Σ11 symmetric tilt grain boundary in Al. However, at higher inclination angles (*e.g.*, the $\Sigma 11\,(557)_1 / (771)_2$ boundary in Fig. 4.9(c)), the C structural unit of the Σ11 (113) STGB is not observed. Instead, the boundary is composed of a combination of D and E structural units from the Σ11 (332) STGB, which arrange to form {111} planes on both sides of the boundary.

4. Further examination of the calculated Σ9 asymmetric boundary structures in Cu (Fig. 4.10) confirms that many of these boundaries do not facet into the corresponding symmetric boundaries. The Σ9 asymmetric tilt grain boundary structures show a similar structure — at high inclination angles (*e.g.*, Figs. 4.10(c-e)) only the E structural unit from the Σ9 (221) STGB is observed. Additionally, the observed planes bounding the structural units are the {111} plane in one lattice and the {110} plane in the other lattice, as is observed experimentally [185]. At the $\Sigma 9\,(111)_1 / (115)_2$ asymmetric tilt grain boundary, the boundary facets into the structural units of the Σ3 coherent and incoherent twin boundaries, very similar to the $\Sigma 3\,(111)_1 / \left(11\bar{5}\right)_2$ asymmetric tilt grain boundary structure. This structure is similar to experimentally-observed Σ9 asymmetric tilt boundaries [185].

Based upon prior results of Σ3 ATGBs [78] and results from Σ5/9/11/13 ATGBs in this study, the observed frequency of low index planes in polycrystals does **not** appear

to be associated with low energy cusps in the energy-inclination angle relationship; this conclusion is in contrast to former studies [185]. Instead, the current results indicate that the structure and faceting of asymmetric tilt grain boundaries may play a more prominent role in the observed frequency of low index planes in polycrystalline materials.

## *12.4 Structure and free volume of* $\langle 110 \rangle$ *symmetric tilt grain boundaries with the E structural unit*

In Chapter 5, atomistic simulations were used to investigate the structure and free volume of $\langle 110 \rangle$ symmetric tilt grain boundaries containing the E structural unit from the $\Sigma 9\,(221)\,\theta = 141.1^\circ$ grain boundary. In this chapter, a stereologically-based methodology is used to calculate the grain boundary free volume along with the spacing and connectivity of free volume. The minimum energy equilibrium grain boundary is generated to examine: (i) the grain boundary structure, (ii) a measure of free volume associated with the grain boundary, (iii) spatial correlation functions of the distribution of free volume, and (iv) images of grain boundary free volume distribution. Using the results from these calculations, the influence of free volume spatial distribution and grain boundary structure on dislocation dissociation and nucleation was briefly discussed for boundaries with the E structural unit subjected to tensile loading normal to the interface.

The conclusions from this chapter are as follows:

1. The grain boundary structure and distortion of the E structural unit evolves as a function of the misorientation angle and ratio of E structural units in the boundary. For grain boundaries vicinal to the coherent twin boundary, the E structural unit distorts to the E″ structural unit with a dissociated Shockley partial dislocation. This E″ structural unit is equivalent to the $a_0/3\,\langle 111 \rangle$ disconnection observed in HRTEM images from Al [249–251] and Au [252]. The dissociative reaction that forms this structure is important for understanding the dissociation of partial dislocations for all grain boundaries within the range $109.5^\circ < \theta < 141.1^\circ$.

2. Two-point statistics, in the form of two-point correlation functions and lineal path functions, are useful in quantitatively characterizing the spacing *within* and *between* free volume clusters as well as characterizing the *connectivity* of free volume. These two-point statistics were used to characterize the degree of distortion to the E structural unit as a function of misorientation angle. There are several transitions in the E structural unit for Cu; the E′ and E″ structural units occur as the misorientation angle approaches 180° and 109.5°, respectively. The visualization of these free volume clusters also lends insight into deformation processes, as the free volume indicates areas where the dissociation of partial dislocations occurs in these boundaries.

3. The grain boundary structure and free volume statistics provide a better understanding of dislocation dissociation and nucleation in these Cu grain boundaries. The reaction (see Eq. 5.6) that leads to a *dissociated* partial dislocation with an intrinsic stacking fault for vicinal boundaries to the coherent twin boundary (*e.g.*, the $\Sigma 171\,(11, 11, 10)\,\theta = 114.5°$ grain boundary) also occurs under stress for other grain boundaries within the $109.5° < \theta < 141.1°$ misorientation range. This reaction occurs near free volume in the boundary. Further stress is then required to nucleate and emit a partial dislocation from the boundary in the form of a dislocation loop. This stress may depend on the *spacing* of the dissociated partial dislocations in the grain boundary period direction (which is identical to the spacing between free volume clusters).

## *12.5 Dislocation nucleation in* $\Sigma 3$ *ATGBs*

In Chapter 6, atomistic simulations were used to investigate dislocation nucleation from $\Sigma 3$ asymmetric (inclined) tilt grain boundaries under uniaxial tension applied perpendicular to the boundary. Molecular dynamics was employed based on embedded atom method potentials for Cu and Al at 10 K and 300 K. Results briefly discuss the grain boundary structure and energy from Chapter 3, along with mechanical properties and mechanisms

associated with dislocation nucleation from these Σ3 boundaries. The stress and work required for dislocation nucleation were calculated along with elastic stiffness of the bicrystal configurations, exploring the change in response as a function of inclination angle. Analyses of dislocation nucleation mechanisms for asymmetric Σ3 boundaries in Cu show that dislocation nucleation is preceded by dislocation dissociation from the boundary. Then, dislocations preferentially nucleate in only one crystal on the maximum Schmid factor slip plane(s) for that crystal. However, this crystal is not simply predicted based on either the Schmid or non-Schmid factors. The synthesis of these results provides a better understanding of the dislocation nucleation process in these faceted, dissociated grain boundaries.

The conclusions from this chapter are as follows:

1. The mechanical response of Σ3 grain boundaries varies greatly as a function of inclination angle when subjected to uniaxial tension at a constant strain rate. Results show that the stress required for dislocation nucleation is highest at the coherent twin boundary and lowest at intermediate inclination angles. The calculated elastic stiffness of the bicrystal system correlates well with predictions based on the elastic modulus of the adjoining lattices [257]. The large variation of responses (cf. Table 6.2) with inclination angle shows that grain boundary plane plays an important role in mechanical behavior, since misorientation is identical for all 11 boundaries in this study. Additionally, the stress required for dislocation nucleation correlates well with both the strain at peak stress and the work required for dislocation nucleation; these measures are related to force and displacement normal to the interface, both necessary for cohesive zone models for interface separation.

2. The mechanisms for dislocation nucleation in Cu asymmetric boundaries are decomposed into three regimes: low ($\Phi \leq 35.26°$), intermediate ($35.26° < \Phi < 70.53°$), and high ($\Phi \leq 70.53°$) inclination angles. In Cu, the interface structure evolves prior to dislocation nucleation; the glissile partial dislocation (D structural unit) on the

incoherent twin boundary facet dissociates into one of the adjoining crystal lattices. The plane that this dislocation dissociates onto depends more on the grain boundary structure than the Schmid factor for that plane in the adjoining lattice. However, this dissociated structure serves as the nucleation point for partial dislocations that are emitted on the maximum Schmid factor slip planes for that lattice. For low inclination angles, the dissociation and nucleation processes occur on different slip planes; consequently, the stress required for dislocation is relatively high. For intermediate inclination angles, dislocation dissociation and nucleation processes occur on the same slip plane; the stress required for nucleation is low. For high inclination angles, extended dissociation of the boundary results in an increased volume of the 9R phase. The dislocation nucleation process then occurs both at the dissociated structure and within the lattice on the two slip planes with maximum Schmid factor. Again, it is interesting that dislocation nucleation mechanisms can change greatly with inclination angle (*i.e.*, grain boundary plane) for identical misorientations.

3. Dislocation nucleation only occurs in one of the adjoining crystals for Σ3 asymmetric tilt grain boundaries. Schmid and non-Schmid factors from each crystal lattice are unable to accurately predict the crystal lattice into which the partial dislocation preferentially nucleates. However, once the crystal lattice is known, the Schmid factor is able to determine the slip plane that the partial dislocation forms on. Finally, the required stress for heterogeneous dislocation nucleation in Σ3 asymmetric tilt grain boundaries is compared to the stress for homogeneous dislocation nucleation in Cu single crystals of similar orientation [64]; the difference in stress values is due to the presence of the interface. Linear correlations involving either the free volume or grain boundary ledge density are unable to capture this difference; it may require more complicated forms.

## *12.6 Atomistic simulations of dislocation nucleation in copper grain boundaries under uniaxial tension and compression*

In Chapter 7, atomistic modeling of dislocation nucleation in grain boundaries with the E structural unit was investigated under uniaxial tension and compression using molecular dynamics. After obtaining the minimum energy grain boundary structure, molecular dynamics was employed using the Mishin *et al.* [124] Cu embedded-atom method potential at 10 K. The simulation results show several differences in dislocation nucleation with respect to uniaxial tension and compression that are important considerations for higher scale models.

The conclusions from this chapter are as follows:

1. The stress required for dislocation nucleation increases with decreasing spacing of the E structural units ($a_0/3\langle 111\rangle$ disclinations), *i.e.*, the spacing of the grain boundary dislocations impacts the nucleation stress. The nucleation stresses for uniaxial tensile and compressive loading with the quasistatic approach were very similar to the dynamic strain rate of $10^9$ $s^{-1}$. The observed mechanisms were identical.

2. Quite different dislocation nucleation behavior is observed under uniaxial tension (Fig. 7.5) and compression (Fig. 7.6) in copper bicrystal interfaces. For uniaxial tension, partial dislocations are nucleated on the {111} slip plane with the maximum resolved shear stress. However, for uniaxial compression, both partial **and** full dislocations are nucleated on the {111} **and** {100} slip planes with the maximum resolved shear stress. Calculations show that the maximum resolved shear stress (in the direction of slip) on the {100} slip plane is higher than the {111} slip plane for misorientation angles close to the coherent twin boundary. However, dislocations on the {100} slip plane is only observed in compression, indicating that the resolved stress normal to the slip plane may impact the activation of this slip system. Additionally, the resolved normal stress, which is compressive in compression and tensile in tension,

impacts the nucleation of the trailing partial dislocation in low stacking fault energy Cu.

3. Dislocation nucleation mechanisms for individual grain boundaries were also analyzed. For the vicinal twin boundary under tension, the grain boundary partial dislocation is emitted into the lattice on the {111} plane with the highest resolved shear stress, which it dissociated on under zero stress. For compression of the vicinal twin, the 1/3⟨111⟩ disconnection is removed through full dislocation emission on the {100} plane and partial dislocation emission parallel to the coherent twin boundary plane, restoring the boundary to the coherent twin. For the Σ19 boundary, the cooperative emission of partial dislocations from the boundary result in the HCP phase.

These results show that the resolved stress normal to the slip planes plays an important role in the nucleation of dislocations. Moreover, the nucleation of the trailing partial dislocation in low stacking fault energy copper may be explained by the change in the generalized stacking fault energy curve as a function of the resolved normal stress. Further work in this area is needed.

## *12.7 Implications of dislocation nucleation studies on higher scale models*

In Chapter 8, the insight obtained from grain boundary dislocation nucleation studies was discussed along with the potential implications on higher scale models. The structure and nucleation of dislocations at bicrystal boundaries illuminates certain issues pertaining to fundamental understanding of the role of grain boundaries. Here, some important aspects are discussed regarding dislocation nucleation in FCC metals under uniaxial loading applied perpendicular to the boundary plane: (i) dislocation sources or sinks, (ii) tension-compression asymmetry of trailing partial emission in Cu, (iii) the activation energy and volume for grain boundary dislocation nucleation, (v) the influence of grain boundary free volume on dislocation nucleation, and (vi) the influence of grain boundary free volume

on dislocation nucleation. This understanding may benefit understanding of behavior of nanocrystalline and polycrystalline FCC metals.

The conclusions from this chapter are as follows:

1. Dislocation sources at grain boundaries can act in several different ways. For instance, the grain boundary dislocation source may be located either in the grain boundary or within the lattice near potential stress concentrators, such as the intersection of ATGB facets. The grain boundary dislocation source can act as a perfect sink/source of dislocations – by emitting dislocation content from the boundary – or can act as an imperfect source, if the dislocation content of the boundary is assumed to decrease during dislocation nucleation.

2. Tension/compression simulations show that the nucleation of the trailing partial dislocation in copper depends on the resolved stress normal to the (111) slip plane. Examples are shown for both homogeneous dislocation nucleation in single crystals and heterogeneous dislocation nucleation from grain boundaries. The tension/compression asymmetry with respect to dislocation nucleation suggests that the stable stacking fault energy $\gamma_{SF}$, and maybe even the ratio $\gamma_{SF}/\gamma_{USF}$, are not be able to capture the influence of the resolved normal stress. More work should be conducted to understand the influence of the resolved normal stress on dislocation nucleation and the generalized stacking fault energy curve.

3. The temperature has a noticeable effect on the nucleation stress for $\Sigma 3$ asymmetric tilt grain boundaries. To account for the influence of thermal activation, the activation volume and activation energy are used. The activation volumes are $\approx 0.5 - 3\ b^3$ and the activation energies are $\approx 0.24 - 0.28$ eV, indicating the increased temperature and rate sensitivity at small volumes for both single crystals and grain boundaries.

## *12.8 Dislocation nucleation model for single crystals and interfaces*

In Chapter 9, the dislocation nucleation stresses calculated from atomistic simulations are directly correlated with continuum parameters related to the resolved stresses. Molecular dynamics (MD) simulations were used to model dislocation nucleation at or near symmetric tilt bicrystal copper interfaces with ⟨100⟩ or ⟨110⟩ misorientation axes. MD simulations indicated that orientation of the opposing lattice regions and the presence of certain structural units are two critical attributes of the interface structure that affect the stress required for dislocation nucleation. Boundaries that contain the E structural unit are found to emit dislocations at comparatively low tensile stress magnitudes. A simple model was proposed to illustrate the impact of interfacial porosity and stresses acting on the slip plane in non-glide directions on tensile interface strength. Accounting for interfacial porosity through an average measure was found to be sufficient to model the tensile strength of boundaries with a ⟨100⟩ misorientation axis and many boundaries with a ⟨110⟩ misorientation axis.

The conclusions from this chapter are as follows:

1. Aside from the coherent $\Sigma 3\,(111)\,\theta = 109.5^\circ$ boundary, no increase in tensile strength (or other special behavior) is observed at boundaries with low-order CSL character. Increased tensile strength at the $\Sigma 3\,(111)\,\theta = 109.5^\circ$ boundary can be attributed to the homogeneous nucleation of dislocations within each lattice for this orientation. For all other models, failure in uniaxial tension occurs by way of partial dislocation nucleation from the bicrystal interface. The partial dislocation nucleation event may be accompanied by structural rearrangement prior to emission (coarsening or the emission of short stacking fault facets) that locally improves the coherency of the interface.

2. MD simulations indicate that the orientation of the opposing lattice regions relative to the applied stress and the presence of certain structural units are two critical features of the interface structure that affect the tensile interface strength. Specifically,

boundaries that contain the E structural unit nucleate dislocations at low applied tensile stresses.

3. MD simulations on both single crystal and interface models indicate that non-Schmid effects must be incorporated when formulating a model for dislocation nucleation. Specifically, the stress normal to the slip plane is found to play a significant role in the dislocation nucleation event for boundaries with the ⟨100⟩ misorientation axis.

4. Accounting for interfacial porosity through an average measure based on coordination number is found to be sufficient to model the tensile strength of boundaries with the ⟨100⟩ tilt axis and many boundaries with the ⟨110⟩ tilt axis. However, for ⟨110⟩ boundaries that contain the E structural unit, it is likely that a higher-order model must be invoked that includes the effect of porosity gradients or more detailed information concerning the relationship between structural unit configuration and slip system orientation.

## *12.9 Atomistic simulations of homogeneous dislocation nucleation in single crystal copper*

In chapter 10, a second generation model is described, which correlates dislocation nucleation stresses calculated from atomistic simulations with continuum parameters related to the resolved stresses. Molecular dynamics simulations are used to investigate how the stress required for homogeneous nucleation of partial dislocations in single crystal copper under uniaxial tension changes as a function of crystallographic orientation. An embedded-atom method potential for Cu is employed at temperatures of 10 K and 300 K. Results indicate that non-Schmid parameters are required to describe dislocation nucleation for certain single crystal orientations. Specifically, the stereographic triangle can be divided into two regions: a region where dislocation nucleation is dominated by the conventional Schmid factor (the resolved shear stress in the direction of slip) and a region where dislocation nucleation is dominated by the normal factor (the resolved stress normal to the slip plane).

A continuum relationship that incorporates Schmid and non-Schmid terms to correlate the stress required for dislocation nucleation over all tensile axis orientations within the stereographic triangle is presented. The significance of this work is that simulation results are cast into an atomistically-inspired continuum formulation for partial dislocation loop nucleation in FCC single crystals.

The conclusions from this chapter are as follows:

1. *Homogeneous* dislocation nucleation in FCC Cu single crystals depends on both the Schmid factor $SF$ and the non-Schmid normal factor $NF$, where $SF$ and $NF$ represent the resolved shear stress in the direction of slip and the resolved tensile stress normal to the slip plane, respectively. In general, atomistic simulation results show that the uniaxial tensile stress required for dislocation nucleation decreases as both $SF$ and $NF$ increase (*i.e.*, as the corresponding resolved stress component increases). The dislocation nucleation stress is interpolated and plotted on a basic stereographic triangle as a function of the tensile axis orientation (Fig. 10.4) to show how tensile axis affects the stress required for homogeneous dislocation nucleation in single crystals. Moreover, by comparing to the contour plots for $SF$ and $NF$ (Figure 10.3), it is apparent that there are certain regions on the stereographic triangle where the nucleation stress correlates much more strongly with the normal factor $NF$ than the conventional Schmid factor $SF$ (*e.g.*, along the [100]-[110] boundary).

2. The influence of temperature on the uniaxial tensile stress required for homogeneous dislocation nucleation in single crystals is studied at two temperatures: 10 K and 300 K. Figure 10.4 shows that the stress behavior is fairly similar at the two temperatures, aside from the change in the magnitudes. However, at higher temperatures (with increased thermal assistance), the percent decrease in the stress for dislocation nucleation from 10 K to 300 K is greater for those orientations that require a higher stress to nucleate dislocations at 10 K. Therefore, the [111] tensile axis exhibits a

larger decrease in stress (35.26%) than the [110] tensile axis direction (24.15%). This trend is stronger for tensile axis orientations aligned for single slip.

3. A constitutive equation and criterion (Eq. 10.3) is proposed to correlate the uniaxial tensile stress required for dislocation nucleation with $SF$ and $NF$ for all tensile axis orientations. This criterion allows for a transition between two distinct regions of the stereographic triangle: an $SF$-dominated dislocation nucleation region and an $NF$-dominated dislocation nucleation region. A least squares regression fit the calculated data shows good agreement with Eq. 10.3 (*cf.*, Figure 10.9).

## *12.10 Influence of single crystal orientation on homogeneous dislocation nucleation under uniaxial loading*

In this chapter, atomistic modeling of *homogeneous* dislocation nucleation in Cu single crystals were investigated under uniaxial tension and compression using molecular dynamics with the Mishin EAM potential [124]. By sampling different loading axis orientations, these simulations examine the influence of Schmid and non-Schmid stress components on dislocation nucleation.

The conclusions from this chapter are as follows:

1. *Homogeneous* dislocation nucleation in FCC Cu single crystals depends on both the Schmid factor $SF$ and the non-Schmid normal factor $NF$, where $SF$ and $NF$ represent the resolved shear stress in the slip direction and the resolved tensile stress normal to the slip plane, respectively. In general, atomistic simulation results show that the uniaxial tensile nucleation stress decreases as both $SF$ and $NF$ increase (*i.e.*, as the corresponding resolved stress component increases). The dislocation nucleation stress is interpolated and plotted on a basic stereographic triangle as a function of the loading axis orientation (Figs. 11.7 and 11.9) to show how the loading axis affects the stress required for homogeneous dislocation nucleation in single crystals. In uniaxial tension, it is apparent that there are certain regions on the stereographic triangle

where the nucleation stress correlates much more strongly with the normal factor $NF$ than the conventional Schmid factor $SF$ (*e.g.*, along the [100]-[110] boundary).

2. The influence of lattice rotation on the resolved stresses was investigated using an elastic deformation gradient informed by the evolution of the MD simulation cell lengths. In uniaxial tension at 10 K, $SF$ and $NF$ *decreased* by an average of 2.5% and 14.2%, respectively. In uniaxial compression at 10 K, $SF$ and $NF$ *increased* by an average of 1.5% and 16.8%, respectively. However, the most significant resolved stress component explaining asymmetries in dislocation nucleation between uniaxial tension and compression is still the resolved normal stress.

3. A constitutive equation and criterion (Eq. 11.6) was proposed to correlate the uniaxial tensile nucleation stress with $SF$ and $NF$ for all axis orientations [81]. This criterion allows for a transition between two distinct regions of the stereographic triangle: an $SF$-dominated dislocation nucleation region and an $NF$-dominated dislocation nucleation region. In this work, the evolution of $SF$ and $NF$ as a function of elastic strain is considered. The observed trend is the same. However, a similar phenomenological form could not be obtained for dislocation nucleation in single crystals under uniaxial compression.

4. The tension-compression asymmetry in dislocation nucleation may be attributed to the resolved stress normal to the slip plane on which the dislocation nucleates. In tension, this normal stress is tensile, and in compression, it is compressive. The normal stress accounts for higher dislocation nucleation stresses in compression than in tension. Additionally, large tension-compression asymmetries in the stresses required for dislocation nucleation trend with large values of $NF$, *i.e.*, large resolved normal stresses.

5. The influence of temperature on the stress required for homogeneous dislocation nucleation in single crystals is studied at two temperatures: 10 K and 300 K.

Figs. 11.15(a) and 11.15(b) show that the stress behavior is fairly similar at the two temperatures, aside from the change in the magnitudes. However, at higher temperatures (with increased thermal assistance), the percent decrease in the stress for dislocation nucleation for temperatures from 10 K to 300 K is greater for those orientations that require a higher stress to nucleate dislocations at 10 K. Therefore, the [111] tensile axis exhibits a larger decrease in stress (35.26%) than the [110] tensile axis direction (24.15%). This trend is stronger for tensile axis orientations aligned for single slip. In general, though, a temperature-dependent constant relates the stresses at 10 K and at 300 K with correlation coefficients of $R^2 = 0.95$, $R^2 = 0.96$, and $R^2 = 0.97$ for tensile nucleation stresses, compressive nucleation stresses, and tension-compression ratios, respectively. Calculations of the temperature dependence of homogeneous dislocation nucleation yield activation volumes of ≈0.5-2 $b^3$ and activation energies of ≈0.30 eV.

6. The dislocation nucleation mechanisms differ between tension and compression. In tension, partial dislocation loops are nucleated in the lattice. In compression, for many orientations, full dislocation loops are nucleated in copper, *i.e.*, both the initial and trailing partial dislocation loops are nucleated. The calculated behavior is attributed to the compressive normal stress that yields a higher nucleation stress than in tension and, possibly, easier nucleation of the trailing partial dislocation loops.

## *12.11 Recommendations for future work*

This dissertation provides the foundation necessary for pursuing a number of different directions which can provide further understanding of plasticity at the atomic scale. While this dissertation has answered the research questions related to dislocation nucleation in grain boundaries and single crystals posed in Chapter 1, further research questions also arise from this better understanding. Some potential research areas are as follows:

1. **Grain boundary properties.** The minimum energy structures obtained from this

work can be subjected to other atomistic simulations to ascertain the effect of the faceted structure of asymmetric tilt grain boundaries on a number of different properties. For instance, there is also a large interest in the mobility of grain boundaries, but most atomistic simulations have concentrated on rather simple symmetric tilt grain boundaries. However, the well-defined structure of the low order CSL asymmetric tilt systems in this work may allow for the correlation of grain boundary properties, such as the mobility, with the structure of asymmetric tilt grain boundaries. In this respect, this work can provide the basis for understanding the structure-property for grain boundaries that are similar to general grain boundaries in polycrystalline materials.

2. **Grain boundary plasticity.** This work has concentrated mainly on dislocation nucleation from boundaries with an applied load perpendicular to the grain boundary. However, in nanocrystalline materials, the grain boundaries are more often inclined with respect to the loading axis, resulting in resolved *shear* stresses within the grain boundary plane. The uniaxial loading applied perpendicular to the grain boundary plane can be considered an upper bound to the dislocation nucleation stresses, while *shear* applied parallel to the grain boundary plane may provide a lower bound for stresses required to initiate boundary plasticity (grain boundary sliding, dislocation nucleation, grain boundary migration, etc. [72]).

3. **Dislocation transmission through grain boundaries.** Dislocation nucleation from the grain boundary relates to plasticity in nanocrystalline materials. At higher scales, the large initial density of dislocations leads to the evolution of the dislocation density through Frank-Read sources and results in a greater importance of dislocation reactions with the grain boundary. Very little work has used atomistic simulations to examine dislocation transmission through the grain boundary, although some experimental work on dislocation transmission exists. The atomic studies that do exist

regard symmetric tilt grain boundaries of relatively simple boundary structure. It is not known how the complex character of asymmetric tilt grain boundaries may form a barrier to dislocation transmission.

4. **Combined tilt-twist boundaries on dislocation nucleation.** The grain boundary character of polycrystalline materials will often contain a twist component to the misorientation between grains. While asymmetric tilt grain boundaries comprise the majority of boundaries in polycrystals, there is a significant fraction of grain boundaries with tilt character, especially about low index axes (*i.e.*, $\langle 111 \rangle$). The addition of a twist component to asymmetric tilt grain boundaries will break the symmetry of the boundary structure with respect to the tilt axis. This, in turn, may complicate the dislocation nucleation event.

5. **Effect of impurities or vacancies on dislocation nucleation.** As mentioned previously, the dislocation nucleation simulations in this work provides an upper bound for the nucleation stress in FCC copper and aluminum. In actual nanocrystalline materials, impurity segregation to the grain boundaries, or vacancies in the grain boundary, may play an important role in aiding dislocation nucleation. Indeed, Li has shown that the Hall-Petch effect can be attributed entirely to the effect of impurity segregation to the grain boundaries [41]. Research in this area can improve our understanding of the role of impurities and vacancies on dislocation nucleation.

6. **Other material systems.** This work helps form a more comprehensive picture of the structure and properties of grain boundaries in FCC metals. However, with the appropriate potentials (*e.g.*, MEAM) the same methodology can be applied to BCC and HCP metals to understand how boundary structure is influenced in these systems. Very little research has focused on understanding how grain boundary degrees of freedom impact interface structure and plasticity in BCC and HCP metals, although a similar motivation – *i.e.*, understanding nanocrystalline and polycrystalline plasticity

– still exists for these systems.

# REFERENCES


[1] Spearot, D. E., Jacob, K. I., and McDowell, D. L. *Mechanics of Materials* **36**(9), 825–847 (2004).

[2] Sutton, A. P. and Vitek, V. *Philosophical Transactions of the Royal Society of London A* **309**(1506), 37–54 (1983).

[3] Gleiter, H. *Progress in Materials Science* **33**(4), 223–315 (1989).

[4] Gleiter, H. *Advanced Materials* **4**(7-8), 474–481 (1992).

[5] Gleiter, H. *Acta Materialia* **48**(1), 1–29 (2000).

[6] Valiev, R. *Nature Materials* **3**(8), 511–516 (2004).

[7] Bringa, E. M., Caro, A., Wang, Y. M., Victoria, M., McNaney, J. M., Remington, B. A., Smith, R. F., Torralva, B. R., and Van Swygenhoven, H. *Science* **309**(5742), 1838–1841 (2005).

[8] Budrovic, Z., Van Swygenhoven, H., Derlet, P. M., Van Petegem, S., and Schmitt, B. *Science* **304**(5668), 273–276 (2004).

[9] Champion, Y., Langlois, C., Guerin-Mailly, S., Langlois, P., Bonnentien, J.-L., and Hytch, M. J. *Science* **300**, 310–311 (2003).

[10] Chen, M., Ma, E., Hemker, K. J., Sheng, H., Wang, Y., and Cheng, X. *Science* **300**, 1275–1277 (2003).

[11] Farkas, D., Van Petegem, S., Derlet, P. M., and Van Swygenhoven, H. *Acta Materialia* **53**(11), 3115–3123 (2005).

[12] Jacobsen, K. W. and Schiøtz, J. *Nature Materials* **1**(1), 15–16 (2002).

[13] Lu, L., Shen, Y. F., Chen, X. H., Qian, L. H., and Lu, K. *Science* **304**(5669), 422–426 (2004).

[14] Ma, E. *Nature Materials* **2**(1), 7–8 (2003).

[15] Ma, E. *Science* **305**(5684), 623–624 (2004).

[16] McFadden, X., Mishra, R. S., Valiev, R. Z., Zhilyaev, A. P., and Mukherjee, A. K. *Nature* **398**(6729), 684–686 (1999).

[17] Murayama, M., Howe, J. M., Hidaka, H., and Takaki, S. *Science* **295**(5564), 2433–2435 (2002).

[18] Schiøtz, J., Di Tolla, F. D., and Jacobsen, K. W. *Nature* **391**(6667), 561–3 (1998).

[19] Schiøtz, J. and Jacobsen, K. W. *Science* **301**(5638), 1357–9 (2003).

[20] Shan, Z., Stach, E. A., Wiezorek, J. M. K., Knapp, J. A., Follstaedt, D. M., and Mao, S. X. *Science* **305**(5684), 654–657 (2004).

[21] Szlufarska, I., Nakano, A., and Vashishta, P. *Science* **309**(5736), 911–914 (2005).

[22] Van Swygenhoven, H. *Science* **296**(5565), 66–67 (2002).

[23] Van Swygenhoven, H., Derlet, P. M., and Frøseth, A. G. *Nature Materials* **3**(6), 399–403 (2004).

[24] Wang, Y. M., Chen, M. W., Zhou, F. H., and Ma, E. *Nature* **419**(6910), 912–915 (2002).

[25] Yamakov, V., Wolf, D., Phillpot, S. R., Mukherjee, A. K., and Gleiter, H. *Nature Materials* **1**(1), 45–48 (2002).

[26] Yamakov, V., Wolf, D., Phillpot, S. R., Mukherjee, A. K., and Gleiter, H. *Nature Materials* **3**(1), 43–7 (2004).

[27] Yip, S. *Nature Materials* **3**(1), 11–12 (2004).

[28] Zhao, Y. S., Zhang, J. Z., Clausen, B., Shen, T. D., Gray, G. T., and Wang, L. P. *Nano Letters* **7**(2), 426–432 (2007).

[29] Zhu, Y. T. and Liao, X. Z. *Nature Materials* **3**(6), 351–352 (2004).

[30] Meyers, M. A., Mishra, A., and Benson, D. J. *Progress in Materials Science* **51**(4), 427–556 (2006).

[31] Hall, E. O. *Physical Society - Proceedings* **64**(381B), 747–753 (1951).

[32] Petch, N. J. *Iron and Steel Institute - Journal* **174**(Part 1), 25–28 (1953).

[33] Nieman, G. W., Weertman, J. R., and Siegel, R. W. *Scripta Metallurgica* **23**(12), 2013–2018 (1989).

[34] Chokshi, A. H., Rosen, A., Karch, J., and Gleiter, H. *Scripta Metallurgica* **23**(10), 1679–84 (1989).

[35] Khan, A. S., Suh, Y. S., Xu, C., Takacs, L., and Haoyue, Z. *International Journal of Plasticity* **22**(2), 195–209 (2006).

[36] Khan, A. S., Haoyue, Z., and Takacs, L. *International Journal of Plasticity* **16**(12), 1459–76 (2000).

[37] Youssef, K. M., Scattergood, R. O., Murty, K. L., and Koch, C. C. *Applied Physics Letters* **85**(6), 929–931 (2004).

[38] Cheng, S., Ma, E., Wang, Y. M., Kecskes, L. J., Youssef, K. M., Koch, C. C., Trociewitz, U. P., and Han, K. *Acta Materialia* **53**(5), 1521–1533 (2005).

[39] Wang, Y. M., Wang, K., Pan, D., Lu, K., Hemker, K. J., and Ma, E. *Scripta Materialia* **48**(12), 1581–1586 (2003).

[40] Sanders, P. G., Eastman, J. A., and Weertman, J. R. *Acta Materialia* **45**(10), 4019–4025 (1997).

[41] Li, J. *Applied Physics Letters* **90**(4), 041912 (2007).

[42] Takeuchi, S. *Scripta Materialia* **44**(8-9), 1483–1487 (2001).

[43] Fu, H., Benson, D., and Meyers, M. *Acta Materialia* **49**(13), 2567–2582 (2001).

[44] Jiang, B. and Weng, G. *Journal of the Mechanics and Physics of Solids* **52**(5), 1125–1149 (2004).

[45] Van Swygenhoven, H. and Derlet, P. M. *Physical Review B* **64**, 224105:1–8 (2001).

[46] Capolungo, L., Jochum, C., Cherkaoui, M., and Qu, J. *International Journal of Plasticity* **21**, 67–81 (2005).

[47] Capolungo, L., Cherkaoui, M., and Qu, J. *International Journal of Plasticity* **23**(4), 561–591 (2007).

[48] Liao, X. Z., Zhou, F., Lavernia, E. J., Srinivasan, S. G., Baskes, M. I., He, D. W., and Zhu, Y. T. *Applied Physics Letters* **83**(4), 632–634 (2003).

[49] Liao, X. Z., Srinivasan, S. G., Zhao, Y. H., Baskes, M. I., Zhu, Y. T., Zhou, F., Lavernia, E. J., and Xu, H. F. *Applied Physics Letters* **84**(18), 3564–3566 (2004).

[50] Yamakov, V., Wolf, D., Phillpot, S. R., and Gleiter, H. *Acta Materialia* **50**(20), 5005–20 (2002).

[51] Van Swygenhoven, H., Spaczer, M., and Caro, A. *Acta Materialia* **47**(10), 3117–3126 (1999).

[52] Van Swygenhoven, H., Dalla Torre, F., and Victoria, M. *Acta Materialia* **50**(15), 3957–3970 (2002).

[53] Van Swygenhoven, H., Derlet, P. M., and Frøseth, A. G. *Acta Materialia* **54**(7), 1975–83 (2006).

[54] Van Swygenhoven, H., Caro, A., and Farkas, D. *Scripta Materialia* **44**(8-9), 1513–1516 (2001).

[55] Frøseth, A., Van Swygenhoven, H., and Derlet, P. M. *Acta Materialia* **52**(8), 2259–2268 (2004).

[56] Yamakov, V., Wolf, D., Salazar, M., Phillpot, S. R., and Gleiter, H. *Acta Materialia* **49**(14), 2713–2722 (2001).

[57] Yamakov, V., Wolf, D., Phillpot, S. R., Mukherjee, A. K., and Gleiter, H. *Philosophical Magazine Letters* **83**(6), 385–393 (2003).

[58] Shimokawa, T., Nakatani, A., and Kitagawa, H. *Physical Review B* **71**(22), 224110–1 (2005).

[59] Schiøtz, J., Vegge, T., Di Tolla, F. D., and Jacobsen, K. W. *Physical Review B* **60**(17), 11971–83 (1999).

[60] Derlet, P. M., Van Swygenhoven, H., and Hasnaoui, A. *Philosophical Magazine* **83**, 3569–3575 (2003).

[61] Schiøtz, J. *Scripta Materialia* **51**(8 SPEC ISS), 837–841 (2004).

[62] Frøseth, A. G., Derlet, P. M., and Van Swygenhoven, H. *Applied Physics Letters* **85**(24), 5863–5865 (2004).

[63] Spearot, D. E., Jacob, K. I., McDowell, D. L., and Plimpton, S. J. *Journal of Engineering Materials and Technology* **127**(4), 374–382 (2005).

[64] Spearot, D., Tschopp, M., Jacob, K., and McDowell, D. *Acta Materialia* **55**(2), 705–714 (2007).

[65] Randle, V. *The Role of the Coincident Site Lattice in Grain Boundary Engineering*. The University Press, Cambridge, (1996).

[66] Randle, V. *Acta Materialia* **47**, 4187–96 (1999).

[67] Randle, V. *Acta Materialia* **52**(14), 4067–4081 (2004).

[68] Shewchuk, J. (1994).

[69] Plimpton, S. *Journal of Computational Physics* **117**(1), 1–19 (1995).

[70] Warner, D. H., Sansoz, F., and Molinari, J. F. *International Journal of Plasticity* **22**(4), 754–774 (2006).

[71] Sansoz, F. and Molinari, J. F. *Scripta Materialia* **50**(10), 1283–8 (2004).

[72] Sansoz, F. and Molinari, J. F. *Acta Materialia* **53**(7), 1931–1944 (2005).

[73] Potirniche, G. P., Horstemeyer, M. F., Wagner, G. J., and Gullett, P. M. *International Journal of Plasticity* **22**(2), 257–278 (2006).

[74] Khan, S. M. A., Zbib, H. M., and Hughes, D. A. *International Journal of Plasticity* **20**(6), 1059–1092 (2004).

[75] Watanabe, T. *Res Mechanica* **11**(1), 47–84 (1984).

[76] Tschopp, M. and McDowell, D. *Journal of Materials Science* , doi: 10.1007 / s10853–007–1626–6 (2007).

[77] Tschopp, M. and McDowell, D. *International Journal of Plasticity* , doi: 10.1016 / j.ijplas.2007.02.010 (2007).

[78] Tschopp, M. and McDowell, D. *Philosophical Magazine A* , in press, doi: 10.1080 / 14786430701255895 (2007).

[79] Tschopp, M. and McDowell, D. *Philosophical Magazine* , doi: 10.1080 / 14786430701455321 (2007).

[80] Tschopp, M. and McDowell, D. *Applied Physics Letters* **90**, 121916:1–3 (2007).

[81] Tschopp, M., Spearot, D., and McDowell, D. *Modelling and Simulation in Materials Science and Engineering* , Submitted for publication (2007).

[82] Tschopp, M., Tucker, G., and McDowell, D. *Acta Materialia* **55**, 3959–3969 (2007).

[83] Allen, M. and Tildesley, D. *Computer Simulations of Liquids*. Clarendon Press, Oxford, (1987).

[84] Haile, J. *Molecular Dynamics Simulation: Elementary Methods*. Wiley, New York, (1992).

[85] Metropolis, N. and Ulam, S. *Journal of the American Statistics Association* **44**, 335–341 (1949).

[86] Metropolis, N., Rosenbluth, A. W., Rosenbluth, M. N., Teller, A. H., and Teller, E. *Journal of Chemical Physics* **21**, 1087–1092 (1953).

[87] Vanderplaats, G. *Numerical Optimization Techniques for Engineering Design*. McGraw-Hill, Inc., New York, (1984).

[88] Press, W. *Numerical Recipes: the art of scientific computing*. Cambridge University Press, New York, (1989).

[89] Spearot, D. *Atomistic Calculations of Nanoscale Interface Behavior in FCC Metals*. PhD thesis, Georgia Institute of Technology, (2005).

[90] Rittner, J. D. and Seidman, D. N. *Physical Review B* **54**(10), 6999 (1996).

[91] Rittner, J. D., Seidman, D. N., and Merkle, K. L. *Physical Review B* **53**(8), 4241–4 (1996).

[92] Wolf, D. *Acta Metallurgica* **38**(5), 781–790 (1990).

[93] Verlet, L. *Physical Review* **159**(98-103) (1967).

[94] Hoover, W. *Physical Review A* **31**, 1695–1697 (1985).

[95] Melchionna, S., Ciccotti, G., and Holian, B. L. *Molecular Physics* **78**(3), 533–44 (1993).

[96] Nose, S. *Molecular Physics* **52**(2), 255–68 (1984).

[97] Spearot, D. E., Jacob, K. I., and McDowell, D. L. *Acta Materialia* **53**(13), 3579–89 (2005).

[98] Zhou, M. and McDowell, D. *Philosophical Magazine A* **82**, 2547–2574 (2002).

[99] Zhou, M. *Proceedings of the Royal Society of London A* **459**, 2347–2392 (2003).

[100] Tsai, D. H. *Journal of Chemical Physics* **70**(3), 1375–82 (1979).

[101] Lutsko, J. *Journal of Applied Physics* **64**, 1152–1154 (1988).

[102] Cormier, J., Rickman, J., and Delph, T. *Journal of Applied Physics* **89**(1), 99–104 (2001).

[103] Zimmerman, J., Webb III, E., Hoyt, J., Jones, R., Klein, P., and Bammann, D. *Modelling and Simulation in Materials Science and Engineering* **12**, S319–S332 (2004).

[104] Horstemeyer, M. F., Baskes, M. I., and Plimpton, S. J. *Theoretical and Applied Fracture Mechanics* **37**(1-3), 49–98 (2001).

[105] Horstemeyer, M. F., Baskes, M. I., and Plimpton, S. J. *Acta Materialia* **49**(20), 4363–74 (2001).

[106] Kelchner, C. L., Plimpton, S. J., and Hamilton, J. C. *Physical Review B* **58**(17), 11085–8 (1998).

[107] Zimmerman, J. A., Kelchner, C. L., Klein, P. A., Hamilton, J. C., and Foiles, S. M. *Physical Review Letters* **87**(16), 165507–1 (2001).

[108] Daw, M. S. and Baskes, M. I. *Physical Review Letters* **50**(17), 1285–8 (1983).

[109] Daw, M. S. and Baskes, M. I. *Physical Review B* **29**(12), 6443–53 (1984).

[110] Stott, M. J. and Zaremba, E. *Physical Review B* **22**(4), 1564–1583 (1980).

[111] Norskov, J. K. *Physical Review B* **26**(6), 2875–2885 (1982).

[112] Foiles, S. M., Baskes, M. I., and Daw, M. S. *Physical Review B* **33**(12), 7983–91 (1986).

[113] Daw, M. S., Foiles, S. M., and Baskes, M. I. *Materials Science Reports* **9**(7-8), 251–310 (1993).

[114] Baskes, M. *Physical Review Letters* **59**, 2666–2669 (1987).

[115] Baskes, M., Nelson, J., and Wright, A. *Physical Review B* **40**, 6085–6100 (1989).

[116] Baskes, M. *Physical Review B* **46**, 2727–2742 (1992).

[117] Baskes, M. and Johnson, R. *Modelling and Simulation in Materials Science and Engineering* **2**, 147–163 (1994).

[118] Sundquist, B. E. *Acta Metallurgica* **12**(1), 67–& (1964).

[119] Grenga, H. E. and Kumar, R. *Surface Science* **61**(1), 283–290 (1976).

[120] Mae, K., Nobata, T., Ishida, H., Motoyama, S., and Hiwatari, Y. *Modelling and Simulation in Materials Science and Engineering* **10**(2), 205–214 (2002).

[121] Lee, B. J. and Baskes, M. I. *Physical Review B* **62**(13), 8564–8567 (2000).

[122] Lee, B. J., Baskes, M. I., Kim, H., and Cho, Y. K. *Physical Review B* **6418**(18) (2001).

[123] Lee, S. B., Sigle, W., and Ruhle, M. *Acta Materialia* **51**(15), 4583–8 (2003).

[124] Mishin, Y., Mehl, M. J., Papaconstantopoulos, D. A., Voter, A. F., and Kress, J. D. *Physical Review B* **63**(22), 224106–1 (2001).

[125] Mishin, Y., Farkas, D., Mehl, M. J., and Papaconstantopoulos, D. A. *Physical Review B* **59**(5), 3393–407 (1999).

[126] Rice, J. R. *Journal of the Mechanics and Physics of Solids* **40**(2), 239–71 (1992).

[127] Zimmerman, J. A., Gao, H., and Abraham, F. F. *Modelling and Simulation in Materials Science and Engineering* **8**(2), 103–15 (2000).

[128] Hartford, J., von Sydow, B., Wahnstrom, G., and Lundqvist, B. I. *Physical Review B* **58**(5), 2487–2496 (1998).

[129] Voter, A. F. and Chen, S. P. Characterization of Defects in Materials Symposium, 175–80 (Mater. Res. Soc, Boston, MA, USA, 1987).

[130] Ercolessi, F. and Adams, J. B. *Europhysics Letters* **26**(8), 583–8 (1994).

[131] Liu, X.-Y., Ercolessi, F., and Adams, J. B. *Modelling and Simulation in Materials Science and Engineering* **12**(4), 665–670 (2004).

[132] Frøseth, A. G., Derlet, P. M., and Van Swygenhoven, H. *Acta Materialia* **52**(20), 5863–70 (2004).

[133] Boyer, R., Li, J., Ogata, S., and Yip, S. *Modelling and Simulation in Materials Science and Engineering* **12**(5), 1017–1029 (2004).

[134] Jonsson, H. and Andersen, H. *Physical Review Letters* **60**, 2295–2298 (1988).

[135] Clarke, A. and Jonsson, H. *Physical Review E* **47**, 3975–3984 (1993).

[136] Bulatov, V. and Cai, W. *Physical Review Letters* **89**, 115501:1–4 (2002).

[137] Li, J., Ngan, A. H. W., and Gumbsch, P. *Acta Materialia* **51**(19), 5711–42 (2003).

[138] Van Swygenhoven, H. and Weertman, J. R. *Materials Today* **9**(5), 24–31 (2006).

[139] Spearot, D. E., Jacob, K. I., and McDowell, D. L. *International Journal of Plasticity* **23**(1), 143–160 (2007).

[140] Van Swygenhoven, H., Derlet, P. M., and Hasnaoui, A. *Advanced Engineering Materials* **5**(5), 345–50 (2003).

[141] Van Swygenhoven, H., Derlet, P. M., and Hasnaoui, A. *Physical Review B* **66**(2), 024101–1 (2002).

[142] Yamakov, V., Wolf, D., Phillpot, S. R., and Gleiter, H. *Acta Materialia* **51**(14), 4135–47 (2003).

[143] Ogata, S., Ju, L., and Yip, S. *Science* **298**(5594), 807–11 (2002).

[144] Bollmann, W. *Crystal Defects and Crystalline Interfaces*. Springer-Verlag, Berlin, (1970).

[145] Wang, G., Sutton, A. P., and Vitek, V. *Acta Metallurgica* **32**(7), 1093–104 (1984).

[146] Chandra, N. and Dang, P. *Journal of Materials Science* **34**(4), 655–666 (1999).

[147] Hasson, G., Boos, J. Y., Herbeuval, I., Biscondi, M., and Goux, C. *Surface Science* **31**, 115–37 (1971).

[148] Sutton, A. P. and Vitek, V. *Philosophical Transactions of the Royal Society of London A* **309**(1506), 1–36 (1983).

[149] Medlin, D. L., Mills, M. J., Stobbs, W. M., Daw, M. S., and Cosandey, F. *Proceedings of the Materials Research Society* **295**, 91–6 (1993).

[150] Mills, M. J., Daw, M. S., Thomas, G. J., and Cosandey, F. *Ultramicroscopy* **40**(3), 247–257 (1992).

[151] Bachurin, D., Murzaev, R., and Nazarov, A. *The Physics of Metals and Metallography* **96**(6), 551–61 (2003).

[152] Tomar, V. and Zhou, M. *Journal of Mechanics and Physics of Solids* **55**(5), 1053–1085 (2007).

[153] Randle, V. *The Measurement of Grain Boundary Geometry*. Institute of Physics Publishing, Bristol, (1993).

[154] Sutton, A. P. and Balluffi, R. W. *Interfaces in Crystalline Materials*. Clarendon Press, Oxford, (1995).

[155] Watanabe, T. *Materials Science and Engineering A* **176**(1-2), 39–49 (1994).

[156] Palumbo, G., King, P. J., Aust, K. T., Erb, U., and Lichtenberger, P. C. *Scripta Metallurgica et Materialia* **25**(8), 1775–80 (1991).

[157] Watanabe, T., Tsurekawa, S., Kobayashi, S., and Yamaura, S. *Materials Science and Engineering A* **410-411**, 140–7 (2005).

[158] Wolf, U., Ernst, F., Muschik, T., Finnis, M. W., and Fischmeister, H. F. *Philosophical Magazine A* **66**(6), 991–1016 (1992).

[159] Ernst, F., Finnis, M. W., Koch, A., Schmidt, C., Straumal, B., and Gust, W. *Zeitschrift Für Metallkunde* **87**(11), 911–22 (1996).

[160] Minkwitz, C., Herzig, C., Rabkin, E., and Gust, W. *Acta Materialia* **47**(4), 1231–9 (1999).

[161] Miyamoto, H., Ikeuchi, K., and Mimaki, T. *Scripta Materialia* **50**(12), 1417–1421 (2004).

[162] Randle, V. *Acta Materialia* **46**(5), 1459–80 (1997).

[163] Randle, V. *Scripta Materialia* **54**(6), 1011–1015 (2006).

[164] Saylor, D. M., El Dasher, B. S., Rollett, A. D., and Rohrer, G. S. *Acta Materialia* **52**(12), 3649–3655 (2004).

[165] Kim, C.-S., Hu, Y., Rohrer, G. S., and Randle, V. *Scripta Materialia* **52**(7), 633–7 (2005).

[166] Schwartz, A. J., King, W. E., and Kumar, M. *Scripta Materialia* **54**(6), 963–968 (2006).

[167] Kumar, M., Schwartz, A. J., and King, W. E. *Acta Materialia* **50**(10), 2599–2612 (2002).

[168] Guyot, B. M. and Richards, N. L. *Materials Science and Engineering A* **395**(1-2), 87–97 (2005).

[169] Molodov, D. A. and Konijnenberg, P. J. *Scripta Materialia* **54**(6), 977–981 (2006).

[170] Deus, A. M., Fortes, M. A., Ferreira, P. J., and Vander Sande, J. B. *Acta Materialia* **50**(13), 3317–30 (2002).

[171] Molodov, D. A., Gottstein, G., Heringhaus, F., and Shvindlerman, L. S. *Scripta Materialia* **37**(8), 1207–13 (1997).

[172] Shen, Y. F., Lu, L., Lu, Q. H., Jin, Z. H., and Lu, K. *Scripta Materialia* **52**(10), 989–994 (2005).

[173] Ma, E., Wang, Y. M., Lu, Q. H., Sui, M. L., Lu, L., and Lu, K. *Applied Physics Letters* **85**(21), 4932–4934 (2004).

[174] Lu, L., Schwaiger, R., Shan, Z. W., Dao, M., Lu, K., and Suresh, S. *Acta Materialia* **53**(7), 2169–79 (2005).

[175] Zhang, X., Misra, A., Wang, H., Nastasi, M., Embury, J. D., Mitchell, T. E., Hoagland, R. G., and Hirth, J. P. *Applied Physics Letters* **84**(7), 1096–1098 (2004).

[176] Zhang, X., Misra, A., Wang, H., Shen, T. D., Nastasi, M., Mitchell, T. E., Hirth, J. P., Hoagland, R. G., and Embury, J. D. *Acta Materialia* **52**(4), 995–1002 (2004).

[177] Zhang, X., Wang, H., Chen, X. H., Lu, L., Lu, K., Hoagland, R. G., and Misra, A. *Applied Physics Letters* **88**(17), 173116 (2006).

[178] Robertson, I. M., Beaudoin, A., Al-Fadhalah, K., Chun-Ming, L., Robach, J., Wirth, B. D., Arsenlis, A., Ahn, D., and Sofronis, P. *Materials Science and Engineering A* **400-401**, 245–50 (2005).

[179] Frøseth, A. G., Derlet, P. M., and Van Swygenhoven, H. *Scripta Materialia* **54**(3), 477–481 (2006).

[180] Frøseth, A. G., Van Swygenhoven, H., and Derlet, P. M. *Acta Materialia* **53**(18), 4847–4856 (2005).

[181] Jin, Z. H., Gumbsch, P., Ma, E., Albe, K., Lu, K., Hahn, H., and Gleiter, H. *Scripta Materialia* **54**(6), 1163–1168 (2006).

[182] Wolf, D. *Acta Metallurgica* **37**(7), 1983–93 (1989).

[183] Wolf, D. *Acta Metallurgica* **37**(10), 2823–33 (1989).

[184] Wolf, D. *Acta Metallurgica et Materialia* **38**(5), 791–8 (1990).

[185] Merkle, K. L. and Wolf, D. *Philosophical Magazine A* **65**(2), 513–30 (1992).

[186] Hofmann, D. and Finnis, M. W. *Acta Metallurgica et Materialia* **42**(10), 3555–3567 (1994).

[187] Schmidt, C., Ernst, F., Finnis, M. W., and Vitek, V. *Physical Review Letters* **75**(11), 2160–3 (1995).

[188] Ernst, F., Finnis, M. W., Hofmann, D., Muschik, T., Schonberger, U., Wolf, U., and Methfessel, M. *Physical Review Letters* **69**(4), 620–623 (1992).

[189] Schmidt, C., Finnis, M. W., Ernst, F., and Vitek, V. *Philosophical Magazine A* **77**(5), 1161–1184 (1998).

[190] Zhang, H., Mendelev, M. I., and Srolovitz, D. J. *Scripta Materialia* **52**(12), 1193–1198 (2005).

[191] Zhang, H. and Srolovitz, D. J. *Acta Materialia* **54**(3), 623–633 (2006).

[192] Nishida, M. and Wayman, C. M. *Metallography* **21**(3), 255–73 (1988).

[193] Wang, Z. G., Zu, X. T., Feng, X. D., Mo, H. Q., and Zhou, J. M. *Materials Letters* **58**(25), 3141–3144 (2004).

[194] Brandon, D. G., Ralph, B., Ranganathan, S., and Wald, M. S. *Acta Metallurgica* **12**(7), 813–821 (1964).

[195] Sutton, A. P. and Balluffi, R. W. *Acta Metallurgica* **35**(9), 2177–2201 (1987).

[196] Wolf, U., Gumbsch, P., Ichinose, H., and Fischmeister, H. F. *Journal de Physique (Paris), Colloque* **C1**(1), 359–366 (1990).

[197] Campbell, G. H., Chan, D. K., Medlin, D. L., Angelo, J. E., and Carter, C. B. *Scripta Materialia* **35**(7), 837–42 (1996).

[198] Marquis, E. A., Hamilton, J. C., Medlin, D. L., and Leonard, F. *Physical Review Letters* **93**(15), 156101–1 (2004).

[199] Straumal, B. B., Semenov, V. N., Khruzhcheva, A. S., and Watanabe, T. *Journal of Materials Science* **40**(4), 871–874 (2005).

[200] Barg, A. I., Rabkin, E., and Gust, W. *Acta Metallurgica et Materialia* **43**(11), 4067–74 (1995).

[201] Straumal, B. B., Polyakov, S. A., and Mittemeijer, E. J. *Acta Materialia* **54**(1), 167–172 (2006).

[202] Straumal, B. B., Polyakov, S. A., Bischoff, E., Gust, W., and Baretzky, B. *Acta Materialia* **53**(2), 247–54 (2005).

[203] Straumal, B. B., Polyakov, S. A., Bischoff, E., Gust, W., and Mittemeijer, E. J. *Interface Science* **9**(3-4), 287–292 (2001).

[204] Hsieh, T. E. and Balluffi, R. W. *Acta Metallurgica* **37**(8), 2133–2139 (1989).

[205] Herring, C. *Physical Review* **82**(1), 87 (1951).

[206] Brokman, A., Bristowe, P. D., and Balluffi, R. W. *Scripta Metallurgica* **15**(2), 201–6 (1981).

[207] Bishop, G. H. and Chalmers, B. *Scripta Metallurgica* **2**(2), 133–40 (1968).

[208] Sutton, A. P. and Vitek, V. *Philosophical Transactions of the Royal Society of London A* **309**(1506), 55–68 (1983).

[209] Kronberg, M. L. and Wilson, F. H. *American Institute of Mining and Metallurgical Engineers - Journal of Metals* **1**(8, Sec 3), 501–514 (1949).

[210] Sutton, A. P. *Acta Metallurgica* **36**(5), 1291–1299 (1988).

[211] Duparc, O., Poulat, S., Larere, A., Thibault, J., and Priester, L. *Philosophical Magazine A* **80**(4), 853–70 (2000).

[212] Medlin, D. L., Campbell, G. H., and Carter, C. R. *Acta Materialia* **46**(14), 5135–42 (1998).

[213] Medlin, D. L., Foiles, S. M., and Cohen, D. *Acta Materialia* **49**(18), 3689–97 (2001).

[214] Carter, C. B., Medlin, D. L., Angelo, J. E., and Mills, M. J. *Materials Science Forum* **207-209**, 209–12 (1996).

[215] Hirth, J. and Lothe, J. *Theory of Dislocations*. John Wiley and Sons, New York, (1982).

[216] Ortiz, M. *Transactions of the ASME. Journal of Applied Mechanics* **66**(2), 289–98 (1999).

[217] Koslowski, M. and Ortiz, M. *Modelling and Simulation in Materials Science and Engineering* **12**(6), 1087–97 (2004).

[218] Koslowski, M., Cuitino, A. M., and Ortiz, M. *Journal of the Mechanics and Physics of Solids* **50**(12), 2597–2635 (2002).

[219] Wang, Y. U., Jin, Y. M., Cuitino, A. M., and Khachaturyan, A. G. *Acta Materialia* **49**(10), 1847–57 (2001).

[220] Shen, C. and Wang, Y. *Acta Materialia* **52**(3), 683–691 (2004).

[221] Wolf, D. *Philosophical Magazine A* **62**(4), 447–464 (1990).

[222] Wolf, D. *Journal of Materials Research* **5**(8), 1708–1730 (1990).

[223] Wolf, D. *Acta Metallurgica* **32**(2), 245–258 (1984).

[224] Wolf, D. *Acta Metallurgica* **32**(5), 735–748 (1984).

[225] Schwartz, D., Bristowe, P. D., and Vitek, V. *Acta Metallurgica* **36**(3), 675–687 (1988).

[226] Seki, A., Hellman, O., and Tanaka, S.-i. *Scripta Materialia* **34**(12), 1867–1870 (1996).

[227] Otsuki, A. *Acta Materialia* **49**(10), 1737–1745 (2001).

[228] Zhang, J.-M., Wei, X.-M., and Xin, H. *Applied Surface Science* **243**(1-4), 1–6 (2005).

[229] Wei, X.-M., Zhang, J.-M., and Xu, K.-W. *Applied Surface Science* **253**(2), 854–858 (2006).

[230] Wei, X.-M., Zhang, J.-M., and Xu, K.-W. *Applied Surface Science* **252**(20), 7331–7336 (2006).

[231] Saylor, D. M., Morawiec, A., and Rohrer, G. S. *Acta Materialia* **51**, 3663–3674 (2003).

[232] Rohrer, G., Randle, V., Kim, C., and Hu, Y. *Acta Materialia* **54**, 4489–4502 (2006).

[233] Kim, C.-S., Rollett, A. D., and Rohrer, G. S. *Scripta Materialia* **54**(6), 1005–1009 (2006).

[234] Rohrer, G., Saylor, D. M., El Dasher, B., Adams, B. L., Rollett, A. D., and Wynblatt, P. *Zeitschrift Für Metallkunde* **95**, 197–214 (2004).

[235] Goukon, N., Yamada, T., and Kajihara, M. *Acta Materialia* **48**(11), 2837–2842 (2000).

[236] Wolf, D. and Merkle, K. *Materials Interfaces (eds D. Wolf and S. Yip*. Chapman & Hall, London, (1992).

[237] Muschik, T., Laub, W., Finnis, M. W., and Gust, W. *Zeitschrift Für Metallkunde* **84**(9), 596–604 (1993).

[238] Zhang, J., Ma, F., and Xu, K. *Applied Surface Science* **229**, 34–42 (2004).

[239] Merkle, K. L. *J. Phys. Chem. Solids* **55**, 991 (1994).

[240] Clarebrough, L. M. and Forwood, C. T. *Physica Status Solidi a-Applied Research* **60**(1), 51–57 (1980).

[241] Forwood, C. T. and Clarebrough, L. M. *Acta Metallurgica* **32**(5), 757–771 (1984).

[242] Goodhew, P. J., Tan, T. Y., and Balluffi, R. W. *Acta Metallurgica* **26**(4), 557–567 (1978).

[243] Krakow, W., Wetzel, J. T., and Smith, D. A. *Philosophical Magazine A* **53**(5), 739–754 (1986).

[244] Tschopp, M., Tucker, G., and McDowell, D. In *TMS 2007 Symposium Proceedings: Plasticity from the Atomic Scale to Constitutive Laws*, (2007).

[245] King, A. H. and Smith, D. A. *Acta Crystallographica A* **A36**, 335–43 (1980).

[246] Duparc, O. H., Couziniè, J.-P., Thibault-Pènisson, J., Lartigue-Korinek, S., Dècamps, B., and Priester, L. *Acta Materialia* **55**(5), 1791–1800 (2007).

[247] Tewari, A., Gokhale, A. M., Spowart, J. E., and Miracle, D. B. *Acta Materialia* **52**(2), 307–19 (2004).

[248] Poulat, S., Thibault, J., and Priester, L. *Interface Science* **8**(1), 5–15 (2000).

[249] Medlin, D. L., Carter, C. B., Angelo, J. E., and Mills, M. J. *Philosophical Magazine A* **75**(3), 733–747 (1997).

[250] Medlin, D. L. In *Advances in Twinning*, Ankem, S. and Pande, C., editors, volume 46, 29–40. TMS, (1999).

[251] Foiles, S. M. and Medlin, D. L. volume A319-321 of *Mater. Sci. Eng. A, Struct. Mater., Prop. Microstruct. Process. (Switzerland)*, 102–6 (Elsevier, Asilomar, CA, USA, 2001).

[252] Marquis, E. A. and Medlin, D. L. *Philosophical Magazine Letters* **85**(8), 387–394 (2005).

[253] Brandon, D. G. *Acta Metallurgica* **14**(11), 1479–1484 (1966).

[254] Couziniè, J. P., Dècamps, B., and Priester, L. *International Journal of Plasticity* **21**(4), 759–75 (2005).

[255] Goux, C. *Canadian Metallurgical Quarterly* **13**(1), 9–31 (1974).

[256] Zhu, T., Li, J., Samanta, A., Kim, H. G., and Suresh, S. *Proceedings of the National Academy of Sciences* **104**(9), 3031–3036 (2007).

[257] Hosford, W. *The mechanics of crystals and textured polycrystals*. Oxford University Press, New York, (1993).

[258] Krenn, C. R., Roundy, D., Morris, J. W., J., and Cohen, M. L. volume A319-321 of *Mater. Sci. Eng. A, Struct. Mater., Prop. Microstruct. Process. (Switzerland)*, 111–14 (Elsevier, Asilomar, CA, USA, 2001).

[259] Roundy, D., Krenn, C. R., Cohen, M. L., and Morris, J. W., J. *Physical Review Letters* **82**(13), 2713–16 (1999).

[260] Tschopp, M. and McDowell, D. In *Proceedings of the 16th European Conference of Fracture*, Gdoutos, E., editor, (2006).

[261] Dimiduk, D., Woodward, C., LeSar, R., and Uchic, M. *Science* **312**, 1188–1190 (2006).

[262] Uchic, M., Dimiduk, D., Florando, J., and Nix, W. *Science* **305**, 986–989 (2004).

[263] Uchic, M. and Dimiduk, D. *Materials Science and Engineering A* **400-401**, 268–278 (2005).

[264] Volkert, C. A. and Lilleodden, E. T. *Philosophical Magazine* **86**(33-35), 5567–5579 (2006).

[265] Volkert, C. A., Lilleodden, E. T., Kramer, D., and Weissmuller, J. *Applied Physics Letters* **89**(6) (2006).

[266] Humphrey, W., Dalke, A., and Schulten, K. *Journal of Molecular Graphics* **14**, 33–38 (1996).

[267] Leach, A. M., McDowell, M., and Gall, K. *Advanced Functional Materials* **17**(1), 45–53 (2007).

[268] Shenoy, M., Gordon, A., McDowell, D., and Neu, R. *Journal of Engineering Materials and Technology* **127**(3), 325–336 (2005).

[269] Shenoy, M., Kumar, R., and McDowell, D. *International Journal of Fatigue* **27**(2), 113–127 (2005).

[270] Vitek, V. *Phys. Status Solidi* **18**, 687–701 (1966).

[271] Vitek, V. *Philosophical Magazine* **18**, 773–786 (1968).

[272] Hirth, J. P. and Pond, R. C. *Acta Materialia* **44**(12), 4749–4763 (1996).

[273] Asaro, R. and Suresh, S. *Acta Materialia* **53**, 3369–3382 (2005).

[274] Zhu, T., Li, J., Samanta, A., Leach, A., and Gall, K. *Nature Materials* **(submitted for publication)** (2007).

[275] Wang, Y. M. and Ma, E. *Materials Science and Engineering A* **375-377**, 46–52 (2004).

[276] Wang, Y. M., Hamza, A., and Ma, E. *Acta Materialia* **54**, 2715–2726 (2006).

[277] Schuh, C. A., Mason, J. K., and Lund, A. C. *Nature Materials* **4**(8), 617–621 (2005).

[278] Kogure, Y., Kosugi, T., Doyama, M., and Kaburaki, H. *Materials Science and Engineering A* **442**, 71–74 (2006).

[279] Conrad, H. and Jung, K. *Materials Science and Engineering A* **391**, 272–284 (2005).

[280] Lim, L. C. *Acta Metallurgica* **35**(7), 1653–1662 (1987).

[281] Field, D. P. and Adams, B. L. *Acta Metallurgica Et Materialia* **40**(6), 1145–1157 (1992).

[282] Palumbo, G. and Aust, K. T. *Acta Metallurgica Et Materialia* **38**(11), 2343–2352 (1990).

[283] Watanabe, T., Yamada, M., and Karashima, S. *Philosophical Magazine A* **63**(5), 1013–1022 (1991).

[284] Watanabe, T. and Tsurekawa, S. *Acta Materialia* **47**(15-16), 4171–4185 (1999).

[285] Krenn, C. R., Roundy, D., Morris J.W, J., and Cohen, M. L. *Materials Science and Engineering A* **317**(1-2), 44–48 (2001).

[286] Cai, W., Bulatov, V. V., Chang, J. P., Li, J., and Yip, S. *Philosophical Magazine* **83**(5), 539–567 (2003).

[287] Grigoriadis, P., Karakostas, T., Komninou, P., and Pontikis, V. *Materials Science Forum* **294-2**, 177–180 (1999).

[288] Steinmann, P., Kuhl, E., and Stein, E. **35**(33), 4437–56 (1998).

[289] Van Swygenhoven, H. and Caro, A. *Physical Review B* **58**(17), 11246–51 (1998).

[290] Wang, W. and Lu, K. *Philosophical Magazine* **86**(33-35), 5309–5320 (2006).

[291] Chen, J., Wang, W., Qian, L., and Lu, K. *Scripta Materialia* **49**, 645–650 (2003).

[292] Gerberich, W., Nelson, J., Lilleodden, E., Anderson, P., and Wyrobek, J. *Acta Metallurgica et Materialia* **44**(9), 3585–3598 (1996).

[293] de la Fuente, O. R., Zimmerman, J. A., González, M. A., de la Figuera, J., Hamilton, J. C., Pai, W. W., and Rojo, J. M. *Physical Review Letters* **88**(3), 036101 Jan (2002).

[294] Xu, D. S., Yang, R., Li, J., Chang, J. P., Wang, H., Li, D., and Yip, S. *Computational Materials Science* **36**(1-2), 60–64 (2006).

[295] Li, J., Van Vliet, K., Zhu, T., Yip, S., and Suresh, S. *Nature* **418**(6895), 307–310 (2002).

[296] Van Vliet, K. J., Ju, L., Ting, Z., Yip, S., and Suresh, S. *Physical Review B* **67**(10), 104105–1 (2003).

[297] Zhu, T., Li, J., Van Vliet, K. J., Ogata, S., Yip, S., and Suresh, S. *Journal of the Mechanics and Physics of Solids* **52**(3), 691–724 (2004).

[298] Miller, R. and Acharya, A. *Journal of the Mechanics and Physics of Solids* **52**, 1507–1525 (2004).

[299] Van der Giessen, E. and Needleman, A. *Modelling and Simulation in Materials Science and Engineering* **3**(5), 689–735 (1995).

[300] Zbib, H., Rhee, M., and Hirth, J. *International Journal of Mechanical Science* **40**, 113–127 (1998).

[301] Rhee, M., Zbib, H. M., Hirth, J. P., Huang, H., and de la Rubia, T. *Modelling and Simulation in Materials Science and Engineering* **6**(4), 467–492 (1998).

[302] Duesberry, M. and Vitek, V. *Acta Materialia* **46**, 1481–1492 (1998).

[303] Ito, K. and Vitek, V. *Philosophical Magazine A* **81**(5), 1387–1407 (2001).

[304] Qin, Q. and Bassani, J. *Journal of the Mechanics and Physics of Solids* **40**(4), 813–33 (1992).

[305] Lund, A. C. and Schuh, C. A. *Acta Materialia* **51**(18), 5399–5411 (2003).

[306] Fatemi, A. and Socie, D. *Fatigue Fract Eng Mater Struct* **11**, 149–165 (1988).

[307] Diao, J., Gall, K., and Dunn, M. L. *Nano Letters* **4**(10), 1863–1867 (2004).

[308] Tomar, V. and Zhou, M. *Applied Physics Letters* **88**(23), 233107 (2006).

[309] Lund, A. C., Nieh, T. G., and Schuh, C. A. *Physical Review B* **69**(1), 12101–1 (2004).

[310] Lund, A. C. and Schuh, C. A. *Acta Materialia* **53**(11), 3193–3205 (2005).

[311] Xu, G. and Argon, A. *Philosophical Magazine Letters* **80**(9), 605–611 (2000).

[312] Xu, G. and Argon, A. *Materials Science and Engineering A* **319-321**, 144–147 (2001).

[313] Gutkin, M. Y. and Ovid'ko, I. A. *Applied Physics Letters* **88**, 211901:1–3 (2006).

[314] Lilleodden, E. T., Zimmerman, J. A., Foiles, S. M., and Nix, W. D. *Journal of the Mechanics and Physics of Solids* **51**(5), 901–920 (2003).

[315] Mason, J. K., Lund, A. C., and Schuh, C. A. *Physical Review B (Condensed Matter and Materials Physics)* **73**(5), 54102–1 (2006).

[316] Zuo, L., Ngan, A. H. W., and Zheng, G. P. *Physical Review Letters* **94**, 095501:1–4 (2005).

[317] Park, H. S., Gall, K., and Zimmerman, J. A. *Journal of the Mechanics and Physics of Solids* **54**(9), 1862–1881 (2006).

# VITA

Mark A. Tschopp Jr. received both his B.S. (summa cum laude) and his M.S in Metallurgical Engineering from the University of Missouri-Rolla. Following graduation with his M.S. degree, Mark worked at General Motors Powertrain in the Advanced Materials Development Center (AMDC) and the Casting Development and Validation Center (CDVC) in Saginaw, MI. While at General Motors, Mark worked with the Saginaw Metal Casting Operations in Saginaw, MI and GM Powertrain-Defiance in Defiance, OH. After several years in industry, he returned to academia to pursue his Ph.D. in Materials Science and Engineering from Georgia Institute of Technology. Mark Tschopp was married to Meredith A. Manley on July $5^{th}$, 2003 and their first son, Samuel Becher Tschopp, was born on December $19^{th}$, 2006.